2009

Development of a Fluoroscopic Radiostereometric Analysis System With an Application to Glenohumeral Joint Kinematics

Angela E. Kedgley

DEVELOPMENT OF A FLUOROSCOPIC RADIOSTEREOMETRIC ANALYSIS SYSTEM WITH AN APPLICATION TO GLENOHUMERAL JOINT KINEMATICS

(SPINE TITLE: DEVELOPMENT AND APPLICATION OF A FLUOROSCOPIC RSA SYSTEM)

(Thesis Format: Integrated Article)

by

Angela E. Kedgley

Department of Mechanical and Materials Engineering
Graduate Program in Engineering Science

Submitted in partial fulfillment
of the requirements for the degree of
Doctor of Philosophy

The School of Graduate and Postdoctoral Studies
The University of Western Ontario
London, Ontario, Canada
December, 2009

ABSTRACT

Ideally, joint kinematics should be measured with high accuracy, void of skin motion artefact, in three dimensions, and under dynamic conditions. Radiostereometric analysis (RSA) has the potential to fulfill all of these requirements. The objectives of this thesis were (1) to implement and validate a fluoroscopy-based RSA system, (2) to determine the effect of varying the calibration frame, (3) to correct image distortion, (4) to investigate errors in coordinate system creation for glenohumeral (shoulder) joint kinematics, (5) to introduce a new coordinate system definition for the scapula with limited radiation exposure, and (6) to use RSA to examine glenohumeral joint motions *in-vivo*.

An RSA system consisting of two portable C-arm fluoroscopy units and two personal computers was assembled. Calibration was performed using a custom-made calibration frame. Images were digitized and RSA reconstruction was performed using custom-written software.

Images taken using fluoroscopy under ideal conditions can produce reconstructions that are as accurate as those taken with digital radiography, with standard errors of measurement of 43μm and 0.23° and 36μm and 0.12°, respectively. RSA is more accurate than optical tracking for rigid body motion. The fluoroscopes may be positioned at angles less than 135° without affecting the accuracy of reconstruction. A global polynomial approach to distortion correction is appropriate for use with RSA; however, the polynomial degree must be determined for each system with an independent accuracy measure.

An alternative scapular coordinate system was introduced to decrease the required radiation exposure for coordinate system creation by approximately half. The kinematic angles obtained using the alternative coordinate system were different from those obtained using the International Society of Biomechanics standard; however, the differences are not clinically significant.

As a first clinical application, glenohumeral joint translation was examined. The preliminary data suggests that humeral head position does not differ in active and static joint positioning.

Fluoroscopy allows subjects to be examined while in motion and should enable substantial improvements to the study of even subtle *in-vivo* kinematics. It is likely that the RSA system will lead to an increased understanding of the effects of disease progression, surgical techniques and rehabilitation protocols on joint motion.

Keywords: fluoroscopy; radiostereometric analysis (RSA); calibration; distortion correction; scapula coordinate system; kinematics

CO-AUTHORSHIP

This work could not have been completed without the assistance of others, whom the author thankfully acknowledges. The contributions that they have made are detailed below.

Chapter 1: Angela Kedgley – wrote manuscript; Cynthia Dunning – reviewed and revised manuscript; James Johnson – reviewed and revised manuscript; Thomas Jenkyn – reviewed and revised manuscript.

Chapter 2: Angela Kedgley – designed system and wrote manuscript; Cynthia Dunning – reviewed and revised manuscript; James Johnson – reviewed and revised manuscript; Thomas Jenkyn – designed system and reviewed and revised manuscript.

Chapter 3: Angela Kedgley – designed study, collected data, analyzed data, and wrote manuscript; Anne-Marie Allen – collected data; Adam Crymble – collected data; Trevor Birmingham – designed study, reviewed data, and reviewed and revised manuscript; Thomas Jenkyn – designed study, reviewed data and reviewed and revised manuscript.

Chapter 4: Angela Kedgley – designed study, collected data, analyzed data, and wrote manuscript; Adam Crymble – collected data; Thomas Jenkyn – designed study, reviewed data, and reviewed and revised manuscript.

Chapter 5: Angela Kedgley – designed study, collected data, analyzed data, and wrote manuscript; Adam Crymble – collected data; Anne-Marie Allen – collected data, and reviewed and revised manuscript; Thomas Jenkyn – designed study, reviewed data, and reviewed and revised manuscript.

Chapter 6: Angela Kedgley – designed study, collected data, analyzed data, and wrote manuscript; Cynthia Dunning – designed study, reviewed data, and reviewed and revised manuscript.

Chapter 7: Angela Kedgley – designed study, collected data, analyzed data, and wrote manuscript; Anne-Marie Allen – collected data; Adam Crymble – collected data; Kristin Whitney – collected data; John Henry – operated fluoroscopes; Marie-Eve LeBel – designed study and performed surgeries; George Athwal – designed study and performed surgeries; Cynthia Dunning – reviewed and revised manuscript; James Johnson – reviewed and revised manuscript; Thomas Jenkyn – designed study and reviewed and revised manuscript;

Chapter 8: Angela Kedgley – wrote manuscript; Cynthia Dunning – reviewed and revised manuscript; James Johnson – reviewed and revised manuscript; Thomas Jenkyn – reviewed and revised manuscript.

TABLE OF CONTENTS

LIST OF TABLES

LIST OF FIGURES

LIST OF APPENDICES

LIST OF ABBREVIATIONS, SYMBOLS AND NOMENCLATURE

° – degree(s)

% – percent

2D – two-dimensional

3D – three-dimensional

α – humeral elevation angle

β – rotation angle to the humeral plane of elevation

γ – angle of humeral rotation about the shaft of the humerus

μm – micrometre(s)

AA – acromial angle

AC – acromioclavicular joint

ANOVA – analysis of variance

c - cosine

CAD – computer-aided design

CF-90, CF-105, CF-120, and CF-135 – angular configurations of the calibration frame

cm – centimetre(s)

CMM – coordinate measuring machine

CT – computed tomography

DLT – direct linear transform

DOF – degree(s) of freedom

EvaRT – EVa Real-Time

f – focal point

FL-90, FL-105, FL-120, and FL-135 – angular configurations of the fluoroscopy units

fRSA – fluoroscopic radiostereometric analysis

HH – humeral head centre

hum – humerus

Hz – hertz

I_3 – identity matrix (3 by 3)

IA – inferior angle

ICC – intraclass correlation coefficient

II – image intensifier

ISB – International Society of Biomechanics

kV – kilovolt

LE – lateral epicondyle

mA - milliampere

ME – medial epicondyle

MIMICS – Materialise's Interactive Medical Image Control System

mm – millimetre(s)

mpg – moving picture experts group

MRI – magnetic resonance imaging

ms – millisecond(s)

O – origin vector

OP – object point

PC – coracoid process

${}^{y}_{x}R$ – rotation matrix expressing x with respect to y (3 by 3)

RMS – root mean squared

ROM – range of motion

rot - rotation

RSA – radiostereometric analysis

s – sine or second(s)

SA – superior angle

scap – scapula

SN – scapular notch

SRCC – Spearman rank correlation coefficient

${}^{y}_{x}T$ – transformation matrix expressing x with respect to y (4 by 4)

tiff – tagged image file format

TS – trigonum spinae scapulae

WOQIL - Wolf Orthopaedic Quantitative Imaging Laboratory

CHAPTER 1 – INTRODUCTION

OVERVIEW: Orthopaedic biomechanics research is not a new field but the tools of study have been rapidly evolving. This chapter describes the most common methods presently in use for quantifying joint kinematics, and outlines the evolution of radiostereometric analysis as well as its current uses. It then provides a brief description of the anatomical background of the shoulder that is required for Chapters 6 and 7, focusing on the glenohumeral joint, and the techniques that have been used to study its kinematics. The chapter concludes with the rationale, objectives and hypotheses of this work.[1]

1.1 TRADITIONAL BIOMECHANICAL ANALYSIS METHODS

Biomechanics is the application of mechanical principles and methods to living creatures (see Hoffman, 2009). Its study has been of interest to scientists and researchers for more than two thousand years, as evidenced by the works of Aristotle (384-322 BC; see Fung, 1968), da Vinci (1452-1519; see Simpson, 2009), Galileo (1564-1642; see Fung, 1968), Borelli (1608-1679; see Andriacchi and Alexander, 2000), and Thompson (1860-1948; see Mow and Huiskes, 2005), to name a few. Orthopaedics literally means "to straighten children" (see Mow and Huiskes, 2005), but today it has a much broader meaning, encompassing the protection and restoration of all parts of the skeletal system, including its ligaments, joints, and other structures, for people young and old. While the base of knowledge in orthopaedic biomechanics has steadily expanded, and technology

[1] Specialized terminology found in this and the subsequent chapters is defined in Appendix A.

has certainly progressed, many questions still remain about disease progression, compensation, and recovery.

The study of biomechanics consists of two distinct parts: kinematics and kinetics. Kinematics is the study of motions without reference to the forces that cause those motions, while kinetics is the study of the forces (see Winter, 2005a). In this thesis the motions of interest are specifically those of the bones of the human body. This thesis will focus on improving the quantification of kinematics only.

There any many techniques that have evolved over the years to assist physicians, surgeons, and scientists in their quest to accurately quantify human joint motion both *in-vivo* and *in-vitro*; however, the measurement of *in-vivo* kinematics arguably poses many more difficulties. The devices that have been used *in-vivo* include goniometers, potentiometers, and inclinometers, photographic and video cameras, optical and electromagnetic tracking systems, and imaging techniques. Each of these has an application for which it is most suitable, along with advantages and drawbacks as described below.

1.1.1 GONIOMETERS, POTENTIOMETERS AND INCLINOMETERS

Perhaps the simplest devices currently in use for determining kinematics are goniometers and inclinometers. A goniometer is a protractor with two long arms that rotate about a central axis, which may be attached to the limb segments on either side of a joint of interest. The joint angle is read manually; therefore, it may only be used for static positions. A potentiometer may be incorporated to allow electronic readings, which may then be used to measure static or dynamic motions. An inclinometer is a device that provides angles relative to horizontal. These may also be read manually or electronically.

Advantages of goniometers and inclinometers include the fact that they are inexpensive, portable and output is instantly available. However, they can measure one angle only, they may be difficult to align correctly with the bones of interest and their measurements are highly dependent upon correctly locating the landmarks with which they are aligned (Armstrong *et al.*, 1998). In addition, goniometers may inhibit the motion of the subject and they generally function only as pure hinges, so they are not useful for measuring complex joint motions or making very precise or accurate measurements, especially on limb segments where there may be a significant mass of soft-tissue between the skin and bone (see Winter, 2005b). When comparing goniometric measurements, the best agreements are found between angles measured by the same investigator, using the same device (Armstrong *et al.*, 1998). Edwards *et al.* (2004) used a goniometer to measure knee flexion on subjects with total knee arthroplasty and found that 22% of readings were more than 5° different from radiographic measurements. Triffitt *et al.* (1999) used an inclinometer to quantify elevation and abduction of the arm and then performed a study of the reproducibility of these same motions. For asymptomatic subjects, the difference between two readings with a 95% confidence interval was 24°–33° (Triffitt *et al.*, 1999). Hence, goniometers and inclinometers are most appropriate for quick, single joint, range of motion (ROM) readings, where high accuracy and precision are not required.

1.1.2 PHOTOGRAPHIC AND VIDEO CAMERAS

Standard high speed photographic and video camera techniques are a simple way of capturing full body motion without interfering with the subject. In North America, standard video cameras have a fixed frame rate of 30 frames per second, while the frame

rate of movie cameras may be varied (see Winter, 2005b). One of the advantages of using film or video cameras is that there is no hindrance to the motion of the subject as there are often no markers. However, if markers are used, many may be employed because they can be very small, and without wires. Furthermore, the systems are portable and reasonably inexpensive. These make photographic and video cameras particularly suitable for the quantification of kinematics during sporting activities, which generally cannot be performed properly in a controlled laboratory environment, and during which markers may interfere with the normal motions. The major drawback is the time required for digitization of the landmarks or markers applied to the subject, as this is typically done manually (see Winter, 2005b). Without the use of multiple cameras, measurements may only be made in two dimensions. In addition, projection errors may occur with the use of a single camera, as the motion of the subject may not be exactly in line with the camera (Bechard *et al.*, 2009), and when using a video camera, the limited sample rate may be an issue. Standard video cameras have recently been used for a variety of applications, with some examples being to examine the rowing stroke (Bechard *et al.*, 2009) and the soccer throw-in (Linthorne and Everett, 2006), while high speed video cameras have been used to examine sprint starts (Bradshaw *et al.*, 2007) and the long jump (Bridgett and Linthorne, 2006). The accuracy of kinematic measurements obtained using photographic or video data will vary greatly, and are dependent upon many factors such as the distance from the subject, the use of markers, and the applicability of the sample rate that is used. In order to alleviate the problem of projection errors, the data from two (or more) cameras are combined by calibrating the volume of interest using the

same method as that employed by optical tracking systems, which are described in the section following. This allows kinematics to be quantified in three dimensions.

1.1.3 Optical and Electromagnetic Tracking Systems

To more accurately quantify motion in three dimensions optical and electromagnetic tracking systems are employed. Optical motion analysis systems use a series of cameras that track sets of either passive (light-reflecting) or active (light-emitting) markers. Passive systems, such as the six-camera real-time motion analysis system (Hawk cameras, EVa Real-Time (EVaRT) software system, Motion Analysis Corp., Santa Rosa, California, USA) at the Wolf Orthopaedic Quantitative Imaging Laboratory (WOQIL), track reflective markers. Active systems, such as the Optotrak (Northern Digital Inc., Waterloo, Ontario, Canada), track infrared diodes that may be either wired or wireless. In both cases, markers are placed either directly over anatomical landmarks or on other locations on the body segments of interest.

Generally the positions of the markers are determined using the direct linear transform (DLT) approach, because it provides flexibility in the positioning of the cameras and is reasonably accurate for motions on the order of those observed during gait (Chen *et al.*, 1994). Using this technique, a calibration frame consisting of a set of precisely positioned markers is imaged by all cameras and 11 transformation coefficients are then calculated (Chen *et al.*, 1994). While optical motion analysis systems are generally known for their usage in the study of gait analysis, it has been shown that with specialized calibration, they can be also be used within a small measurement volume with accuracies of up to 0.094 mm (Everaert *et al.*, 1999). An advantage to using an optical motion analysis system when compared with traditional video cameras is that multiple

cameras may be easily employed, increasing the chances of a correct reconstruction. In addition, while some manual identification of the points may be required by the operator during reconstruction, the points themselves are automatically located by the cameras. A disadvantage is the sensitivity of optical systems to interference with the line of sight from the markers to the cameras. Optical motion analysis systems have recently been used to examine the shoulder (Leroux *et al.*, 1992; Klopčar and Lenarčič, 2006; van Andel *et al.*, 2008), spine (Pollock *et al.*, 2009), knee (Hunt *et al.*, 2008; Vanwanseele and Parker, 2009), and foot (Jenkyn and Nicol, 2007; Leardini *et al.*, 2007) *in-vivo*.

Electromagnetic systems, such as the Flock of Birds (Ascension Technologies, Burlington, Vermont, USA) and the FASTRAK (Polhemus, Colchester, Vermont, USA) use a transmitter to track a series of receivers in six degrees of freedom (DOF; *i.e.*, three translations and three rotations). Three sets of orthogonal coils contained in each of the transmitter and receivers enable the determination of both location and orientation. A study conducted by Milne *et al.* (1996) revealed that the Flock of Birds has an optimal operating range where the receivers are between 22.5 cm and 64.0 cm from the transmitter, in which the mean positional error is 0.25 mm and the mean rotational error over a 1° to 20° range is 1.6% of the rotational increment, with a rotational resolution of 0.1°. The advantage of using an electromagnetic system over an optical system is that magnetic fields can pass through most materials, metals excepted, so there does not have to be a direct line of sight between the transmitter and the receivers. Also, each receiver has its own coordinate system; therefore, to track a body segment only one receiver is required, as opposed to three optical markers (McQuade and Smidt, 1998). The disadvantages include the fact that the magnetic fields may be distorted by ferrous

materials, producing errors in locating the positions of the receivers (Meskers *et al.*, 1999). In addition, in most cases the systems are not wireless, and as the study by Milne *et al.* (1996) showed, they have a very restricted optimal operating volume. Despite these limitations they have recently been used to quantify *in-vivo* kinematics of the shoulder (McQuade and Smidt, 1998; Meskers *et al.*, 1998b; Vermeulen *et al.*, 2002; Rundquist *et al.*, 2003; Ebaugh *et al.*, 2005; Fayad *et al.*, 2006; Meskers *et al.*, 2007), the elbow (Van Roy *et al.*, 2005), the spine (Burnett *et al.*, 2008; Ma *et al.*, 2009), and the hip, knee and ankle (Gribble *et al.*, 2009), to name a few joints.

The overall advantages of using either an optical or electromagnetic tracking system include the high sampling frequency and the capacity to be fully dynamic (see Prendergast *et al.*, 2005). The EVaRT system at the WOQIL can sample at up to 200 frames per second, much faster than a standard video camera. Additionally, data are presented in an absolute spatial reference frame (see Winter, 2005b), making analysis less complicated. Disadvantages include the high price of such systems and, in the case of most electromagnetic and some active marker systems, interference of wires, which may result in subjects exhibiting non-representative movement. But worst than these, the main disadvantage of optical and electromagnetic tracking systems is the potential for skin motion artefact.

1.1.4 SKIN MOTION ARTEFACT

Kinematics describe changes in position and orientation of objects with time, in three-dimensional (3D) space. In order to determine the positions of segments relative to one another, each needs to have a coordinate system associated with it. These coordinate systems can then be related to one another. However, it is impossible to place any

marker set in the identical location on two consecutive individuals because human anatomy varies considerably. Therefore, a global coordinate system cannot be employed to compare kinematics between individuals. Consequently, coordinate systems must be created on each bone segment, so that clinically relevant joint kinematics may be determined. In biomechanics, bones are considered to be rigid bodies, so bone-based coordinate systems are created by using osseous landmarks – repeatedly locatable reference points on each bone. Anatomical landmark identification has the potential to introduce errors since landmarks are actually relatively large and are often curved surfaces (Della Croce *et al.*, 1999). Points are preferable over ridges as they are more repeatably digitized (Veeger *et al.*, 2003). At least three non-collinear points on each bone are required for the creation of Cartesian coordinate systems. Anatomical landmark identification for the shoulder is addressed in Chapter 6.

If bony landmarks are to be located, they must be digitized through the skin. Skin motion artefact refers to the errors that are created due to a combination of inertial effects of soft tissue, skin deformation and sliding, and motion due to muscle contractions (Leardini *et al.*, 2005). Detailed joint movement is not possible when skin motion artefact is present because the magnitudes of the errors are larger than those of the measurement systems, are task dependent and not reproducible between subjects (Leardini *et al.*, 2005; Benoit *et al.*, 2006). As a result, to obtain highly accurate results it is only possible to record static positions (de Groot, 1997; Meskers *et al.*, 1998b; Hébert *et al.*, 2000). When comparing the position of the scapula obtained by skin-fixed electromagnetic tracking receivers to that obtained from landmark palpations, Meskers *et al.* (2007) found rotational differences of up to 7° when elevating in the sagittal plane and

up to 13° when elevating in the frontal plane. If skin motion artefact errors are too large they may actually render the results of a kinematic analysis unusable (Benoit *et al.*, 2006). Therefore, optical and electromagnetic tracking devices are best-suited to large-scale motions where small errors are not as relevant.

In order to avoid the problem of skin motion artefact, optical motion analysis systems and electromagnetic systems may be used in conjunction with bone pins (as recently done by Harryman *et al.*, 1992; Lafortune *et al.*, 1992; Reinschmidt *et al.*, 1997; Koh *et al.*, 1998; Karduna *et al.*, 2001; McClure *et al.*, 2001; Bourne *et al.*, 2004; Benoit *et al.*, 2006; Nester *et al.*, 2007). While this technique provides good kinematic data, it is generally too invasive to be practical for larger study sizes. There is the potential risk of infection and subjects may experience discomfort, rendering them unable to move in their normal manner. Also, with large subcutaneous translations, passive motion of the skin and active muscle contractions may interfere with the bone pins by moving or bending them (Karduna *et al.*, 2000; Benoit *et al.*, 2006). For these reasons the use of percutaneous bone pins is relatively rare.

Other solutions to the problem of skin motion artefact have included numerical algorithms based on linear regression (Meskers *et al.*, 1998a), least-squares (Södkervist and Wedin, 1993; Chèze *et al.*, 1995; Veldpaus *et al.*, 1998), filtering (Cerveri *et al.*, 2005), and linear interpolation and approximation (Dumas and Chèze, 2009).

1.1.5 Medical Imaging Techniques

As previously stated, one of the biggest factors limiting the improvement of the study of human joint motion is skin motion artefact (Cappozzo *et al.*, 1996; Andriacchi and Alexander, 2000). Medical imaging techniques have the advantage of allowing the

bones to be viewed directly, removing skin motion artefact. There are three main imaging techniques used in orthopaedic biomechanics. These are plane x-ray and fluoroscopy, computed tomography (CT) and magnetic resonance imaging (MRI).

1.1.5.1 PLANE X-RAY AND FLUOROSCOPY

Plane x-ray images are two-dimensional (2D) projections of an object onto a film, produced by the interaction of x-rays with the various tissues of the body. Fluoroscopes are similar to plane x-rays systems; however, they produce a real-time moving image. Fluoroscopes will be discussed in more detail in Section 2.1. One of the primary advantages of using plane x-rays for imaging studies is their prevalence in medical practice. Among other joints, plane x-rays have recently been used to study kinematics of the knee (Frankel *et al.*, 1971), the shoulder (Poppen and Walker, 1976; Howell *et al.*, 1988; Burkhart, 1992), and the spine (Dunk *et al.*, 2009). Plane fluoroscopy has also recently been used to examine several joints, including the shoulder (Talkhani and Kelly, 2001), the spine (Auerbach *et al.*, 2007), the foot (Wearing *et al.*, 1998), and the knee (Wada *et al.*, 2001).

The disadvantages of using plane x-rays and fluoroscopy include exposure to ionizing radiation. Also, the use of 2D imaging techniques to record a 3D motion has inherent dangers in that projection errors are unavoidable, and it is highly unlikely that the motion will occur exactly in the plane of the image (see Freedman and Munro, 1966; van der Helm and Pronk, 1995; de Groot, 1999). In order to achieve this, the axis of rotation of the chosen joint should be perpendicular to the image plane. However, the axes of most joints are not constantly in one plane throughout a ROM (see Duck *et al.*,

2003), making this requirement impossible to achieve. It may also be difficult to position the subjects precisely in the plane that is required (see Howell *et al.*, 1988).

1.1.5.2 Computed Tomography

A CT scan is obtained by taking a series of x-ray image views that are then reformatted by a computer using the principle of backprojection to obtain images of 'slices' though the object (see Bushberg *et al.*, 2002a). From these images orthogonal projections of the object may be viewed and 3D models of objects can be reconstructed. Because of the time required to obtain all of the images in a CT scan, measurements are generally static. Cine CT scanners have been used to image objects in motion, by repeatedly scanning a single 'slice' of the object (see Shapeero *et al.*, 1988); however, the slice must be selected carefully to obtain the desired information.

Advantages of using CT include the relative ease of obtaining 3D positions of the bones of interest. CT scanners are available in most clinical institutions. The most significant disadvantage of CT scans is the radiation exposure to the patient. This will limit the number of positions that may be imaged. In addition, as stated previously, most scanners are designed to image static objects only. Joint kinematics have been determined using CT scans predominantly at the forearm, wrist, and hand (Wolfe *et al.*, 2000; Baeyens *et al.*, 2006; Leventhal *et al.*, 2008), but also at the ankle (Beimers *et al.*, 2008).

1.1.5.3 Magnetic Resonance Imaging

MRI uses magnetic field gradients and phase offsets to localize nuclear magnetic resonance signals from individual volume elements within a subject, enabling the

creation of images that very clearly distinguish between tissue types (see Bushberg *et al.*, 2002b). Unlike plane x-rays or CT scans, MRI is able to depict cartilage contact areas, ligaments, tendons, and muscle bodies. The advantages of MRI include the fact that it is non-invasive, clinically available, and capable of imaging soft tissues as well as bones (see McPherson *et al.*, 2005). The disadvantages include its expense in terms of both time and money. Image acquisition times of up to five minutes (see von Eisenhart-Rothe *et al.*, 2004) prevent dynamic studies, and may restrict the slice-thickness that is attainable due to subject fatigue (see Patel *et al.*, 2004). The closed-coil magnets of most MRI systems may pose problems for patients with claustrophobia and full weight bearing motions are not possible *in-vivo* in these systems (see McPherson *et al.*, 2005). In addition, in the case where metal implants are present, inhomogeneities in the magnetic field are produced, resulting in distortion of the image (see Patel *et al.*, 2004).

There are also several safety issues associated with MRI scans. These include the presence of strong and varying magnetic fields; the long term effects of which are not well known (see Bushberg *et al.*, 2002b). Within these fields, negative effects may be caused by the substantial torque placed upon implants, prostheses, and pacemakers, and possible heating of non-metallic implant materials which may occur (Bushberg *et al.*, 2002b). The gradient coils also produce considerable noise when in operation, which may make subjects uncomfortable (see Bushberg *et al.*, 2002b).

Kinematics of the knee have been determined using a closed-coil MRI system in a supine position for various flexion angles, up to 60° (Patel *et al.*, 2004) and in an open MRI system up to 90° (Todo *et al.*, 1999; von Eisenhart-Rothe *et al.*, 2004). Kinematics of the shoulder were examined using an open MRI system during static positions of

abduction and a limited number of isometrically loaded abduction positions (Graichen *et al.*, 2000b). Another study examined internal and external rotation of the shoulder in a closed-coil system (Rhoad *et al.*, 1998).

Dynamic studies are possible using cine and cine-phase contrast MRI and have been performed in the shoulder (Bonutti *et al.*, 1993; Cardinal *et al.*, 1996), and the knee (Sheehan *et al.*, 1998). The disadvantage is that due to the extensive time required to capture the images, data is only collected in a single plane. Therefore motion must be very well aligned with the chosen plane or errors will result (see Sheehan *et al.*, 1998).

1.2 RADIOSTEREOMETRIC ANALYSIS

Ideally, joint kinematics should be measured with high accuracy – void of skin motion artefact, in 3D, under dynamic conditions, with minimal time and monetary expense. Radiostereometric analysis (RSA) has the potential to fulfill all of these requirements.

The reconstruction of the 3D positions of objects from coincident pairs of plane x-ray films was first documented in 1898 by Davidson (see Kärrholm, 1989; Selvik, 1989). Two x-rays were taken of an object from different angles, and silk threads were used to connect points on the images to their associated x-ray sources. The threads intersected at the original positions of the points in 3D space. This is possible because the x-rays are not significantly deflected from their straight-line path as they pass through the object of interest (see Selvik, 1989). For quite a time thereafter, stereoscopes were used to measure distances between points within virtual stereoscopic x-ray images, due to the difficulties of identifying corresponding points in the pairs of images (see Selvik, 1989). In the 1960s and 1970s there was a rapid increase in the application of mathematical

theory to photogrammetry. The position of the projection centre and the image plane within a camera was determined, and the use of a calibration object to improve accuracy was introduced (see Selvik, 1989). These methods were then applied to x-ray photogrammetry. In 1974, Selvik published his thesis "Roentgen stereophotogrammetry: A method for the study of the kinematics of the skeletal system" describing the use of "roentgenography" to determine distinct points within an object and to measure small relative displacements (Selvik, 1989). This was the beginning of modern RSA.

1.2.1 TRADITIONAL RSA

Traditional RSA uses two static x-ray views to provide two simultaneous images of the object of interest from different angles. Often, the object of interest has radio-opaque beads (markers) rigidly implanted to aid in determination of object positions. Using two views of the same markers, their positions are reconstructed into 3D coordinates. There has been significant debate about the true accuracy of traditional RSA. Accuracy and precision depend on many factors including the software used for analysis (Bragdon *et al.*, 2004), the positioning of the beads (Madanat *et al.*, 2005), the method of digitization of the beads (Börlin *et al.*, 2002), the radiographic technique (Bragdon *et al.*, 2004), and the calibration frame (Cai *et al.*, 2008). For instance, the use of digital radiography has been found to be superior to the use of conventional films (Bragdon *et al.*, 2004). As such, it is important for each system to be independently validated. Kärrholm *et al.* (1997) reported the errors of the RSA system used until 1995 at the Sahlgren Hospital in Sweden, as quantified by a phantom and a coordinate measurement machine, to be on average –7 μm to 25 μm (±40 μm to 214 μm) and –0.03° to 0.02° (±0.04° to 0.3°). In a clinical setting the precision obtained by double

examination of several series of hips was reported to be between 0.15 mm and 0.6 mm and between 0.3° and 2° with 99% confidence (Kärrholm *et al.*, 1997). Using human and canine cadaveric models, Önsten *et al.* (2001) obtained prediction intervals of displacements with 95% confidence of ±47 μm to ±121 μm in the human model and ±45 μm to ±74 μm in the canine model. Bragdon *et al.* (2002) quantified the accuracy using bone models for the specific application of total hip replacement and found an accuracy of 55 μm. Madanat *et al.* (2005) obtained accuracies of ±6 μm over distances of 25 μm to 5 mm and ±0.073° over rotations of 1/6° to 2°. Cai *et al.* (2008) also used a bone model, although this time it was a knee, to quantify accuracy and obtained accuracies of 11 μm by utilizing a novel custom-made calibration frame. Therefore, it appears that accuracies are steadily improving. High accuracies means smaller numbers of subjects are required in studies, as significance may be reached more quickly.

Because the accuracies are so high, RSA was quickly adopted by the orthopaedic biomechanics community, and has found many uses including studying growth (Kärrholm *et al.*, 1984), prosthetic fixation and total joint component migration (Kärrholm *et al.*, 1994; Ryd *et al.*, 1995; Nilsson and Dalén, 1998; Alfaro-Adrián *et al.*, 1999; Hilding *et al.*, 2000; Nagels *et al.*, 2002), joint kinematics (Egund *et al.*, 1978; de Lange *et al.*, 1985; Kärrholm *et al.*, 1988; Lundberg, 1989; Uvehammer *et al.*, 2000; Axelsson and Karlsson, 2005; Hallström and Kärrholm, 2006), stability (Löfvenberg *et al.*, 1989; Johnsson *et al.*, 1992), healing (Fridén *et al.*, 1992; Ragnarsson *et al.*, 1993), and polyethylene wear (Baldursson *et al.*, 1979; Önsten *et al.*, 1998). It has been used to examine many joints, including the shoulder (Nagels *et al.*, 2002; Hallström and Kärrholm, 2006), the spine (Egund *et al.*, 1978; Johnsson *et al.*, 1992; Axelsson and

Karlsson, 2005), the hip (Baldursson *et al.*, 1979; Ragnarsson *et al.*, 1993; Kärrholm *et al.*, 1994; Önsten *et al.*, 1998; Alfaro-Adrián *et al.*, 1999), the knee (Kärrholm *et al.*, 1988; Fridén *et al.*, 1992; Ryd *et al.*, 1995; Nilsson and Dalén, 1998; Hilding *et al.*, 2000; Uvehammer *et al.*, 2000), and the foot and ankle (Kärrholm *et al.*, 1984; Löfvenberg *et al.*, 1989; Lundberg, 1989).

There are three commercially available software packages that are used for clinical RSA studies: the UmRSA system (RSA Biomedical, Umeå, Sweden), the WinRSA system (Tilly Medical Products AB, Lund, Sweden), and the Medis model-based RSA system (Medis specials, Leiden, The Netherlands).

Clearly, the fact that only static images may be taken is a drawback to traditional RSA. This means that continuous motions must be approximated by a sequential series of positions. This is not always appropriate. For instance, it has been shown that kinematics of the scapula are not the same under static and dynamic conditions (Fayad *et al.*, 2006).

1.2.2 DYNAMIC RSA

In order to capture kinematics during motion, dynamic RSA was introduced. Film exchangers were employed to allow multiple images to be taken in quick succession. At first, the knee was imaged under non-physiological weightbearing conditions with the subject seated, as this was fairly simple to implement using the RSA equipment at the time (Jonsson *et al.*, 1989). The sample rate could be altered but it was slow – between 2 and 4 frames per second (Jonsson *et al.*, 1989; Uvehammer *et al.*, 2000; Hallström and Kärrholm, 2006). To enable faster sample rates, a high speed camera could be placed behind an image intensifier (Tashman and Anderst, 2003; Tashman *et al.*,

2004). Using this approach, Tashman *et al.* (2004) sampled knee kinematics during running at 250 frames per second.

1.2.3 RSA AND FLUOROSCOPY

In order to obtain dynamic measurements of *in-vivo* kinematics using clinically available equipment, fluoroscopy and RSA (fRSA) have been integrated. As was mentioned in Section 1.1.5.1, fluoroscopes produce a real-time moving image that is similar to an x-ray. This provides the benefits of dynamic RSA at sample rates greater than those obtainable using film exchangers but without the cost associated with custom-made equipment. Both single plane (Garling *et al.*, 2005) and dual plane (Koning *et al.*, 2007) techniques have been implemented. Until this point, fluoroscopy has predominantly been used with model-based RSA, a type of RSA in which computer-aided design (CAD) models are used in place of beads for determining locations and orientations of objects.

1.2.4 THE USE OF TANTALUM

In clinical studies, as distinct anatomical landmarks are often not present, the bones of interest have 0.5 mm, 0.8 mm or 1.0 mm diameter tantalum beads inserted to provide highly repeatable markers within the segments (see Selvik *et al.*, 1983; Valstar *et al.*, 2002). The use of spherical markers means that their projections will not be altered with the viewing angle of the fluoroscopes (see Valstar *et al.*, 2002). The use of between six and nine beads per bone to be observed is recommended (Valstar *et al.*, 2005). Tantalum was originally chosen as it is bio-inert and is highly absorptive of x-rays (Selvik *et al.*, 1983). Unfortunately the implantation of such beads into subjects not

undergoing surgery is invasive, carries the risk of infection, and may cause restriction of normal movement for several days (see Hogfors *et al.*, 1991). Therefore, at the University of Western Ontario beads are not implanted into any patient who is not already undergoing a surgical procedure on the joint of interest. In studies where beads have been inserted into healthy normal subjects under local anaesthesia, any swelling and stiffness was reported to be resolved within one week (Lundberg, 1989).

There are no known serious risks resulting from the implantation of the beads in the short or long term. In a study conducted by Aronson *et al.* (1985) no inflammatory reaction was present in the region of 0.5 mm tantalum beads and 0.5 by 1.5 mm and 0.37 by 1.2 mm tantalum pins 5–48 weeks after insertion into the distal fibular region. Similarly, in another study, no dissolution of tantalum was detected, no inflammatory response was observed, and new bone growth and remodelling was seen after 4 weeks following implantation of 1 mm diameter tantalum wires in the subcutaneous abdominal connective tissue and femoral diaphyses of rats (Matsuno *et al.*, 2001). In addition, it has been shown that tantalum may offer benefits over currently used orthopaedic implant materials with respect to bacterial adhesion and therefore infection rates (Schildhauer *et al.*, 2006).

Furthermore, there are no risks to subjects regarding airport security, as there is not enough metal present to set off a detector. Even joint replacements, which have a vastly greater amount of metal, have been proven to not activate airport security (Basu *et al.*, 1997).

That said, care must be taken to ensure the beads are successfully implanted in the bone. Eldridge *et al.* (1998) performed a review of 64 patients who underwent total hip

arthroplasty and had a median of four 0.8 mm diameter tantalum beads inserted in their proximal femurs and found that 40% of patients had one or more extra-osseous beads. That amounts to approximately 13% of beads being misplaced. There was no relation found between either the experience of the surgeon or the operative approach and bead misplacement. Lawrie *et al.* (2003) also performed a review of total hip replacement patients. Radiographs of 97 patients were reviewed and the relative incidence of misplaced beads was 2% in the femur and 6% in the pelvis. The variation between the two studies may be due to different bead insertion devices and techniques. The major concern associated with misplaced beads is third body wear, should any of the misplaced beads migrate into a joint. The other drawback to extra-osseous beads is that they cannot be used for RSA as they are not rigidly implanted.

1.3 THE SHOULDER COMPLEX

The shoulder was chosen as the site of the first clinical application of the work described in this thesis. The reason for this was two-fold. First, there are many clinical questions about the shoulder that are as yet unanswered. Second, this joint goes through its full ROM while not moving very far in 3D space. This makes it ideal for study using imaging techniques, particularly RSA, where the capture volume is relatively small.

The shoulder complex (Figure 1.1) is a complicated system that is composed of three joints, two articulations, three bones and a large number of muscles, tendons, and ligaments. The upper limb is designed to allow the hand to be used most efficiently (Reid, 1969), and to enable that, the shoulder complex has the largest ROM of any joint complex in the human body (Koh *et al.*, 1998). Abnormalities in any one of the shoulder joints tend to reduce the overall ROM of the whole limb (Neer, 1990).

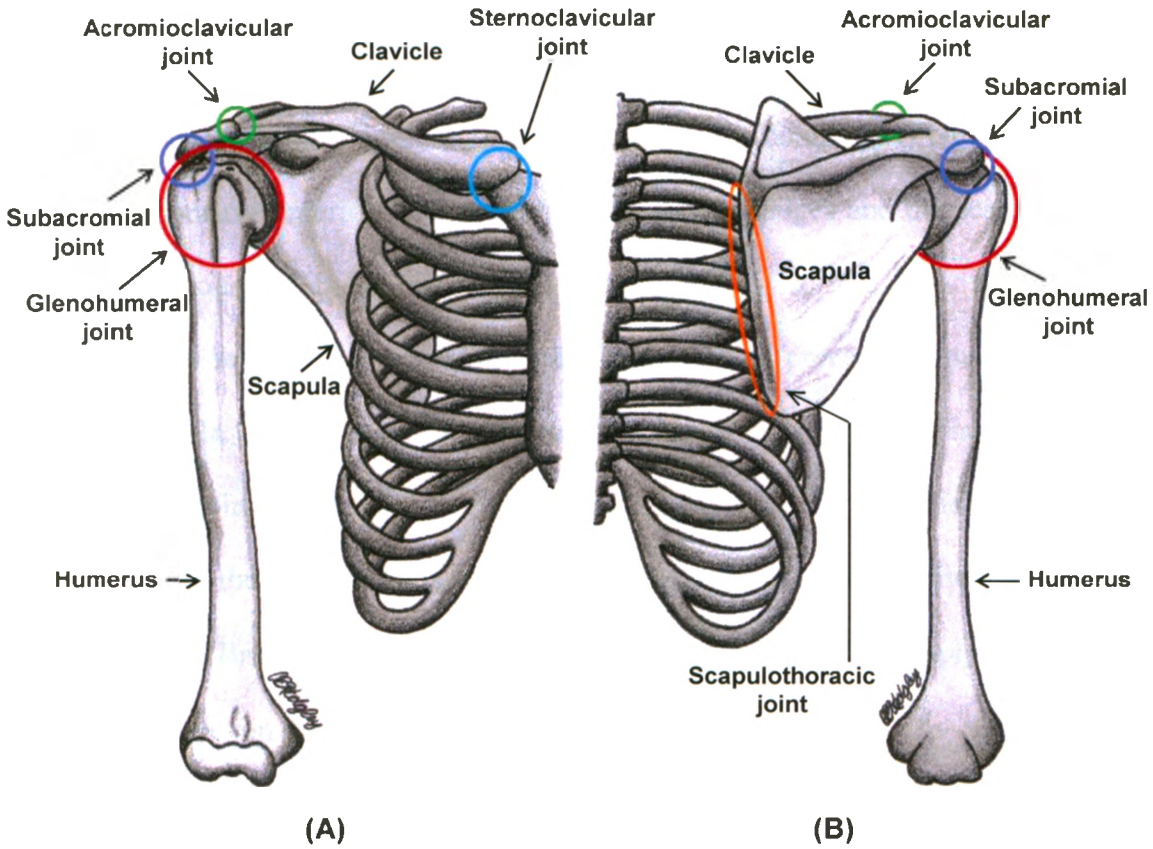

Figure 1.1 The shoulder complex
Pictured are the glenohumeral, scapulothoracic, acromioclavicular, sternoclavicular, and subacromial joints in **(A)** anterior and **(B)** posterior views of the right side.

1.3.1 ANATOMY

This thesis focuses specifically on one of the joints in the shoulder complex (*i.e.*, the glenohumeral joint); however, in order to understand the intricacies of this joint, a brief overview of the anatomy of the whole complex follows.

1.3.1.1 BONES AND JOINTS

The three bones of the shoulder complex are the scapula, the humerus and the clavicle. The scapula (Figure 1.2) is a thin, triangular bone that is curved slightly such that is it concave anteriorly. The medial and superior edges and the scapular spine are thicker regions of bone and act as reinforcements to the thin subscapular and infraspinatus fossae. The acromion, spine and coracoid process are the three processes on the scapula. All three serve as muscle attachment sites. The acromion serves as the articulation point of the scapula with the clavicle as well. The coracoid process may also serve to limit the anterior translation of the humeral head when the shoulder is abducted to 90° (see O'Brien *et al.*, 1998). The glenoid fossa, often called simply the glenoid, is a shallow hollow on the caudolateral region of the scapula.

The humerus (Figure 1.3) is the proximal bone of the upper limb. The humeral head lies at the proximal end of the humerus and forms one third of a sphere (see Morrey *et al.*, 1998). Other important landmarks are the greater and lesser tuberosities, the bicipital groove, the deltoid tuberosity and the medial and lateral epicondyles. The tuberosities serve as muscle attachment sites and the bicipital groove provides a pathway for the tendon of the long head of the biceps.

The clavicle is an S-shaped bone that lies between the scapula and the trunk. It serves as an attachment point for several muscles and is forced to rotate in relation to the

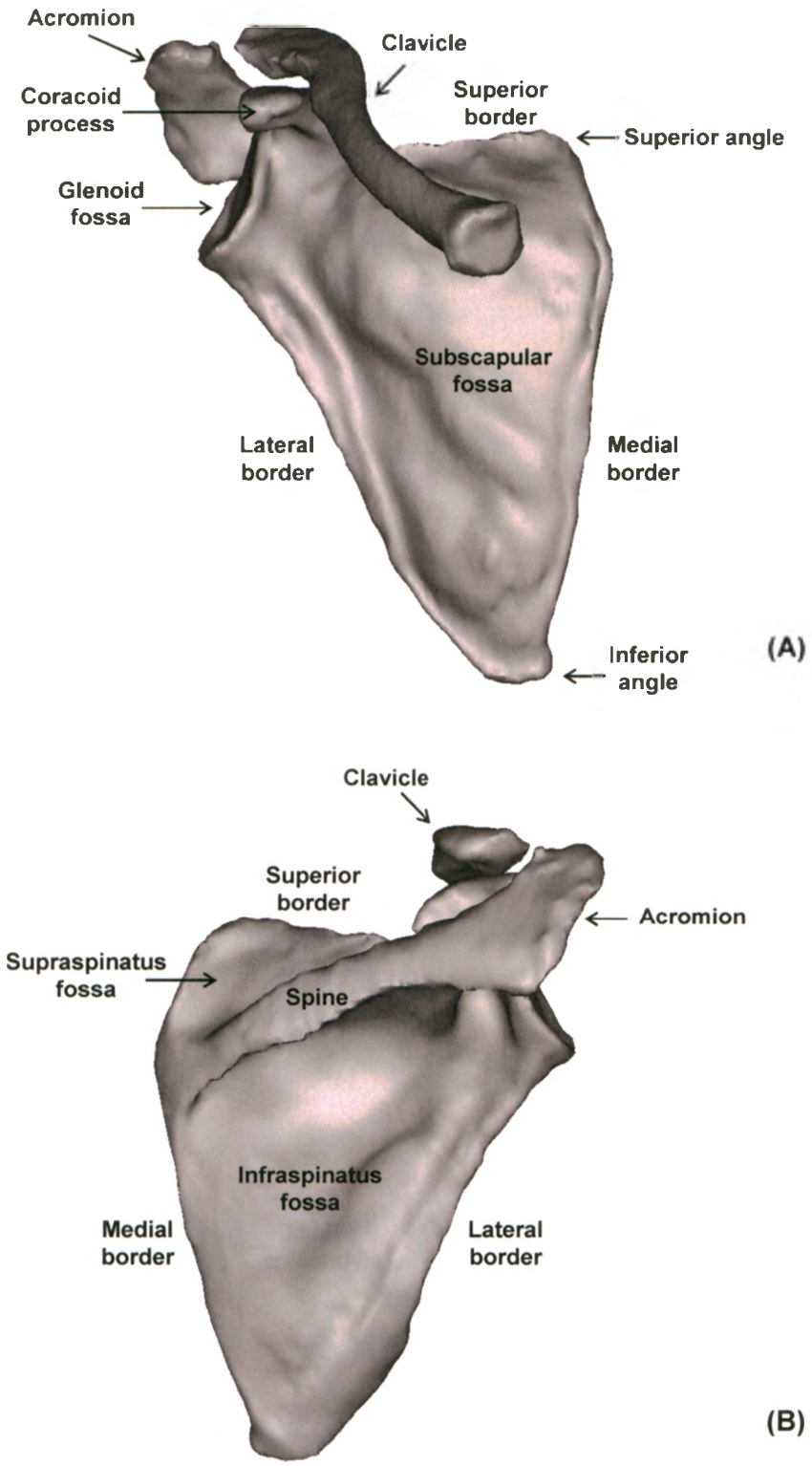

Figure 1.2 The osseous anatomy of the scapula and clavicle
(A) Anterior and **(B)** posterior views of a right scapula and clavicle with the landmarks of interest noted. (Images of a model created from a clinical CT scan.)

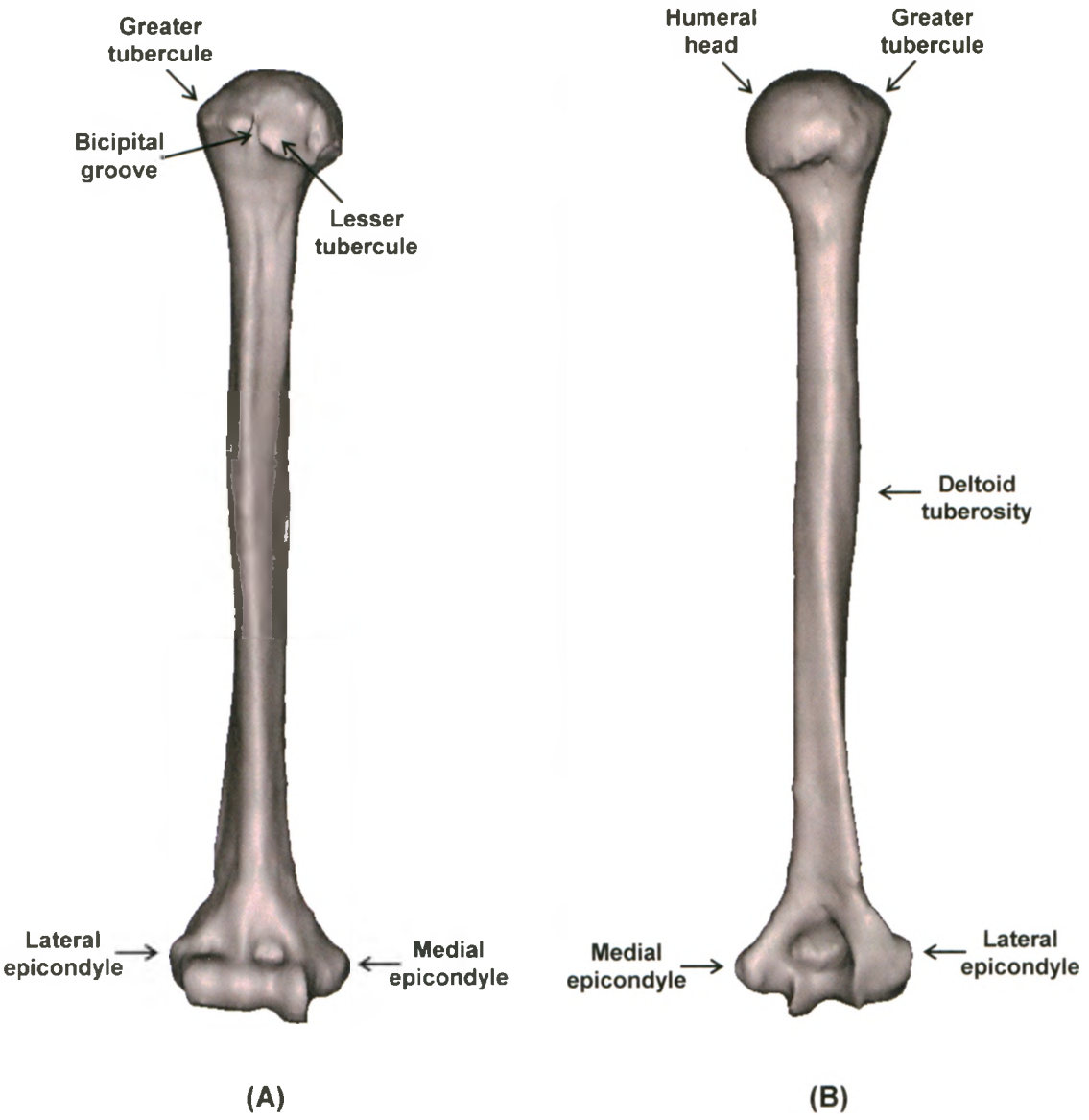

Figure 1.3 The osseous anatomy of the humerus
(A) Anterior and **(B)** posterior views of a right humerus with the landmarks of interest noted. (Images of a model created from a clinical CT scan.)

scapula throughout the ROM of the upper limb (see Neer, 1990).

The three joints of the shoulder complex are the glenohumeral joint, the sternoclavicular joint, and the acromioclavicular joint (Figure 1.1). The two articulations are the scapulothoracic joint and the subacromial joint. An articulation differs from a true articular joint, as there is no bone-on-bone motion. Each joint and articulation performs two important functions: restricting undesired motions and allowing desired motions (see Jobe, 1998).

The glenohumeral joint is traditionally considered the "shoulder joint". It consists of the articular joint between the head of the humerus and the glenoid fossa on the scapula, and has the largest ROM of all synovial joints in the human body (see Howell *et al.*, 1988; An *et al.*, 1991; Lippitt and Matsen, 1993; Curl and Warren, 1996; Karduna *et al.*, 1996; Halder *et al.*, 2001). The head of the humerus is much larger than the glenoid and therefore only a portion of the head is in contact with the glenoid at any time (see Saha, 1971; Neer, 1990; Soslowsky *et al.*, 1992; Morrey *et al.*, 1998). Perhaps surprisingly, motion of the humeral head consists of both rotation and translation (see Poppen and Walker, 1976; Howell *et al.*, 1988; Wuelker *et al.*, 1994; Kelkar *et al.*, 2001). It has been shown that during an interval of 30° of arm elevation; however, the instant centre of rotation lies within 5 mm of the centre of the humeral head (Poppen and Walker, 1976; Perry, 1988a), implying that the centre of rotation of the glenohumeral joint is located approximately at the centre of the humeral head. Therefore in an idealized model, the glenohumeral joint may therefore be approximated as a ball-and-socket joint with no translations, and three rotational DOF (Howell *et al.*, 1988; Iannotti *et al.*, 1992; Culham and Peat, 1993; McMahon *et al.*, 1995; Veeger *et al.*, 1997; Rhoad

et al., 1998). Any number of injuries or pathologies, including glenohumeral arthritis, instability, or rotator cuff tears may induce larger than normal amounts of translation in the glenohumeral joint under conditions of active motion (Poppen and Walker, 1976; Howell *et al.*, 1988).

The sternoclavicular joint lies between the sternum and the medial end of the clavicle, and allows the clavicle to move within a cone-shaped volume. This is a saddle-shaped plane synovial joint, which functions almost as a ball-and-socket joint (see Culham and Peat, 1993).

The acromioclavicular joint is the meeting between the acromion of the scapula and the lateral end of the clavicle. This joint moves very little and does not significantly contribute to the ROM of the upper arm (see Neer, 1990). It does provide some stabilization to the scapula by acting as a pivot, and its loading is primarily compression as the muscles pull the humerus towards the trunk.

The scapulothoracic joint consists of the plane of separation between the scapula and the subscapularis muscle from the thorax. The scapulothoracic joint provides approximately 40% of the motion which occurs in abduction, thereby increasing the available ROM by delaying the impingement of the greater tuberosity of the humerus on the acromion of the scapula. The rotation of the scapula in relation to the thorax also repositions the glenoid fossa, causing the joint force to remain directed inside the articular cavity and placing the glenoid cavity more directly beneath the humeral head, which in turn decreases the demand placed upon the deltoid muscle in abduction (see Perry, 1988b; Jobe, 1998).

The subacromial joint is also an articulation. It lies between the acromion, the coracoid process, and the humerus.

1.3.1.2 MUSCLES

There are numerous muscles that cross the shoulder complex and enable motion to take place. These muscles can be divided into three groups – the scapulohumeral muscles, the axioscapular muscles, and the axiohumeral muscles. The origins and insertions of many of these muscles are shown in Figure 1.4 and Figure 1.5.

The scapulohumeral muscles are those muscles that have their origins on the scapula and their insertions on the humerus. These are the deltoid, the rotator cuff complex, and the coracobrachialis. The deltoid muscle consists of three distinct sections: anterior, middle and posterior. All three sections assist in abducting the humerus and between them they contribute approximately 50% of the moment necessary for elevation (Hess, 2000). The anterior portion of the deltoid also aids in flexion, as well as in internal rotation of the humerus. Conversely, the posterior portion aids in arm extension as well as in external rotation of the humerus. The coracobrachialis muscle is active in flexion as well as adduction (see Jobe, 1998).

The axioscapular muscles originate on the thoracic cage and insert on the scapula. The muscles which comprise this group are serratus anterior, the levator scapulae, the trapezius, the pectoralis minor, and the rhomboids. These muscles all assist in the movement of the scapula.

The axiohumeral muscles have their origins on the thoracic cage and their insertions on the humerus. There are two muscles in this group, the pectoralis major and the latissimus dorsi. The function of the pectoralis major depends upon its starting

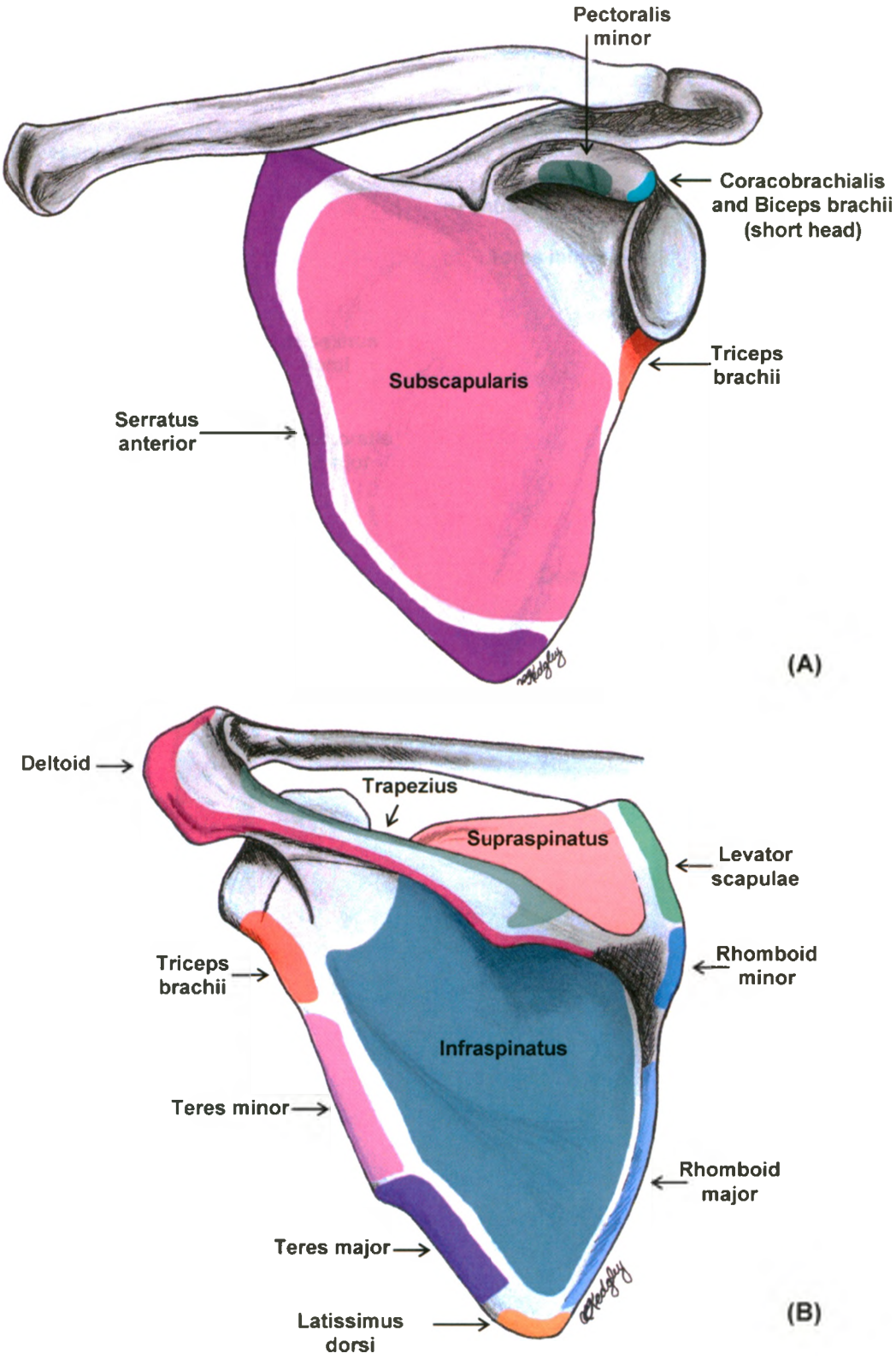

Figure 1.4 The muscular origins and insertions on the scapula
(A) Anterior and **(B)** posterior views of a left scapula.

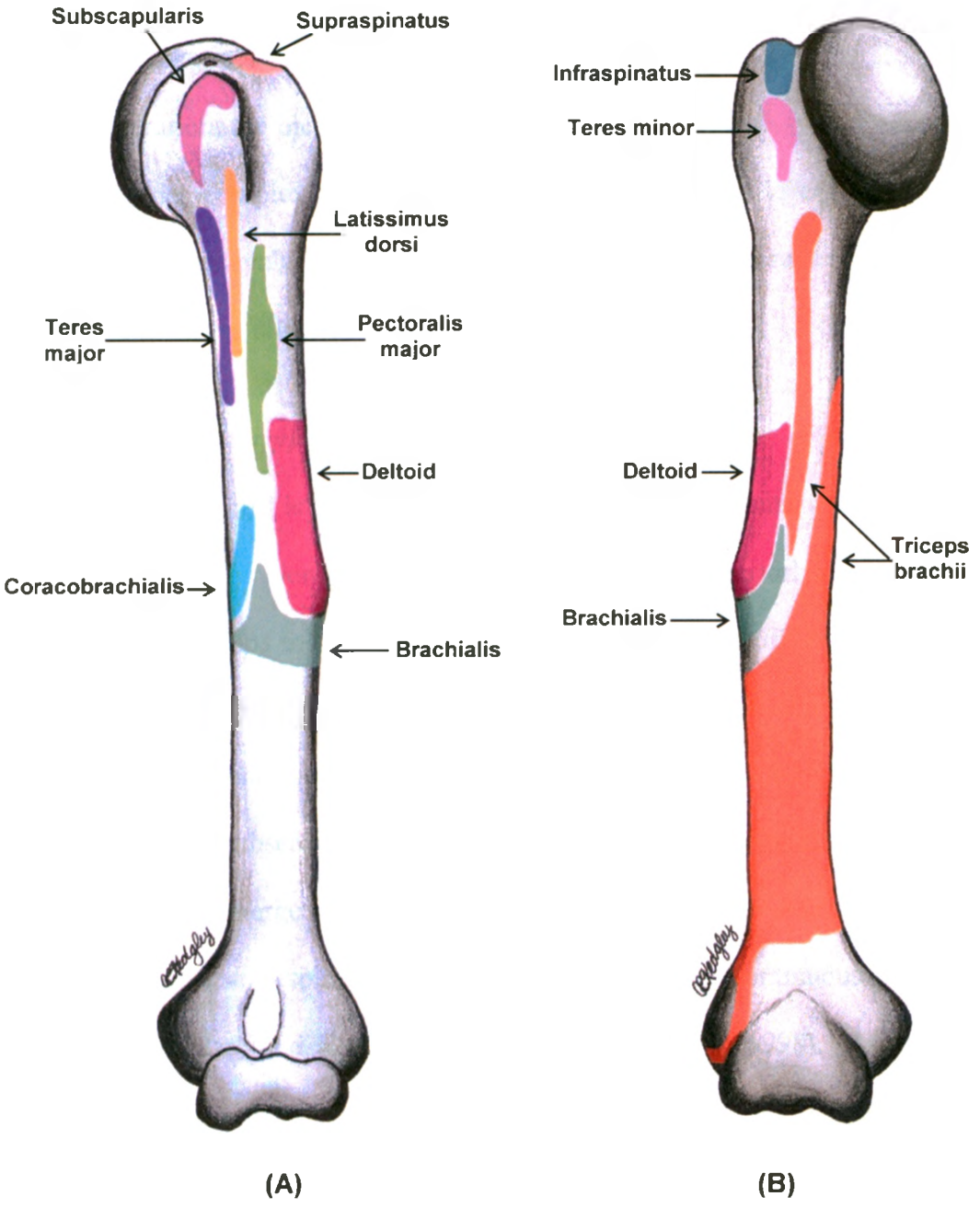

Figure 1.5 The muscular origins and insertions on the humerus
(A) Anterior and **(B)** posterior views of a left humerus.

position (see Jobe, 1998); however, it is known to be a powerful adductor and internal rotator. Internal rotation, adduction, and extension are assisted by the latissimus dorsi (see Jobe, 1998). In the case of a loss of function in the posterior deltoid, the latissimus dorsi may act as a substitute (see Neer, 1990).

In addition, the biceps brachii and the triceps brachii both exhibit some influence on the shoulder complex despite the fact that they primarily affect the elbow. Both originate on the scapula and the biceps brachii inserts on the radius while the triceps brachii inserts on the ulna.

1.3.1.3 ROTATOR CUFF

The rotator cuff is composed of the joint capsule, ligaments, muscles, and tendons that encircle the glenohumeral joint anteriorly, superiorly, and posteriorly. Kinematically, it helps to stabilize the glenohumeral joint, contribute to the elevation of the upper limb (see Neer, 1990; Sharkey *et al.*, 1994; Wuelker *et al.*, 1995), and rotate the humerus about its longitudinal axis (see Neer, 1990). The muscles of the rotator cuff are the supraspinatus, subscapularis, infraspinatus, and teres minor and major. The tendons of the rotator cuff merge with the capsule surrounding the glenohumeral joint, with the infraspinatus and supraspinatus tendons blending into one continuous band near their insertions (see Clark and Harryman, 1992; Minagawa *et al.*, 1998). As a result, it has been hypothesized that contraction of one muscle in the rotator cuff may actually influence the neighbouring muscle tendons (Soslowsky *et al.*, 1997). The supraspinatus muscle originates from the supraspinous fossa of the scapula and inserts on the greater tuberosity of the humerus. There are conflicting reports regarding its precise function; however, it is agreed that a significant function of the supraspinatus muscle is to assist in

holding the humeral head in the glenoid socket throughout the full ROM of the arm (see Wuelker *et al.*, 1994). It is active in any motion that involves elevation (see Howell *et al.*, 1986).

The subscapular fossa is the origin for the subscapularis, and the lesser tuberosity of the humerus is its insertion point. The subscapularis assists in internal rotation (see Jobe, 1998) and flexion of the humerus (see Bassett *et al.*, 1990), as well as stabilization of the humeral head. The infraspinatus originates at the infraspinatus fossa of the scapula and inserts on the greater tuberosity of the humerus, covering the posterior section of the supraspinatus. The infraspinatus is most significant as a stabilizer of the glenohumeral joints, but it also serves as an external rotator of the humerus (see Neer, 1990), and as a contributor to abduction (see Liu *et al.*, 1997; Mura *et al.*, 2003). The teres major and minor muscles are adductors of the humerus, with the teres major also functioning as an internal rotator of the humerus, and the teres minor functioning as an external rotator. Both also have a role in stabilization of the glenohumeral joint (see Neer, 1990).

1.3.2 FUNCTION

Ultimately, the function of the shoulder complex is to allow for multiple pathways of motion to be used by the hand to reach a target point. Additionally, each bone has its own specific roles to play. The scapula's main function is to provide attachment sites for the muscles that move and stabilize the shoulder and upper thorax (see Jobe, 1998). As well, the scapula provides a link between the upper limb and the thorax, and a moveable platform to help support the upper limb. It also plays a key role in positioning the upper limb and increasing its ROM (see Neer, 1990). The function of the humerus is to allow the hand to act with force on the environment while transmitting the loads applied by the

muscles to the trunk. The clavicle maintains the separation between the arm and the centre of the body that is necessary to ensure optimal movement of the upper limb. It also transmits any shocks received by the upper limb to the trunk.

1.3.3 MOTIONS

Motions can be defined by a combination of motion pairs – abduction and adduction, flexion and extension, horizontal flexion and extension, and internal and external rotation (Figure 1.6). The term scapulohumeral (or scapulothoracic) rhythm describes the relationship between the motions that occur during arm elevation in the glenohumeral and scapulothoracic joints. The overall ROM that may be achieved is divided between these two joints, and thus, scapulohumeral rhythm is generally expressed as a ratio of glenohumeral motion to scapulothoracic motion. Clinically, the ratio is approximated as 2:1 (see Perry, 1998a). However, it has been shown that the ratio is variable over the ROM, and is inconsistent between subjects (Freedman and Munro, 1966; Doody *et al.*, 1970; Ludewig *et al.*, 1996; Graichen *et al.*, 2000b; Talkhani and Kelly, 2001). Factors that may affect the ratio include anatomical variation between individuals, the plane or arc of elevation selected (whether flexion or abduction or somewhere in between), and the load on the arm (Peat, 1986). One study has also demonstrated that abduction velocity affects the ratio (Sugamoto *et al.*, 2002). In women the average scapulohumeral ROM is 171°, while in men the average is 167° (Perry, 1988a). The ROM in every direction decreases with age.

Dividing the motion between two joints enables the muscles that act across each joint to operate optimally (see Jobe, 1998). The scapulohumeral rhythm also brings the glenoid fossa beneath the humerus as the arm is raised; thereby assisting the muscles in

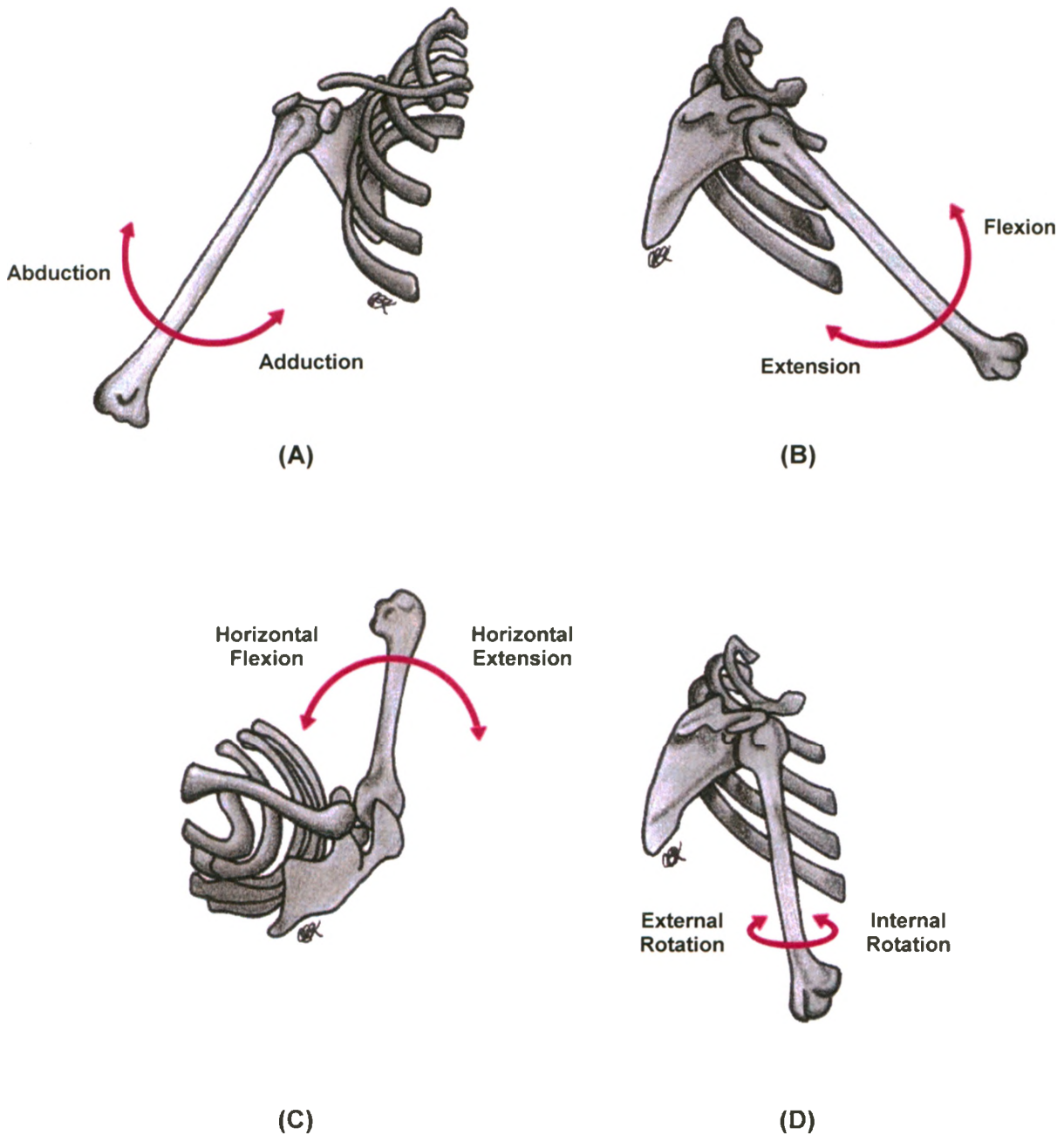

Figure 1.6 Motions of the upper arm
(A) Abduction/adduction: movement in the scapular plane, **(B)** flexion/extension: movement in the sagittal plane, **(C)** horizontal flexion/extension: movement in the transverse plane, and **(D)** internal/external rotation: rotation about the humeral axis.

supporting the weight of the upper limb (see Perry, 1988b; Jobe, 1998). Moreover, if the full ROM were assigned to only one joint, the joint would not function because the muscles would become trapped in the articulation (see van der Helm and Pronk, 1995).

The plane of the scapula is often used as the reference for abduction. This is not the same as the frontal plane of the body. The scapular plane is angled 30° to 45° anterior to the frontal plane. Elevation in the plane of the scapula occurs spontaneously in patients with limited strength as this is the plane in which the deltoid and supraspinatus muscles are optimally aligned for elevation (see Poppen and Walker, 1976; Perry, 1988a). Elevation in planes anterior to the plane of the scapula is simultaneously accompanied by external rotation to prevent impingement of the humeral head on the acromion (see Browne *et al.*, 1990; An *et al.*, 1991), to loosen the inferior glenohumeral ligaments (see Morrey *et al.*, 1998), and to ensure that there is sufficient humeral cartilage for articulation with the glenoid (see Jobe and Iannotti, 1995). To achieve maximum elevation in planes posterior to the scapula, elevation is simultaneously accompanied by internal rotation (see Browne *et al.*, 1990; An *et al.*, 1991).

1.4 KINEMATICS OF THE GLENOHUMERAL JOINT

International standards have been developed to enable comparisons of kinematic data between labs, and these will be followed here. Data for such kinematic analyses of the glenohumeral joint have been obtained using all of the biomechanical methods described in Section 1.1 and will be highlighted below.

1.4.1 BONE COORDINATE SYSTEMS

As was previously stated, it is impossible to place any marker set – be they reflective markers for an optical tracking system or beads for an RSA system – in the same location on each subject. To quantify glenohumeral joint motion, the position and orientation of the humerus relative to the scapula are required. Therefore a coordinate system must be established on each of these bones. Coordinate systems are created according to the convention established by the International Society of Biomechanics (ISB) (Wu *et al.*, 2005). As there are three rotational DOF in the glenohumeral joint, three rotations are required to describe the orientation of the humerus relative to the scapula. The axes of the bone coordinate systems are placed to allow these rotations to be clinically meaningful (*i.e.*, the rotation to the plane in which elevation occurs, the angle of elevation, and internal/external rotation).

Coordinate systems are created by first taking a CT scan of the bones of interest. Models of the bones are created using software such as Materialise's Interactive Medical Image Control System (MIMICS) with a MedCAD module (Materialise, Ann Arbor, Michigan, USA). Each landmark is digitized with a point and the positions of all of the beads are determined. See Appendix B for more information on this process using MIMICS. It has been shown that CT scans have a spatial accuracy of 99.2 ± 0.8% of distances measured (Smith *et al.*, 1989). The digitization process must be conducted carefully, as errors made in the location of the bony landmarks result in fixed errors in the locations of the bone coordinate systems, and therefore in the rotations of the joint (Della Croce *et al.*, 2005).

Once the bony landmarks are digitized, bone coordinate systems are created. A 3 by 3 rotation matrix relating the bone coordinate system relative to the marker-based coordinate system is defined as,

$$ {}^{marker}_{bone}R = \left[{}^{marker}\vec{X}_{bone} \quad {}^{marker}\vec{Y}_{bone} \quad {}^{marker}\vec{Z}_{bone} \right] \qquad \textbf{(Eq. 1.1)} $$

where ${}^{marker}\vec{X}_{bone}$, ${}^{marker}\vec{Y}_{bone}$, and ${}^{marker}\vec{Z}_{bone}$ are the bone coordinate system axes (*i.e.*, 3 by 1 matrices) described in the marker reference frame. A transformation matrix of the bone relative to the markers,

$$ {}^{marker}_{bone}T = \left[\begin{array}{ccc|c} & {}^{marker}_{bone}R & & {}^{marker}O_{bone} \\ \hline 0 & 0 & 0 & 1 \end{array} \right] \qquad \textbf{(Eq. 1.2)} $$

follows, in which:

${}^{marker}_{bone}R$ = the rotation matrix relating the bone coordinate system to the marker-based coordinate system

${}^{marker}O_{bone}$ = the location of the origin of the bone coordinate system in the marker-based coordinate system

1.4.1.1 SCAPULAR COORDINATE SYSTEM

To enable the creation of the scapular coordinate system three bony landmarks (Figure 1.7) are digitized. These landmarks are the most caudal point of the scapula, the inferior angle (IA), the most dorsolateral point on the scapula, the acromial angle (AA), and the mid-point of the triangular surface on the medial border of the scapula in line with the scapular spine, the trigonum spinae scapulae, (TS).

The lateral axis of the coordinate system, $\vec{Z}_{scap}$, is defined as a unit vector from

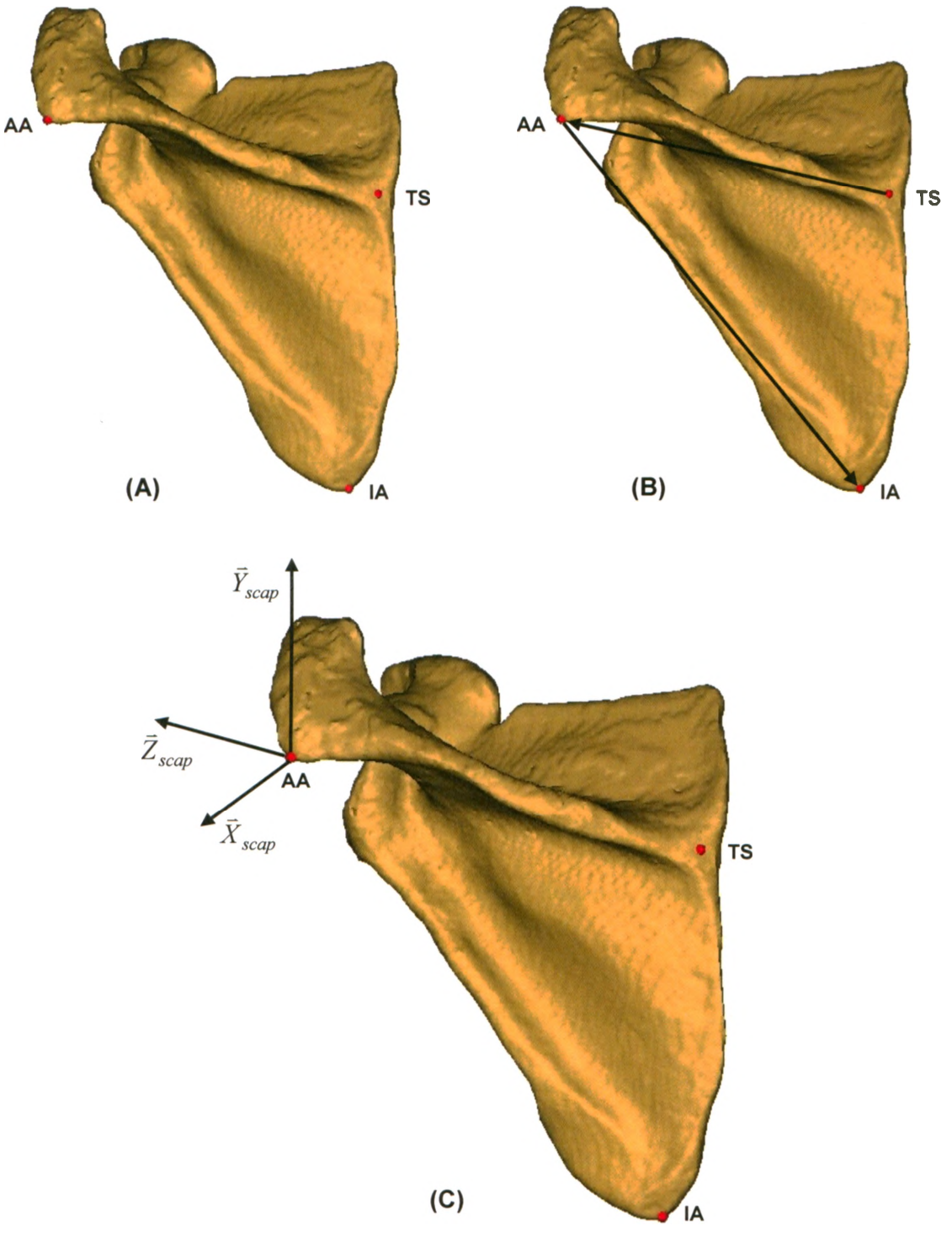

Figure 1.7 The scapular coordinate system
(A) The digitized landmarks on the scapula: the Inferior Angle (IA), the acromioclavicular joint (AC), the acromial angle (AA), and the trigonum spinae scapulae (TS). **(B)** The vectors used in the creation of the **(C)** scapular coordinate system. (Images of a model created from a clinical CT scan with points added in MIMICS.)

TS to AA. An inferiomedial vector is created from AA to IA. The vector cross product of this vector and $-\vec{Z}_{scap}$ is then taken to give the anteriorly-pointing $\vec{X}_{scap}$. Finally, the superiorly-pointing axis, $\vec{Y}_{scap}$, is created as the vector cross product of $\vec{Z}_{scap}$ and $\vec{X}_{scap}$.

The origin of the scapular coordinate system, O_{scap}, is established as the point AA. Therefore, the transformation matrix between the marker-based coordinate system and the scapular coordinate system may be written as:

$$ {}^{marker}_{scap}T = \left[\begin{array}{ccc|c} {}^{marker}\vec{X}_{scap} & {}^{marker}\vec{Y}_{scap} & {}^{marker}\vec{Z}_{scap} & {}^{marker}O_{scap} \\ \hline 0 & 0 & 0 & 1 \end{array}\right] \qquad \textbf{(Eq. 1.3)} $$

1.4.1.2 HUMERAL COORDINATE SYSTEM

To enable the creation of the humeral coordinate system three points are digitized (Figure 1.8). These are the most caudal point on the medial epicondyle (ME), the most caudal point on the lateral epicondyle (LE), and the centre of the humeral head (HH). In order to find HH, a sphere is created with the articular surface using MIMICS (see Appendix B) since it has been shown that the humeral head may be sphere fit (see Soslowsky *et al.*, 1992a).

The superior axis of the humeral coordinate system was created as a unit vector from the midpoint of the epicondyles to HH and designated as $\vec{Y}_{hum}$. An anterior vector, $\vec{X}_{hum}$, was created from the cross product of the vector from LE to ME and $\vec{Y}_{hum}$. The laterally-pointing, $\vec{Z}_{hum}$, was created as the vector cross product of $\vec{X}_{hum}$ and $\vec{Y}_{hum}$. The origin of the humeral coordinate centre, O_{hum}, was defined to be HH. It then follows that the transformation matrix between the marker-based coordinate system and the humeral coordinate system may be written as:

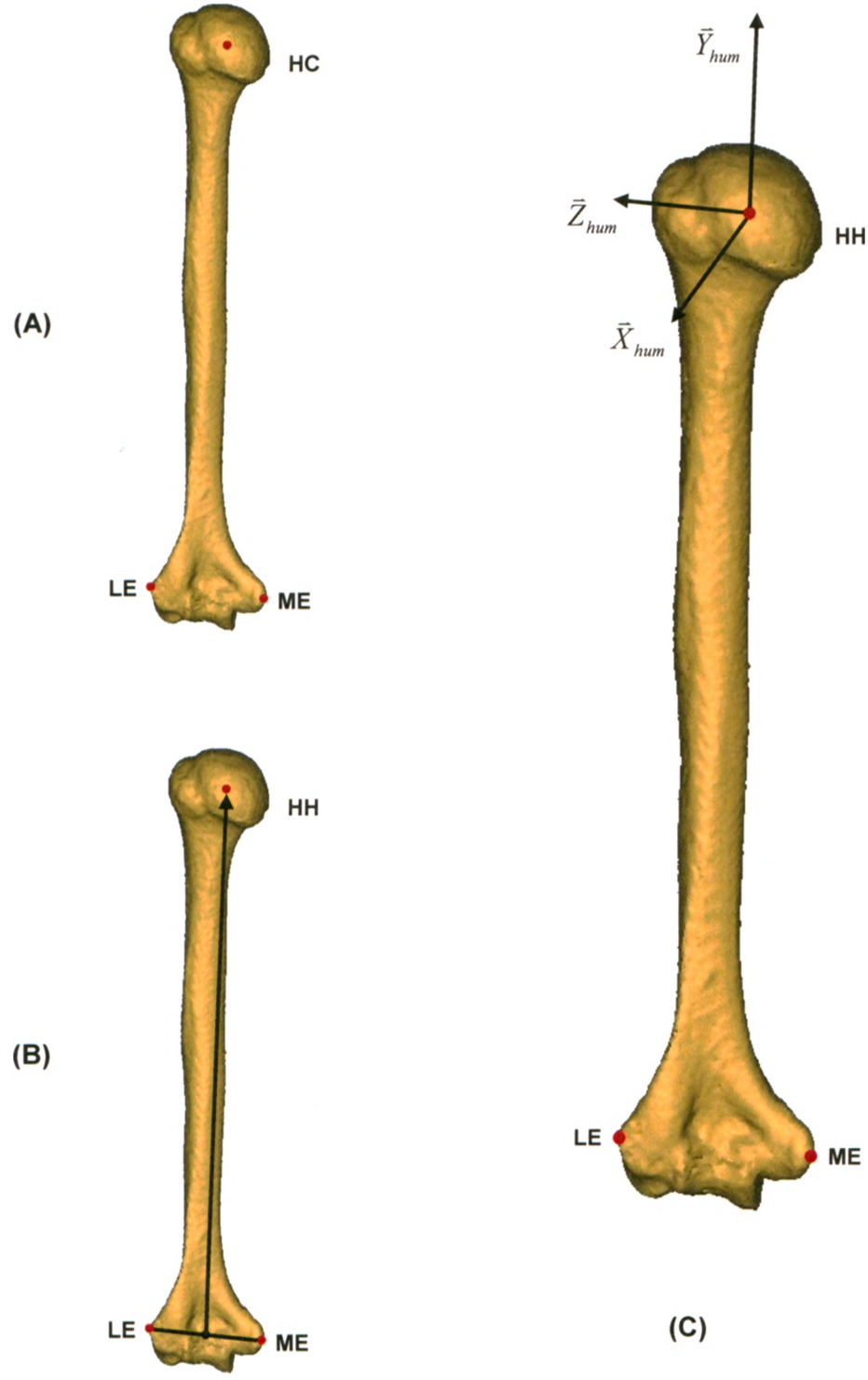

Figure 1.8 The humeral coordinate system
(A) The digitized landmarks on the humerus: the medial epicondyle (ME), the lateral epicondyle (LE), and the centre of the humeral head (HH). **(B)** The vectors used in the creation of **(C)** the humeral coordinate system. (Images of a model created from a clinical CT scan with points added in MIMICS.)

$$ {}^{marker}_{hum}T = \left[\begin{array}{ccc|c} {}^{marker}\vec{X}_{hum} & {}^{marker}\vec{Y}_{hum} & {}^{marker}\vec{Z}_{hum} & {}^{marker}O_{hum} \\ \hline 0 & 0 & 0 & 1 \end{array}\right] \quad \textbf{(Eq. 1.4)} $$

1.4.1.3 SIGN CONVENTIONS

Because the same bony landmarks are used to create coordinate systems on both right and left limbs, the X-axes do not point in the same anatomical directions in both cases. In the left shoulder the X-axes point posteriorly, while in the right shoulder the X-axes point anteriorly. Therefore, in order to obtain consistent kinematic outcome measures the following motions were established as being positive: planes of elevation forward from neutral, elevation, and external rotation.

1.4.2 GLENOHUMERAL JOINT KINEMATICS

Since the desired results of kinematic analyses are clinically meaningful interpretations of the rotations and translations that occur at a joint, the relationship between the coordinate systems on the scapula and humerus must be established. This is also done according to the conventions established by the ISB (Wu *et al.*, 2005). The translation of HH relative to the scapula is simply the change in position of O_{hum} within the scapular frame of reference.

The clinically relevant rotations of the glenohumeral joint are calculated by performing a Y-X-Y Euler angle analysis (see Winter, 2005c). An Euler angle analysis defines the orientation of one object with respect to another by the use of three independent rotation parameters. These rotations take place about the axes of a Cartesian coordinate system. The orientation of the axis about which each rotation takes place is dependent upon the preceding rotations; therefore, the sequence of rotations has an effect

on the outcome. It is assumed that the two frames of reference are initially aligned (Figure 1.9). Rotations then take place about: (A) the Y-axis of the scapular coordinate system ($\vec{Y}_{scap}$), giving the rotation to the plane in which elevation occurs (β); (B) the X-axis of the humeral coordinate system ($\vec{X}_{hum}$), giving the angle of elevation (α); and finally (C) the Y-axis of the humeral coordinate system ($\vec{Y}_{hum}$), giving the angle of rotation about the shaft of the humerus (γ). It should be noted that since the assumption behind the kinematics is that the coordinate systems were initially aligned, the initial rotation may equivalently have taken place about the $\vec{Y}_{hum}$, therefore this is how it will be written from now on. The sequence of rotations may be written in matrix-form as the product of three individual rotation matrices, or as a single rotation matrix for the three rotations as shown:

$$ {}^{scap}_{hum}R = rot(\vec{Y}_{hum},\beta)\cdot rot(\vec{X}'_{hum},\alpha)\cdot rot(\vec{Y}''_{hum},\gamma) \qquad \textbf{(Eq. 1.5)} $$

$$ = \begin{bmatrix} c\beta & 0 & s\beta \\ 0 & 1 & 0 \\ -s\beta & 0 & c\beta \end{bmatrix} \begin{bmatrix} 1 & 0 & 0 \\ 0 & c\alpha & -s\alpha \\ 0 & s\alpha & c\alpha \end{bmatrix} \begin{bmatrix} c\gamma & 0 & s\gamma \\ 0 & 1 & 0 \\ -s\gamma & 0 & c\gamma \end{bmatrix} $$

$$ = \begin{bmatrix} c\beta c\gamma - s\beta c\alpha s\gamma & s\beta s\alpha & c\beta s\gamma + s\beta c\alpha c\gamma \\ s\alpha s\gamma & c\alpha & -s\alpha c\gamma \\ -s\beta c\gamma - c\beta c\alpha s\gamma & c\beta s\alpha & -s\beta s\gamma + c\beta c\alpha c\gamma \end{bmatrix} \qquad \textbf{(Eq. 1.6)} $$

where:

rot($\vec{Y}_{hum}$,β) = rotation about $\vec{Y}_{hum}$ of magnitude β;

c = cosine; and

s = sine

In order to describe the location of the humerus relative to the scapula, a series of

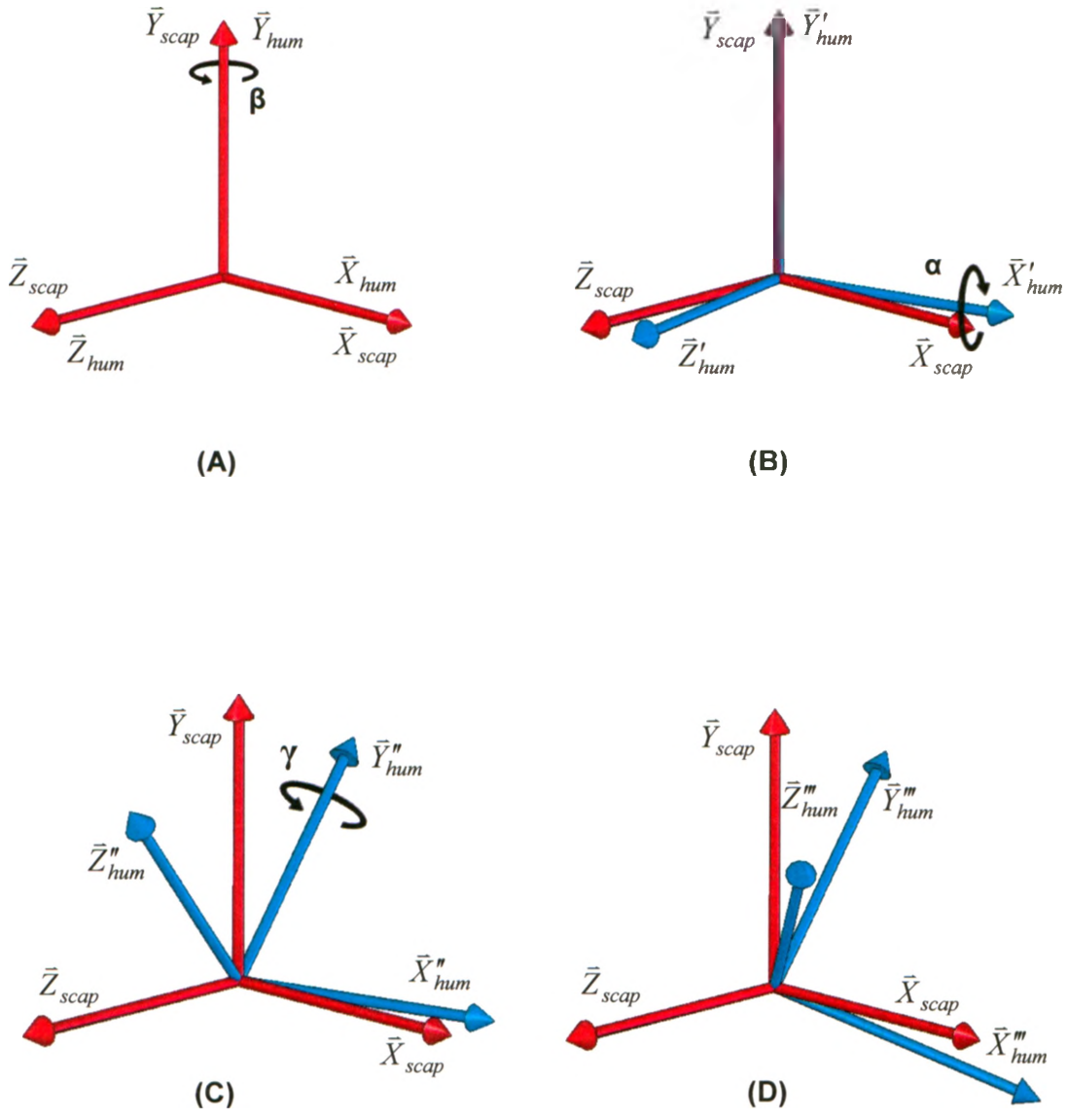

Figure 1.9 Euler Y-X-Y rotations
Rotations about **(A)** the Y-axis of the scapular coordinate system, **(B)** the X'-axis of the humeral coordinate system and **(C)** the Y"-axis of the humeral coordinate system. **(D)** The resulting coordinate systems.

transformation matrices must be combined as shown:

$$
\begin{aligned}
{}^{scap}_{hum}T &= {}^{scap}_{marker-scap}T \cdot {}^{marker-scap}_{lab}T \cdot {}^{lab}_{marker-hum}T \cdot {}^{marker-hum}_{hum}T \\
&= \left[\begin{array}{c|c} {}^{scap}_{hum}R & {}^{scap}P_{hum,origin} \\ \hline 0 \quad 0 \quad 0 & 1 \end{array}\right] \\
&= \begin{bmatrix} r_{11} & r_{12} & r_{13} & x \\ r_{21} & r_{22} & r_{23} & y \\ r_{31} & r_{32} & r_{33} & z \\ 0 & 0 & 0 & 1 \end{bmatrix}
\end{aligned}
\qquad \textbf{(Eq. 1.7)}
$$

where:

${}^{scap}_{marker-scap}T = \left[{}^{marker-scap}_{scap}T\right]^{-1}$ = the transformation matrix describing the position and orientation of the markers on the scapula relative to the scapular bone coordinate system;

${}^{marker-scap}_{lab}T$ = the transformation matrix describing the lab coordinate system relative to the position and orientation of the scapula marker coordinate system;

${}^{lab}_{marker-hum}T$ = the transformation matrix describing the position and orientation of the humerus marker coordinate system, relative to the lab; and

${}^{marker-hum}_{hum}T$ = the transformation matrix describing the humeral bone coordinate system relative to the humerus marker coordinate system.

In order to describe the rotation of the humerus relative to the scapula, Equation 1.6 is compared with Equation 1.7 to obtain:

$$\text{Plane of elevation: } \beta = \begin{cases} \arctan 2\left(\dfrac{r_{12}/\sin\alpha}{r_{32}/\sin\alpha}\right); \text{right shoulder} \\ -\arctan 2\left(\dfrac{r_{12}/\sin\alpha}{r_{32}/\sin\alpha}\right); \text{left shoulder} \end{cases} \quad \textbf{(Eq. 1.8)}$$

$$\text{Angle of elevation: } \alpha = \begin{cases} -\arctan 2\left(\dfrac{-\sqrt{{r_{12}}^2+{r_{32}}^2}}{r_{22}}\right); \text{right shoulder} \\ -\arctan 2\left(\dfrac{-\sqrt{{r_{12}}^2+{r_{32}}^2}}{r_{22}}\right); \text{left shoulder} \end{cases} \quad \textbf{(Eq. 1.9)}$$

$$\text{External / Internal rotation: } \gamma = \begin{cases} -\arctan 2\left(\dfrac{r_{21}/\sin\alpha}{-r_{23}/\sin\alpha}\right); \text{right shoulder} \\ \arctan 2\left(\dfrac{r_{21}/\sin\alpha}{-r_{23}/\sin\alpha}\right); \text{left shoulder} \end{cases} \quad \textbf{(Eq. 1.10)}$$

where arctan2 is the four quadrant inverse tangent function, with results between pi and -pi. This differs from the standard inverse tangent function which has results in the first and fourth quadrants only.

The sin α terms in the numerators and denominators of the definitions for both β and γ would seem to cancel out; however, this could potentially change the signs of the numerators and denominators. Since the arctan2(y,x) function provides the solution to arctan(y,x) while using the signs of x and y to determine the quadrant in which the resultant angle lies, the cancellation of the sin α terms could lead to incorrect solutions for β and γ. When the angle of elevation is 0° or 180° singularities develop, as the first and third axes of rotation are aligned. This is known as gimbal lock. No instances of gimbal lock were observed during this work; however, if there were any, they would have appeared as unexpected values of the first and third angles of rotation.

1.4.3 THE STUDY OF GLENOHUMERAL JOINT BIOMECHANICS

The final study of this thesis aims specifically to quantify the kinematics of the two bones whose motion provides the majority of the ROM of the shoulder. One of the major hurdles in studying shoulder, and specifically scapular, motion is that by describing abnormal motions, it is implicitly assumed that the normal motions have been quantified (Hébert *et al.*, 2000). Unfortunately, the precise kinematics of the shoulder complex still remains unresolved. By more fully understanding the kinematics of the shoulder complex, the treatment of problems such as frozen shoulder, rotator cuff tears, glenohumeral instability, and other shoulder pathologies may be better assessed and possibly improved.

Due to the substantial soft tissue covering of the scapula and the lack of palpable bony landmarks it is very difficult to track scapular kinematics during dynamic activities (Lucchetti *et al.*, 1998; McClure *et al.*, 2001). Goniometers have been used to determine the ratio of scapulothoracic to glenohumeral joint motions (Doody *et al.*, 1970). Optical (Hébert *et al.*, 2000; Bourne *et al.*, 2004) and electromagnetic (McQuade and Smidt, 1998; Meskers *et al.*, 1998b; Karduna *et al.*, 2000; McClure *et al.*, 2001; Karduna *et al.*, 2001; Vermeulen *et al.*, 2002; Rundquist *et al.*, 2003) tracking devices attached to the skin or clothing have been used by many groups to record motion in three dimensions for *in-vivo* studies. As previously mentioned, measurement errors due to soft tissue covering have been shown to be task dependent and not reproducible among subjects, making these errors difficult to filter from the actual motion (Leardini *et al.*, 2005). It has been demonstrated that these errors may even be so large as to apparently measure joint dislocations when none occur (Leardini *et al.*, 2005). Scapular rotation has been

quantified using landmark digitization techniques (van der Helm and Pronk, 1995; Ludewig *et al.*, 1996; Meskers *et al.*, 1998b; Hébert *et al.*, 2000; Bourne *et al.*, 2004) with some success, but this may only be used in static positions. Bony landmarks that are not palpable have been found using both functional and predictive approaches (Cappozzo *et al.*, 2005). In addition, it has been shown that for joints in which the primary motion occurs in a single plane (such as the scapulothoracic joint), errors in the identification of bony landmarks have a dramatic effect upon the measured magnitudes of rotations in planes other than the primary (Della Croce *et al.*, 2005). To more accurately measure joint motion, bone pins have been implanted directly into the target bone through the skin (Harryman *et al.*, 1992; Koh *et al.*, 1998; Karduna *et al.*, 2001; McClure *et al.*, 2001); however, this approach has many drawbacks as was discussed in Section 1.1.4.

Imaging techniques used for measuring shoulder kinematics include 2D x-ray studies (Freedman and Munro, 1966; Poppen and Walker, 1976; Howell and Kraft, 1991; de Groot *et al.*, 1998), RSA (Hogfors *et al.*, 1991; Bey *et al.*, 2006; Hallström and Kärrholm, 2006), MRI in two (Iannotti *et al.*, 1992; Bonutti *et al.*, 1993; Cardinal *et al.*, 1996) and three dimensions (Rhoad *et al.*, 1998; Graichen *et al.*, 2000a), and single plane fluoroscopy (Burkhart, 1992; Talkhani and Kelly, 2001; Sugamoto *et al.*, 2002).

1.5 RATIONALE

The rationale for this work consists of several distinct parts. The incorporation of fluoroscopy with traditional RSA will allow the capture of moving images and thereby facilitate the study of *in-vivo* kinematics under dynamic conditions. Kinematic analyses will be much more reliable when skin motion artefact has been eliminated. The investigation of a variety of calibration frame configurations and a number of distortion

correction orders will improve the accuracy of results obtained from RSA. The examination of the errors resulting from landmark digitization and subsequent propagation through glenohumeral joint kinematics will provide a better estimate of the magnitude of the overall errors of the system. The introduction of a new scapular coordinate system will allow a decrease in the radiation exposure required for subjects undergoing RSA. Finally, the examination of the kinematics of the glenohumeral joint using RSA following rotator cuff repair will provide insight into changes in kinematics as healing takes place and the patients undergo physical therapy.

1.6 OBJECTIVES AND HYPOTHESES

The objectives of this thesis were: (1) to implement a fluoroscopy-based RSA system, (2) to validate the system and compare it to existing biomechanical tracking technology, (3) to determine the effect of various configurations of the calibration frame, (4) to examine the intricacies of distortion correction, (5) to investigate the inter- and intra-investigator errors involved in creating the coordinate systems for glenohumeral joint kinematics, (6) to introduce a new coordinate system definition for the scapula and (7) to apply the system to examine motions of the glenohumeral joint *in-vivo*.

The primary hypothesis (1) was that the system would have superior accuracy and precision when compared with the existing biomechanical tracking technology. It was also hypothesized (2) that an alternate calibration frame configuration could improve the accuracy of the RSA reconstruction, as could (3) the proper implementation of a distortion correction scheme. Furthermore, it was hypothesized that (4) a new definition for the scapular coordinate system could be found that could be considered to be equivalent to the current ISB standard coordinate system. Finally, it was hypothesized

that (5) the new fluoroscopy-based RSA system would prove to be a useful clinical tool, able to quantify longitudinal changes in kinematics following surgical interventions and post-operative rehabilitation, specifically at the glenohumeral joint.

1.7 THESIS OVERVIEW

Chapter 2 describes the components of the RSA system that was developed. Chapter 3 presents the study which was done to assess the precision and accuracy of the system and compare it to a commercial optical tracking system. Chapter 4 shows the evaluation of a range of calibration frame configurations. Chapter 5 contains the results of the investigation of distortion correction. Chapter 6 examines the inter- and intra-investigator errors of digitization of landmarks from CT scans, specifically with regard to their effects on glenohumeral joint kinematics and looks at an alternate approach to creating the scapular coordinate system. Chapter 7 presents some preliminary *in-vivo* glenohumeral joint kinematic data. Chapter 8 summarizes the conclusions drawn from this work, outlines its significance, and suggests some potential work which may follow.

1.8 REFERENCES

Alfaro-Adrian, J., Gill, H.S., and Murray, D.W. (1999) Cement migration after THR. A comparison of charnley elite and exeter femoral stems using RSA. *J. Bone Joint Surg. Br.* 81[1], 130-134.

An, K.N., Browne, A.O., Korinek, S., Tanaka, S., and Morrey, B.F. (1991) Three-dimensional kinematics of glenohumeral elevation. *J. Orthop. Res.* 9[1], 143-149.

Andriacchi, T.P. and Alexander, E.J. (2000) Studies of human locomotion: past, present and future. *J. Biomech.* 33[10], 1217-1224.

Armstrong, A.D., MacDermid, J.C., Chinchalkar, S., Stevens, R.S., and King, G.J. (1998) Reliability of range-of-motion measurement in the elbow and forearm. *J. Shoulder Elbow Surg.* 7, 573-580.

Aronson, A.S., Jonsson, N., and Alberius, P. (1985) Tantalum markers in radiography. An assessment of tissue reactions. *Skeletal. Radiol.* 14[3], 207-211.

Auerbach, J.D., Wills, B.P., McIntosh, T.C., and Balderston, R.A. (2007) Evaluation of spinal kinematics following lumbar total disc replacement and circumferential fusion using in vivo fluoroscopy. *Spine* 32[5], 527-536.

Axelsson, P. and Karlsson, B.S. (2005) Standardized provocation of lumbar spine mobility: three methods compared by radiostereometric analysis. *Spine* 30[7], 792-797.

Baeyens, J.P., Van Glabbeek, F., Goossens, M., Gielen, J., Van Roy, P., and Clarys, J.P. (2006) In vivo 3D arthrokinematics of the proximal and distal radioulnar joints during active pronation and supination. *Clin. Biomech.* 21[Suppl 1], S9-12.

Baldursson, H., Egund, N., Hansson, L.I., and Selvik, G. (1979) Instability and wear of total hip prostheses determined with roentgen stereophotogrammetry. *Arch. Orthop. Trauma Surg.* 95[4], 257-263.

Bassett, R.W., Browne, A.O., Morrey, B.F., and An, K.N. (1990) Glenohumeral muscle force and moment mechanics in a position of shoulder instability. *J. Biomech.* 23[5], 405-415.

Basu, P., Packer, G.J., and Himstedt, J. (1997) Detection of orthopaedic implants by airport metal detectors. *J. Bone Joint Surg. Br.* 79[3], 388-389.

Bechard, D.J., Nolte, V., Kedgley, A.E., and Jenkyn, T.R. (2008) Total kinetic energy production of body segments is different between racing and training pace in elite Olympic rowers. *Sports Biomech.* 8[3], 199-211.

Beimers, L., Tuijthof, G.J., Blankevoort, L., Jonges, R., Maas, M., and van Dijk, C.N. (2008) In-vivo range of motion of the subtalar joint using computed tomography. *J. Biomech.* 41[7], 1390-1397.

Benoit, D.L., Ramsey, D.K., Lamontagne, M., Xu, L., Wretenberg, P., and Renstrom, P. (2006) Effect of skin movement artifact on knee kinematics during gait and cutting motions measured in vivo. *Gait Posture* 24[2], 152-164

Bey, M.J., Zauel, R., Brock, S.K., and Tashman, S. (2006) Validation of a new model-based tracking technique for measuring three-dimensional, in vivo glenohumeral joint kinematics. *J. Biomech. Eng.* 128[4], 604-609.

Bonutti, P.M., Norfray, J.F., Friedman, R.J., and Genez, B.M. (1993) Kinematic MRI of the shoulder. *J. Comput. Assist. Tomogr.* 17[4], 666-669.

Börlin, N., Thien, T., and Kärrholm, J. (2002) The precision of radiostereometric measurements. Manual vs. digital measurements. *J. Biomech.* 35[1], 69-79.

Bourne, D., Choo, A.M., Regan, W., MacIntyre, D., and Oxland, T.R. (2004) Accuracy of measuring change in scapular position with digitization of bony landmarks. *Proc. Inst. Mech. Eng. H.* 223[3], 349-361.

Bradshaw, E.J., Maulder, P.S., and Keogh, J.W. (2007) Biological movement variability during the sprint start: performance enhancement or hindrance? *Sports Biomech.* 6[3], 246-260.

Bragdon, C.R., Malchau, H., Yuan, X., Perinchief, R., Kärrholm, J., Borlin, N., Estok, D.M., and Harris, W.H. (2002) Experimental assessment of precision and accuracy of radiostereometric analysis for the determination of polyethylene wear in a total hip replacement model. *J. Orthop. Res.* 20[4], 688-695.

Bragdon, C.R., Estok, D.M., Malchau, H., Kärrholm, J., Yuan, X., Bourne, R., Veldhoven, J., and Harris, W.H. (2004) Comparison of two digital radiostereometric analysis methods in the determination of femoral head penetration in a total hip replacement phantom. *J. Orthop. Res.* 22[3], 659-664.

Bridgett, L.A. and Linthorne, N.P. (2006) Changes in long jump take-off technique with increasing run-up speed. *J. Sports Sci.* 24[8], 889-897.

Browne, A.O., Hoffmeyer, P., Tanaka, S., An, K.N., and Morrey, B.F. (1990) Glenohumeral elevation studied in three dimensions. *J. Bone Joint Surg. Br* 72[5], 843-845.

Burnett, A., O'Sullivan, P., Ankarberg, L., Gooding, M., Nelis, R., Offermann, F., and Persson, J. (2008) Lower lumbar spine axial rotation is reduced in end-range sagittal postures when compared to a neutral spine posture. *Man. Ther.* 13[4], 300-306.

Bushberg, J.T., Seibert, J.A., Leidholdt, E.M., and Boone, J.M. (2002a) Computed Tomography. In: *The Essential Physics of Medical Imaging.* Lippincott Williams & Wilkins, Philadelphia. pp. 327-372.

Bushberg, J.T., Seibert, J.A., Leidholdt, E.M., and Boone, J.M. (2002b) Magnetic Resonance Imaging (MRI). In: *The Essential Physics of Medical Imaging.* Lippincott Williams & Wilkins, Philadelphia. pp. 415-467.

Burkhart, S.S. (1992) Fluoroscopic comparison of kinematic patterns in massive rotator cuff tears. A suspension bridge model. *Clin. Orthop. Relat. Res.* [284], 144-152.

Cai, R., Yuan, X., Rorabeck, C., Bourne, R.B., and Holdsworth, D.W. (2008) Development of an RSA calibration system with improved accuracy and precision. *J. Biomech.* 41[4], 907-911.

Cappozzo, A., Catani, F., Leardini, A., Benedetti, M.G., and Croce, U.D. (1996) Position and orientation in space of bones during movement: experimental artefacts. *Clin. Biomech.* 11[2], 90-100.

Cappozzo, A., Croce, U.D., Leardini, A., and Chiari, L. (2005) Human movement analysis using stereophotogrammetry. Part 1: theoretical background. *Gait Posture* 21[2], 186-196.

Cardinal, E., Buckwalter, K.A., and Braunstein, E.M. (1996) Kinematic magnetic resonance imaging of the normal shoulder: assessment of the labrum and capsule. *Can. Assoc. Radiol. J.* 47[1], 44-50.

Cerveri, P., Pedotti, A., and Ferrigno, G. (2005) Kinematical models to reduce the effect of skin artifacts on marker-based human motion estimation. *J. Biomech.* 38[11], 2228-2236.

Chen, L., Armstrong, C.W., and Raftopoulos, D.D. (1994) An investigation on the accuracy of three-dimensional space reconstruction using the direct linear transformation technique. *J. Biomech.* 27[4], 493-500.

Chèze, L., Fregly, B.J., and Dimnet, J. (1995) A solidification procedure to facilitate kinematic analyses based on video system data. *J. Biomech.* 28[7], 879-884.

Clark, J.M. and Harryman, D.T. (1992) Tendons, ligaments, and capsule of the rotator cuff. Gross and microscopic anatomy. *J. Bone Joint Surg. Am.* 74[5], 713-725.

Culham, E. and Peat, M. (1993) Functional anatomy of the shoulder complex. *J. Orthop. Sports Phys. Ther.* 18[1], 342-350.

Curl, L.A. and Warren, R.F. (1996) Glenohumeral joint stability. Selective cutting studies on the static capsular restraints. *Clin. Orthop.* [330], 54-65.

de Groot, J.H. (1997) The variability of shoulder motions recorded by means of palpation. *Clin. Biomech.* 12[7-8], 461-472.

de Groot, J.H., Valstar, E.R., and Arwert, H.J. (1998) Velocity effects on the scapulo-humeral rhythm. *Clin. Biomech.* 13[8], 593-602.

de Groot, J.H. (1999) The scapulo-humeral rhythm: effects of 2-D roentgen projection. *Clin. Biomech.* 14[1], 63-68.

de Lange, A., Kauer, J.M., and Huiskes, R. (1985) Kinematic behavior of the human wrist joint: a roentgen-stereophotogrammetric analysis. *J. Orthop. Res.* 3[1], 56-64.

Della Croce, U., Cappozzo, A., and Kerrigan, D.C. (1999) Pelvis and lower limb anatomical landmark calibration precision and its propagation to bone geometry and joint angles. *Med. Biol. Eng. Comput.* 37[2], 155-161.

Della Croce, U., Leardini, A., Chiari, L., and Cappozzo, A. (2005) Human movement analysis using stereophotogrammetry. Part 4: Assessment of anatomical landmark misplacement and its effects on joint kinematics. *Gait Posture* 21[2], 226-237.

Doody, S.G., Freedman, L., and Waterland, J.C. (1970) Shoulder movements during abduction in the scapular plane. *Arch. Phys. Med. Rehabil.* 51[10], 595-604.

Duck, T.R., Dunning, C.E., King, G.J., and Johnson, J.A. (2003) Variability and repeatability of the flexion axis at the ulnohumeral joint. *J. Orthop. Res.* 21[3], 399-404.

Dumas, R. and Cheze, L. (2009) Soft tissue artifact compensation by linear 3D interpolation and approximation methods. *J. Biomech.* 42[13], 2214-7.

Dunk, N.M., Kedgley, A.E., Jenkyn, T.R., and Callaghan, J.P. (2009) Evidence of a pelvis-driven flexion pattern: are the joints of the lower lumbar spine fully flexed in seated postures? *Clin. Biomech.* 24[2], 164-168.

Ebaugh, D.D., McClure, P.W., and Karduna, A.R. (2005) Three-dimensional scapulothoracic motion during active and passive arm elevation. *Clin. Biomech.* 20[7], 700-709.

Edwards, J.Z., Greene, K.A., Davis, R.S., Kovacik, M.W., Noe, D.A., and Askew, M.J. (2004) Measuring flexion in knee arthroplasty patients. *J. Arthroplasty* 19[3], 369-372.

Egund, N., Olsson, T.H., Schmid, H., and Selvik, G. (1978) Movements in the sacroiliac joints demonstrated with roentgen stereophotogrammetry. *Acta Radiol. Diagn.* 19[5], 833-846.

Eldridge, J.D., Avramidis, K., Lee, M., and Learmonth, I.D. (1998) Tantalum ball position after total hip arthroplasty. *J. Bone Joint Surg. Br.* 80[3], 414-416.

Everaert, D.G., Spaepen, A.J., Wouters, M.J., Stappaerts, K.H., and Oostendorp, R.A. (1999) Measuring small linear displacements with a three-dimensional video motion analysis system: determining its accuracy and precision. *Arch. Phys. Med. Rehabil.* 80[9], 1082-1089.

Fayad, F., Hoffmann, G., Hanneton, S., Yazbeck, C., Lefevre-Colau, M.M., Poiraudeau, S., Revel, M., and Roby-Brami, A. (2006) 3-D scapular kinematics during arm elevation: effect of motion velocity. *Clin. Biomech.* 21[9], 932-941.

Frankel, V.H., Burstein, A.H., and Brooks, D.B. (1971) Biomechanics of internal derangement of the knee. Pathomechanics as determined by analysis of the instant centers of motion. *J. Bone Joint Surg. Am.* 53[5], 945-962.

Freedman, L. and Munro, R.R. (1966) Abduction of the arm in the scapular plane: scapular and glenohumeral movements. A roentgenographic study. *J. Bone Joint Surg. Am.* 48[8], 1503-1510.

Fridén, T., Ryd, L., and Lindstrand, A. (1992) Laxity and graft fixation after reconstruction of the anterior cruciate ligament. A roentgen stereophotogrammetric analysis of 11 patients. *Acta Orthop. Scand.* 63[1], 80-84.

Fung, Y.C.B. (1968) Biomechanics: Its scope, history, and some problems of continuum mechanics in physiology. *Appl. Mech. Rev.* 21[1], 1-20.

Garling, E.H., Kaptein, B.L., Geleijns, K., Nelissen, R.G., and Valstar, E.R. (2005) Marker configuration model-based roentgen fluoroscopic analysis. *J. Biomech.* 38[4], 893-901.

Graichen, H., Stammberger, T., Bonel, H., Karl-Hans, E., Reiser, M., and Eckstein, F. (2000a) Glenohumeral translation during active and passive elevation of the shoulder - a 3D open-MRI study. *J. Biomech.* 33[5], 609-613.

Graichen, H., Stammberger, T., Bonel, H., Haubner, M., Englmeier, K.H., Reiser, M., and Eckstein, F. (2000b) Magnetic resonance-based motion analysis of the shoulder during elevation. *Clin. Orthop.* [370], 154-163.

Gribble, P.A. and Robinson, R.H. (2009) Alterations in knee kinematics and dynamic stability associated with chronic ankle instability. *J. Athl. Train.* 44[4], 350-355.

Halder, A.M., Halder, C.G., Zhao, K.D., O'Driscoll, S.W., Morrey, B.F., and An, K.N. (2001) Dynamic inferior stabilizers of the shoulder joint. *Clin. Biomech.* 16[2], 138-143.

Hallström, E. and Kärrholm, J. (2006) Shoulder kinematics in 25 patients with impingement and 12 controls. *Clin. Orthop. Relat. Res.* 448, 22-27.

Harryman, D.T., Sidles, J.A., Harris, S.L., and Matsen, F.A., III (1992) Laxity of the normal glenohumeral joint: A quantitative in vivo assessment. *J. Shoulder Elbow Surg.* 1[2], 66-74.

Hébert, L.J., Moffet, H., McFadyen, B.J., and St Vincent, G. (2000) A method of measuring three-dimensional scapular attitudes using the optotrak probing system. *Clin. Biomech.* 15[1], 1-8.

Hess, S.A. (2000) Functional stability of the glenohumeral joint. *Man. Ther.* 5[2], 63-71.

Hilding, M., Ryd, L., Toksvig-Larsen, S., and Aspenberg, P. (2000) Clodronate prevents prosthetic migration: a randomized radiostereometric study of 50 total knee patients. *Acta Orthop. Scand.* 71[6], 553-557.

Hoffman, S.J. (2009) *Introduction to kinesiology: Studying physical activity.* Human Kinetics, Windsor. p. 501.

Hogfors, C., Peterson, B., Sigholm, G., and Herberts, P. (1991) Biomechanical model of the human shoulder joint – II. The shoulder rhythm. *J. Biomech.* 24[8], 699-709.

Howell, S.M., Imobersteg, A.M., Seger, D.H., and Marone, P.J. (1986) Clarification of the role of the supraspinatus muscle in shoulder function. *J. Bone Joint Surg. Am.* 68[3], 398-404.

Howell, S.M., Galinat, B.J., Renzi, A.J., and Marone, P.J. (1988) Normal and abnormal mechanics of the glenohumeral joint in the horizontal plane. *J. Bone Joint Surg. Am.* 70[2], 227-232.

Howell, S.M. and Kraft, T.A. (1991) The role of the supraspinatus and infraspinatus muscles in glenohumeral kinematics of anterior shoulder instability. *Clin. Orthop.* [263], 128-134.

Hunt, M.A., Birmingham, T.B., Jenkyn, T.R., Giffin, J.R., and Jones, I.C. (2008) Measures of frontal plane lower limb alignment obtained from static radiographs and dynamic gait analysis. *Gait Posture* 27[4], 635-640.

Iannotti, J.P., Gabriel, J.P., Schneck, S.L., Evans, B.G., and Misra, S. (1992) The normal glenohumeral relationships. An anatomical study of one hundred and forty shoulders. *J. Bone Joint Surg. Am.* 74[4], 491-500.

Jenkyn, T.R. and Nicol, A.C. (2007) A multi-segment kinematic model of the foot with a novel definition of forefoot motion for use in clinical gait analysis during walking. *J. Biomech.* 40[14], 3271-3278.

Jobe, C.M. and Iannotti, J.P. (1995) Limits imposed on glenohumeral motion by joint geometry. *J. Shoulder Elbow Surg.* 4[4], 281-285.

Jobe, C.M. (1998) Gross anatomy of the shoulder. In: Rockwood, C.A., Jr. and Matsen, F. (Eds.) *The Shoulder* W.B. Saunders Company, Philadelphia. pp. 34-96.

Johnsson, R., Stromqvist, B., Axelsson, P., and Selvik, G. (1992) Influence of spinal immobilization on consolidation of posterolateral lumbosacral fusion. A roentgen stereophotogrammetric and radiographic analysis. *Spine* 17[1], 16-21.

Jonsson, H., Kärrholm, J., and Elmqvist, L.G. (1989) Kinematics of active knee extension after tear of the anterior cruciate ligament. *Am. J. Sports Med.* 17[6], 796-802.

Karduna, A.R., Williams, G.R., Williams, J.L., and Iannotti, J.P. (1996) Kinematics of the glenohumeral joint: influences of muscle forces, ligamentous constraints, and articular geometry. *J. Orthop. Res.* 14[6], 986-993.

Karduna, A.R., McClure, P.W., and Michener, L.A. (2000) Scapular kinematics: effects of altering the Euler angle sequence of rotations. *J. Biomech.* 33[9], 1063-1068.

Karduna, A.R., McClure, P.W., Michener, L.A., and Sennett, B. (2001) Dynamic measurements of three-dimensional scapular kinematics: a validation study. *J. Biomech. Eng.* 123[2], 184-190.

Kärrholm, J., Hansson, L.I., and Selvik, G. (1984) Changes in tibiofibular relationships due to growth disturbances after ankle fractures in children. *J. Bone Joint Surg. Am.* 66[8], 1198-1210.

Kärrholm, J., Selvik, G., Elmqvist, L.G., and Hansson, L.I. (1988) Active knee motion after cruciate ligament rupture. Stereoradiography. *Acta Orthop. Scand.* 59[2], 158-164.

Kärrholm, J. (1989) Roentgen stereophotogrammetry. Review of orthopedic applications. *Acta Orthop. Scand.* 60[4], 491-503.

Kärrholm, J., Borssen, B., Lowenhielm, G., and Snorrason, F. (1994) Does early micromotion of femoral stem prostheses matter? 4-7-year stereoradiographic follow-up of 84 cemented prostheses. *J. Bone Joint Surg. Br.* 76[6], 912-917.

Kärrholm, J., Herberts, P., Hultmark, P., Malchau, H., Nivbrant, B., and Thanner, J. (1997) Radiostereometry of hip prostheses. Review of methodology and clinical results. *Clin. Orthop. Relat. Res.* [344], 94-110.

Kelkar, R., Wang, V.M., Flatow, E.L., Newton, P.M., Ateshian, G.A., Bigliani, L.U., Pawluk, R.J., and Mow, V.C. (2001) Glenohumeral mechanics: a study of articular geometry, contact, and kinematics. *J. Shoulder Elbow Surg.* 10[1], 73-84.

Klopčar, N. and Lenarčič, J. (2006) Bilateral and unilateral shoulder girdle kinematics during humeral elevation. *Clin. Biomech.* 21[Suppl 1], S20-S26.

Koh, T., Grabiner, M., and Brems, J. (1998) Three-dimensional in vivo kinematics of the shoulder during humeral elevation. *J. Appl. Biomech.* 14 [3], 312-326.

Komistek, R.D., Dennis, D.A., and Mahfouz, M. (2003) In vivo fluoroscopic analysis of the normal human knee. *Clin. Orthop. Relat. Res.* [410] 69-81.

Koning, O.H.J., Kaptein, B.L., Garling, E.H., Hinnen, J.W., Hamming, J.F., Valstar, E.R., and vanBockel, J.H. (2007) Assessment of three-dimensional stent-graft dynamics by using fluoroscopic roentgenographic stereophotogrammetric analysis. *J. Vasc. Surg.* 46[4], 773–779.

Lafortune, M.A., Cavanagh, P.R., Sommer, H.J., III, and Kalenak, A. (1992) Three-dimensional kinematics of the human knee during walking. *J. Biomech.* 25[4], 347-357.

Lawrie, D.F., Downing, M.R., Ashcroft, G.P., and Gibson, P.H. (2003) Insertion of tantalum beads in RSA of the hip: variations in incidence of extra-osseous beads with insertion site. *Acta. Orthop. Scand.* 74[4], 404-407.

Leardini, A., Chiari, L., Croce, U.D., and Cappozzo, A. (2005) Human movement analysis using stereophotogrammetry. Part 3. Soft tissue artifact assessment and compensation. *Gait Posture* 21[2], 212-225.

Leardini, A., Benedetti, M.G., Berti, L., Bettinelli, D., Nativo, R., and Giannini, S. (2007) Rear-foot, mid-foot and fore-foot motion during the stance phase of gait. *Gait Posture* 25[3], 453-462.

Leroux, J.L., Micallef, J.P., Bonnel, F., and Blotman, F. (1992) Rotation-abduction analysis in 10 normal and 20 pathologic shoulders. Elite system application. *Surg. Radiol. Anat.* 14[4], 307-313.

Leventhal, E.L., Wolfe, S.W., Moore, D.C., Akelman, E., Weiss, A.P., and Crisco, J.J. (2008) Interfragmentary motion in patients with scaphoid nonunion. *J. Hand Surg. Am.* 33[7], 1108-1115.

Linthorne, N.P. and Everett, D.J. (2006) Release angle for attaining maximum distance in the soccer throw-in. *Sports Biomech.* 5[2], 243-260.

Lippitt, S. and Matsen, F. (1993) Mechanisms of glenohumeral joint stability. *Clin. Orthop.* [291], 20-28.

Liu, J., Hughes, R.E., Smutz, W.P., Niebur, G., and Nan-An, K. (1997) Roles of deltoid and rotator cuff muscles in shoulder elevation. *Clin. Biomech.* 12[1], 32-38.

Löfvenberg, R., Kärrholm, J., Selvik, G., Hansson, L.I., and Ahlgren, O. (1989) Chronic lateral instability of the ankle. Roentgen stereophotogrammetry of talar position. *Acta Orthop. Scand.* 60[1], 34-39.

Lucchetti, L., Cappozzo, A., Cappello, A., and Della, C.U. (1998) Skin movement artefact assessment and compensation in the estimation of knee-joint kinematics. *J. Biomech.* 31[11], 977-984.

Ludewig, P.M., Cook, T.M., and Nawoczenski, D.A. (1996) Three-dimensional scapular orientation and muscle activity at selected positions of humeral elevation. *J. Orthop. Sports Phys. Ther.* 24[2], 57-65.

Lundberg, A. (1989) Kinematics of the ankle and foot. In vivo roentgen stereophotogrammetry. *Acta Orthop. Scand. Suppl.* 233, 1-24.

Ma, H.T., Griffith, J.F., Yang, Z., Kwok, A.W., Leung, P.C., and Lee, R.Y. (2009) Kinematics of the lumbar spine in elderly subjects with decreased bone mineral density. *Med. Biol. Eng. Comput.* 47[7], 783-789.

Madanat, R., Makinen, T.J., Moritz, N., Mattila, K.T., and Aro, H.T. (2005) Accuracy and precision of radiostereometric analysis in the measurement of three-dimensional micromotion in a fracture model of the distal radius. *J. Orthop. Res.* 23[2], 481-488.

Matsuno, H., Yokoyama, A., Watari, F., Uo, M., and Kawasaki, T. (2001) Biocompatibility and osteogenesis of refractory metal implants, titanium, hafnium, niobium, tantalum and rhenium. *Biomaterials* 22[11], 1253-1262.

McClure, P.W., Michener, L.A., Sennett, B.J., and Karduna, A.R. (2001) Direct 3-dimensional measurement of scapular kinematics during dynamic movements in vivo. *J. Shoulder Elbow Surg.* 10[3], 269-277.

McMahon, P.J., Debski, R.E., Thompson, W.O., Warner, J.J., Fu, F.H., and Woo, S.L. (1995) Shoulder muscle forces and tendon excursions during glenohumeral abduction in the scapular plane. *J. Shoulder Elbow Surg.* 4[3], 199-208.

McPherson, A., Kärrholm, J., Pinskerova, V., Sosna, A., and Martelli, S. (2005) Imaging knee position using MRI, RSA/CT and 3D digitisation. *J. Biomech.* 38[2], 263-268.

McQuade, K.J. and Smidt, G.L. (1998) Dynamic scapulohumeral rhythm: the effects of external resistance during elevation of the arm in the scapular plane. *J. Orthop. Sports Phys. Ther.* 27[2], 125-133.

Meskers, C.G., van der Helm, F.C., Rozendaal, L.A., and Rozing, P.M. (1998a) In vivo estimation of the glenohumeral joint rotation center from scapular bony landmarks by linear regression. *J. Biomech.* 31[1], 93-96.

Meskers, C.G., Vermeulen, H.M., de Groot, J.H., van der Helm, F.C., and Rozing, P.M. (1998b) 3D shoulder position measurements using a six-degree-of-freedom electromagnetic tracking device. *Clin. Biomech.* 13[4-5], 280-292.

Meskers, C.G., Fraterman, H., van der Helm, F.C., Vermeulen, H.M., and Rozing, P.M. (1999) Calibration of the "Flock of Birds" electromagnetic tracking device and its application in shoulder motion studies. *J. Biomech.* 32[6], 629-633.

Meskers, C.G., van de Sande, M.A., and de Groot, J.H. (2007) Comparison between tripod and skin-fixed recording of scapular motion. *J. Biomech.* 40[4], 941-946.

Milne, A.D., Chess, D.G., Johnson, J.A., and King, G.J. (1996) Accuracy of an electromagnetic tracking device: a study of the optimal range and metal interference. *J. Biomech.* 29[6], 791-793.

Minagawa, H., Itoi, E., Konno, N., Kido, T., Sano, A., Urayama, M., and Sato, K. (1998) Humeral attachment of the supraspinatus and infraspinatus tendons: an anatomic study. *Arthroscopy* 14[3], 302-306.

Morrey, B.F., Itoi, E, and An, K N (1998) Biomechanics of the shoulder. In: Rockwood, C.A., Jr. and Matsen, F. (Eds.) *The Shoulder.* W.B. Saunders Company, Philadelphia. pp. 233-276.

Mow, V.C. and Huiskes, R. (2005) A brief history of science and orthopaedic biomechanics. In: Mow, V.C. and Huiskes, R. (Eds.), *Basic orthopaedic biomechanics and mechano-biology.* Lippincott Williams & Wilkins, Philadelphia. pp. 1-27.

Mura, N., O'Driscoll, S.W., Zobitz, M.E., Heers, G., Jenkyn, T.R., Chou, S.M., Halder, A.M., and An, K.N. (2003) The effect of infraspinatus disruption on glenohumeral torque and superior migration of the humeral head: a biomechanical study. *J. Shoulder Elbow Surg.* 12[2], 179-184.

Nagels, J., Valstar, E.R., Stokdijk, M., and Rozing, P.M. (2002) Patterns of loosening of the glenoid component. *J. Bone Joint Surg. Br.* 84[1], 83-87.

Neer, C.S. (1990) Anatomy of shoulder reconstruction. In: *Shoulder Reconstruction.* W.B. Saunders Company, Philadelphia. pp. 1-39.

Nester, C., Jones, R.K., Liu, A., Howard, D., Lundberg, A., Arndt, A., Lundgren, P., Stacoff, A., and Wolf, P. (2007) Foot kinematics during walking measured using bone and surface mounted markers. *J. Biomech.* 40[15], 3412-3423.

Nilsson, K.G. and Dalén, T. (1998) Inferior performance of Boneloc bone cement in total knee arthroplasty: a prospective randomized study comparing Boneloc with Palacos using radiostereometry (RSA) in 19 patients. *Acta Orthop. Scand.* 69[5], 479-483.

O'Brien, S.J., Allen, A.A., Fealy, S., Rodeo, S.A., and Arnoczky, S.P. (1998) Developmental anatomy of the shoulder and anatomy of the glenohumeral joint. In: Rockwood, C.A. and Matsen, F. (Eds.), *The Shoulder.* W.B. Saunders Company, Philadelphia. pp. 1-33.

Önsten, I., Carlsson, A.S., and Besjakov, J. (1998) Wear in uncemented porous and cemented polyethylene sockets: a randomised, radiostereometric study. *J. Bone Joint Surg. Br.* 80[2], 345-350.

Önsten, I., Berzins, A., Shott, S., and Sumner, D.R. (2001) Accuracy and precision of radiostereometric analysis in the measurement of THR femoral component translations: human and canine in vitro models. *J. Orthop. Res.* 19[6], 1162-1167.

Patel, V.V., Hall, K., Ries, M., Lotz, J., Ozhinsky, E., Lindsey, C., Lu, Y., and Majumdar, S. (2004) A three-dimensional MRI analysis of knee kinematics. *J. Orthop. Res.* 22[2], 283-292.

Peat, M. (1986) Functional anatomy of the shoulder complex. *Phys. Ther.* 66[12], 1855-1865.

Perry, J. (1988a) Biomechanics of the shoulder. In: Rowe, C.R. (Ed.) *The Shoulder* Churchill Livingstone Inc., New York. pp. 1-15.

Perry, J. (1988b) Muscle control of the shoulder. In: Rowe, C.R. (Ed.) *The Shoulder* Churchill Livingstone Inc., New York. pp. 17-34.

Pollock, C.L., Jenkyn, T.R., Jones, I.C., Ivanova, T.D., and Garland, S.J. (2009) Electromyography and kinematics of the trunk during rowing in elite female rowers. *Med Sci. Sports Exerc.* 41[3], 628-636.

Poppen, N.K. and Walker, P.S. (1976) Normal and abnormal motion of the shoulder. *J. Bone Joint Surg. Am.* 58[2], 195-201.

Prendergast, P.J., van der Helm, F.C.T., and Duda, G.N. (2005) Analysis of muscle and joint loads. In: Mow, V.C. and Huiskes, R. (Eds.), *Basic orthopaedic biomechanics and mechano-biology.* Lippincott Williams & Wilkins, Philadelphia. pp. 1-27.

Ragnarsson, J.I., Boquist, L., Ekelund, L., and Kärrholm, J. (1993) Instability and femoral head vitality in fractures of the femoral neck. *Clin. Orthop. Relat. Res.* [287], 30-40.

Reid, D. (1969) The shoulder girdle: its function as a unit in abduction. *Physiotherapy* 55[2], 57-59.

Reinschmidt, C., vandenBogert, A.J., Lundberg, A., Nigg, B.M., Murphy, N., Stacoff, A., and Stano, A. (1997) Tibiofemoral and tibiocalcaneal motion during walking: external vs. skeletal markers. *Gait Posture* 6[2], 98-109.

Rhoad, R.C., Klimkiewicz, J.J., Williams, G.R., Kesmodel, S.B., Udupa, J.K., Kneeland, J.B., and Iannotti, J.P. (1998) A new in vivo technique for three-dimensional shoulder kinematics analysis. *Skeletal Radiol.* 27[2], 92-97.

Rundquist, P.J., Anderson, D.D., Guanche, C.A., and Ludewig, P.M. (2003) Shoulder kinematics in subjects with frozen shoulder. *Arch. Phys. Med. Rehabil.* 84[10], 1473-1479.

Ryd, L., Albrektsson, B.E., Carlsson, L., Dansgard, F., Herberts, P., Lindstrand, A., Regner, L., and Toksvig-Larsen, S. (1995) Roentgen stereophotogrammetric analysis as a predictor of mechanical loosening of knee prostheses. *J. Bone Joint Surg. Br.* 77[3], 377-383.

Saha, A.K. (1971) Dynamic stability of the glenohumeral joint. *Acta Orthop. Scand.* 42[6], 491-505.

Schildhauer, T.A., Robie, B., Muhr, G., and Koller, M. (2006) Bacterial adherence to tantalum versus commonly used orthopedic metallic implant materials. *J. Orthop. Trauma* 20[7], 476-484.

Selvik, G., Alberius, P., and Aronson, A.S. (1983) A roentgen stereophotogrammetric system. Construction, calibration and technical accuracy. *Acta Radiol.Diagn.* 24[4], 343-352.

Selvik, G. (1989) Roentgen stereophotogrammetry. A method for the study of the kinematics of the skeletal system. *Acta Orthop. Scand. Suppl.* 232, 1-51.

Shapeero, L.G., Dye, S.F., Lipton, M.J., Gould, R.G., Galvin, E.G., and Genant, H.K. (1988) Functional dynamics of the knee joint by ultrafast, cine-CT. *Invest. Radiol.* 23[2], 118-123.

Sharkey, N.A., Marder, R.A., and Hanson, P.B. (1994) The entire rotator cuff contributes to elevation of the arm. *J. Orthop. Res.* 12[5], 699-708.

Sheehan, F.T., Zajac, F.E., and Drace, J.E. (1998) Using cine phase contrast magnetic resonance imaging to non-invasively study in vivo knee dynamics. *J. Biomech.* 31[1], 21-26.

Simpson, K. (2009) Biomechanics of physical activity. In: Hoffman, S.J. (Ed.), *Introduction to kinesiology: Studying physical activity.* Human Kinetics, Windsor. pp. 265-292.

Smith, D.K., Berquist, T.H., An, K.N., Robb, R.A., and Chao, E.Y. (1989) Validation of three-dimensional reconstructions of knee anatomy: CT vs MR imaging. *J. Comput. Assist. Tomogr.* 13[2], 294-301.

Söderkvist, I. and Wedin, P.A. (1993) Determining the movements of the skeleton using well-configured markers. *J. Biomech.* 26[12], 1473-1477.

Soslowsky, L.J., Flatow, E.L., Bigliani, L.U., and Mow, V.C. (1992) Articular geometry of the glenohumeral joint. *Clin. Orthop.* [285], 181-190.

Soslowsky, L.J., Carpenter, J.E., Bucchieri, J.S., and Flatow, E.L. (1997) Biomechanics of the rotator cuff. *Orthop. Clin. North Am.* 28[1], 17-30.

Sugamoto, K., Harada, T., Machida, A., Inui, H., Miyamoto, T., Takeuchi, E., Yoshikawa, H., and Ochi, T. (2002) Scapulohumeral rhythm: relationship between motion velocity and rhythm. *Clin. Orthop. Relat. Res.* [401], 119-124.

Talkhani, I.S. and Kelly, C.P. (2001) Movement analysis of asymptomatic normal shoulders: a preliminary study. *J. Shoulder Elbow Surg.* 10[6], 580-584.

Tashman, S. and Anderst, W. (2003) In-vivo measurement of dynamic joint motion using high speed biplane radiography and CT: application to canine ACL deficiency. *J. Biomech. Eng.* 125[2], 238-245.

Tashman, S., Collon, D., Anderson, K., Kolowich, P., and Anderst, W. (2004) Abnormal rotational knee motion during running after anterior cruciate ligament reconstruction. *Am. J. Sports Med.* 32[4], 975-983.

Todo, S., Kadoya, Y., Moilanen, T., Kobayashi, A., Yamano, Y., Iwaki, H., and Freeman, M.A. (1999) Anteroposterior and rotational movement of femur during knee flexion. *Clin. Orthop. Relat. Res.* [362], 162-170.

Triffitt, P.D., Wildin, C., and Hajioff, D. (1999) The reproducibility of measurement of shoulder movement. *Acta Orthop. Scand.* 70, 322-324.

Uvehammer, J., Kärrholm, J., Brandsson, S., Herberts, P., Carlsson, L., Kärlsson, J., and Regner, L. (2000) In vivo kinematics of total knee arthroplasty: flat compared with concave tibial joint surface. *J. Orthop. Res.* 18[6], 856-864.

Valstar, E.R., Nelissen, R.G.H.H., Reiber, J.H.C., and Rozing, P.M. (2002) The use of Roentgen stereophotogrammetry to study micromotion of orthopaedic implants. *ISPRS J. Photo. Rem. Sens.* 56[5-6], 376-389.

Valstar, E.R., Gill, R., Ryd, L., Flivik, G., Börlin, N., and Kärrholm, J. (2005) Guidelines for standardization of radiostereometry (RSA) of implants. *Acta Orthop.* 76[4], 563–572.

van Andel, C.J., Wolterbeek, N., Doorenbosch, C.A., Veeger, D.H., and Harlaar, J. (2008) Complete 3D kinematics of upper extremity functional tasks. *Gait Posture* 27[1], 120-127.

van der Helm, F.C. and Pronk, G.M. (1995) Three-dimensional recording and description of motions of the shoulder mechanism. *J. Biomech. Eng.* 117[1], 27-40.

Van Roy, P., Baeyens, J.P., Fauvart, D., Lanssiers, R., and Clarijs, J.P. (2005) Arthro-kinematics of the elbow: study of the carrying angle. *Ergonomics* 48[11-14], 1645-1656.

Vanwanseele, B., Parker, D., and Coolican, M. (2009) Frontal knee alignment: three-dimensional marker positions and clinical assessment. *Clin. Orthop. Relat. Res.* 467[2], 504-509.

Veeger, H.E., Yu, B., An, K.N., and Rozendal, R.H. (1997) Parameters for modeling the upper extremity. *J. Biomech.* 30[6], 647-652.

Veeger, H.E., van der Helm, F.C., Chadwick, E.K., and Magermans, D. (2003) Toward standardized procedures for recording and describing 3-D shoulder movements. *Behav. Res. Methods Instrum. Comput.* 35[3], 440-446.

Veldpaus, F.E., Woltring, H.J., and Dortmans, L.J. (1988) A least-squares algorithm for the equiform transformation from spatial marker co-ordinates. *J. Biomech.* 21[1], 45-54.

Vermeulen, H.M., Stokdijk, M., Eilers, P.H., Meskers, C.G., Rozing, P.M., and Vliet Vlieland, T.P. (2002) Measurement of three dimensional shoulder movement patterns with an electromagnetic tracking device in patients with a frozen shoulder. *Ann. Rheum. Dis.* 61[2], 115-120.

von Eisenhart-Rothe, R., Siebert, M., Bringmann, C., Vogl, T., Englmeier, K.H., and Graichen, H. (2004) A new in vivo technique for determination of 3D kinematics and contact areas of the patello-femoral and tibio-femoral joint. *J. Biomech.* 37[6], 927-934.

Wada, M., Tatsuo, H., Kawahara, H., Sato, M., and Baba, H. (2001) In vivo kinematic analysis of total knee arthroplasty with four different polyethylene designs. *Artif. Organs* 25[1], 22-28.

Wearing, S.C., Urry, S., Perlman, P., Smeathers, J., and Dubois, P. (1998) Sagittal plane motion of the human arch during gait: a videofluoroscopic analysis. *Foot Ankle Int.* 19[11], 738-742.

Winter, D.A. (2005a) Biomechanics as an interdiscipline. In: *Biomechanics and motor control of human movement.* John Wiley & Sons, Hoboken, New Jersey. pp. 1-12.

Winter, D.A. (2005b) Kinematics. In: *Biomechanics and motor control of human movement.* John Wiley & Sons, Hoboken, New Jersey. pp. 13-58.

Winter, D.A. (2005c) Three-dimensional kinematics and kinetics. In: *Biomechanics and motor control of human movement.* John Wiley & Sons, Hoboken, New Jersey. pp. 180-202.

Wolfe, S.W., Neu, C., and Crisco, J.J. (2000) In vivo scaphoid, lunate, and capitate kinematics in flexion and in extension. *J. Hand Surg. [Am.]* 25[5], 860-869.

Wu, G., van der Helm, F.C., Veeger, H.E., Makhsous, M., van Roy, P., Anglin, C., Nagels, J., Karduna, A.R., McQuade, K., Wang, X., Werner, F.W., and Buchholz, B. (2005) ISB recommendation on definitions of joint coordinate systems of various joints for the reporting of human joint motion--Part II: shoulder, elbow, wrist and hand. *J. Biomech.* 38[5], 981-992.

Wuelker, N., Schmotzer, H., Thren, K., and Korell, M. (1994) Translation of the glenohumeral joint with simulated active elevation. *Clin. Orthop.* [309], 193-200.

Wuelker, N., Wirth, C.J., Plitz, W., and Roetman, B. (1995) A dynamic shoulder model: reliability testing and muscle force study. *J. Biomech.* 28[5], 489-499.

CHAPTER 2 – THE WOQIL FLUOROSCOPIC RSA SYSTEM

OVERVIEW: This chapter describes the components of the fluoroscopic RSA system and the development and validation of those components that were custom-made. It also describes the digitization and RSA algorithms as well as some common sources of error and how they are quantified.

2.1 FLUOROSCOPY UNITS

A fluoroscopy unit consists of an x-ray tube and its associated filters, along with a collimator and a phosphor screen onto which the x-rays are incident, once they have passed through the object of interest (Figure 2.1; see Bushberg *et al.*, 2002). The energy of the x-rays is dictated by the applied voltage in the x-ray tube, which may be adjusted by the operator. Filters are generally used to remove the low energy x-rays which would most likely not reach the phosphor detector. The collimator restricts the area through which the x-rays travel using pairs of shutters. X-rays pass through the object of interest, are attenuated to varying degrees depending upon the materials through which they pass, and are incident upon the phosphor screen. As the x-rays strike the screen, photons are released by the photoelectric effect. The phosphor screen is coupled to an image intensifier (II) that amplifies the light, differentiating fluoroscopy from traditional radiography. The II is in turn coupled to a video camera through an aperture that adjusts the light energy of the signal and lenses that focus the image. In this way, moving x-ray images can be viewed in real time.

Images may be taken using fluoroscopy units in one of two ways. The first is

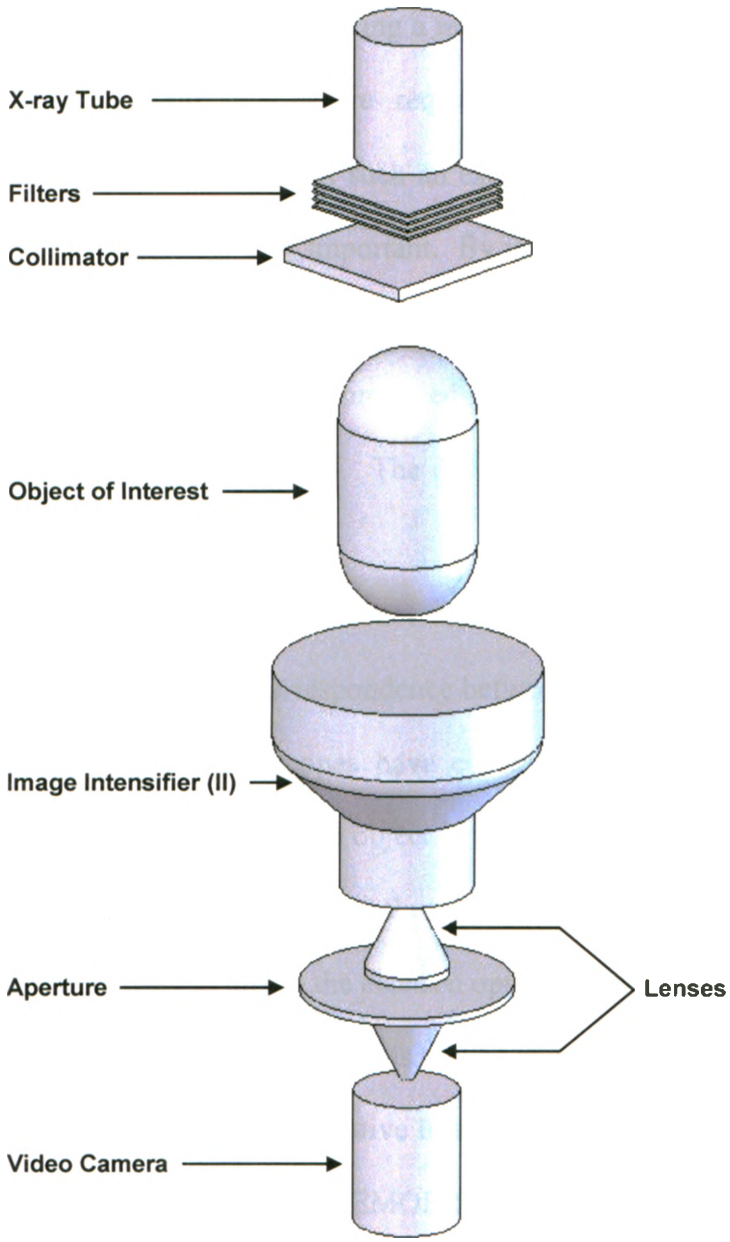

Figure 2.1 Components of the fluoroscopy unit
The main components of the fluoroscopy system include the x-ray tube that generates the x-rays, the filters that remove the low energy rays, the collimator that restricts the field of view, the object of interest, the image intensifier that amplifies the image signal, lenses for focusing, an aperture for adjusting the gain of the system, and a video camera to capture the images.

digital radiography. This captures a still image, much like that which would be obtained via traditional x-ray. The second is fluoroscopy, in which a stream of images is captured at a rate of 30 frames per second, creating a moving x-ray. In order to obtain a "movie" of just 30 seconds, 900 images are required. Understandably, using traditional radiography, the radiation dose from such an examination would be unacceptably high. This is where the II becomes very important. By using specialized phosphor technology in a vacuum tube, the number of light photons emitted as a function of the x-rays applied is amplified, allowing images to be produced using more than one hundred times less radiation (see Bushberg *et al.*, 2002). The downside is that amplification of the signal results in added noise in the image.

Theoretically, since x-rays are not deflected to any appreciable amount when passing through an object, the correspondence between an object and its image is strictly central projection. The fluoroscopes have conical fields of view; therefore, due to diverging ray principles, the closer an object is to the II, the smaller it will appear. Most basically, the images produced by the fluoroscopes look like a scaled version of the object of interest. However, due to the electron optics that are used within the IIs, there is some distortion present in the images. This will be addressed in Section 2.3.

The Wolf Orthopaedic Quantitative Imaging Laboratory (WOQIL) has two 9 inch fluoroscopy units (Figure 2.2; SIREMOBIL Compact-L mobile C-arms, Siemens Medical Solutions Canada Inc., Mississauga, Canada). These are portable C-arm units, meaning that the x-ray tube and II are fixed on opposite ends of a C-shaped arm, which can be positioned in a wide variety of locations and orientations. A brief user's manual for the operation of the fluoroscopy units is contained in Appendix C.

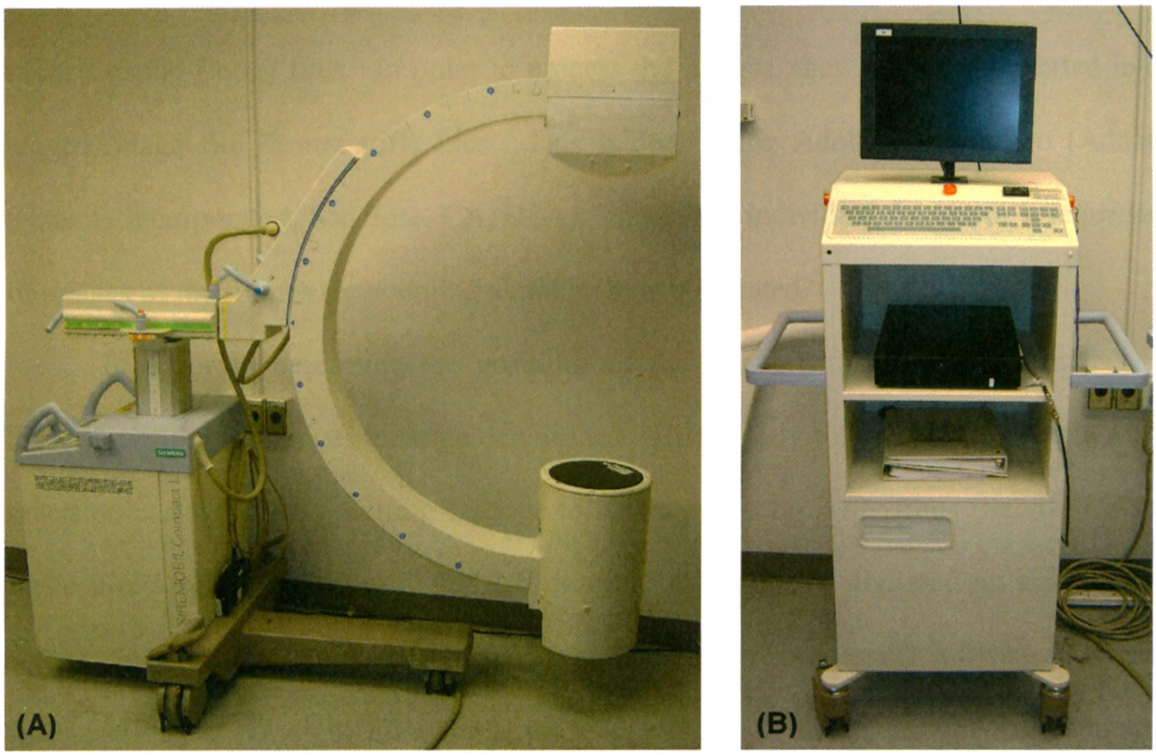

Figure 2.2 SIREMOBIL Compact-L mobile C-arm fluoroscopy unit
(A) The C-arm fluoroscopy unit with the x-ray source at the top of the arm and the image intensifier at the bottom of the arm. **(B)** The accompanying video display and control panel.

2.2 IMAGE PROCESSING

Images from each fluoroscopy unit are transferred to a personal computer via a video capture device (DVD Xpress DX2, ADS Technologies Inc., Cerritos, CA, USA), where they are recorded by the accompanying software (Capture Wizard, ADS Technologies Inc., Cerritos, CA, USA). Output from the fluoroscopy units is saved on the personal computers by the Capture Wizard software in the form of moving picture experts group (mpg) files. In order to process the images, they must be converted into tagged image file format (tiff) files. This is done using Adobe Premier Pro (Adobe Systems Incorporated, San Jose, CA, USA). Images of individual frames or a sequence of images of the frames representing a motion may be created.

In order to determine the positions of the beads within the laboratory, their location within the images must be determined. Historically this was done using a high precision cartographer's plotting carriage to locate points on x-ray films (Selvik, 1989). Since x-ray images are now digital, the image points may be digitized on a computer screen. Incorporating automated or semi-automated image processing software increases the objectivity of the digitizations. For the work conducted herein, custom-written image processing software (pick_points.m; see Appendix D) was created in MATLAB (The MathWorks, Natick, MA, USA). It enables four types of images to be digitized: images for calibration, images for distortion correction, images for synchronizing the radiostereometric analysis (RSA) system with the optical motion analysis system, and images of other objects with beads affixed whose motion is to be tracked.

Processing is the same for all four types of images. The image to be digitized is specified and it appears in a separate window. Due to the coordinate system definitions

within MATLAB, the image appears up-side-down. When digitizing points that are to be reconstructed in three dimensions, there is the option to zoom in on the area that is to be digitized. This allows a more accurate digitization to be obtained if points are located close together.

Points are manually selected by the user with a cursor controlled by the computer's mouse. Other groups have used a parabolic model of the marker fitted to the marker's grey value profile (Vrooman *et al.*, 1998), two dimensional Mexican hat filters (Buck *et al.*, 2003), and edge detection (Østgaard *et al.*, 1997; Vrooman *et al.*, 1998) to determine marker locations within the images. The method used in this dissertation is one of weighted pixel values (Gronenschild, 1997; Cerveri *et al.*, 2002; Holdsworth *et al.*, 2005). A graphical representation of this process is shown in Figure 2.3. For each point selected, the darkest pixel in the surrounding region is found. From this, an area is created that contains the marker whose location the user wishes to determine. This area is filled according to the shades of the pixels that surrounded it. The size of the area depends upon the type of image being digitized, as the markers vary dramatically in size. In this way the background of the image is subtracted, leaving only the marker of interest. Subtracting the background of the image eliminates problems associated with non-uniform brightness across the II due to other objects in the field of view and uneven focussing of electron optics (Cho and Johnson, 1998). The process to find the darkest pixel is repeated and a second centre point is found. A weighted average of the shades of the pixels surrounding this centre point is used to determine the centre of the point that was originally picked by the user. The locations of all the user-selected points in the image are then exported to an Excel (Microsoft Corporation, Seattle, WA, USA) file.

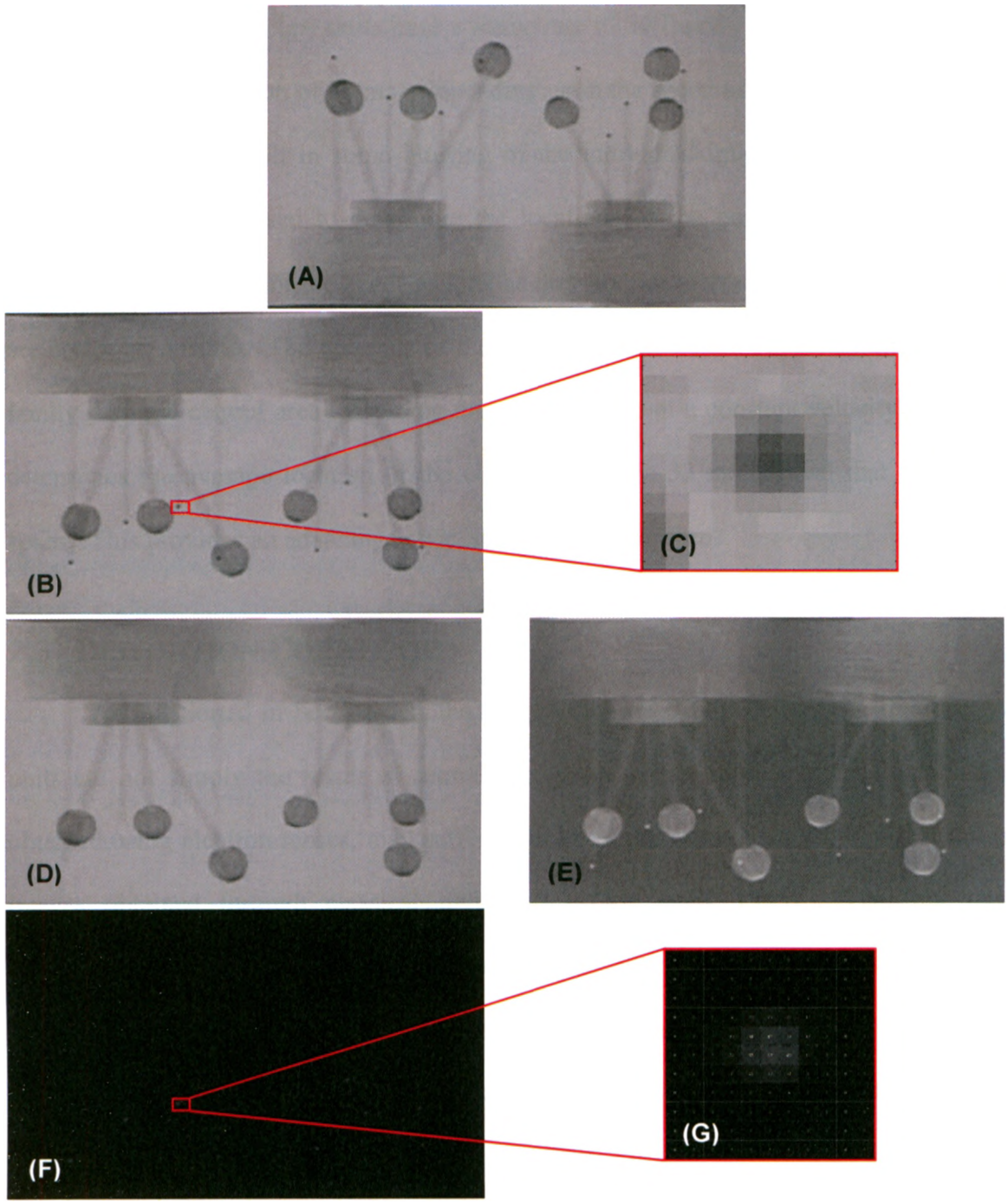

Figure 2.3 A graphical representation of the algorithm behind the program pick_points.m

The image to be digitized is specified **(A)**. It is then turned up-side-down **(B)** to accommodate the image co-ordinate system definitions within MATLAB. Points are chosen using the mouse and a sub-image around each point **(C)** is created. The centre of the bead is found and the region is filled according to the shades of the pixels that surround it to remove the bead from the image **(D)**. The original image is inverted **(E)** and the inverted image of the filled image is subtracted, yielding the beads only **(F)**. The location of each bead is determined using the pixel shades from a subimage **(G)**.

Since the fluoroscopy units have a frame rate of 30 frames per second, each image has a temporal resolution of 33 ms. Depending upon the speed of any motion in the field of view, this may result in some blurring of the individual image frames. Because a weighted average is used to determine the locations of the points, digitization is not affected by the motion of the beads as long as they are not blurred to the extent that they are no longer visible. The tail-ends of the path of motion of the object are shown more faintly than the central area (assuming the object moves at a constant velocity), so RSA determines the average location of the object within the 33 ms interval that the image spans. This provides an advantage over circle fitting algorithms.

2.3 DISTORTION CORRECTION

As mentioned in Section 2.1, the images that are obtained from the fluoroscopy units are not simply the result of central projection. Fluoroscopic images, which are obtained using electron lenses, may suffer from all of the primary aberrations that affect images obtained through classical light optics (see Jareš, 1985). The first four aberrations: spherical aberration, coma, astigmatism, and curvature of field may cause the blurring and therefore affect the spatial resolution of the images (see Rudin *et al.*, 1991). However, while blurring may be measured, it cannot be corrected by the user. The fifth primary aberration is distortion of the image (see Rudin *et al.*, 1991). This may be corrected by the user in post-processing and therefore was addressed in this thesis.

Distortion may occur as a result of lens optics, but it also may occur as a result of the curvature of the II and the effect of Earth's magnetic fields and the magnetic fields of other electronic devices on electron paths (see van der Zweet *et al.*, 1995). These three causes result in two distinct modes of distortion. Pin-cushion distortion is primarily due

to the process by which the electrons are focused within the II as it requires a curved photocathode (Figure 2.4B; see Rudin *et al.*, 1991; Bushberg *et al.*, 2002). This distortion may be corrected to some extent within the II; though due to the propriety nature of such technology it is difficult to know the extent of the correction. S-shaped, spiral, or pocket handkerchief distortion occurs primarily as a result of Earth's or other electronic devices' magnetic fields (Figure 2.4C). Video monitors, for instance, may generate localized magnetic fields that are much stronger than that associated with Earth (van der Zweet *et al.*, 1995). These fields are variable, and dependent upon the orientation of the II, but may be corrected using shielding and a coil that creates a magnetic field in opposition to that created by Earth or other objects (see Rudin *et al.*, 1991). As the exact source and the degree of variability of distortion are difficult to characterize, it is not recommended that a single distortion image be used at all times. In fact, if the variability in the distortion due to Earth's and other electronics' magnetic fields is large enough, errors may be introduced into the data that may be larger than those that existed before correction for distortion was applied (van der Zweet *et al.*, 1995).

Instead, distortion is corrected on a day-to day basis in a manner to account for all possible sources of induced error. In order to perform the correction, a 15 mm x 15 mm grid of 131 stainless steel beads each 2 mm in diameter was created on a 9.5 mm Delrin sheet. For optimal results, the number of beads in the distortion grid needed to be at least a factor of three more than the number of minimum number required (Fahrig *et al.*, 1997). This minimum is dictated by the correction scheme that is chosen and is discussed in the text that follows. Schematic drawings of the distortion correction grid may be

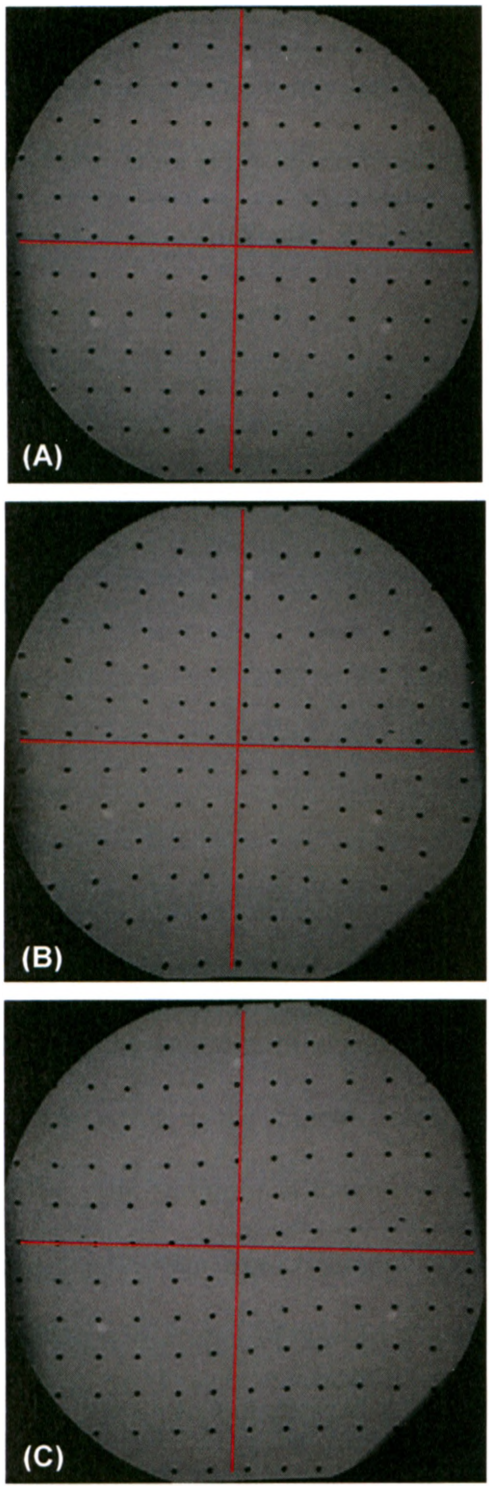

Figure 2.4 The effects of distortion
Images of the distortion correction grid **(A)** without distortion, **(B)** with simulated pincushion distortion and **(C)** with simulated S-shaped distortion. Cross-hairs have been drawn on the images to emphasize the differences between them.

found in Appendix E. The positions of these beads were precisely determined with the use of a coordinate measuring machine (DEA Swift, Hexagon Metrology Services Ltd.., London, UK). The details of the digitization may be found in Appendix F. The grid rigidly attaches to a ring that fits into a ridge in the housing of the IIs. Following data collection, the grid is placed over each II (Figure 2.5) and an image is obtained of the distorted positions of the beads. In this way a location-specific correction may be determined for all sections of the image. Due to the time-variable and orientation-dependent nature of s-shaped distortion, correction is performed for every set of data collected.

Either a local or a global approach to distortion correction may be taken. In a local approach the distortion vector at each point in the grid is calculated. The vector at an arbitrary point is then found using linear or non-linear interpolation between the three (Boone *et al.*, 1991; Schueler and Hu, 1995) or four (Cho *et al.*, 1995; van der Zweet *et al.*, 1995; Gronenschild, 1999) or sixteen (Cerveri *et al.*, 2002) beads surrounding the point. Local distortion correction algorithms are more prone to the influence of image noise or errors in digitization, as the coordinates of only three or four beads are used for the distortion correction of any point in the image (Fahrig *et al.*, 1997; Gronenschild, 1999; Fantozzi *et al.*, 2003). In addition, a local correction scheme will produce discontinuities between each "cell" – the area contained within three or four beads – in the image (Gronenschild, 1997; Liu *et al.*, 1999). In a global approach the distortion vector at each point is again calculated but these data are then used to determine an overall expression for the distortion within the image. This may be calculated according to Cartesian (Chakraborty, 1987; Fahrig *et al.*, 1997; Gronenschild, 1997; Liu *et al.*,

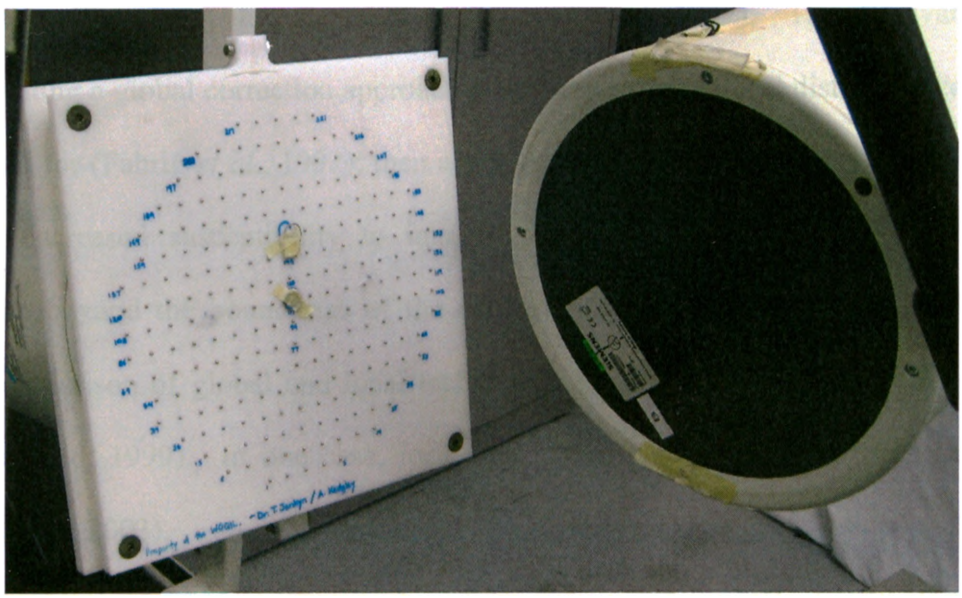

Figure 2.5 The distortion correction grid
The distortion correction grid, consisting of a 15 mm x 15 mm grid of 131 stainless steel beads each 2 mm in diameter, was created on a 9.5 mm Delrin sheet. It is shown mounted to the II on the left.

1999; Fantozzi *et al.*, 2003; Holdsworth *et al.*, 2005) or radial (Rudin *et al.*, 1991) coordinates of the image. The positions of the beads in the image are related to their known positions according to a polynomial or, in one case, thin-plate splines (Fantozzi *et al.*, 2003). The number of coefficients in the polynomial will dictate the minimum number of beads that are required for a solution. For instance, a polynomial with a maximum degree of one in each of x and y ($z = a + by + cx + dxy$) has four coefficients (a, b, c and d). Cartesian polynomial fits are preferred, as distortion is usually non-radial due to the effects of s-shaped distortion (Gronenschild, 1997). The disadvantage of implementing a global correction approach is that any extreme local distortions cannot be accounted for (Fahrig *et al.*, 1997); then again, none are to be expected. The advantages are the decreased susceptibility to image noise and the ability to extrapolate the correction beyond the boundaries of the calibration points (Fahrig *et al.*, 1997). In a direct comparison of global and local techniques, the former was found to be superior (Gronenschild, 1999). In one case, local and global approaches have been combined (Soimu *et al.*, 2003).

In this thesis, a global approach to distortion correction is taken using a fifth order polynomial in Chapters 3, 4, and 6 and a fourth order polynomial in Chapter 7, relating the positions of the beads in the x- and y-axes of the image to the known positions of the beads in x- and y-coordinates of the grid. The polynomial coefficients are obtained from a web-based program (located at zunzun.com). The order of the polynomial was altered because of the results of the study that is documented in Chapter 5. Distortion correction was performed using a custom-written MATLAB program. More details regarding this correction process and its validation may be found in Chapter 5.

2.4 CALIBRATION

The fluoroscopes are not fixed within the laboratory and may be positioned in a wide range of orientations, giving great freedom in obtaining the best views of the subject. However, this makes calibration extremely important. The calibration routine establishes the coordinate system of the laboratory and determines the positions of the fluoroscopes. It also determines the relationships that are required to complete the three-dimensional reconstruction of points of interest. In order to calibrate the system, the positions of markers must be known in both the laboratory frame and the image frames. Calibration must be performed every time the fluoroscopes are moved. Most commonly it is performed before (and/or after) every data collection session. If either of the fluoroscopes is bumped during a testing session, a new set of calibration images must be taken. There are two types of calibration frames that are commonly used. The first is used with a uniplanar RSA configuration, in which the two imaging devices are placed side-by-side (see Valstar *et al.*, 2005). The second is used with a biplanar RSA configuration, in which the two imaging devices are placed orthogonally to one another (see Valstar *et al.*, 2005). In order to maximize the volume which is available for RSA, the goal is to have the largest portions of the fields of view of each fluoroscope overlapping. The WOQIL system is calibrated with a custom-made calibration object, detailed below, similar to the biplanar calibration frames described in the literature.

2.4.1 CALIBRATION FRAME

The calibration frame was constructed from 9.5 mm acrylic sheet. It consists of two planes called fiducial planes and two planes called control planes that are positioned such that one fiducial plane and one control plane can be seen in each fluoroscopic image

with the fiducial planes adjacent to the IIs. Each fiducial and control plane is embedded with 45 beads in a 9 bead by 5 bead matrix. The fiducial points are 1 mm in diameter and have a grid spacing of 20 mm by 25 mm. The control points are 2 mm in diameter and have a grid spacing of 15 mm by 20 mm. Selvik's original calibration frame had only 9 beads on each plane (Selvik *et al.*, 1983); however, the large number of fiducial and control points allows greater flexibility in the configuration of the fluoroscopes and compensates for the fact that all points will not be visible in every calibration image. Studies in optical motion analysis systems have shown that evenly distributing the control points over the whole region of interest will result in the best calibration results (Chen *et al.*, 1994). RSA investigations have shown that precision is proportional to the number of beads available for calibration but that bead spacing has a negligible effect (Cai *et al.*, 2008). The calibration frame may be mounted to a tripod via a universal joint. This allows the frame to be positioned as optimally as possible within the field of view. Schematic drawings of the frame may be found in Appendix E.

For the first three studies (Chapters 3, 4 and 5) the fiducial and control planes were attached to a large base upon which the planes could be adjusted into one of four parallelogram configurations with opposing planes parallel to one another and the larger angle of the parallelogram being 90°, 105°, 120° or 135°. The fiducial and control planes were 317.46 mm apart in the orthogonal configuration. A comparison of the results obtained using the various configurations of the calibration frame can be found in Chapter 4. As a result of the study contained in Chapter 4 of this thesis, the calibration frame was modified and for the remaining studies (Chapters 6 and 7) the fiducial and

control planes were affixed to a smaller base where the angles between the planes were permanently set at 90°.

2.4.2 METHODOLOGY

The fiducial points establish a two-dimensional transformation between each image coordinate system and the laboratory coordinate system (Figure 2.6; Kärrholm, 1989; Selvik, 1989). From the known coordinates of the fiducial marks in both the image (x', y') and laboratory (x, y) coordinate systems, the parameters of the projective transformations (a_1, a_2, a_4, b_1, b_2, b_4, d_1 and d_2) can be determined:

$$x = \frac{a_1x'+b_1y'+d_1}{a_4x'+b_4y'+1} \quad \textbf{(Eq. 2.1a)}$$

$$x(a_4x'+b_4y'+1) = a_1x'+b_1y'+d_1 \quad \textbf{(Eq. 2.1b)}$$

$$y = \frac{a_2x'+b_2y'+d_2}{a_4x'+b_4y'+1} \quad \textbf{(Eq. 2.2a)}$$

$$y(a_4x'+b_4y'+1) = a_2x'+b_2y'+d_2 \quad \textbf{(Eq. 2.2b)}$$

There are eight parameters, so four fiducial points are necessary (each yielding two coordinates). By combining equations 2.1b and 2.2b for four fiducial points into matrix form, the projective transformation for each fluoroscope is found by using the following:

$$\begin{bmatrix} x_1' & y_1' & 0 & 0 & -x_1'x_1 & -y_1'x_1 & 1 & 0 \\ 0 & 0 & x_1' & y_1' & -x_1'y_1 & -y_1'y_1 & 0 & 1 \\ x_2' & y_2' & 0 & 0 & -x_2'x_2 & -y_2'x_2 & 1 & 0 \\ 0 & 0 & x_2' & y_2' & -x_2'y_2 & -y_2'y_2 & 0 & 1 \\ x_3' & y_3' & 0 & 0 & -x_3'x_3 & -y_3'x_3 & 1 & 0 \\ 0 & 0 & x_3' & y_3' & -x_3'y_3 & -y_3'y_3 & 0 & 1 \\ x_4' & y_4' & 0 & 0 & -x_4'x_4 & -y_4'x_4 & 1 & 0 \\ 0 & 0 & x_4' & y_4' & -x_4'y_4 & -y4_1'y_4 & 0 & 1 \end{bmatrix} \begin{bmatrix} a_1 \\ b_1 \\ a_2 \\ b_2 \\ a_4 \\ b_4 \\ d_1 \\ d_2 \end{bmatrix} = \begin{bmatrix} x_1 \\ y_1 \\ x_2 \\ y_2 \\ x_3 \\ y_3 \\ x_4 \\ y_4 \end{bmatrix} \quad \textbf{(Eq. 2.3)}$$

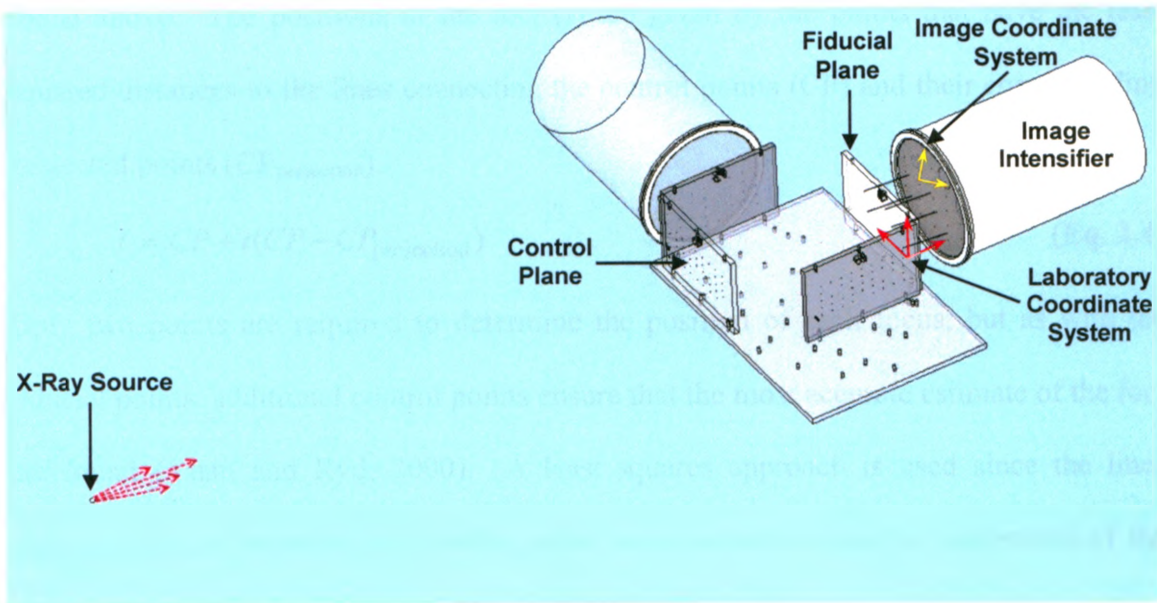

Figure 2.6 Use of the fiducial planes
Projective transformations are determined from the locations of the points on the fiducial plane in both the laboratory and image coordinate systems.

While only four points are required, additional fiducial points ensure that the best possible set of parameters is found. All combinations of four points are tested, and the combination with the lowest error is chosen.

The exact positions of the foci of the x-ray units – the points at which the x-rays originate – are found using the control planes of the calibration frame (Figure 2.7; Kärrholm, 1989; Selvik, 1989). The projections of the control points on the fiducial planes are found using their positions on the images and the projective transformations found above. The positions of the foci (f) are given by the points that have the least squared distances to the lines connecting the control points (CP) and their corresponding projected points ($CP_{projection}$).

$$f = CP + t(CP - CP_{projection}) \quad \textbf{(Eq. 2.4)}$$

Only two points are required to determine the position of each focus, but as with the fiducial points, additional control points ensure that the most accurate estimate of the foci are found (Yuan and Ryd, 2000). A least squares approach is used since the lines generally do not intersect at a perfect point due to errors. Once the calibration of the system is complete, *i.e.*, the projective transformation parameters and the positions of the foci are found, the fluoroscopes cannot be touched, as any motion will render the calibration invalid. All calibration calculations were performed using programs that were custom-written in MATLAB.

2.5 SYNCHRONIZATION

In order to allow RSA to be performed on trials in which motion occurs, it must be known which frames of the videos from the two fluoroscopy units are taken at any given point in time. As each fluoroscopy unit is activated via either a hand trigger or a foot

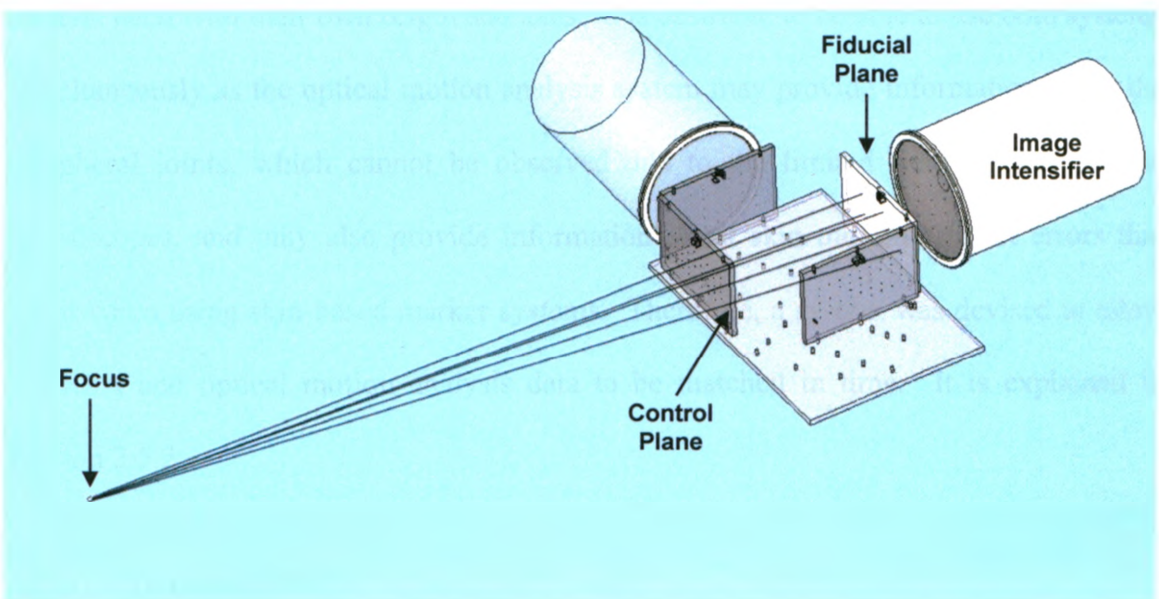

Figure 2.7 Use of the control planes
The position of the focus of each fluoroscopy unit is found using the points on the control plane and their projected locations on the fiducial plane.

pedal, and the units are not connected in any way, it cannot be guaranteed that images will be captured at the same time. If RSA is performed on the points from two images that were not taken at the same time, the three-dimensional (3D) reconstruction will be invalid. Therefore, a method was required to ensure that images from the two fluoroscopy units were matched correctly. This method is described in Section 2.5.1.

Similarly, the optical motion analysis system is completely separate from the fluoroscopy units. The two systems are calibrated separately and therefore the laboratory space is defined by both an RSA coordinate system and a motion analysis coordinate system, each with their own origin and axes. It is desirable to be able to use both systems simultaneously as the optical motion analysis system may provide information about the peripheral joints, which cannot be observed due to the limited field of view of the fluoroscopes, and may also provide information about skin motion artefact errors that occur when using skin-based marker systems. Therefore, a system was devised to allow the RSA and optical motion analysis data to be matched in time. It is explained in Section 2.5.2.

2.5.1 FLUOROSCOPES

In order to synchronize the two fluoroscopy units, a custom-designed device was constructed to allow a visual verification (Figure 2.8). The device consists of two drums, each with a wire embedded in it, which rotate synchronously as dictated by proximity switches. The drums are controlled by two stepper motors whose speed is dictated by the operator. They can rotate at 0.5 Hz, 0.8 Hz, 1.1 Hz, 1.4 Hz, 1.8 Hz, or 2.0 Hz; although in order to effectively synchronize the fluoroscopes they must rotate at 2.0 Hz. They are strapped onto the IIs such that the wire on each drum is visible in its respective image.

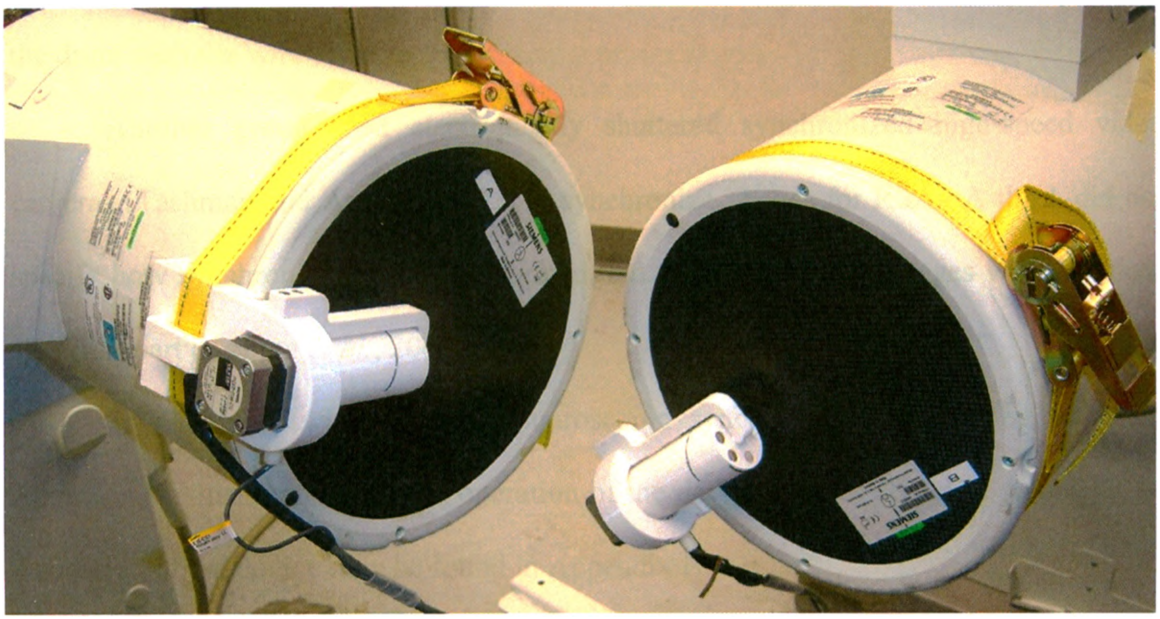

Figure 2.8 The drums of the fluoroscopic synching device mounted to the image intensifiers

Obviously they must be secured prior to calibration and motion of the drums is started prior to the recording of any images of the object of interest. The phase of motion of each drum is determined by a wire scale embedded in the arm (Figure 2.9). When the drums are rotating at 2 Hz, an increment of one frame in a video sequence will result in a change of approximately one "tick" on the scale. During image processing, the beginning of a sequence of images may be determined by matching the phases of the drums. This is a novel technique for the synchronization of two fluoroscopes. A limitation to this approach is the possibility of human error in interpreting the position of the drum with the wire scale.

Another group used electronically shuttered synchronized high-speed video cameras (Tashman and Anderst, 2003) to synchronize images for RSA. A third, did not specify how synchronization was performed, but did state the two images were acquired 12.7 ms apart (Koning *et al.*, 2007).

Schematic drawings for the fluoroscopic synching device may be found in Appendix E. Instructions for the operation of the device may be found in Appendix G. Validation of the device may be found in Appendix H.

2.5.2 FLUOROSCOPES AND MOTION ANALYSIS

A tertiary coordinate system is employed to match the data obtained from the optical motion analysis and RSA systems (Stagni *et al.*, 2006). A small calibration frame (Figure 2.10), consisting of three brass spheres wrapped in reflective tape, was constructed. Being metal, the balls can be seen clearly on the fluoroscopy images and therefore a 3D reconstruction of their positions within the RSA laboratory space can be performed. Being reflective, the balls can also be located by the optical tracking system

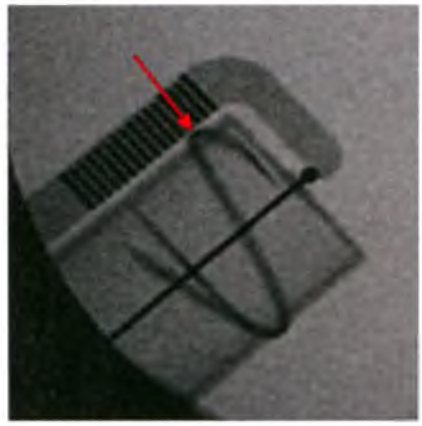

Figure 2.9 Image of the fluoroscopic synching device
The phase of the drum is indicated by the position of the wire wrapped around the drum in a helical fashion, relative to the scale embedded in the arm (as indicated by the arrow).

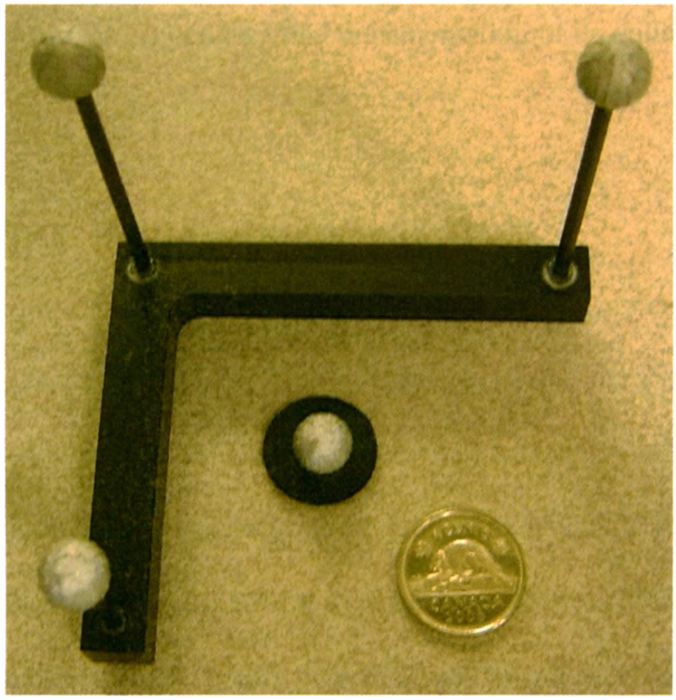

Figure 2.10 The synching device for the optical motion analysis system
A small calibration frame consisting of three brass balls coated in reflective tape, and one brass marker for use with the skin-mounted marker set.

and their 3D positions with the laboratory space of the tracking system can also be determined. This frame is used in conjunction with a fourth brass ball (also in Figure 2.10), similarly wrapped to be reflective, which is placed on the subject during testing. This marker is identical to other reflective markers that may be used for optical motion analysis.

A sequence of RSA data may be time-matched to a sequence of optical motion analysis data by finding the location of the brass reflective marker within the tertiary coordinate system. The frames where the RSA and EvaRT positions are most similar are the ones that were taken at the same point in time. Calculating the position of the marker in the new coordinate systems and then determining the time points at which they match is performed by the program "synching.m" (see Appendix D). Schematic drawings for the optical motion analysis synching device may be found in Appendix E. Instructions for its use may be found in Appendix I and documentation of its validation may be found in Appendix J.

2.6 THREE-DIMENSIONAL RECONSTRUCTION

The algorithm for RSA is well-established and well-documented in the literature (Selvik, 1989; Valstar *et al.*, 2002). The coordinates of the markers of the object are projected onto the fiducial planes. A line connecting the focus of the chosen x-ray unit and the projected point will pass through the object point (Figure 2.11). The 3D position of the object point (OP) lies at the intersection of the two lines (l_1 and l_2) created by the projections on the fiducial planes (PP_1 and PP_2) and two foci (f_1 and f_2). Where the equations of the two lines are:

$$l_1 = f_1 + \tau(f_1 - PP_1) \qquad \textbf{(Eq. 2.5a)}$$

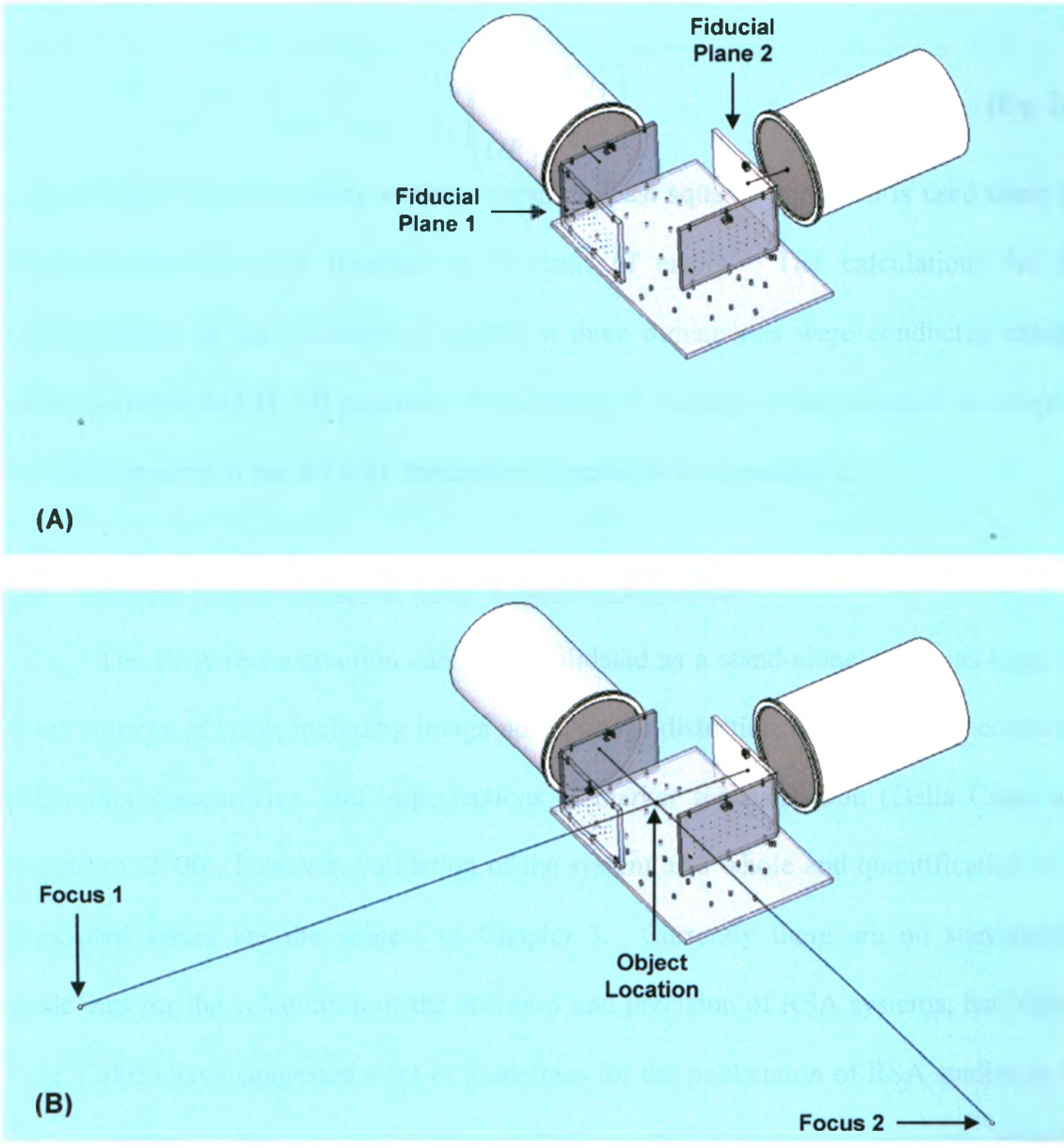

Figure 2.11 Location of objects
Lines are created between **(A)** the projections of the images of an object on the fiducial planes and **(B)** the respective foci of each fluoroscope. The object of interest may be found at the intersection of the two lines.

$$l_2 = f_2 + \varepsilon(f_2 - PP_2) \qquad \textbf{(Eq. 2.5b)}$$

for all values of τ and ε. To find the intersection point the least squares solution to the following equation is found:

$$\begin{bmatrix} (PP_1 - f_1) & 0 & I_3 \\ 0 & (PP_2 - f_2) & I_3 \end{bmatrix} \begin{bmatrix} \tau \\ \varepsilon \\ OP \end{bmatrix} = \begin{bmatrix} f_1 \\ f_2 \end{bmatrix} \qquad \textbf{(Eq. 2.6)}$$

where I_3 is a 3 by 3 identity matrix. Again, a least squares approach is used since the lines generally do not intersect as a result of errors. The calculations for the reconstruction of the locations of points in three dimensions were conducted using a custom-written MATLAB program. A summary of the steps to be followed to complete the RSA process in the WOQIL laboratory is included as Appendix K.

2.7 Sources of Error and Their Analysis

The RSA reconstruction cannot be validated as a stand-alone entity, as there are many sources of error, including image noise, image distortion, digitization inaccuracies, calibration inaccuracies, and imperfections in marker reconstruction (Della Croce and Cappozzo, 2000); however, validation of the system as a whole and quantification of its associated errors are the subject of Chapter 3. Currently there are no standardized guidelines for the calculation of the accuracy and precision of RSA systems, but Valstar *et al.* (2005) have suggested a set of guidelines for the publication of RSA studies in the clinical setting. The required accuracy of the system is dependent upon the intended application. In the case where joint kinematics are desired, accuracies may be on the order of 0.5 mm and 2°. However, if the effects of small motions are the subject of examination, such as pathological changes due to abnormal joint tracking, accuracies need to be better – on the order of 0.01 mm and 0.5°.

Errors in the use of the system may be classified as either systematic or random (see Chiari *et al.*, 2005; Derbyshire *et al.*, 2009). Systematic errors affect the accuracy of the RSA measurements and may create a bias in the outcome. They may be due to inaccuracies in the calibration, including the effects of image distortion. Two other types of systematic errors that may result when performing RSA are incorrect matching of the two image points of a marker, resulting in the reconstruction of a marker position that does not exist and loose markers (see Nyström *et al.*, 1994). In addition, if bone-based coordinate systems are being used in the analysis, incorrect landmark identification may result in serious errors. It has been shown using optical markers that in cases where joint rotations are primarily performed in a single plane, the errors in rotations outside this plane are strongly susceptible to errors in landmark locations (Della Croce *et al.*, 2005). The effect of variations in the location of anatomical landmarks used to determine kinematics of the shoulder is investigated in Chapter 6.

Random errors will affect the precision of the RSA measurements and may include electronic noise, the digitization process, merging of two beads with one another, or phantom markers. Yuan and Ryd (2000) performed a computer analysis of error propagation as a result of errors in fiducial points, control points and object points individually and together. Errors in locating object positions within the images have the largest effects on overall errors in object position, while errors in locating fiducial marks have the smallest influence (Yuan and Ryd, 2000). Yuan *et al.* (1997) developed a model to study error propagation for relative motion, that is, motion between two objects whose positions are both being measured by RSA. It was validated with computer simulations and determined that errors in translation were strongly affected by the distances between

the rigid bodies and the orientations of the bodies (Yuan *et al.*, 1997). This may have a particular bearing on the quantification of kinematics, where rotations and translations may be quite large.

There are two measures of error that apply specifically to the use of RSA. These are condition number and mean error of rigid body fitting, which are discussed below.

2.7.1 CONDITION NUMBER

It has been suggested that the best way to ensure high accuracies in RSA analyses is to insert the beads such that they create a large rigid body with many markers (Ryd *et al.*, 2000). The condition number is a measure of the distribution of the beads within a segment (see Valstar *et al.*, 2005). High values indicate poor distributions. It is calculated as described by Nyström *et al.* (1994), as the inverse of the difference between the errors in the best and second best solutions to the RSA matching problem, multiplied by the errors of the best solution. It may also be calculated through singular value decomposition as described by Södkervist and Wedin (1993). The geometrical interpretation of the condition number is the inverse square root of the sum of the squares of the distances between each bead and an arbitrary straight line passing through the markers on a segment (Södkervist and Wedin, 1993; Ryd *et al.*, 2000). As a low number is desired, this indicates that the markers should be placed such that they do not form a straight line. The recommended upper limit for the condition number is 110 (Valstar *et al.*, 2005).

2.7.2 *Mean Error of Rigid Body Fitting*

The mean error of rigid body fitting is a measure of how little motion there is between beads, and therefore how well the construct that consists of these beads approximates a rigid body. The mean error of rigid body fitting is the average difference in the distances between all the markers on one segment from one examination to another (Nyström *et al.*, 1994, Valstar *et al.*, 2005). It has been suggested that this not exceed 0.35 mm (Valstar *et al.*, 2005) and previous studies have found typical values to be between 0.1 mm and 0.25 mm (Kärrholm *et al.*, 1997). The precision of RSA analyses has been shown to decrease as the mean error of rigid body fitting increases (Ryd, 1986).

2.7.3 *The Double Examination*

While the accuracy of any system must be determined by a comparison with another system that has a significantly better resolution, there are several difficulties that arise when using RSA. As with any clinical study, there may be large variations in the accuracies of measurements taken for individual subjects (see Ryd *et al.*, 2000). In the clinical setting when RSA is being used to quantify stability or component loosening, there is no need to obtain a computed tomography (CT) scan of the subject. Therefore, there is no way to accurately determine the spacing between the implanted beads. Mathematically, if there are no systematic errors, and hence only random errors in a system, the repeatability of a measurement will give a measure of both its accuracy and precision (see Ranstam *et al.*, 2000). Therefore, in many cases, two measurements are taken of each subject at each visit. In fact, double examinations are recommended in the literature for all clinical studies (Valstar *et al.*, 2005).

Due to the fact that CT scans have been acquired of the subject who participated in the clinical study described in Chapter 7, the double examination technique has not been used in this thesis. The distances between the beads obtained using RSA may instead be compared to those found using the CT scans, providing an independent comparison.

2.8 SUMMARY

This chapter detailed the design of the WOQIL fluoroscopic RSA system. Each component was described individually and references were given to the appendices with additional information for the interested reader. The system consists of two fluoroscopy units, allowing dynamic motions to be captured with much less radiation exposure than would be required by traditional x-ray machines. The benefit of mobile fluoroscopes over fixed x-ray machines is that they can be positioned to best accommodate the object(s) of interest. The validation of this system is contained in the chapters that follow.

2.9 REFERENCES

Boone, J.M., Seibert, J.A., Barrett, W.A., and Blood, E.A. (1991) Analysis and correction of imperfections in the image intensifier-TV-digitizer imaging chain. *Med. Phys.* 18[2], 236-242.

Buck, D., Alber, M., and Nusslin, F. (2003) Potential and limitations of the automatic detection of fiducial markers using an amorphous silicon flat-panel imager. *Phys. Med. Biol.* 48[6], 763-774.

Bushberg, J.T., Seibert, J.A., Leidholdt, E.M., and Boone, J.M. (2002) Fluoroscopy. In: *The Essential Physics of Medical Imaging.* Lippincott Williams & Wilkins, Philadelphia. pp. 231-254.

Cai, R., Yuan, X., Rorabeck, C., Bourne, R.B., and Holdsworth, D.W. (2008) Development of an RSA calibration system with improved accuracy and precision. *J. Biomech.* 41[4], 907-911.

Cerveri, P., Forlani, C., Borghese, N.A., and Ferrigno, G. (2002) Distortion correction for x-ray image intensifiers: local unwarping polynomials and RBF neural networks. *Med. Phys.* 29[8], 1759-1771.

Chakraborty, D.P. (1987) Image intensifier distortion correction. *Med. Phys.* 14[2], 249-252.

Chen, L., Armstrong, C.W., and Raftopoulos, D.D. (1994) An investigation on the accuracy of three-dimensional space reconstruction using the direct linear transformation technique. *J. Biomech.* 27[4], 493-500.

Chiari, L., Croce, U.D., Leardini, A., and Cappozzo, A. (2005) Human movement analysis using stereophotogrammetry. Part 2: instrumental errors. *Gait Posture* 21[2], 197-211.

Cho, P.S., Johnson, R.H., and Griffin, T.W. (1995) Cone-beam CT for radiotherapy applications. *Phys. Med. Biol.* 40[11], 1863-1883.

Cho, P.S. and Johnson, R.H. (1998) Automated detection of BB pixel clusters in digital fluoroscopic images. *Phys. Med. Biol.* 43[9], 2677-2683.

Della Croce, U. and Cappozzo, A. (2000) A spot check for estimating stereophotogrammetric errors. *Med. Biol. Eng. Comput.* 38[3], 260-266.

Della Croce, U., Leardini, A., Chiari, L., and Cappozzo, A. (2005) Human movement analysis using stereophotogrammetry. Part 4: Assessment of anatomical landmark misplacement and its effects on joint kinematics. *Gait Posture* 21[2], 226-237.

Derbyshire, B., Prescott, R.J., and Porter, M.L. (2009) Notes on the use and interpretation of radiostereometric analysis. *Acta Orthop.* 80[1], 124-130.

Fahrig, R., Moreau, M., and Holdsworth, D.W. (1997) Three-dimensional computed tomographic reconstruction using a C-arm mounted XRII: Correction of image intensifier distortion. *Med. Phys.* 24[7], 1097–1106.

Fantozzi, S., Cappello, A., and Leardini, A. (2003) A global method based on thin-plate splines for correction of geometric distortion: an application to fluoroscopic images. *Med. Phys.* 30[2], 124-131.

Gronenschild, E. (1997) The accuracy and reproducibility of a global method to correct for geometric image distortion in the x-ray imaging chain. *Med. Phys.* 24[12], 1875-1888.

Gronenschild, E. (1999) Correction for geometric image distortion in the x-ray imaging chain: Local technique versus global technique. *Med. Phys.* 26 [12], 2602–2616.

Holdsworth, D.W., Pollmann, S.I., Nikolov, H.N., and Fahrig, R. (2005) Correction of XRII geometric distortion using a liquid-filled grid and image subtraction. *Med. Phys.* 32[1], 55-64.

Jareš, V. (1985) The effect of electron optics on the properties of the x-ray image intensifier. *Adv. Electron. Elect. Phys.* 64B, 549-559.

Kärrholm, J. (1989) Roentgen stereophotogrammetry. Review of orthopedic applications. *Acta Orthop. Scand.* 60[4], 491-503.

Kärrholm, J., Herberts, P., Hultmark, P., Malchau, H., Nivbrant, B., and Thanner, J. (1997) Radiostereometry of hip prostheses. Review of methodology and clinical results. *Clin. Orthop. Relat. Res.* [344], 94-110.

Koning, O.H.J., Kaptein, B.L., Garling, E.H., Hinnen, J.W., Hamming, J.F., Valstar, E.R., and vanBockel, J.H. (2007) Assessment of three-dimensional stent-graft dynamics by using fluoroscopic roentgenographic stereophotogrammetric analysis. *J. Vasc. Surg.* 46[4], 773–779.

Liu, R.R., Rudin, S., and Bednarek, D.R. (1999) Super-global distortion correction for a rotational C-arm X-ray image intensifier. *Med. Phys.* 26[9], 1802–1810.

Nyström, L., Söderkvist, I., and Wedin, P.A. (1994) A note on some identification problems arising in roentgen stereo photogrammetric analysis. *J. Biomech.* 27[10], 1291-1294.

Østgaard, S.E., Gottlieb, L., Toksvig-Larsen, S., Lebech, A., Talbot, A., and Lund, B. (1997) Roentgen stereophotogrammetric analysis using computer-based image-analysis. *J. Biomech.* 30[9], 993-995.

Ranstam, J., Ryd, L., and Onsten, I. (2000) Accurate accuracy assessment: Review of basic principles. *Acta Orthop. Scand.* 71[1], 106–108.

Rudin, S., Bednarek, D.R., and Wong, R. (1991) Accurate characterization of image intensifier distortion. *Med. Phys.* 18[6], 1145–1151.

Ryd, L. (1986) Micromotion in knee arthroplasty. A roentgen stereophotogrammetric analysis of tibial component fixation. *Acta Orthop. Scand. Suppl.* 220, 1-80.

Ryd, L., Yuan, X., and Lofgren, H. (2000) Methods for determining the accuracy of radiostereometric analysis (RSA). *Acta Orthop. Scand.* 71[4], 403-408.

Schueler, B. and Hu, X. (1995) Correction of image intensifier distortion for three-dimensional x-ray angiography. *Proc. SPIE* 2432, 272-279.

Selvik, G., Alberius, P., and Aronson, A.S. (1983) A roentgen stereophotogrammetric system. Construction, calibration and technical accuracy. *Acta Radiol. Diagn.* 24[4], 343-352.

Selvik, G. (1989) Roentgen stereophotogrammetry. A method for the study of the kinematics of the skeletal system. *Acta Orthop. Scand. Suppl.* 232, 1-51.

Söderkvist, I. and Wedin, P.A. (1993) Determining the movements of the skeleton using well-configured markers. *J. Biomech.* 26[12], 1473-1477.

Soimu, D., Badea, C., and Pallikarakis, N. (2003) A novel approach for distortion correction for X-ray image intensifiers. *Comput. Med. Imaging Graph.* 27[1], 79-85.

Stagni, R., Fantozzi, S., and Cappello, A. (2006) Propagation of anatomical landmark misplacement to knee kinematics: performance of single and double calibration. *Gait Posture* 24[2], 137-141.

Tashman, S. and Anderst, W. (2003) In-vivo measurement of dynamic joint motion using high speed biplane radiography and CT: application to canine ACL deficiency. *J. Biomech. Eng.* 125[2], 238-245.

Valstar, E.R., Nelissen, R.G.H.H., Reiber, J.H.C., and Rozing, P.M. (2002) The use of Roentgen stereophotogrammetry to study micromotion of orthopaedic implants. *ISPRS J. Photo. Rem. Sens.* 56[5-6], 376-389.

Valstar, E.R., Gill, R., Ryd, L., Flivik, G., Börlin, N., and Kärrholm, J. (2005) Guidelines for standardization of radiostereometry (RSA) of implants. *Acta Orthop.* 76[4], 563–572.

van der Zwet, P.M., Meyer, D.J., and Reiber, J.H. (1995) Automated and accurate assessment of the distribution, magnitude, and direction of pincushion distortion in angiographic images. *Invest. Radiol.* 30[4], 204-213.

Vrooman, H.A., Valstar, E.R., Brand, G.-J., Admiraal, D.R., Rozing, P.M., and Reiber, J.H.C. (1998) Fast and accurate automated measurements in digitized stereophotogrammetric radiographs. *J. Biomech.* 31[5], 491–498.

Yuan, X., Ryd, L., and Blankevoort, L. (1997) Error propagation for relative motion determined from marker positions. *J. Biomech.* 30[9], 989-992.

Yuan, X. and Ryd, L. (2000) Accuracy analysis for RSA: a computer simulation study on 3D marker reconstruction. *J. Biomech.* 33[4], 493-498.

CHAPTER 3 – COMPARATIVE ACCURACY OF RADIOSTEREOMETRIC AND OPTICAL TRACKING SYSTEMS

OVERVIEW: This chapter discusses the overall accuracy of the system using both digital radiography and fluoroscopy, combining the effects of calibration, distortion correction, point digitization, and point reconstruction. It also compares the accuracy of the RSA approach with that achieved by an optical tracking system.[2]

3.1 INTRODUCTION

Camera-based optical tracking systems are the most common method of quantifying three-dimensional (3D) joint kinematics. As discussed in Section 1.1.3, the direct linear transform algorithm reconstructs the 3D locations of reflective or active markers placed on the skin over anatomic landmarks. Alternatively, bone pins topped with a cluster of reflective markers may be inserted into bones of interest, removing any potential for skin motion artefact. Radiostereometric analysis (RSA) provides an alternate method of quantifying joint positioning *in-vivo*. Recently, fluoroscopy and RSA have been integrated (*i.e.*, fRSA). This has the potential for accuracy surpassing that of optical tracking methods and approaching that of RSA with digital radiography. Work has been done previously to assess the accuracy, bias, and precision of RSA systems (Tashman and Anderst, 2003; Li *et al.*, 2004; Ioppolo *et al.*, 2007; Koning *et al.*, 2007). One study used fRSA as the gold standard to quantify the accuracy of a skin-mounted

[2] A version of this work has been published: Kedgley, A.E., Birmingham, T., and Jenkyn, T.R. (2009) Comparative accuracy of radiostereometric and optical tracking systems. *Journal of Biomechanics* 42[9], 1350-1354 (see Appendix L for letter of permission)

tracking system (Garling *et al.*, 2007). However, no previous research has quantified and directly compared the measurement error for these three methods. The purposes of this study were to quantify and compare the accuracy of traditional RSA, fRSA and optical motion tracking. It was hypothesized that the differences between true translations and rotations and those measured with fRSA would be significantly smaller than those measured with optical tracking, but significantly greater than those measured using traditional RSA performed using digital radiography.

3.2 METHODS

The fRSA system, image processing software and RSA analysis software described in Chapter 2 were used. The system was calibrated with the custom-made calibration object described in Section 2.4.1. Three phantoms, each consisting of three stainless steel spheres (1 mm diameter) were constructed. A cluster of three reflective markers was rigidly attached to each phantom. The locations of the reflective markers were tracked by a real-time motion analysis system in 3D space using a four-camera optical motion analysis system (Hawk cameras, EvaRT system, Motion Analysis Corp., Santa Rosa, California, USA). The fluoroscopy units were positioned at right angles to one another, such that the phantoms could be seen in both images (Figure 3.1). Before tracking the phantoms, several images of the calibration object were collected to calibrate the RSA system. Translation and rotation were quantified.

To quantify translation, one of the phantoms was mounted to the base of a precision cross-slide table (Model VCT514, Sowa Tool and Machine Co. Ltd., Kitchener, Ontario, Canada) to provide a fixed reference location throughout testing. A second phantom was mounted to the moveable tabletop. The applied translation was quantified

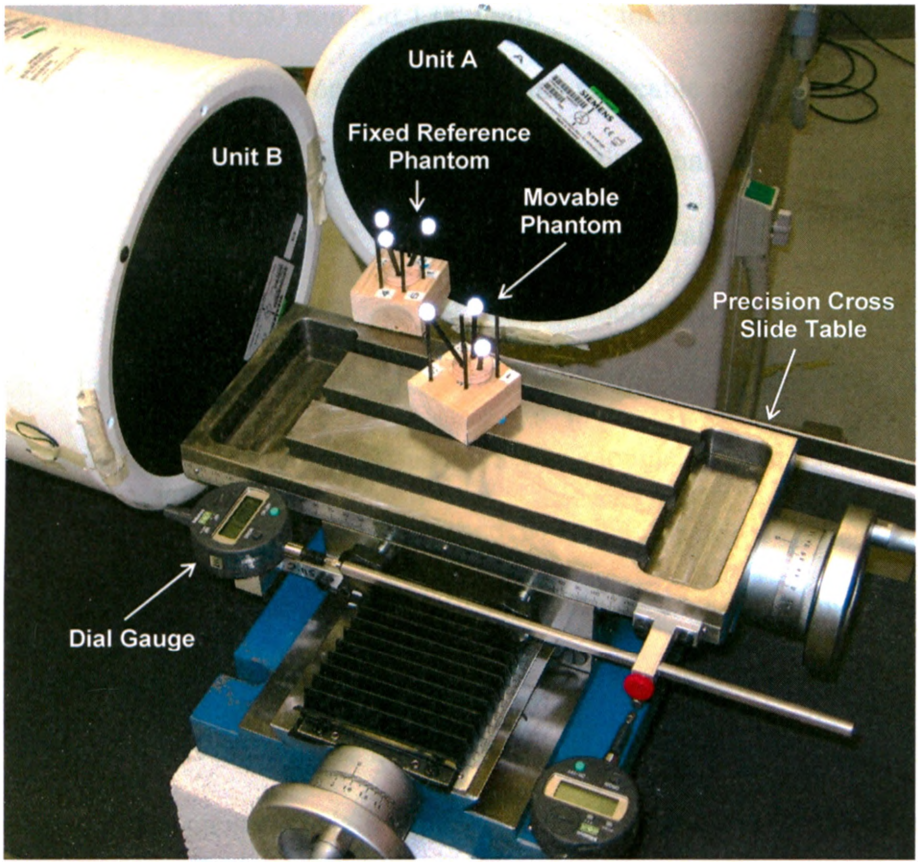

Figure 3.1 Translation experimental setup
The two fluoroscopy units were placed at approximately right angles to one another. One phantom was mounted to the base of a precision cross slide table and a second phantom was mounted to the moveable top of the table. The applied translation was quantified by a dial-gauge rigidly mounted to the mechanism of the cross slide table.

by a dial-gauge (resolution: 0.001 mm; accuracy: 0.003 mm; ID-S112, Mitutoyo Corporation, Kawasaki, Japan) rigidly mounted to the mechanism of the cross-slide table. The position of the tabletop was altered in increments of 0.25 mm and 0.50 mm along a single degree of freedom, with three measurements being taken over each 1.00 mm interval (*i.e.*, at 0.25 mm, 0.50 mm and 1.00 mm). The total distance traveled was 11.00 mm. At each position, the locations of the fixed and moveable phantoms were quantified using digital radiography RSA, fRSA and optical motion analysis. Three directions of translation were tested with respect to the fluoroscopes: parallel to fluoroscopy unit A, parallel to fluoroscopy unit B and diagonal to both fluoroscopy units, at approximately 45° to each. The system was recalibrated prior to the testing along each axis.

To quantify rotation, the third phantom was mounted to the base of a precision rotation table (Model HV-6, Sowa Tool and Machine Co. Ltd., Kitchener, Ontario, Canada) to provide a fixed reference. The first phantom was again mounted rigidly to the tabletop. The applied rotation was quantified by a second dial-gauge that rigidly mounted to the rotation table. The table was rotated such that increments of 0.25 mm were read on the dial-gauge. This resulted in a rotation of 0.170°. The total distance travelled by the dial-gauge was 11.5 mm (7.70°). Again, the locations of the fixed and moveable phantoms were quantified using RSA, fRSA, and optical motion analysis. One axis of rotation was tested.

For all cases, the positions of the beads within the fluoroscopy images were digitized and the 3D positions of the beads were calculated using the standard RSA algorithm (Selvik, 1989) as described in Section 2.6. Distortion correction was performed on both the fluoroscopy images and the digital radiography images using a

global approach by means of a fifth-order polynomial (Liu *et al.*, 1999). This will be described further in Chapter 5.

To determine translation, for each phantom at each location, the centroid of the three beads and the centroid of the three reflective markers were determined. Translation was quantified as the change in distance between the reference phantom and the moveable phantom on the tabletop. To determine rotation angle, a coordinate system was created using the fixed phantom and the beads or markers on the moving phantom were transformed into the new, fixed frame of reference. Rotation was then quantified as the change in angle of a vector between any pair of the three points on the moving phantom.

The agreement between actual (dial-gauge) and measured translations and rotations was evaluated using intraclass correlation coefficients (ICC type 2,1) (Shrout and Fleiss, 1979) and the error in individual translations was quantified using the standard error of measurement (Streiner and Norman, 1995). Agreement was also examined using Bland and Altman plots of the difference between values against the mean of the values (Bland and Altman, 1986). The difference scores between the dial-gauge and fRSA translations were then compared to those obtained with traditional RSA and optical tracking systems using paired t-tests. Lastly, difference scores obtained under different axes of translation were further compared with paired t-tests.

3.3 RESULTS

During translation, the mean error of rigid body fitting for traditional RSA was 0.054 ± 0.014 mm for the static phantom and 0.084 ± 0.009 mm for the moving phantom, averaged over all axes of motion. Similarly, for fRSA the mean error of rigid body fitting was 0.129 ± 0.009 mm for the static phantom and 0.109 ± 0.0325 mm for the moving

phantom. During rotation, the mean errors of rigid body fitting using traditional RSA were 0.067 and 0.172 mm for the static and moving phantoms, respectively. Using fRSA they were 0.134 and 0.161 mm for the static and moving phantoms, respectively. The ICCs and standard errors of measurement for all measurement modalities and all axes of translation are listed in Table 3.1. Very good agreement was found between the actual and measured translations for all modalities with all ICCs being greater than 0.99. Bland–Altman plots for the diagonal axis are shown in Figure 3.2. The difference scores between the dial-gauge and fRSA translations were not significantly different than those using traditional RSA ($p = 0.469$), but were significantly lower than those using the optical system ($p < 0.001$). Using digital radiography, measured translations along the diagonal axis were found to have significantly smaller errors than measured translations along either of the other two axes ($p = 0.018$ and 0.021). Using fluoroscopy, measured translations along the 45° axis were found to have significantly smaller errors than translations along the axis parallel to fluoroscopy unit B ($p = 0.041$).

The ICCs and standard errors of measurement for rotation are listed in Table 3.2. Very good agreement was found between the actual and measured rotations for both RSA and fRSA (ICCs > 0.99), and to a lesser extent for the optical system (ICC = 0.94). Bland–Altman plots for rotation are shown in Figure 3.3. The difference scores between the dial-gauge and fRSA translations were significantly different than those using digital radiography ($p < 0.001$) with RSA resulting in smaller errors. Difference scores for both types of RSA were significantly lower than those of the optical system ($p < 0.001$).

3.4 DISCUSSION

This study showed that images taken using fluoroscopy under ideal conditions

Table 3.1 Intra-class correlation coefficients (ICCs) and standard errors of measurement for the three imaging modalities along all axes of translation tested

Imaging Mode	Axis	ICC	Standard Error of Measurement (mm)
Digital radiography	Diagonal	0.9999	0.036
Digital radiography	Parallel to A	0.9996	0.032
Digital radiography	Parallel to B	0.9997	0.039
Fluoroscopy	Diagonal	0.9998	0.043
Fluoroscopy	Parallel to A	0.9995	0.040
Fluoroscopy	Parallel to B	0.9998	0.050
Optical	Diagonal	0.9986	0.071
Optical	Parallel to A	0.9951	0.109
Optical	Parallel to B	0.9994	0.069

Table 3.2. Intra-class correlation coefficients (ICCs) and standard errors of measurement using all three imaging modalities for rotation

Imaging Mode	ICC	Standard Error of Measurement (°)
Digital radiography	0.9970	0.121
Fluoroscopy	0.9904	0.229
Optical	0.9386	0.613

(A)

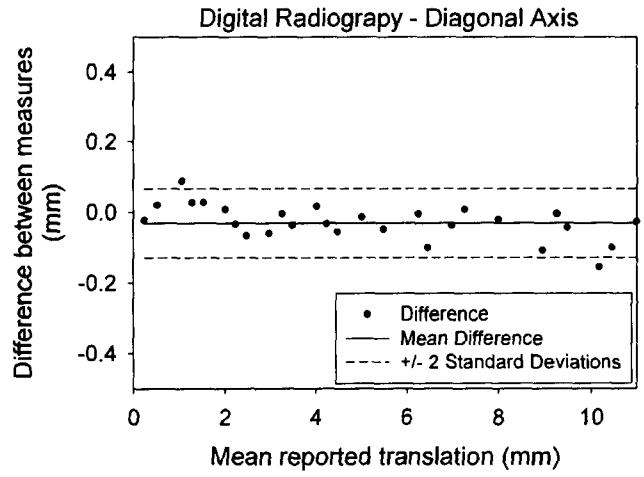

(B)

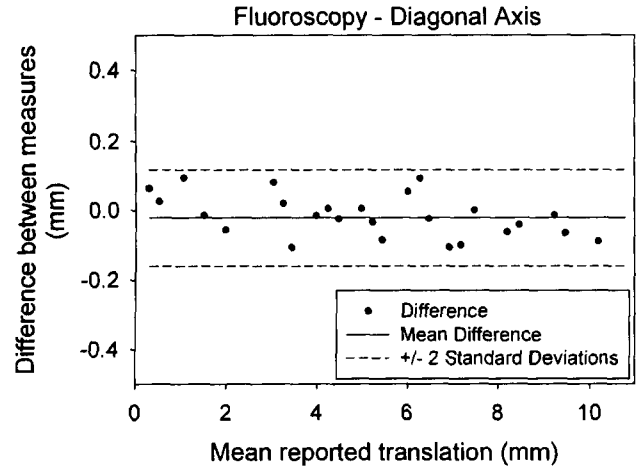

(C)

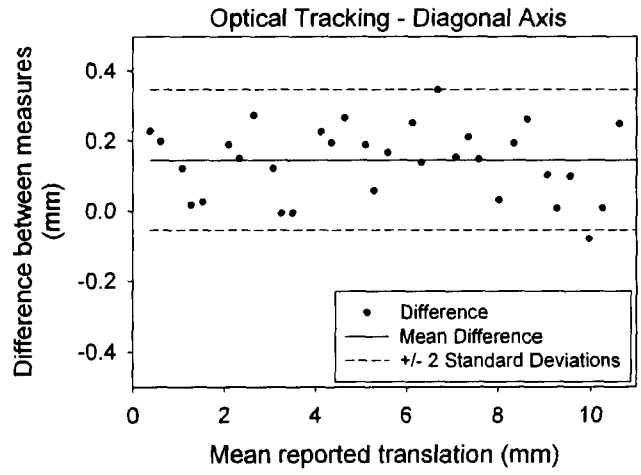

Figure 3.2 Bland-Altman plots for the three imaging modalities during translation

(A) Digital radiography, **(B)** fluoroscopy and **(C)** optical motion analysis for translation along the diagonal axis of motion. The horizontal axis in all plots is the mean translation of the two measures (dial-gauge versus the particular imaging modality) and the vertical axis is the difference between the two measures.

(A)

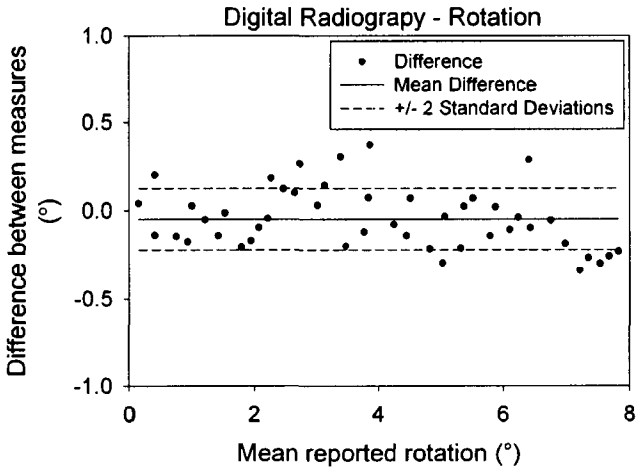

(B)

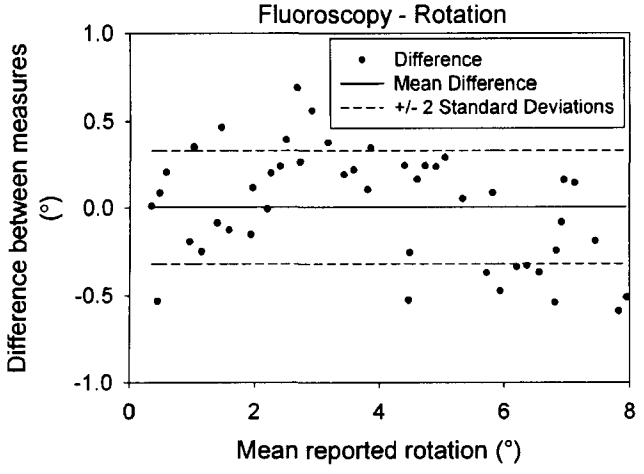

(C)

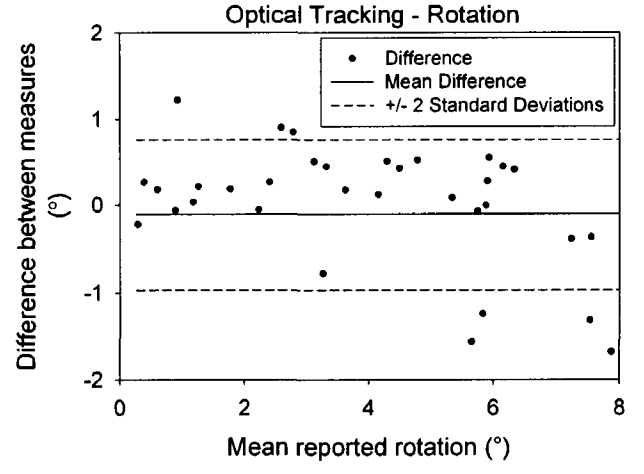

Figure 3.3 Bland-Altman plots for the three imaging modalities during rotation

(A) Digital radiography, **(B)** fluoroscopy and **(C)** optical motion analysis. The horizontal axis in all plots is the mean rotation of the two measures (dial-gauge versus the particular imaging modality) and the vertical axis is the difference between the two measures.

– in this case a phantom – can produce RSA reconstructions that are as accurate as those taken with digital radiography. Results also show that fRSA is significantly more accurate in tracking a rigid body than an optical tracking system. These findings suggest that, if feasible, the insertion of tantalum beads to track kinematics is likely more accurate than the use of reflective markers, even if these are attached to bone pins.

Furthermore, examination of the results from the three translational axes of motion suggests that the main plane of interest should be positioned such that it lies at 45° to both fluoroscopy units in order to take advantage of the increased accuracy. Since fluoroscopic images may be taken while the subject is in motion, comparable accuracy for RSA obtained with fluoroscopy and digital radiography suggests that fRSA should enable substantial improvements to the study of even very subtle *in-vivo* kinematics. The importance of studying dynamic activities should be acknowledged, because when joints are in motion the inertias of the body segments are incorporated, thereby more realistically replicating the activities of daily living. However, a major drawback with fluoroscopy is the blurring that occurs when motion is too quick. Additional research is, therefore, needed to determine how the accuracy of fRSA changes with increasing object velocities.

It should also be noted that fRSA (and RSA using digital radiography taken with fluoroscopy units) has the added disadvantage of a small capture volume – generally limited to one joint. The combination of fRSA with an optical tracking system may provide the solution to this dilemma. While optical motion analysis proved to be less accurate than RSA, the accuracies attained were nonetheless very good and it should certainly still be considered an excellent method for rigid body tracking. Clearly there

are many situations where the use of optical surface markers is more appropriate for the study of kinematics than the implantation of tantalum beads. Practically, the greatest problem with the use of reflective markers is the error that arises in the rigid body assumption when markers are attached to the skin. Optical motion analysis accuracy may also be influenced by the placement of the tracking cameras. Although it is possible that the accuracies obtained using the optical system in this study may have been improved had the cameras been placed closer to the translation table, shrinking the capture volume, it was thought that mimicking the conditions most often used for *in-vivo*, functional testing was important. Also, additional care must be taken when processing data from optical motion analysis systems. For example, if aberrant trials had not been detected during post-processing in the present study, accuracy results would have dropped dramatically (ICC = 0.53, SEM = 1.721).

Ultimately, it is the clinical question being addressed by a study and the accuracy that is required of the results that will determine which modality is best for examining 3D kinematics. In conclusion, the present findings suggest that under ideal conditions, accuracy of fRSA is comparable to RSA, greater than optical tracking and highest when measured at 45° to the fluoroscopy units.

3.5 REFERENCES

Bland, J.M. and Altman, D.G. (1986) Statistical methods for assessing agreement between two methods of clinical measurement. *Lancet* 1[8476], 307–310.

Garling, E.H., Kaptein, B.L., Mertens, B., Barendregt, W., Veeger, H.E.J., Nelissen, R.G.H.H., and Valstar, E.R. (2007) Soft-tissue artefact assessment during step-up using fluoroscopy and skin-mounted markers. *J. Biomech.* 40[Suppl 1], S18–S24.

Ioppolo, J., Börlin, N., Bragdon, C., Li, M., Price, R., Wood, D., Malchau, H., and Nivbrant, B. (2007) Validation of a low-dose hybrid RSA and fluoroscopy technique: determination of accuracy, bias and precision. *J. Biomech.* 40[3], 686–692.

Koning, O.H.J., Kaptein, B.L., Garling, E.H., Hinnen, J.W., Hamming, J.F., Valstar, E.R., and vanBockel, J.H. (2007) Assessment of three-dimensional stent-graft dynamics by using fluoroscopic roentgenographic stereophotogrammetric analysis. *J. Vasc. Surg.* 46[4], 773–779.

Li, G., Wuerz, T.H., and Defrate, L.E. (2004) Feasibility of using orthogonal fluoroscopic images to measure in vivo joint kinematics. *J. Biomech. Eng.* 126[2], 314–318.

Liu, R.R., Rudin, S., and Bednarek, D.R. (1999) Super-global distortion correction for a rotational C-arm X-ray image intensifier. *Med. Phys.* 26[9], 1802–1810.

Selvik, G. (1989) Roentgen stereophotogrammetry. A method for the study of the kinematics of the skeletal system. *Acta Orthop. Scand. Suppl.* 232, 1–51.

Shrout, P.E. and Fleiss, J.L. (1979) Intraclass correlations: uses in assessing rater reliability. *Psychol. Bull.* 86[2], 420–428.

Streiner, D.L. and Norman, G.R. (1995) Reliability. In: *Health Measurement Scales: A Practical Guide to their Development and Use.* Oxford University Press, New York. pp. 104-127.

Tashman, S. and Anderst, W. (2003) In-vivo measurement of dynamic joint motion using high speed biplane radiography and CT: application to canine ACL deficiency. *J. Biomech. Eng.* 125[2], 238–245.

CHAPTER 4 – RSA CALIBRATION ACCURACY OF A FLUOROSCOPY-BASED SYSTEM USING NON-ORTHOGONAL IMAGES FOR MEASURING FUNCTIONAL KINEMATICS

OVERVIEW: This chapter describes the adjustable calibration frame that was designed to improve the accuracy of calibration when the two fluoroscopes are not oriented orthogonally. Calibration precisions and accuracies are compared with results attained using the traditionally-designed, orthogonal calibration frame.[3]

4.1 INTRODUCTION

Traditionally, biplanar radiostereometric analysis (RSA) uses two imaging devices – whether plane x-rays or fluoroscopy image intensifiers – placed perpendicularly to one another (Selvik, 1989; Valstar *et al.*, 2005). As described in Section 2.4, a calibration frame establishes a coordinate system for the region of interest and determines the locations of the two imaging devices. In order to do this, each imaging device must "see" two planes – a fiducial plane and a control plane. The fiducial plane creates a transformation from the image coordinate system to the laboratory coordinate system. The control plane determines the focal point from which the x-rays originate. If the imaging devices are perpendicular, the pairs of fiducial and control planes are at 90° angles to one another (Valstar *et al.*, 2005). An alternate approach uses a uniplanar calibration frame (Valstar *et al.*, 2005). This is more common when the two

[3] A version of this work has been published: Kedgley, A.E. and Jenkyn, T.R. (2009) RSA calibration accuracy of a fluoroscopy-based system using nonorthogonal images for measuring functional kinematics. *Medical Physics* 36[7], 3176-3180 (see Appendix L for letter of permission)

imaging devices are oriented at a small angle relative to one other. In practice, to obtain the optimal views of an articular joint or anatomical structure, a nontraditional orientation is often required, especially if movement through a range of motion is of interest.

As discussed in Sections 2.3 and 2.7 several aspects of RSA have been examined in the literature in an attempt to improve accuracies, including distortion correction, error propagation, and techniques for clinical quantification. Nonetheless, only one study has considered a different calibration frame design by examining bead distribution, bead spacing, and number of beads in a calibration frame (Cai *et al.*, 2008). Soavi *et al.* (2000) examined the effects of altering the distance between the imaging plane and the focus of the x-rays, as well as the convergence angle of the images for plane x-rays. Douglas *et al.* (2004) studied the effects of separation angle on three-dimensional (3D) reconstruction accuracy using a method similar to the direct linear transform (DLT) approach. However, no studies have quantitatively examined whether the relative angle of the image planes has an effect on the repeatability and accuracy of the 3D reconstruction of points using fluoroscopy-based RSA.

The aims of this study were to quantify the accuracy of RSA performed with non-orthogonally positioned imaging devices using (1) an orthogonal calibration frame (pairs of fiducial and control planes oriented at 90° to each other) and (2) a calibration frame with pairs of fiducial and control planes at relative angles of greater than 90° (Figure 4.1). It was hypothesized that a more accurate calibration would be obtained when the fiducial and control planes were parallel to the image intensifiers.

4.2 METHODS

The fluoroscopic RSA system, image processing software and RSA analysis

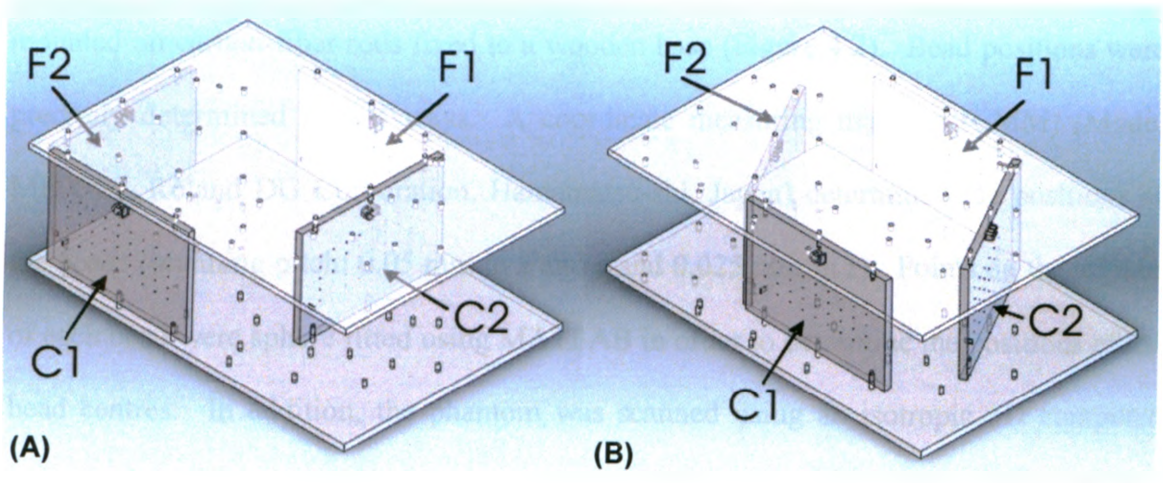

Figure 4.1 The calibration frame
(A) In the 90° configuration (CF-90) and **(B)** in one of the three parallelogram configurations (this one for 120°, CF-120). Fiducial (F1 and F2) and control (C1 and C2) planes are labeled.

software described in Chapter 2 were used. The custom-designed calibration frame described in Section 2.4.1 was utilized. Fiducial and control planes could be adjusted into one of four angular configurations [90° (CF-90), 105° (CF-105), 120° (CF-120), and 135° (CF-135)], with opposing planes parallel to one another. The fiducial and control planes were 317.46 mm apart in CF-90. The laboratory coordinate system and the coordinates of the markers on the object were determined as described in Sections 2.4.2 and 2.6.

An accuracy phantom was constructed with four 1 mm stainless steel beads mounted on carbon-fiber rods fixed to a wooden base (Figure 4.2). Bead positions were precisely determined in two ways. A coordinate measuring machine (CMM) (Model MDX-20, Roland DG Corporation, Hamamatsu-shi, Japan) determined the positions of the beads (scanning pitch: 0.05 mm in x and y and 0.025 mm in z). Points on the surface of each bead were sphere fitted using MATLAB in order to determine the positions of the bead centres. In addition, the phantom was scanned using an isotropic 3D computed tomography (CT) acquisition (Lightspeed VCT, GE Healthcare, Piscataway, New Jersey, USA) with the following parameters: 0.625 mm sections, 140 kV, 200 mA, 1 s rotation time, and reconstruction via a bone algorithm. Analysis was performed using MIMICS software with a MedCAD module. Thresholding and sphere-fitting operations were performed to determine the centres of the beads. In each case, the distances between the beads were determined.

The two fluoroscopes were positioned in a range of angular configurations as listed in Table 4.1. The system was calibrated for each condition with the calibration frame such that the pairs of fiducial and control planes were parallel to the image

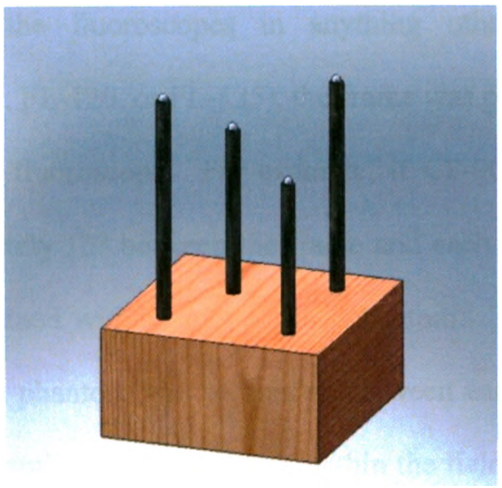

Figure 4.2 The accuracy phantom
Four 1 mm stainless steel beads mounted on carbon fiber rods fixed securely to a wooden base. Distances between the beads ranged from 25.11 mm (bead 1 to bead 4) to 41.95 mm (bead 1 to bead 3).

Table 4.1 The combinations of fluoroscopic angles and calibration frames that defined each tested condition
For each condition 40 repeated pairs of images were obtained without moving the phantom. Then, 16 pairs of images between which the phantom was moved to a different, randomly selected location were obtained. This made for a total of 56 RSA reconstructions per condition.

Condition	**Fluoroscopy unit configuration** (the number indicates the angle (°) between the image intensifiers)	**Calibration frame employed** (the number indicates the angle (°) between the pairs of fiducial and control planes)
1	FL-90	CF-90
2	FL-105	CF-105
3	FL-105	CF-90
4	FL-120	CF-120
5	FL-120	CF-90
6	FL-135	CF-135
7	FL-135	CF-90

intensifiers or using CF-90 (Table 4.1, Figure 4.3 and Figure 4.4). In the cases where CF-90 was used with the fluoroscopes in anything other than the orthogonal configuration (*i.e.*, FL-105, FL-120, or FL-135), the frame was positioned such that it had equivalent angles to each fluoroscope. For example, if CF-90 was used with FL-120 there would be approximately 15° between the frame and each image intensifier. Forty pairs of images were obtained without moving the phantom. This was followed by 16 pairs of images where the phantom was reoriented between each set, being rotated and moved to a different, randomly selected location within the field of view. This made for a total of 56 RSA reconstructions per condition. Locations were chosen such that the entire field of view was tested. The grid described in Section 2.3 was employed to allow for postprocessing image correction. This was done following each condition. The kVp and mA were set automatically by the fluoroscopy units and were 51 kVp and 0.4 mA for the calibration frame and 49 kVp and 0.3 mA for the phantoms.

The positions of the beads in the calibration frame, phantom, and distortion correction images were located as described in Section 2.2. Distortion correction was performed by means of a global approach using a fifth order polynomial fit (Liu *et al.*, 1999). For the Wolf Orthopaedic Quantitative Imaging Laboratory (WOQIL)'s applications of RSA, in which bones or implants are moving with respect to one another, relative bead locations and not absolute bead positions within the field of view are most important. Therefore, the distances between the four beads of the phantom were the measures of interest. The distances between each pair of beads were measured and compared with the distances obtained from the CMM machine and the CT scan. The errors were averaged to give an overall error for the RSA reconstruction. In this case, the

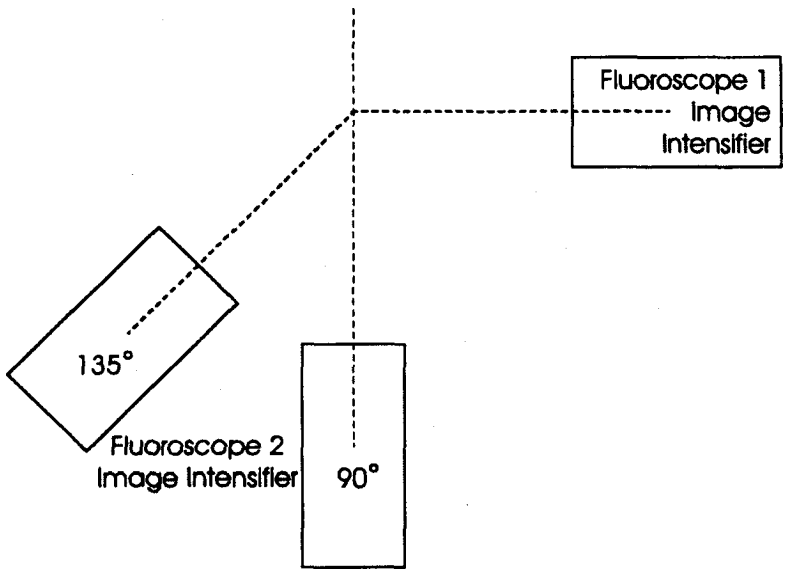

Figure 4.3 Orientation of the fluoroscopy units
The image intensifier of fluoroscopy unit 1 was maintained at a constant position and the image intensifier of fluoroscopy unit 2 is shown at 90° and 135°.

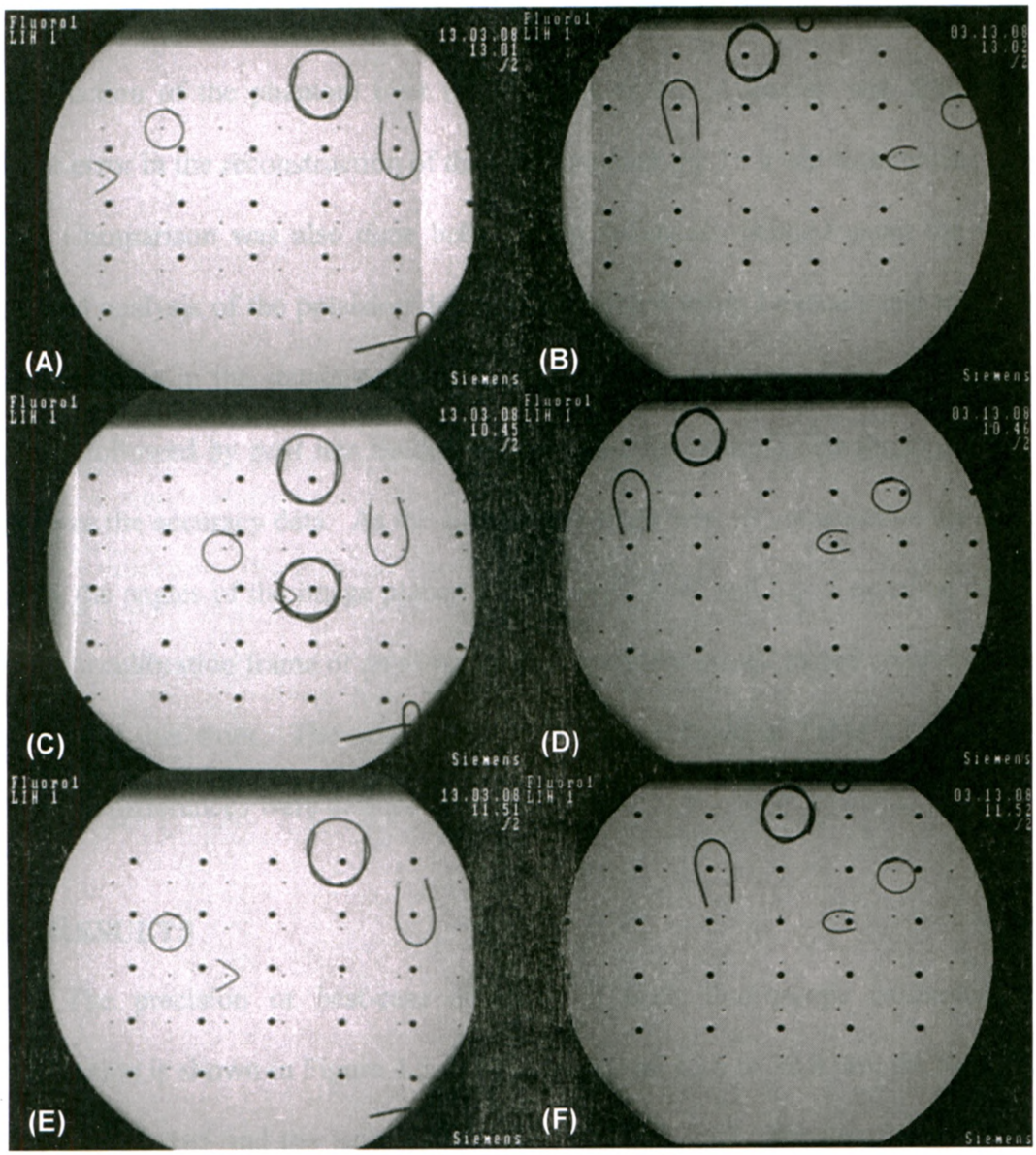

Figure 4.4 Sample fluoroscopy images
Images of the calibration frame obtained by the fluoroscopy units **(A & B)** with the fluoroscopy units at 90° to each other, **(C & D)** with the fluoroscopy units at 105° to each other and the calibration frame in the 105° orientation (CF-105), and **(E & F)** with the fluoroscopy units at 105° to each other and the calibration frame in the 90° configuration (CF-90). In order to correctly identify the beads in the images, wire loops are stuck into the calibration frame; these may be repositioned according to which portion of the frame is visible.

precision and best-case accuracy of the system are the same, since each set of 40 image pairs (Fahrig *et al.*, 1997) was taken without any movement of the phantom (Ranstam *et al.*, 2000). Precision was defined as the standard deviation of the error in the reconstruction of the phantom over the 40 static trials. Accuracy was defined as the average error in the reconstruction of the phantom over the 16 trials with motion between them. Comparison was also done between the distances obtained using the CT scan. Statistical analysis of the precision data was performed using Levene's test to determine any differences in the standard deviations of the configurations. One-way analyses of variance followed by *post hoc* Student-Newman-Keuls multiple comparisons were used to analyze the accuracy data. As the aims of this study were (1) to examine the effects of varying the angles of the image planes while using CF-90 and (2) to examine the effects of using a calibration frame of an alternate configuration, not all paired comparisons were the focus of this work. The relevant comparisons are listed in Table 4.2. Statistically significant differences were defined as $p < 0.05$.

4.3 RESULTS

The precision or best-case accuracy of each fluoroscope calibration frame configuration is shown in Figure 4.5. They range from 15.6 to 22.8 μm, the former using CF-90 and FL-105 and the latter using CF-135 and FL-135. No significant differences were seen between the precisions for any of the relevant comparisons (listed in Table 4.2).

With respect to accuracy (Figure 4.6), the values are in the ranges 90.0 ± 24.0 μm for CF-105 and FL-105 and 277.2 ± 120.9 μm for CF-135 and FL-135. As the relative angle between the fluoroscopes was changed and the planes of the calibration frame were

Table 4.2 The combinations of fluoroscopic angles and calibration frames that were statistically compared

To determine the effect of varying the fluoroscopy unit configuration		To determine the effect of using an alternative calibration frame	
FL-90, CF-90	FL-105, CF-90	FL-105, CF-105	FL-105, CF-90
FL-90, CF-90	FL-105, CF-105	FL-120, CF-120	FL-120, CF-90
FL-90, CF-90	FL-120, CF-90	FL-135, CF-135	FL-135, CF-90
FL-90, CF-90	FL-120, CF-120		
FL-90, CF-90	FL-135, CF-90		
FL-90, CF-90	FL-135, CF-135		

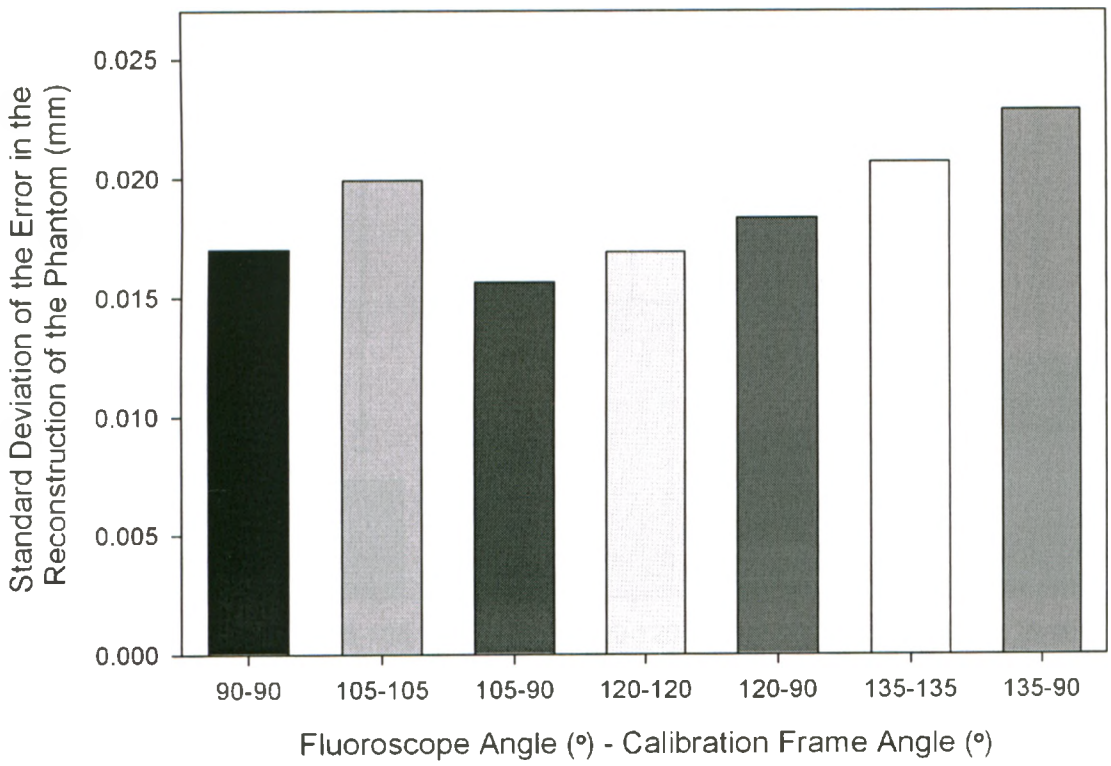

Figure 4.5 Precision of the reconstruction
Defined as the standard deviation of the error in the reconstruction of the phantom over the 40 static trials. The darker bars indicate the use of CF-90.

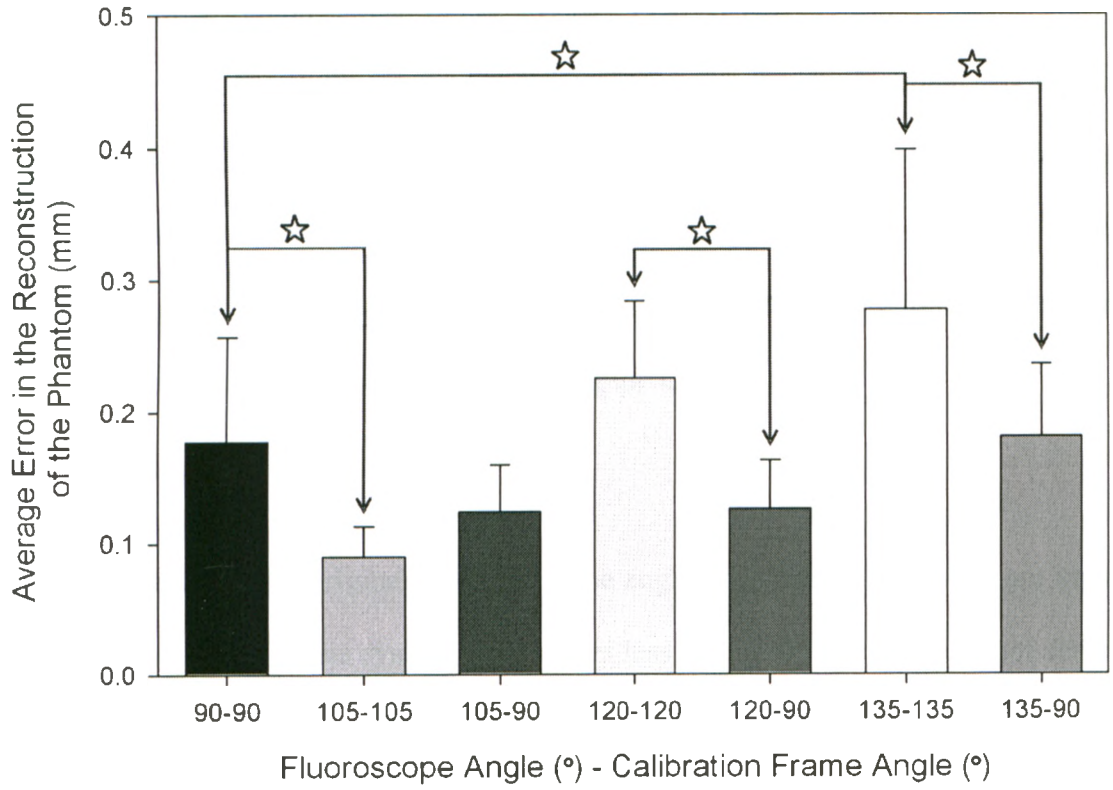

Figure 4.6 Accuracy of the reconstruction
Mean (± 1 SD) of the error in the reconstruction of the phantom over the 16 trials with motion between them. Significant differences ($p < 0.05$) are indicated by a star (☆). The darker bars indicate the use of CF-90.

changed to match them, no difference in accuracy was seen between CF-90 used with FL-90 and CF-120 used with FL-120. FL-105 used with CF-105 proved to be better ($p = 0.002$) and FL-135 used with CF-135 proved to be worse ($p < 0.001$) than CF-90 used with FL-90. Differences were also found between the use of CF-90 and CF-120 with FL-120 ($p < 0.001$) and between the use of CF-90 and CF-135 with FL-135 ($p < 0.001$), with the use of CF-90 being superior in both cases. When calibrating using CF-90, no differences were found between FL-90, FL-105, FL-120, and FL-135 ($p > 0.064$).

There were no differences in the number of fiducial or control beads that were visible in the field of view when the frame was aligned parallel to the fluoroscopes versus when CF-90 was used. Comparing all the errors in the distances between the beads as obtained from the CMM machine and using the CT scan, errors were found to be between 163 μm larger and 195 μm smaller when using the CT scan data.

4.4 DISCUSSION

Contrary to the original hypothesis, the angled calibration frame did not improve the overall accuracy of the system. For angles less than 120° accuracy did not decrease; however, using CF-90 it was possible to calibrate the system with the fluoroscopes at any angle less than or equal to 135° with equivalent or better accuracy than that obtained with the fluoroscopes at right angles. It is thought that this is due to the fact that the projective transformations, created from the fiducial planes, are altered by the relative angle between the image plane and the calibration frame, but remain valid. This allows RSA reconstruction to proceed correctly. Errors may have been introduced into the system through a variety of avenues including the stochastic nature of x-rays, leading to blurred beads, image distortion from external electromagnetic fields, and other sources of image

noise (*i.e.*, from the fluorescent screen or unit electronics). The bead location algorithm was resistant to small amounts of bead blur. A global distortion correction algorithm was used to remove image distortion and the least-squares method of reconstruction addressed other system noise. While efforts were made to decrease the effects of the aforementioned sources of error, it should be noted that the accuracies of such systems will always face limitations.

Most other studies examining the accuracy and precision of the RSA method have been conducted using plane x-rays rather than fluoroscopy units. Even so, precisions obtained in this study (15.6–22.8 μm) are comparable to those obtained by other researchers, 8 μm (Cai *et al.*, 2008), 50–140 μm (Douglas *et al.*, 2004), 14 μm (Bragdon *et al.*, 2002), 30 μm (Önsten *et al.*, 2001), and 121 μm (Vrooman *et al.*, 1998), despite the fact that all of these studies were conducted under slightly different conditions. In retrospect, 40 trials were more than necessary to obtain the desired results. Multiple trials were not conducted at different positions within the capture volume due to the time required for manual digitization of each trial. However, precision was not expected to change as a function of location within the capture volume.

It is more difficult to compare the accuracies obtained by this study with those of other studies, since most other investigators have determined the accuracies of microscale motions, while this study examined errors in determining distances that were two orders of magnitude larger. This study also examined distances between single beads rather than coordinate systems obtained from groups of beads. One study exists with similar distances between beads to those seen in this study. Douglas *et al.* (2004) compared the accuracies for a range of separation angles between two images for reconstruction of 3D

coordinates using a modified DLT approach and found mean errors to be on the order of 0.75 mm. They found that reconstruction errors increased as the relative angles between images decreased, with the greatest increases between relative angles of less than 30°. This study used a pyramidal calibration frame with beads much larger than those used in the present study (10 mm in diameter) and a different reconstruction algorithm. Soavi *et al.* (2000) also examined non-orthogonal images for RSA and found no effect of relative image angle using x-ray tubes over a range of 30°–90°. While these two studies examined relative angles of less than 90°, due to the nature of x-rays, their results may be compared to this study as follows: A relative image angle of 75° is equivalent to 105° in this study, 60° is equivalent to 120°, and 45° is equivalent to 135°. Therefore, it is reasonable that no differences were found in this study when using CF-90 to calibrate configurations FL-90, FL-105, FL-120, and FL-135.

CT scans are generally used to determine the positions of the beads relative to the locations of bony landmarks, which are used to create the bone-based coordinate systems required to calculate clinically relevant kinematic parameters. This study showed that the positions of the beads can be determined from a CT scan with accuracies on the order of the errors of the RSA reconstruction.

The results of this study show that the relative angles of the fluoroscopes less than 135° do not affect the accuracy of RSA reconstruction. Therefore, RSA may be performed with the imaging devices at relative angles other than 90° while calibrating with a calibration object with pairs of fiducial and control planes oriented orthogonally to each other. This allows greater freedom in positioning the equipment and obtaining more desirable x-ray views.

4.5 REFERENCES

Bragdon, C.R., Malchau, H., Yuan, X., Perinchief, R., Karrholm, J., Börlin, N., Estok, D.M., and Harris, W.H. (2002) Experimental assessment of precision and accuracy of radiostereometric analysis for the determination of polyethylene wear in a total hip replacement model. *J. Orthop. Res.* 20[4], 688–695.

Cai, R., Yuan, X., Rorabeck, C., Bourne, R.B., and Holdsworth, D.W. (2008) Development of an RSA calibration system with improved accuracy and precision. *J. Biomech.* 41[4], 907–911.

Douglas, T.S., Vaughan, C.L., and Wynne, S.M. (2004) Three-dimensional point localisation in low-dose x-ray images using stereophotogrammetry. *Med. Biol. Eng. Comput.* 42[1], 37–43.

Fahrig, R., Moreau, M., and Holdsworth, D.W. (1997) Three-dimensional computed tomographic reconstruction using a C-arm mounted XRII: Correction of image intensifier distortion. *Med. Phys.* 24[7], 1097–1106.

Liu, R.R., Rudin, S., and Bednarek, D.R. (1999) Super-global distortion correction for a rotational C-arm X-ray image intensifier. *Med. Phys.* 26[9], 1802–1810.

Önsten, I., Berzins, A., Shott, S., and Sumner, D.R. (2001) Accuracy and precision of radiostereometric analysis in the measurement of THR femoral component translations: Human and canine in vitro models. *J. Orthop. Res.* 19[6], 1162–1167.

Ranstam, J., Ryd, L., and Onsten, I. (2000) Accurate accuracy assessment: Review of basic principles. *Acta Orthop. Scand.* 71[1], 106–108.

Selvik, G. (1989) Roentgen stereophotogrammetry. A method for the study of the kinematics of the skeletal system. *Acta Orthop. Scand. Suppl.* 232, 1–51.

Soavi, R., Motta, M., Visani, A., Bragonzoni, L., and Loreti, I. (2000) 3D coordinate computation by RSA under non-standard conditions. *Conf. Proc. IEEE Eng. Med. Biol. Soc.* 1, 570–572.

Valstar, E.R., Gill, R., Ryd, L., Flivik, G., Börlin, N., and Kärrholm, J. (2005) Guidelines for standardization of radiostereometry (RSA) of implants. *Acta Orthop.* 76[4], 563–572.

Vrooman, H.A., Valstar, E.R., Brand, G.-J., Admiraal, D.R., Rozing, P.M., and Reiber, J.H.C. (1998) Fast and accurate automated measurements in digitized stereophotogrammetric radiographs. *J. Biomech.* 31[5], 491–498.

CHAPTER 5 – IMAGE INTENSIFIER DISTORTION CORRECTION FOR FLUOROSCOPIC RSA: THE NEED FOR INDEPENDENT ACCURACY ASSESSMENT

OVERVIEW: This chapter discusses the effects of various degrees of polynomials that are employed in a global approach to distortion correction for the images used for fluoroscopic RSA.[4]

5.1 INTRODUCTION

Fluoroscopic images, as described in Section 2.3, are subject to the primary aberrations that affect images obtained through classical light optics (Jareš, 1985), and correction of these aberrations has been the subject of many previous investigations (Chakraborty, 1987; Rudin *et al.*, 1991; Schueler and Hu, 1995; Fahrig *et al.*, 1997; Gronenschild, 1997; Gronenschild, 1999; Liu *et al.*, 1999; Cerveri *et al.*, 2002; Fantozzi *et al.*, 2003; Soimu *et al.*, 2003; Holdsworth *et al.*, 2005). Distortion of the images is present in two distinct modes, as discussed in Section 2.3: pin-cushion distortion and s-shaped, spiral, or pocket handkerchief distortion (see Bushberg *et al.*, 2002; van der Zwet *et al.*, 1995). Unfortunately, it is difficult to know the extent to which these modes of distortion have been corrected by the manufacturer.

In the past, both local and global approaches to post-processing distortion correction have been taken, or in one case local and global approaches have been combined (Fantozzi *et al.*, 2003). In a direct comparison of global and local techniques,

[4] A version of this work has been submitted for publication: Kedgley, A.E., Allen, A.V., and Jenkyn, T.R. (2009) Image intensifier distortion correction for fluoroscopic RSA: The need for independent accuracy assessment. Submitted to *Medical Physics*.

the global technique was found to be superior (Gronenschild, 1997). The limitations of local distortion correction algorithms have been stated in Section 2.3. In a global approach the distortion vector at each point is calculated and these data are then used to determine an overall expression for the distortion within the image in either Cartesian (Chakraborty, 1987; Fahrig *et al.*, 1997; Gronenschild, 1997; Gronenschild, 1999; Fantozzi *et al.*, 2003; Holdsworth *et al.*, 2005) or radial (Rudin *et al.*, 1991) coordinates. The positions of the beads in the image are related to the known bead positions according to the chosen polynomial.

Most distortion correction is performed with diagnostic imaging applications in mind; that is, quantitative coronary angiography, three-dimensional (3D) reconstructions, stereotaxic angiography, and radiotherapy treatment (see Gronenschild, 1999). Testing a range of polynomial functions in order to determine the one that best corrects for image distortion is not a new concept. To determine optimal polynomial formulations, others have examined the residuals and root mean squared (RMS) errors of the fit of the polynomial (Rudin *et al.*, 1991; Liu *et al.*, 1999; Soimu *et al.*, 2003) or tested their correction on the same grid in a different position, or another grid (Schueler and Hu, 1995; Fahrig *et al.*, 1997; Gronenschild, 1997; Gronenschild, 1999; Cerveri *et al.*, 2002; Fantozzi *et al.*, 2003; Holdsworth *et al.*, 2005). One study used a phantom in addition to other evaluation methods to quantify correction for digital tomosynthesis (Soimu *et al.*, 2003). However, no studies have determined the efficacy of distortion correction for radiostereometric analysis (RSA) using an independent phantom.

The aim of this study was to compare the effects of a range of polynomials for distortion correction using a global approach by examining the fit of the chosen

polynomial to the points on the distortion grid, the distances between the points of the grid in a second position, and the overall accuracy of the RSA reconstruction. It was hypothesized that the two outcome measures would lead to the same, most suitable, polynomial.

5.2 METHODS

The two previously described x-ray fluoroscopes were used in this study. The grid of stainless steel beads, described in Section 2.3 was used for distortion correction. Following data collection, the grid was placed over each image intensifier (II) and images of the distorted positions of the grid beads were obtained.

The positions of the beads in each fluoroscopic image were manually located using the custom-written software described in Section 2.2 (MATLAB, The MathWorks Inc., Natick, MA, USA). Distortion correction was performed using a global approach with a range of polynomial fits, from first degree in each direction (a second order polynomial) through to third degree in each direction (a sixth order polynomial). The full range of polynomials is documented in Table 5.1. Coefficients were determined based on a least squares minimization. Two polynomials were defined for each correction, one for correction in the x-axis of the image (horizontal within the image) and one for correction in the y-axis of the image (vertical within the image). Polynomials were paired for correction such that the order in x for the x-axis was the same as the order in y for the y-axis and vice versa. The number of coefficients in the polynomial dictated the minimum number of beads that were required for a solution. For instance, a polynomial with a maximum degree of one in each of x and y has four coefficients. For optimal results, the number of beads in the distortion grid needed to be at least a factor of three more than the

Table 5.1 The polynomials and their coefficients used in fitting the data for distortion correction

Highest order in x	Highest order in y	Polynomial Equation
1	1	$z = a + by^1 + cx^1 + dx^1y^1$
1	2	$z = a + by^1 + cy^2 + dx^1 + ex^1y^1 + fx^1y^2$
1	3	$z = a + by^1 + cy^2 + dy^3 + ex^1 + fx^1y^1 + gx^1y^2 + hx^1y^3$
2	1	$z = a + by^1 + cx^1 + dx^1y^1 + ex^2 + fx^2y^1$
2	2	$z = a + by^1 + cy^2 + dx^1 + ex^1y^1 + fx^1y^2 + gx^2 + hx^2y^1 + ix^2y^2$
2	3	$z = a + by^1 + cy^2 + dy^3 + ex^1 + fx^1y^1 + gx^1y^2 + hx^1y^3 + ix^2 + jx^2y^1 + kx^2y^2 + lx^2y^3$
3	1	$z = a + by^1 + cx^1 + dx^1y^1 + ex^2 + fx^2y^1 + gx^3 + hx^3y^1$
3	2	$z = a + by^1 + cy^2 + dx^1 + ex^1y^1 + fx^1y^2 + gx^2 + hx^2y^1 + ix^2y^2 + jx^3 + kx^3y^1 + lx^3y^2$
3	3	$z = a + by^1 + cy^2 + dy^3 + ex^1 + fx^1y^1 + gx^1y^2 + hx^1y^3 + ix^2 + jx^2y^1 + kx^2y^2 + lx^2y^3 + mx^3 + nx^3y^1 + ox^3y^2 + px^3y^3$

minimum number required (Fahrig *et al.*, 1997). Therefore, the grid would have needed twelve beads.

To evaluate the correction of the polynomials in isolation, the distortion grid was oriented on each II as would be conducted routinely. The polynomial coefficients and the RMS errors of the fits were determined for each polynomial. The grid was then replaced on the II, such that the beads were translated to an intermediate, staggered, location between the original positions. Distances between the beads were calculated and compared to those measured with the coordinate measuring machine (CMM, DEA Swift, Hexagon Metrology Services Ltd.., London, UK), following correction with the various polynomials. This was done with each of the two IIs in six different positions, covering the full range of their motion.

The fluoroscopy-based RSA system described in Chapter 2 was employed. The custom-designed calibration frame described in Section 2.4.1 was used. The two fluoroscopes were positioned approximately orthogonal to one another. An accuracy phantom, also used in Chapter 4, consisting of four 1 mm stainless steel beads, mounted on carbon fiber rods, fixed securely to a wooden base was placed in the capture volume. Forty pairs of images were obtained without moving the phantom. This was followed by 16 pairs of images where the phantom was randomly moved and rotated within the field of view between each set (Kedgley and Jenkyn, 2009). The voltage and current were set automatically by the fluoroscopy units and were 51 kVp and 0.4 mA for the calibration frame and 49 kVp and 0.3 mA for the phantoms. RSA reconstruction was performed with custom-written software according to the algorithm described in Section 2.6.

The primary measure of interest was the distances between the four beads of the phantom as measured using RSA, with image distortion provided by the range of polynomial fits. The distances between each pair of beads were measured and compared with the distances obtained by using a second CMM (Model MDX-20, Roland DG Corporation, Hamamatsu-shi, Japan; scanning pitch: 0.05 mm in x and y and 0.025 mm in z). An overall error for the RSA reconstruction of each position was calculated by averaging the errors in all the distances. Accuracy was defined as the average error in the reconstruction of the phantom over the 16 trials in which the phantom was moved between each trial. Precision was defined as the standard deviation of the error in the reconstruction of the phantom over the 40 static trials. Secondary measures of interest were the RMS error of the fit of the chosen polynomial to the distortion grid points and the errors in the distortion corrected distances between the points when the grid was replaced on the II.

Statistical analysis of the RMS errors of the fits of the various polynomials, the distances between the beads and the accuracy of the RSA reconstructions were performed using Friedman Repeated Measures Analyses of Variance on Ranks followed by post-hoc Student-Newman-Keuls multiple comparisons. These were also used to compare the results between the two fluoroscopes. Levene's test was used to analyze the precision data to determine any differences in the standard deviations of the RSA reconstructions. Statistically significant differences were defined as $p < 0.05$.

5.3 RESULTS

No differences were found between the two fluoroscopes in the RMS errors as a function of II orientation and polynomial degree. Therefore the results for the two

fluoroscopes were combined to compare the effects of the various polynomial corrections. RMS errors ranged from 58 ± 15 μm in the x-direction and 63 ± 18 μm in the y-direction for a fifth order polynomial of third order in the axis of correction and second order in the perpendicular axis, and 679 ± 321 μm in the x-direction and 410 ± 130 μm in the y-direction for a third order polynomial in each direction (Figure 5.1). Differences were found between distortion correction using a polynomial of order three in the axis of correction and two in the perpendicular axis and all other orders of correction tested ($p < 0.05$).

Similar results were obtained when the distances between the beads of the grid in a second, staggered, position were examined (Figure 5.2). Errors in uncorrected points were 315 ± 43 μm. Average errors in corrected points ranged from 51 ± 3 μm for a fifth order polynomial of third order in the axis of correction and second order in the perpendicular axis, and 181 ± 21 μm for a third order polynomial in each direction. Differences were found between distortion correction using a polynomial of order three in the axis of correction and two in the perpendicular axis and all other orders of correction tested ($p < 0.05$).

The precision of the reconstruction with each set of polynomials is shown in Figure 5.3. They range from 14.6 μm to 24.9 μm, the former using a polynomial of order three in the axis of correction and one in the perpendicular axis and the latter using a first order polynomial in each direction. There were no differences in the precisions of the RSA reconstructions between any of the polynomial corrections.

Average accuracies of the reconstructions ranged from 150 ± 69 μm for a polynomial of third order in the axis of correction and first order in the perpendicular axis

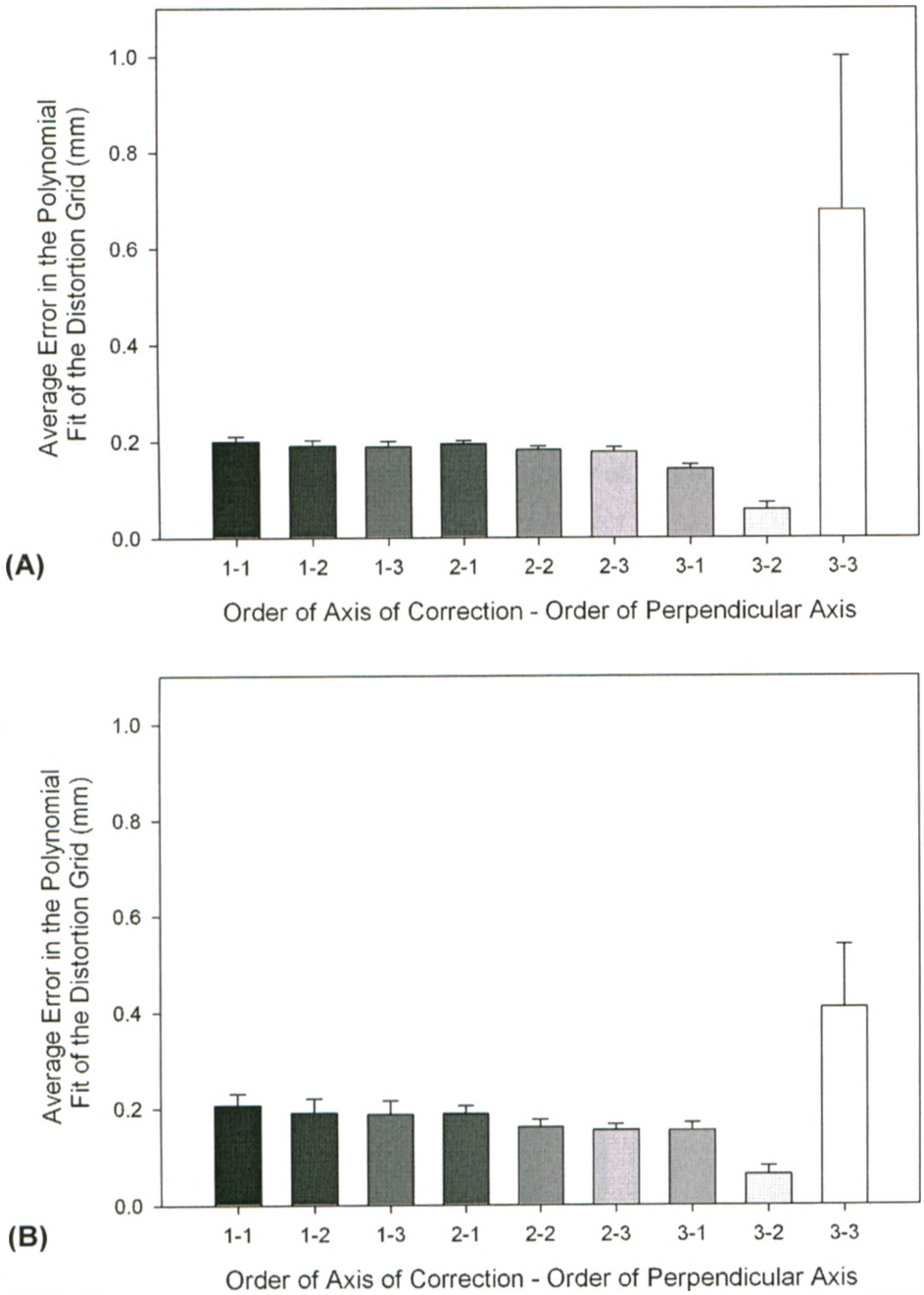

Figure 5.1 RMS errors of the various polynomial models employed
(A) RMS errors in the x-direction and **(B)** RMS errors in the y-direction. Mean (± 1 SD). All corrections were found to be different from 3-2 ($p < 0.05$). Lighter bars indicate higher order polynomial models.

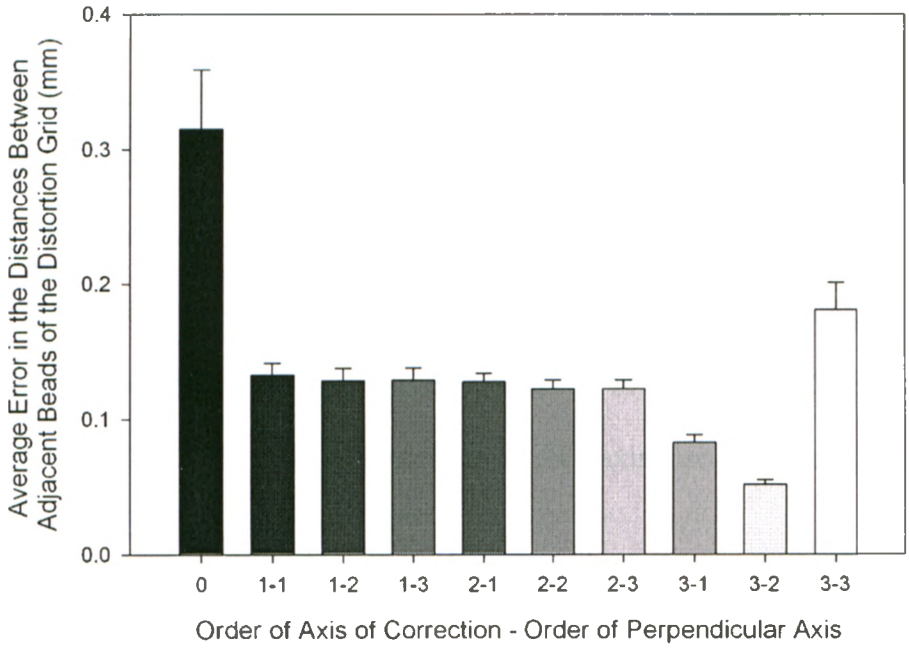

Figure 5.2 Errors in the distances between adjacent beads
Mean (± 1 SD) of the distances measured on a second, staggered, image of the same grid and plotted as a function of the polynomial correction. All corrections were found to be different from 3-2 ($p < 0.05$). Lighter bars indicate higher order polynomial models.

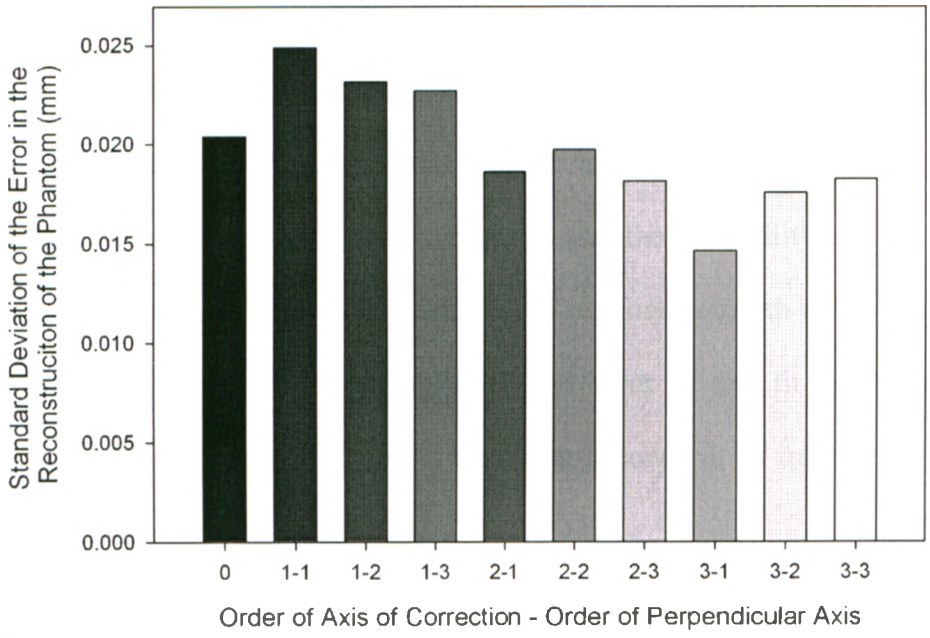

Figure 5.3 Precision of the RSA reconstruction
Defined as the standard deviation of the error in the reconstruction of the phantom over the 40 static trials. Lighter bars indicate higher order polynomial models.

and 457 ± 289 μm for a third order polynomial in each direction (Figure 5.4). RSA reconstruction of the uncorrected points resulted in an error of 193 ± 68 μm. Differences were found between distortion correction using a polynomial of order three in the axis of correction and one in the perpendicular axis and all other orders of correction tested ($p < 0.05$). First order polynomials in the axis of correction always resulted in worse errors than the uncorrected points ($p < 0.05$), regardless of the order of correction in the perpendicular axis. Third order polynomials in each axis also resulted in worse errors ($p < 0.05$).

5.4 DISCUSSION

Contrary to our hypothesis, the polynomial with the smallest RMS error in solving for the polynomial coefficients and the smallest errors in the distances between points on the translated distortion grid did not have the lowest average RSA reconstruction error. This is similar to results found by the only other study to employ a 3D phantom to quantify the results of distortion correction (Soimu *et al.*, 2003). It was found that a fifth order correction resulted in the best polynomial fit; however, as the images were being used for digital tomosynthesis, the variability of the correction coefficients with the fifth order was a concern. Therefore, a fourth order was preferred. In this investigation, the variability of the RMS error of the fit of the sixth order polynomial to the distortion grid points would be a concern, as indicated by the high standard deviations in Figure 5.1.

In this study, the most appropriate choice of polynomial for distortion correction was not found to be dependent upon II orientation. It was, however, found to vary depending upon the intended use of the images. Although most applications of IIs are

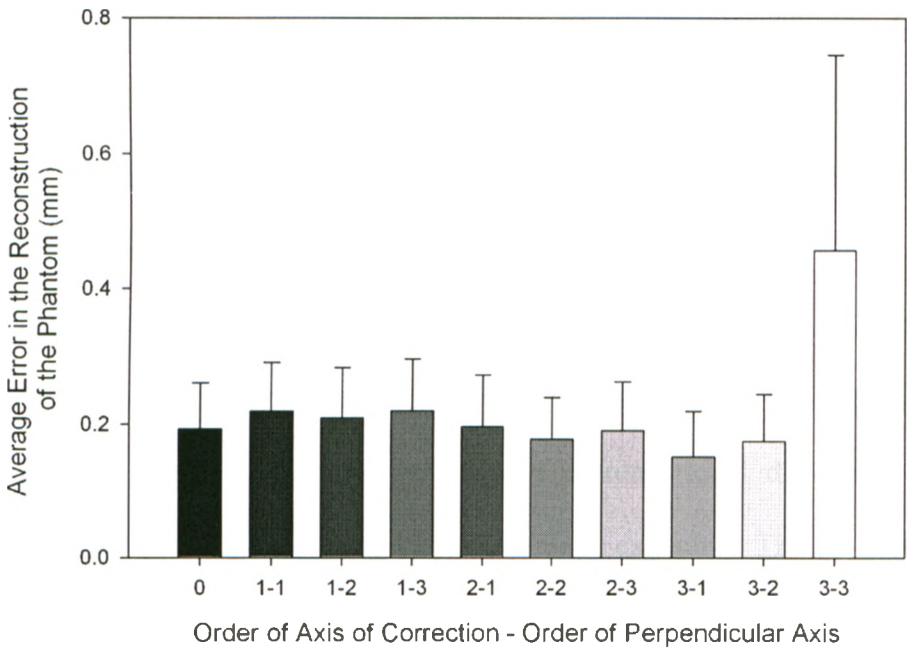

Figure 5.4 Accuracy of the RSA reconstruction
Mean (±1 SD) of the error in the reconstruction of the phantom over the 16 trials with motion between them. All corrections found to be different from 3-1 ($p < 0.05$). Lighter bars indicate higher order polynomial models.

two-dimensional (2D), it is increasingly common to use IIs for 3D analyses. The use of a calibration frame for these 3D applications most likely tempers the effects of distortion – leading to accuracies in the RSA reconstruction using uncorrected points that were far better than anticipated. The distances between the beads in two dimensions indicate that distortion correction plays a much larger role in 2D measurements. As anticipated, the precision of the measurements was not affected by distortion correction.

It has been found that distortion correction requirements may vary between IIs, although this was tested for four different models of two different makes, and not various IIs of the same make and model (Rudin *et al.*, 1991; Gronenschild, 1997). Using the two IIs of our system it was found that, as would be expected, distortion correction requirements did not differ.

The advantages and disadvantages of the various methods of distortion correction have been examined in the literature and it is generally agreed that the main disadvantage of implementing a global approach is that any extreme local distortions cannot be corrected (Fahrig *et al.*, 1997); however, none are to be expected. The advantages are the decreased susceptibility to image noise and the ability to extrapolate the correction beyond the boundaries of the calibration points (Fahrig *et al.*, 1997). It has been pointed out that higher order polynomial corrections tend to result in higher RMS errors as any noise that is present is modeled in addition to the distortion (Gronenschild, 1997; Fantozzi *et al.*, 2003). This may explain why errors from the sixth order polynomial were so high. However, the chosen polynomial must have a sufficient degree to model the distortion; therefore, employing a first order polynomial in the axis of correction was insufficient.

When working with a fluoroscopy-based RSA system, there are always several potential sources of error. These include bead blurring, due to the stochastic nature of x-rays, and image distortion. Bead blurring is addressed through the bead location algorithm, while image distortion is clearly addressed in the current study. The RSA algorithm has several built-in methods of decreasing the effects of other system noise including a least squares method of reconstruction.

The findings of this study suggest that while significant efforts have been made to generalize distortion correction for IIs, correction should be validated with an independent "gold standard" phantom for each particular application for which it is to be used.

5.5 REFERENCES

Bushberg, J.T., Seibert, J.A., Leidholdt, E.M., and Boone, J.M. (2002) Fluoroscopy. In: *The Essential Physics of Medical Imaging.* Lippincott Williams & Wilkins, Philadelphia. pp. 231-254.

Cerveri, P., Forlani, C., Borghese, N.A., and Ferrigno, G. (2002) Distortion correction for x-ray image intensifiers: local unwarping polynomials and RBF neural networks. *Med. Phys.* 29[8], 1759-1771.

Chakraborty, D.P. (1987) Image intensifier distortion correction. *Med. Phys.* 14[2], 249-252.

Fahrig, R., Moreau, M., and Holdsworth, D.W. (1997) Three-dimensional computed tomographic reconstruction using a C-arm mounted XRII: Correction of image intensifier distortion. *Med. Phys.* 24[7], 1097–1106.

Fantozzi, S., Cappello, A., and Leardini, A. (2003) A global method based on thin-plate splines for correction of geometric distortion: an application to fluoroscopic images. *Med. Phys.* 30[2], 124-131.

Gronenschild, E. (1997) The accuracy and reproducibility of a global method to correct for geometric image distortion in the x-ray imaging chain. *Med. Phys.* 24[12], 1875-1888.

Gronenschild, E. (1999) Correction for geometric image distortion in the x-ray imaging chain: Local technique versus global technique. *Med. Phys.* 26 [12], 2602–2616.

Holdsworth, D.W., Pollmann, S.I., Nikolov, H.N., and Fahrig, R. (2005) Correction of XRII geometric distortion using a liquid-filled grid and image subtraction. *Med. Phys.* 32[1], 55-64.

Jareš, V. (1985) The effect of electron optics on the properties of the x-ray image intensifier. *Adv. Electron. Elect. Phys.* 64B, 549-559.

Kedgley, A.E. and Jenkyn, T.R. (2009) RSA calibration accuracy of a fluoroscopy-based system using nonorthogonal images for measuring functional kinematics. *Med. Phys.* 36[7], 3176-3180

Liu, R.R., Rudin, S., and Bednarek, D.R. (1999) Super-global distortion correction for a rotational C-arm X-ray image intensifier. *Med. Phys.* 26[9], 1802–1810.

Rudin, S., Bednarek, D.R., and Wong, R. (1991) Accurate characterization of image intensifier distortion. *Med. Phys.* 18[6], 1145–1151.

Schueler, B. and Hu, X. (1995) Correction of image intensifier distortion for three-dimensional x-ray angiography. *Proc. SPIE* 2432, 272-279.

Soimu, D., Badea, C., and Pallikarakis, N. (2003) A novel approach for distortion correction for X-ray image intensifiers. *Comput. Med. Imaging Graph.* 27[1], 79-85.

van der Zwet, P.M., Meyer, D.J., and Reiber, J.H. (1995) Automated and accurate assessment of the distribution, magnitude, and direction of pincushion distortion in angiographic images. *Invest. Radiol.* 30[4], 204-213.

CHAPTER 6 – AN ALTERNATIVE DEFINITION OF THE SCAPULAR COORDINATE SYSTEM FOR USE WITH RSA

OVERVIEW: This chapter examines the inter- and intra-investigator variations that may occur in landmark digitization and investigates how these variabilities propagate through the kinematic analysis. This chapter also describes an alternate definition for the scapular coordinate system and compares it to the current ISB standard.[5]

6.1 INTRODUCTION

Many different conventions exist for defining the anatomical coordinate systems used to quantify scapular kinematics. This leads to an inability to compare the kinematics reported by various research groups (de Groot, 1997; Anglin and Wyss, 2000; Karduna *et al.*, 2000). Therefore, the International Society of Biomechanics (ISB) proposed a set of coordinate system standards (Wu *et al.*, 2005) that are now recommended (Kontaxis *et al.*, 2009) and have been increasingly employed (Fayad *et al.*, 2008; van Andel *et al.*, 2008). This standard was described in Sections 1.4.1 and 1.4.2.

Landmark digitization is a critical step in creating such an anatomical coordinate system. When performing radiostereometric analysis (RSA), either with a beaded or model-based approach, it is common to employ a computed tomography (CT) scan to obtain the necessary landmarks (Dennis *et al.*, 2005; Bey *et al.*, 2006; Bey *et al.*, 2008; Anderst *et al.*, 2009). The drawback of a CT scan is that the patient is exposed to

[5] A version of this work has been submitted for publication: Kedgley, A.E. and Dunning, C.E. (2009) An alternate definition of the scapular coordinate system for use with RSA. Submitted to *Journal of Biomechanics*

radiation. To obtain the landmarks currently recommended by the ISB, the entire scapula, and therefore also breast and other tissues, must be scanned and thereby exposed to radiation effects.

The purpose of this work was threefold: (1) to quantify the intra- and inter-investigator variabilities of landmark digitization; (2) to investigate an alternate definition of the scapular coordinate system that has repeatedly attainable landmarks and axes as close as possible to those recommended by the ISB, yet requires less radiation exposure; and (3) to compare the glenohumeral joint kinematics resulting from the use of this alternative scapular coordinate system with those obtained using the ISB standard. It was hypothesized that there would be variability in the ability to digitize landmarks repeatably, that an alternative scapular coordinate system could be defined, and that glenohumeral joint kinematics would not differ significantly between the two systems.

6.2 METHODS

Three 0.8 mm stainless steel beads were embedded into each of the scapula and humerus of a shoulder model treated for use in imaging studies (Sawbones®, Pacific Research Laboratories Inc., Vashon, Washington, USA). An isotropic three-dimensional CT scan (Lightspeed VCT, GE Healthcare, Piscataway, New Jersey, USA) was obtained with the following parameters: 0.625 mm sections, 140 kV, 200 mA, 1 s rotation time and reconstruction via a bone algorithm. In addition, to assess the effects of soft tissue and other bony projections, as well as inter-individual shape variation, CT scans of eleven cadaveric specimens were obtained and also reconstructed via a bone algorithm.

Digitization of a specified set of 8 landmarks on the scapula and 3 on the humerus (Table 6.1, Figure 6.1 and Figure 1.3; Meskers *et al.*, 1998; Ebraheim *et al.*, 2000; Wu *et*

Table 6.1 Points that were digitized on the scapula and humerus

Acromial Angle (AA)	Most dorsolateral point on the scapula
Acromioclavicular joint (AC)	Most dorsal point on the joint between the scapula and clavicle, on the scapula.
Inferior angle (IA)	The most caudal point on the scapula.
Inferior point on glenoid (IG)	The most caudal point on the glenoid rim.
Superior angle (SA)	Most superior point on the medial side of the scapula.
Scapular notch (SN)	Centre of the notch on the superior border of the scapula, that lies next to the base of the coracoid process
Tip of coracoid process (PC)	The most ventral point on the processus coracoideus.
Root of the scapular spine (TS)	Trigonum spinae. The midpoint of the triangular surface on the medial scapular border in line with the scapular spine.
Lateral epicondyle (LE)	Most caudal point on lateral epicondyle.
Medial epicondyle (ME)	Most caudal point on medial epicondyle.
Humeral head centre (HH)	Glenohumeral rotation centre.

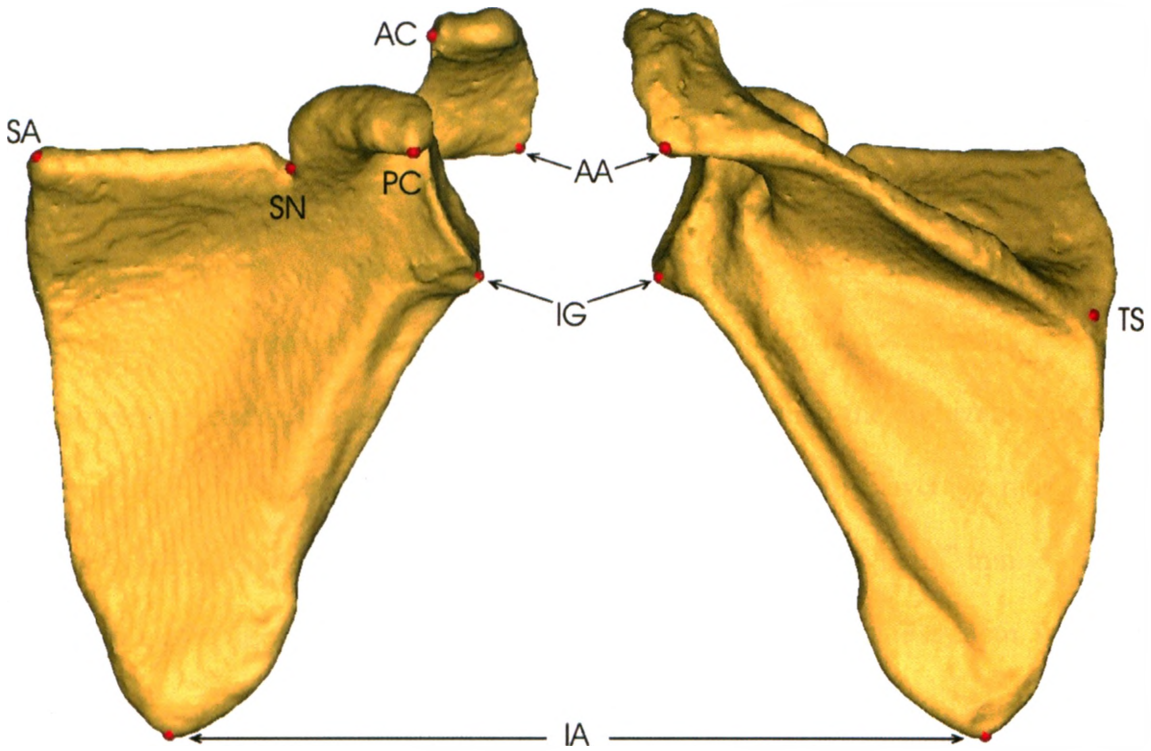

Figure 6.1 Landmarks that were digitized on the scapula
Superior angle (SA), scapular notch (SN), tip of the coracoid process (PC), acromioclavicular joint (AC), acromial angle (AA), most inferior point on the glenoid (IG), root of the scapular spine (TS), and inferior angle (IA). Images are adapted from a model created from a clinical CT scan.

al., 2005) was performed using MIMICS software with a MedCAD module. To quantify the intra-investigator variability of locating landmarks on the scapula, one investigator digitized the CT scans of both the shoulder model and one cadaveric specimen on five separate occasions. To establish the inter-investigator variability, four other participants digitized the same set of landmarks. With the exception of the humeral head centre, the position of each landmark was identified by a single point selection. The humeral head centre was found by fitting a sphere to circles created on each layer of the CT scan that contained its articular surface. The procedures for using MIMICS to locate beads and landmarks of interest, specifically in the shoulder, may be found in Appendix B. All participants were familiar with the software package prior to involvement in the study and all were given the same set of written instructions regarding the digitization process. The variability of the digitized landmarks was quantified by the average radii of the smallest ellipsoid that contained all of the points with a tolerance of $1x10^{-6}$ mm.

Based on these digitization results, an alternative coordinate system was then defined for the scapula using three landmarks that were found to be highly repeatable. To examine the differences between the ISB scapular coordinate system and the alternative scapular coordinate system, both were created by one investigator for each of the eleven cadaveric specimens. The relationship between the coordinate systems was evaluated by examining the trace of the rotation matrix relating the two coordinate systems, with a trace value of three being ideal.

To investigate how the differences in the coordinate system definitions propagate through to the kinematics, the models of the scapula and humerus were placed in fifteen different relative orientations, within the combined range of approximately 15° to 90° of

glenohumeral elevation, 30° of internal rotation to 30° of external rotation, and 0° to 90° of the plane of elevation. In each orientation, a fluoroscopic RSA system (Kedgley *et al.*, 2009) consisting of two fluoroscopy units (SIREMOBIL Compact (L), Siemens Medical Solutions USA Inc., Malvern, Pennsylvania, USA) was used to determine the locations of the beads within the scapula and humerus. Locations of the beads relative to landmarks of interest within the models were determined by thresholding and sphere-fitting operations within MIMICS. Using the relations between the beads and the digitized anatomic landmarks, scapulohumeral kinematics were calculated using a Y-X-Y Euler angle sequence (Kedgley *et al.*, 2007) using the ISB and alternative coordinate systems for each set of landmark digitizations. All kinematic calculations were performed using a custom-written MATLAB code, which may be found in Appendix D.

The inter- and intra- investigator variabilities for digitizations were compared using Mann-Whitney Rank Sum tests. Statistical comparisons of the kinematics obtained from the ISB and alternative coordinate systems were performed using both Wilcoxon Signed Rank tests and Spearman Rank Correlation Coefficients (SRCCs). Variability of the kinematics was defined as the standard deviations of plane of elevation, angle of elevation, and internal-external rotation over all fifteen glenohumeral orientations. Significant differences were defined as $p < 0.05$.

6.3 RESULTS

The inter- and intra-investigator variabilities of landmark selection on the scapula and humerus, as represented by the ellipse with the smallest volume containing all the digitized points for the shoulder model and the cadaveric specimen are listed in Table 6.2 and Table 6.3 respectively. The scapular landmarks with the least inter-investigator

Table 6.2 The individual and average radii of the ellipse with the smallest volume that fit each of the digitized landmarks on the shoulder model, as a measure of inter- or intra-investigator variability of landmark selection

		Inter-investigator					Intra-investigator				
		r1	r2	r3	Average	Rank	r1	r2	r3	Average	Rank
		(mm)					(mm)				
Scapula	AA	0.18	0.89	1.12	0.73	1	0.22	0.48	1.45	0.72	6
	AC	0.33	3.00	3.46	2.27	7	0.12	0.85	3.46	1.48	8
	IA	0.51	1.48	2.04	1.34	5	0.06	0.28	1.48	0.61	5
	IG	0.50	0.73	6.39	2.54	8	0.16	1.08	2.83	1.36	7
	SA	0.29	2.11	2.95	1.78	6	0.07	0.52	0.67	0.42	3
	SN	0.42	0.63	1.17	0.74	3	0.20	0.26	0.68	0.38	2
	PC	0.11	0.51	1.58	0.73	1	0.02	0.35	0.71	0.36	1
	TS	0.28	0.89	1.88	1.02	4	0.14	0.59	0.76	0.50	4
Humerus	ME	0.27	0.35	1.86	0.82	1	0.13	0.52	0.70	0.45	1
	LE	0.28	1.29	1.97	1.18	2	0.16	0.81	1.75	0.91	2
	HH	0.13	0.99	2.85	1.32	3	0.04	1.19	2.66	1.30	3

Table 6.3 The individual and average radii of the ellipse with the smallest volume that fit each of the digitized landmarks on the cadaveric specimen, as a measure of inter- or intra-investigator variability of landmark selection

		Inter-investigator					Intra-investigator				
		r1	r2	r3	Average	Rank	r1	r2	r3	Average	Rank
		(mm)					(mm)				
Scapula	AA	0.59	1.35	3.33	1.76	5	0.17	0.42	1.04	0.54	2
	AC	0.42	3.59	7.25	3.75	8	0.49	1.01	8.52	3.34	8
	IA	0.84	1.10	6.60	2.85	7	0.14	0.34	1.18	0.55	4
	IG	0.21	0.39	4.76	1.78	6	0.34	0.47	2.16	0.99	7
	SA	0.06	1.31	2.48	1.28	3	0.15	0.37	2.06	0.86	6
	SN	0.22	0.81	1.87	0.97	1	0.08	0.19	1.34	0.54	2
	PC	0.10	0.90	2.13	1.04	2	0.19	0.36	1.57	0.71	5
	TS	0.35	1.45	2.72	1.50	4	0.07	0.30	0.61	0.33	1
Humerus	ME	0.15	1.00	2.30	1.15	2	0.04	0.19	0.65	0.30	1
	LE	0.47	0.96	3.24	1.55	3	0.09	0.40	1.46	0.65	3
	HH	0.07	0.47	2.18	0.90	1	0.09	0.28	0.74	0.37	2

variability were the acromial angle (AA), the scapular notch (SN), and the coracoid process (PC) for the shoulder model and the SN, the PC and the superior angle (SA) for the cadaveric specimen. The variability of humeral landmark selection was least for the medial epicondyle (ME) on the shoulder model and least for the humeral head (HH) on the cadaveric specimen. Intra-investigator variability was consistently less than inter-investigator variability.

To meet the objective of reducing the required CT volume, the new coordinate system replaced the inferior angle (IA) in the ISB coordinate system definition with the PC. The SN and SA were also considered as replacements; however, an appropriate set of coordinate system axes, similar to those obtained with the ISB standard, could not be defined (additional data can be found in Appendix M). Using the PC, the Z-axis of the scapula was maintained from the ISB definition as the line passing from the root of the scapular spine (TS) to AA. A second vector was then created, from PC to AA. The Y-axis was defined as the cross product of the z-axis and the second vector for left scapulae and as the cross product of the Z-axis and the negative of the second vector for right scapulae. The cross product of the Y- and Z-axes formed the X-axis. Thus, the directions of the axes were similar to the ISB definition (Figure 6.2). In addition, the origin was maintained at AA. When comparing the two scapular coordinate systems in the eleven cadaveric specimens the trace of the rotation matrix between the two was 2.997 ± 0.002. For two of these specimens the trace was 3.000, indicating a perfect match between the two coordinate systems. The trace of the rotation matrix comparing the two coordinate systems in the shoulder model was 2.998.

Average differences between the three kinematic angles (plane of elevation, angle

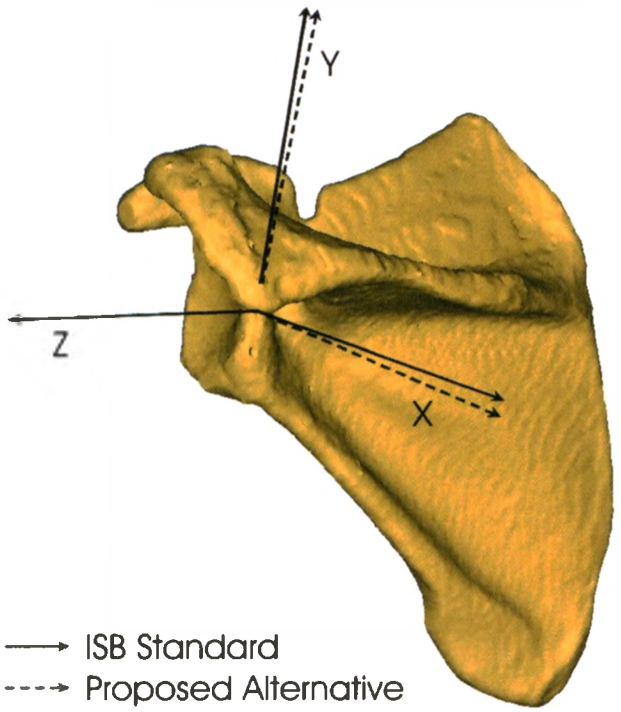

Figure 6.2 Comparison of the ISB recommended axes and alternative axes
ISB axes are based on AA, IA and TS and alternative axes are based on PC, TS and AA. The Z-axis of the proposed alternative axes is the same as the Z-axis of the ISB axes. Image is adapted from a model created from a clinical CT scan.

of elevation, and internal-external rotation) that were calculated using the two coordinate systems of the shoulder model are presented in Table 6.4 for both inter- and intra-investigator data. While the differences in all angles were statistically significant in both cases ($p < 0.001$), the differences were very small in magnitude (less than 5°), and the SRCCs showed excellent association between the two systems.

The average inter- and intra-investigator variabilities are shown in Table 6.5. In the inter-investigator case, for all three kinematic angles, the repeatability was superior for the alternative coordinate system. This was significant for elevation angle ($p < 0.001$) and internal-external rotation ($p = 0.01$). In the intra-investigator case, variability was worse for the plane of elevation with the alternative system ($p = 0.068$).

The mean error of rigid body fitting for RSA (Valstar *et al.*, 2005) averaged over all trials was 0.118 ± 0.078 mm for the scapula and 0.206 ± 0.137 mm for the humerus.

6.4 DISCUSSION

The use of CTs and RSA as tools to quantify accurate *in-vivo* kinematics is becoming progressively more prevalent. As such, radiation exposure has become a concern in orthopaedic biomechanics. It is important to limit this exposure in whatever ways there are available. The exact dosage by which the radiation exposure may be decreased is difficult to quantify as this depends upon a variety of factors, including what other structures (clavicle, humerus or other bones) need to be imaged, and how much of the thyroid, breast and other tissues are exposed. However, based upon the scapula alone, the elimination of IA from the scapular coordinate system approximately halves the required exposure.

In this chapter, an alterative coordinate system for the scapula was defined, which

Table 6.4 Average differences in the calculated kinematic angles
(Mean ± SD), p-values and Spearman rank correlation coefficients (SRCCs) between the use of the ISB standard coordinate system and the proposed alternative coordinate system for all 15 glenohumeral orientations tested.

	Inter-investigator			Intra-investigator		
	Difference (°)	p-value	SRCC	Difference (°)	p-value	SRCC
Plane of elevation	–3.29 ± 3.03	< 0.001	0.990	–3.16 ± 2.93	< 0.001	0.995
Angle of elevation	–0.90 ± 0.92	< 0.001	0.999	–0.83 ± 0.88	< 0.001	0.999
Internal-external rotation	–4.53 ± 2.64	< 0.001	0.985	–4.31 ± 2.57	< 0.001	0.989

Table 6.5 Inter- and intra-investigator variability
As defined by the standard deviation of the resultant kinematic angles for the ISB standard coordinate system and the proposed alternative coordinate system across all 15 glenohumeral orientations tested.

	Inter-investigator			Intra-investigator		
	ISB (°)	Alternative (°)	p-value	ISB (°)	Alternative (°)	p-value
Plane of elevation	0.62	0.61	0.868	0.60	0.84	0.068
Angle of elevation	0.66	0.57	< 0.001	0.43	0.42	0.361
Internal-external rotation	1.05	0.87	0.01	0.63	0.79	0.213

was based on landmarks that were positioned more closely together so as to reduce scanning area and associated radiation. This alternative system used the first, second, and forth most repeatably locatable landmarks in a shoulder model and the second, forth and fifth most repeatably locatable landmarks in a cadaveric specimen as found by five investigators (*i.e.*, AA, PC and TS). The choice of landmarks used was necessary to ensure the requirement that the resulting coordinate system axes closely match those found using the ISB standard. It was interesting to note that the IA was the fifth and seventh most repeatably locatable landmark in the shoulder model and the cadaveric specimen respectively. The similarity of this new, alternative scapular coordinate system as compared to the ISB standard scapular coordinate system was evaluated using the trace of the rotation matrix between the two, and correlation evaluations of the two matrices resulted in perfect scores. In two cases, the two coordinate systems matched perfectly, while in all other cases the match was very close.

The decrease in inter-investigator variability in kinematics with the use of the alternative coordinate system can be attributed to the fact that PC is more repeatably digitizable than IA. The increase in intra-investigator variability in kinematics resulted from the fact that the intra-investigator variability in locating IA was superior to the inter-investigator variability. Therefore, the effect of having the location of PC be more repeatable than the location of IA was negated by the smaller distances between the landmarks. It should be noted that this variability was less than 1° for all angles.

As the trace of the rotation matrix comparing the ISB and alternative scapular coordinate systems for the shoulder model was very close to the average value of the cadaveric specimens, it is able to provide a very good representation of the effects of the

coordinate systems on kinematics. Although the three kinematic angles obtained using the proposed alternative coordinate system were statistically different from those obtained using the ISB standard, the SRCCs demonstrated excellent agreement between the two systems. These differences were very small and in all likelihood are not clinically significant. However, the reduction in radiation exposure is a tremendous advantage of this newly proposed coordinate system.

6.5 REFERENCES

Anderst, W., Zauel, R., Bishop, J., Demps, E., and Tashman, S. (2009) Validation of three-dimensional model-based tibio-femoral tracking during running. *Med. Eng. Phys.* 31[1], 10-16.

Anglin, C. and Wyss, U.P. (2000) Arm motion and load analysis of sit-to-stand, stand-to-sit, cane walking and lifting. *Clin. Biomech.* 15[6], 441-448.

Bey, M., Zauel, R., Brock, S.K., and Tashman, S. (2006) Validation of a new model-based tracking technique for measuring three-dimensional, in vivo glenohumeral joint kinematics. *J. Biomech. Eng.* 128[4], 604-609.

Bey, M., Kline, S.K., Tashman, S., and Zauel, R. (2008) Accuracy of biplane x-ray imaging combined with model-based tracking for measuring *in-vivo* patellofemoral joint motion. *J. Orthop. Surg. Res.* 3, 38.

de Groot, J.H. (1997) The variability of shoulder motions recorded by means of palpation. *Clin. Biomech.* 12[7-8], 461-472.

Dennis, D.A., Mahfouz, M.R., Komistek, R.D., and Hoff, W. (2005) In vivo determination of normal and anterior cruciate ligament-deficient knee kinematics. *J. Biomech.* 38[2], 241-253.

Ebraheim, N.A., Xu, R., Haman, S.P., Miedler, J.D., and Yeasting, R.A. (2000) Quantitative anatomy of the scapula. *Am. J. Orthop.* 29[4], 287-292.

Fayad, F., Roby-Bramib, A., Yazbeck, C., Hanneton, S., Lefevre-Colau, M., Gautheron, V., Poiraudeau, S., and Revel, M. (2008) Three-dimensional scapular kinematics and scapulohumeral rhythm in patients with glenohumeral osteoarthritis or frozen shoulder. *J. Biomech.* 41[2], 326–332.

Karduna, A.R., McClure, P.W., and Michener, L.A. (2000) Scapular kinematics: effects of altering the Euler angle sequence of rotations. *J. Biomech.* 33[9], 1063-1068.

Kedgley, A.E., Mackenzie, G.A., Ferreira, L.M., Drosdowech, D.S., King, G.J.W., Faber, K.J., Johnson, J.A. (2007) The effect of muscle loading on the kinematics of *in vitro* glenohumeral abduction. *J. Biomech.* 40[13], 2953-2960.

Kedgley, A.E., Birmingham, T., and Jenkyn, T.R. (2009) Comparative accuracy of radiostereometric and optical tracking systems. *J. Biomech.* 42[9], 1350-1354.

Kontaxis, A., Cutti, A.G., Johnson, G.R., and Veeger, H.E.J. (2009) A framework for the definition of standardized protocols for measuring upper-extremity kinematics. *Clin. Biomech.* 24[3], 246-253.

Meskers, C.G.M., van der Helm, F.C.T., Rozendaal, L.A., and Rozing, P.M. (1998) In vivo estimation of the glenohumeral joint rotation center from scapular bony landmarks by linear regression. *J. Biomech.* 31[1], 93-96.

Valstar, E.R., Gill, R., Ryd, L., Flivik, G., Börlin, N., and Kärrholm, J. (2005) Guidelines for standardization of radiostereometry (RSA) of implants. *Acta Orthop.* 76[4], 563–572.

van Andel, C.J., Wolterbeek, N., Doorenbosch, C.A.M., Veeger, H.E.J., and Harlaar, J. (2008) Complete 3D kinematics of upper extremity functional tasks. *Gait Posture* 27[1], 120-127.

Wu, G., van der Helm, F.C., Veeger, H.E., Makhsous, M., van Roy, P., Anglin, C., Nagels, J., Karduna, A.R., McQuade, K., Wang, X., Werner, F.W., and Buchholz, B. (2005) ISB recommendation on definitions of joint coordinate systems of various joints for the reporting of human joint motion--Part II: shoulder, elbow, wrist and hand. *J. Biomech.* 38[5], 981-992.

CHAPTER 7 – HUMERAL HEAD POSITION UNDER STATIC AND DYNAMIC POSITIONING: PRELIMINARY DATA

OVERVIEW: This chapter discusses the implementation of the WOQIL fluoroscopic RSA system for the examination of glenohumeral joint motion. The data presented in this chapter are the preliminary results of a larger study examining longitudinal kinematic changes following surgical repair of a rotator cuff tear.

7.1 INTRODUCTION

As mentioned in Section 1.3.1.1, the head of the humerus forms one third of a sphere, while the glenoid fossa is a shallow hollow. The glenohumeral joint is considered to be a ball and socket joint with no translations under ideal conditions; however, injuries such as rotator cuff tears may create larger than normal translations (Poppen and Walker, 1976; Howell *et al.*, 1988). Because this joint has very few bony constraints, the muscles play a much larger role in maintaining joint integrity than in other joints. Also, as stated in Section 1.3.1.3, the rotator cuff plays an important role in glenohumeral joint stabilization and contributes to elevation and rotation of the upper limb (Neer, 1990; Sharkey *et al.*, 1994; Wuelker *et al.*, 1995). The disruption of the rotator cuff alters the normal force distribution around the joint. There is some disagreement in the literature regarding whether normal kinematics can be maintained in actively positioned unstable shoulders without a balanced muscle envelope (Poppen and Walker, 1976; Howell and Kraft, 1991). Radiostereometric analysis (RSA) can allow observations of the joint kinematics post-rotator cuff repair.

As with any surgery, the aim of rotator cuff repair is to restore "normal" joint kinematics and alleviate pain. "Normal" joint kinematics in this case implies very little translation of the humeral head relative to the glenoid fossa as the shoulder moves through its full range of motion. The goal of this preliminary work was to determine the extent of humeral head translation during active abduction of the arm *in-vivo*. In addition, the secondary goal was to quantify humeral head positioning during unconstrained active abduction of the arm and compare this to positioning during unconstrained abduction of the arm held at a series of static positions. It was hypothesized that the humeral head position would not change between static and dynamic positioning.

7.2 METHODS

One male subject diagnosed with a rotator cuff tear and scheduled for surgical repair gave written informed consent to participate in the study. The study was approved by the Office of Research Ethics and the Clinical Research Impact Committee (Appendix N). While undergoing surgery to repair the rotator cuff, the participant had six beads inserted in the scapula and six beads inserted in the humerus (Figure 7.1) to assist with tracking the bones. All beads were tantalum and were 0.8 mm in diameter. Beads were placed using a commercially available bead inserter (Tilly Medical Products AB, Lund, Sweden).

A computed tomography (CT) scan was taken of the scapula, proximal third of the humerus and epicondyles of the humerus. The subject visited the RSA lab to obtain fluoroscopic images of the glenohumeral joint. This visit was scheduled immediately after the subject's follow-up visit with the surgeon at 3 months post-surgery. An x-ray

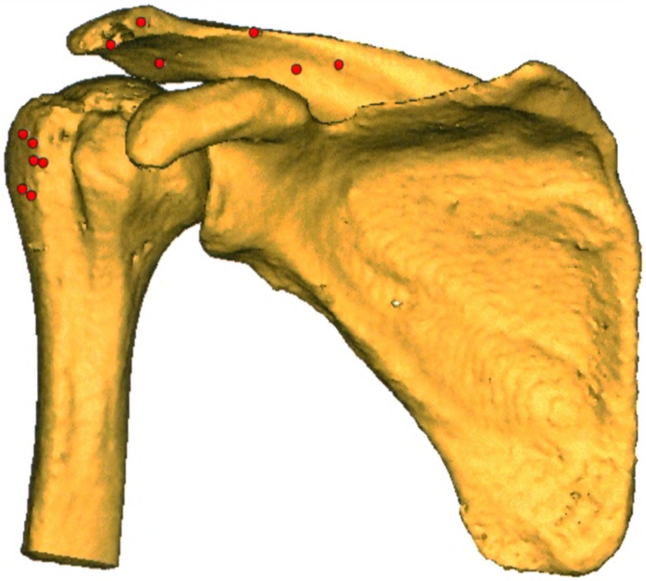

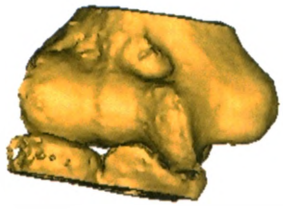

Figure 7.1 Image of the CT scan obtained following rotator cuff repair and bead implantation

A clinical CT scan was obtained the scapula, proximal third of the humerus and epicondyles of the humerus. Implanted beads are shown as red points. The full humerus was not scanned in order to decrease the subject's radiation exposure. (Image of a model created from a clinical CT scan with points added in MIMICS.)

technologist operated the fluoroscopes. The subject was protected with a lead skirt and goggles. The subject was seated on a stool that could be rolled into position between the image intensifiers. The fluoroscopes were positioned to obtain two approximately orthogonal views of the glenohumeral joint and were adjusted to the subject's specific anatomy (Figure 7.2). The subject was then removed from the capture volume so the RSA system could be calibrated with the frame described in Section 2.4.1. Calibration was conducted prior to any data acquisition to prevent the loss of any data in the event that the fluoroscopy units were touched over the course of completing the testing protocol (only part of which is documented herein). In the event that the fluoroscopes were touched, re-calibration could take place and data collection could continue.

The subject was re-positioned in the capture volume and two sets of simultaneous fluoroscopic images were obtained as the subject positioned their arm at resting position (arm at the side) and at 30°, 60°, and 90° of abduction. Two sets of simultaneous fluoroscopic videos were then obtained as the subject performed unconstrained, active abduction through their full range of motion. The image acquisition rate was 30 frames-per-second. Sample fluoroscopy images may be seen in Figure 7.3. Following completion of the full testing protocol, the subject was removed from the capture volume and images of the distortion grid described in Section 2.3 were obtained. Distortion correction was performed with a fourth order polynomial, due to the findings of Chapter 5.

In order to calculate glenohumeral joint kinematics, the positions of the implanted beads were digitized on the fluoroscopic images. Locations of the beads relative to landmarks of interest within the models were determined by thresholding and sphere-

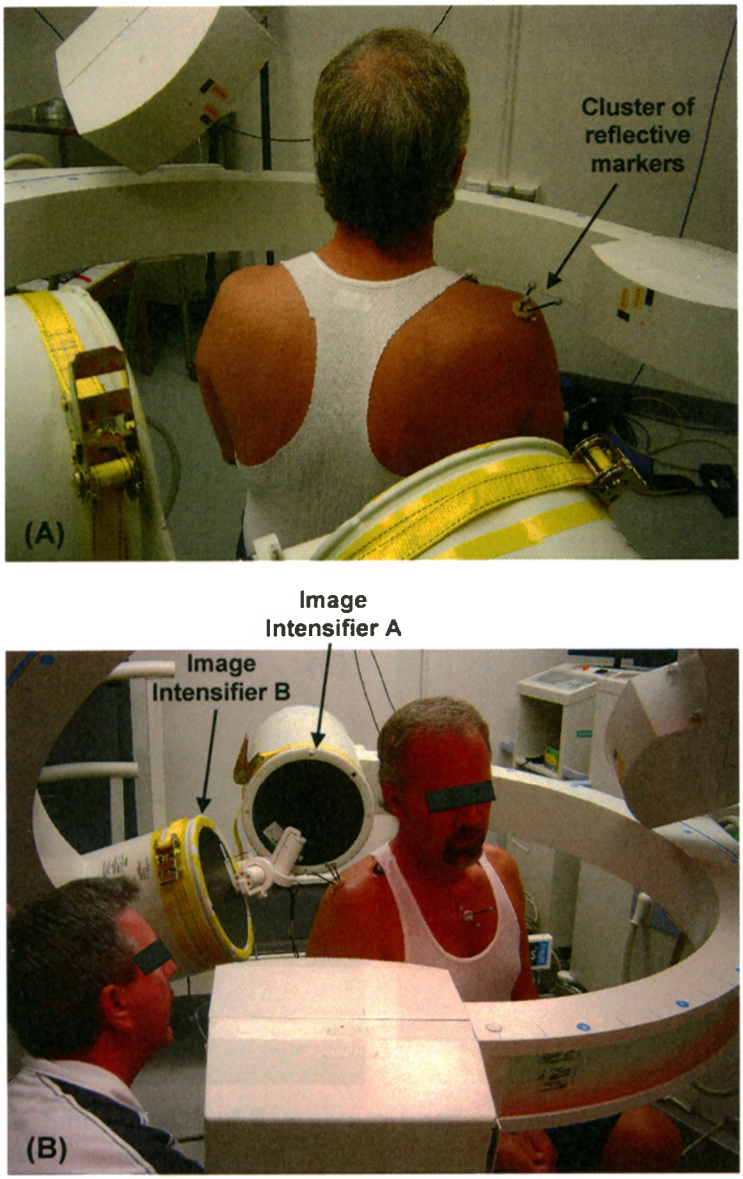

Figure 7.2 The subject positioned within the capture volume of the RSA system

The subject and was seated on a stool and the fluoroscopes were positioned to be approximately orthogonal, with views of the glenohumeral joint. The image intensifiers are labeled to correspond with the images in Figure 7.3. Clusters of reflective markers, for use with the optical tracking system, were also placed on the subject to obtain data for another study.

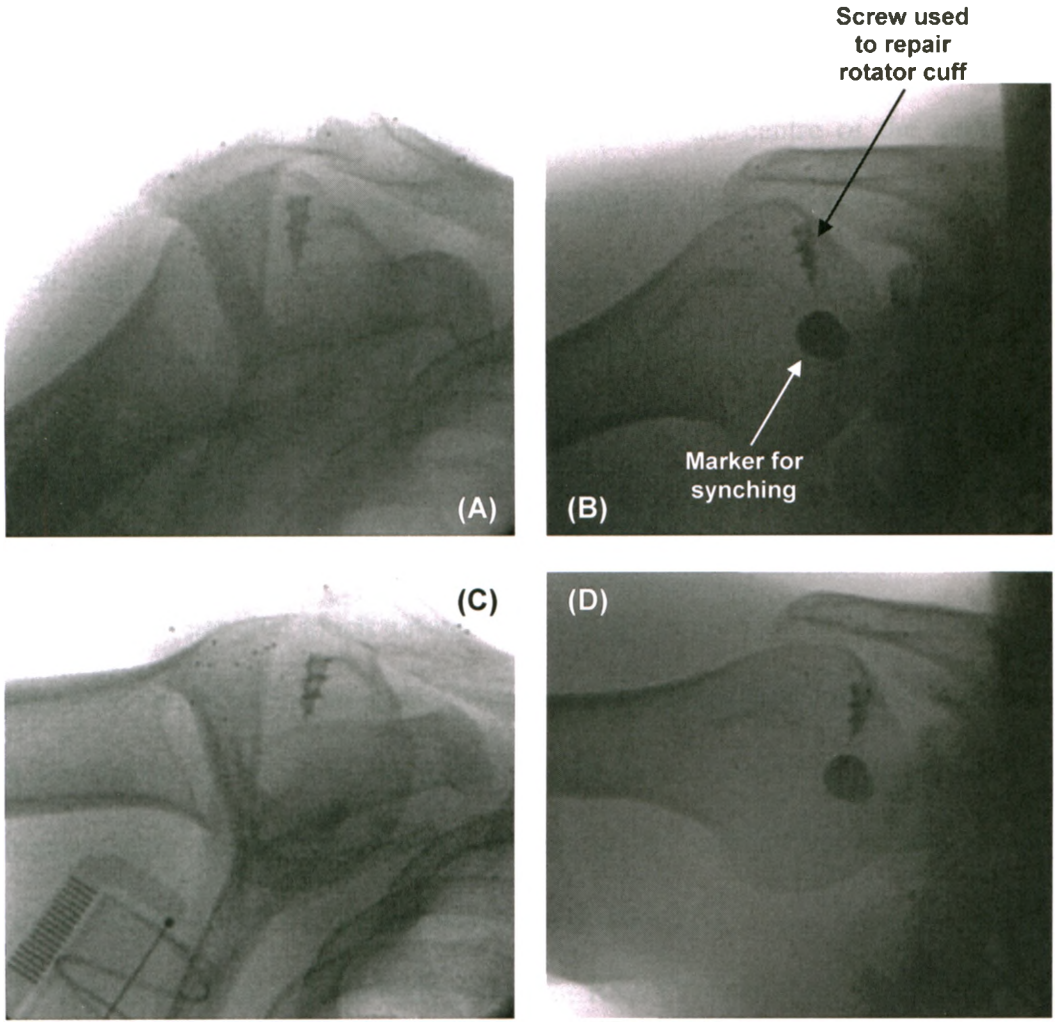

Figure 7.3 Sample pairs of fluoroscopy images obtained to determine glenohumeral joint kinematics
Images obtained of the glenohumeral joint at **(A & B)** approximately 40° and at **(C & D)** approximately 55° of glenohumeral abduction from **(A & C)** fluoroscopy unit A and **(B & D)** fluoroscopy unit B.

fitting operations within MIMICS. Using the relations between the beads and the digitized anatomic landmarks, scapulohumeral kinematics were calculated using a Y-X-Y Euler angle sequence and the ISB coordinate systems, as described in Section 1.4.2. All kinematic calculations were performed using a custom-written MATLAB code, which may be found in Appendix D.

In order to display the results, the positions of the centre of the humeral head relative to the glenoid fossa were plotted in MIMICS. The motion of the centre of the humeral head through abduction was quantified by the smallest ellipsoid that contained the centres, measured at every 5° of abduction, with a tolerance of $1x10^{-6}$ mm.

7.3 RESULTS

As shown in Figure 7.4, the position of the humeral head with respect to the glenoid fossa did not alter much throughout the range of motion. In fact, the centre of the humeral head stayed within an ellipse with radii of 0.93 mm, 1.90 mm and 3.32 mm. The large translation appeared to be in the medial-lateral direction. In addition, when comparing static and dynamic joint positions at 20° and 40° of glenohumeral joint abduction, very minimal differences were seen (Figure 7.5).

The mean error of rigid body fitting for RSA (Valstar *et al.*, 2005) during active abduction for the chosen data points was 0.152 mm for the scapula and 0.116 mm for the humerus.

7.4 DISCUSSION

In agreement with the hypothesis, the humeral head position did not noticeably alter between static and dynamic positioning. The magnitudes of the translations in this

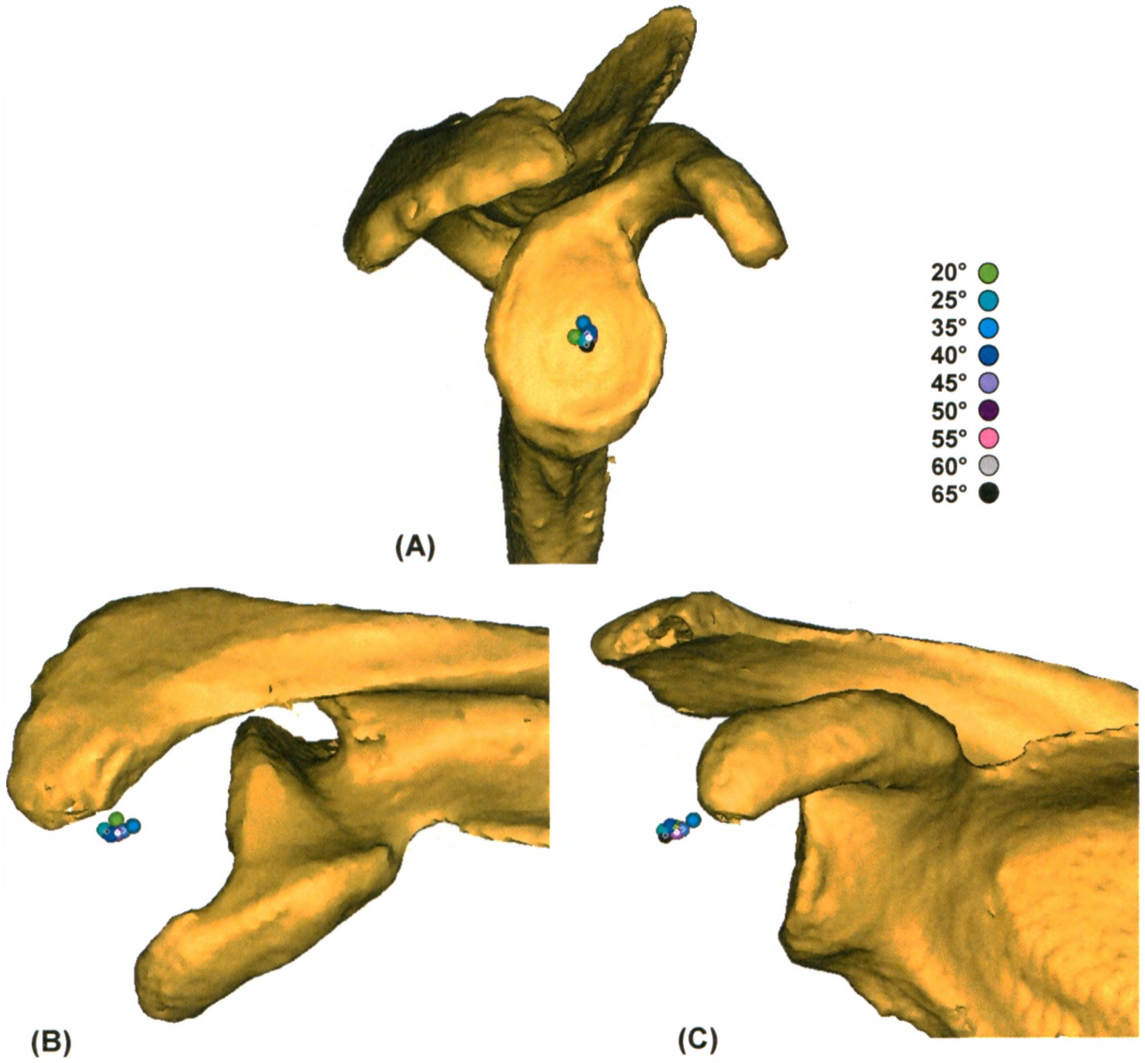

Figure 7.4 Humeral head centre position as a function of glenohumeral abduction angle

(A) Medial-lateral, (B) superior-inferior and (C) anterior-posterior views of humeral head position plotted every 5° from 20° to 65° of unconstrained active glenohumeral abduction. (Images are of a model created from a clinical CT scan with points added in MIMICS.)

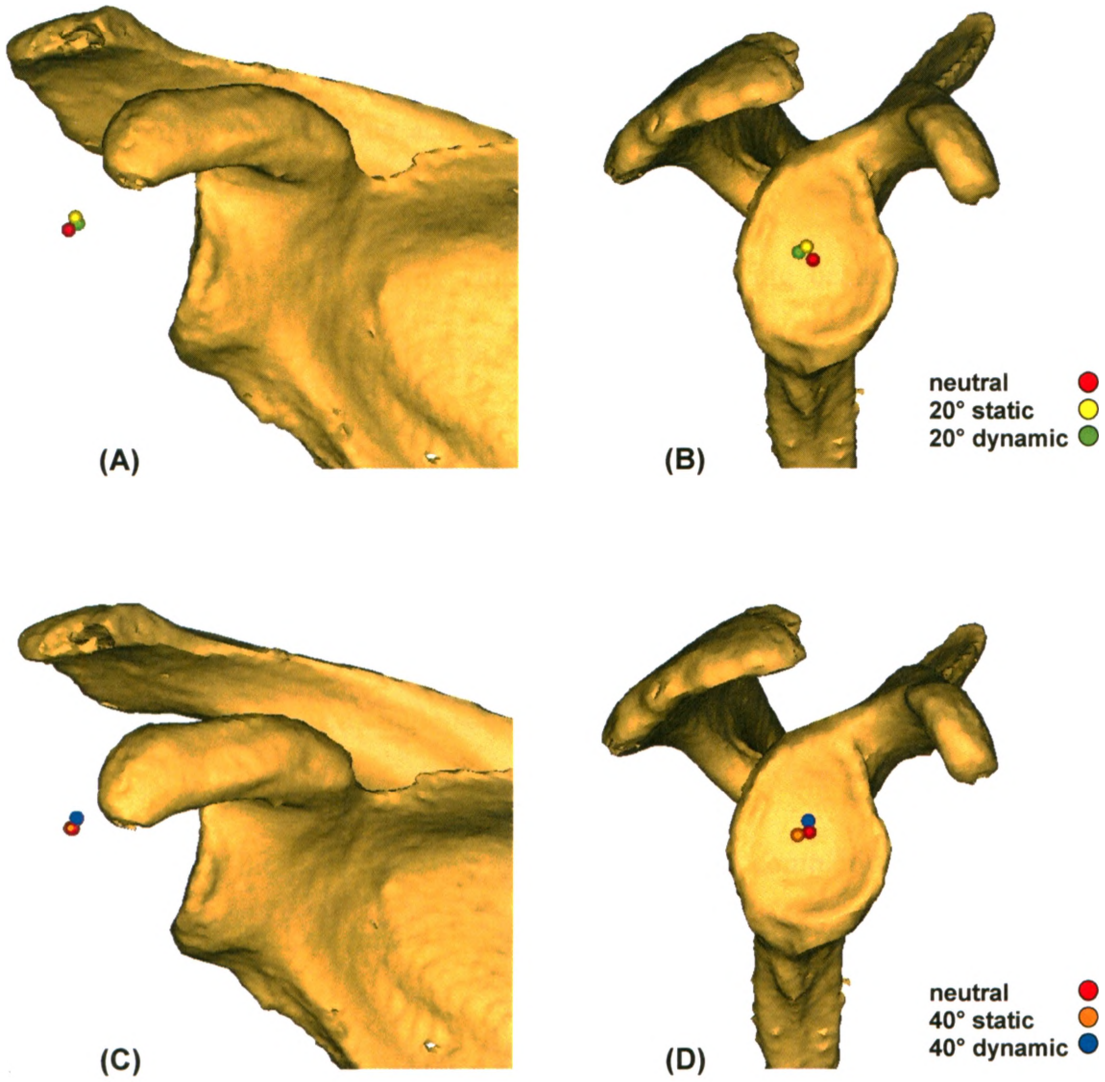

Figure 7.5 Comparison of humeral head centre position for static and dynamic joint positioning
Anterior-posterior **(A & C)** and medial-lateral **(B & D)** views of humeral head position is plotted at 20° **(A & B)** and 40° **(C & D)** of unconstrained static and dynamic glenohumeral abduction. (Images are of a model created from a clinical CT scan with points added in MIMICS.)

preliminary data agree with the findings of Graichen *et al.* (2005), who used an open-magnetic resonance imaging system to examine glenohumeral joint kinematics in static positions and found translations to be on the order of 2 mm. These data also agree with the results obtained by Hallström and Kärrholm (2006) who found medial-lateral translations of 1–2 mm during active abduction using beaded biplanar RSA of healthy subjects.

A major limitation to any clinical study employing beaded RSA is that pre-surgical data cannot be obtained. It is possible that in specific situations if a pre-surgical scope were required, beads could be implanted and kinematics could be examined following the reduction of any swelling and pain associated with the procedure, but these situations are rare. The effects of any post-surgical treatments may be monitored; however, initial baseline measurements will always be missing.

Clearly the use of a single subject is also a limitation of these preliminary data. However, this was a successful implementation of the fluoroscopic RSA system described in this thesis and serves as a basis for the completion of a larger study examining longitudinal kinematic changes following surgical repair of a rotator cuff tear.

7.5 REFERENCES

Hallström, E. and Kärrholm, J. (2006) Shoulder kinematics in 25 patients with impingement and 12 controls. *Clin. Orthop. Relat. Res.* 448, 22-27.

Howell, S.M., Galinat, B.J., Renzi, A.J., and Marone, P.J. (1988) Normal and abnormal mechanics of the glenohumeral joint in the horizontal plane. *J. Bone Joint Surg. Am.* 70[2], 227-232.

Howell, S.M. and Kraft, T.A. (1991) The role of the supraspinatus and infraspinatus muscles in glenohumeral kinematics of anterior shoulder instability. *Clin. Orthop.* [263], 128-134.

Neer, C.S. (1990) Anatomy of shoulder reconstruction. In: *Shoulder Reconstruction.* W.B. Saunders Company, Philadelphia. pp. 1-39.

Poppen, N.K. and Walker, P.S. (1976) Normal and abnormal motion of the shoulder. *J. Bone Joint Surg. Am.* 58[2], 195-201.

Sharkey, N.A., Marder, R.A., and Hanson, P.B. (1994) The entire rotator cuff contributes to elevation of the arm. *J. Orthop. Res.* 12[5], 699-708.

Valstar, E.R., Gill, R., Ryd, L., Flivik, G., Börlin, N., and Kärrholm, J. (2005) Guidelines for standardization of radiostereometry (RSA) of implants. *Acta Orthop.* 76[4], 563–572.

Wuelker, N., Wirth, C.J., Plitz, W., and Roetman, B. (1995) A dynamic shoulder model: reliability testing and muscle force study. *J. Biomech.* 28[5], 489-499.

CHAPTER 8 – GENERAL DISCUSSION AND CONCLUSIONS

OVERVIEW: This chapter summarizes the findings of this research, outlines its strengths and limitations, and lists several recommendations. The potential future directions of research in this area are addressed and the significance of this work is highlighted.

8.1 SUMMARY

Radiostereometric analysis (RSA), while not a new technology, has been newly incorporated with fluoroscopy, to provide a tool for measuring dynamic kinematics with high precision and accuracy. The primary objective of this work was to develop and validate such a system. Benchmarks of kinematic quantification were outlined in Chapter 1. The individual components of the system were described in Chapter 2. The system consists of two 9 inch portable C-arm fluoroscopy units and two personal computers. Images are digitized using custom-written software that was created in MATLAB. Calibration of the RSA system is performed using a custom-made calibration frame. Image distortion is corrected using a global approach with a polynomial fit to the positions of a grid of stainless steel beads. Synchronization of the two fluoroscopy units is accomplished with a visual system and synchronization of the data from the RSA and optical motion analysis systems is achieved through a tertiary coordinate system. The calculations for the reconstruction of the locations of points in three dimensions are conducted using another custom-written MATLAB program.

Validation of the RSA system was the subject of Chapter 3. The purpose was to quantify and compare the accuracy of traditional RSA, RSA using fluoroscopy (fRSA) and optical motion tracking. It was hypothesized that the differences between true translations and rotations and those measured with fRSA would be smaller than those measured with optical tracking, but greater than those measured using traditional RSA performed using digital radiography. Three phantoms, each consisting of three stainless steel spheres and three reflective markers were constructed. The phantoms were fixed to a precision cross-slide table and a precision rotation table. Translation and rotation were quantified. In translation, the difference scores between the dial-gauge and fRSA translations were not significantly different than those using traditional RSA, but were significantly lower than those using the optical system. In rotation, difference scores for both types of RSA were significantly lower than those of the optical system. Therefore, the hypothesis of this study held, and this study showed that images taken using fluoroscopy under ideal conditions can produce RSA reconstructions that are as accurate as those taken with digital radiography. In addition, this study demonstrated that the main plane of interest of a study should be positioned such that it lies at 45° to both fluoroscopy units in order to take advantage of increased accuracy.

Once the system was developed and validated, a novel calibration frame design was created and tested, as described in Chapter 4. It was hypothesized that a more accurate calibration would be obtained when the fiducial and control planes were parallel to each of the image intensifiers. The accuracy of RSA performed with non-orthogonally positioned imaging devices using an orthogonal calibration frame and a calibration frame with pairs of fiducial and control planes at relative angles of greater than 90° was

quantified. While the calibration frame did not result in improved accuracies, the study showed that using the orthogonal calibration frame it was possible to calibrate the system with the fluoroscopes at any angle less than or equal to 135° with equivalent or better accuracy than that obtained with the fluoroscopes at right angles.

Distortion correction was the subject of Chapter 5. A range of global correction schemes, consisting of polynomials of various degrees were tested to determine which was most effective. Outcome measures were the fit of the chosen polynomial to the points on the distortion grid, the distances between the points of the grid in a second position, and the overall accuracy of the RSA reconstruction. RSA reconstruction accuracy was greatest for a polynomial of third order in the axis of correction and first order in the perpendicular axis, resulting in an average error of 150 ± 69 μm. In addition, this study showed that the choice of polynomial for distortion correction was not dependent on image intensifier orientation.

Recognizing that radiation exposure is a significant concern with the clinical implementation of this type of work, an alternative scapular coordinate system was introduced in Chapter 6 in an attempt to decrease the required computed tomography (CT) volume. In addition, the intra- and inter-investigator variabilities of landmark digitization were quantified. It was hypothesized that there would be variability in the ability to digitize landmarks repeatably, that an alternative scapular coordinate system could be defined, and that glenohumeral joint kinematics would not differ between the two systems. The CTs of eleven cadaveric scapulae were used to compare the new scapular coordinate system to the International Society of Biomechanics (ISB) standard. Correlation evaluations of the two matrices resulted in perfect scores. Models of the

scapula and humerus were beaded and placed in fifteen different relative orientations. The resulting glenohumeral kinematics that resulted from using the new scapular coordinate system and the ISB standard were compared. Although the three kinematic angles obtained using the proposed alternative coordinate system were different from those obtained using the ISB standard, the correlation coefficients demonstrated excellent association between the two systems and the results were most likely not clinically significant, validating the hypothesis.

Finally, a clinical application of the system was implemented, examining humeral head translation during abduction of the glenohumeral joint, following surgery for rotation cuff repair. The preliminary data for one subject are presented in Chapter 7.

8.2 STRENGTHS AND LIMITATIONS

The strengths and limitations of each of the individual studies have been mentioned in their respective chapters; however, as the primary goal of this thesis was to develop a new tool for kinematic analysis, there are some overall strengths and limitations of this body of work. The biggest limitation of this technique is that it is invasive. In order for the measurements to be obtained, x-rays and beads must be used. Radiation comes in the form of a CT scan and then as fluoroscopy images for kinematic data acquisition. Beads must be implanted during surgery. The second limitation to this approach is that all images are manually digitized in its current implementation. This places restrictions on how quickly results can be processed. Third, only bony structures are well enough defined in the images to be digitized. This technique cannot be used to examine soft tissue structures such as tendons or ligaments *in-vivo*.

Some additional potential limitations of the described approach include the fact that the capture volume is quite small, limiting the visible region. Also, the maximum capture rate of the fluoroscopy units limits the speed of motions that may be performed, as blurring can occur if motions are performed too quickly. Furthermore, a bi-planar RSA set-up may limit the range of motion of the subjects.

The program that was written to digitize the implanted beads can have difficulties with points that are positioned too closely together, especially if the contrast of one point is significantly different from the other. Using the zooming feature of this program can alleviate this problem to some extent; however, if there are additional metal implants such as joint replacements or excessive hardware in the field of view, the beads may be completely obscured.

The major strength of this research is that by combining fluoroscopy with RSA the system can be used in dynamic situations that a conventional stereographic system cannot. When compared with kinematic examination using a CT scan or plane x-rays, the radiation dose is decreased. As the fluoroscopy units are not enclosed, the full ROM may be examined, which is not the case with a magnetic resonance imaging examination. And perhaps most beneficially, when compared to optical or electromagnetic surface marker systems, fluoroscopy has the advantage that the internal osseous structures can be seen and skin motion artefact is eliminated.

8.3 Recommendations and Future Directions

At this point, following design, validation and preliminary use of the WOQIL fluoroscopic RSA system, several recommendations can be made. They may be grouped as follows:

1. Equipment
    a. The acquisition of fluoroscopes with larger image intensifiers would increase the field of view of each fluoroscope and therefore also greatly improve the capture volume of the RSA system. This would increase the range of motion over which kinematics may be analyzed, and potentially increase the number of joints that may be examined simultaneously, especially in a segment such as the hand, foot or spine.
    b. Flat-panel detectors would aid improving the accuracy of this approach as these IIs do not suffer from pin-cushion distortion (Yaffe and Rowlands, 1997; Seibert, 2006; Davies *et al.*, 2007). In addition, flat-panel detectors have a more uniform response across the field of view and decreased detector bulkiness, which allows for better patient access (Yaffe and Rowlands, 1997; Seibert, 2006). That said, it has been shown that image quality does not necessarily improve with the use of flat-panel detectors (Davies *et al.*, 2007); however, this may be a function of operator experience and training on the new systems (Seibert, 2006).
    c. The incorporation of pulsed fluoroscopy would allow a shorter exposure time per image frame, resulting in reduced blurring of the images. It would also provide the option for a greater radiation dose per image frame while maintaining an equivalent total dose for the examination, as the radiation would not be administered continuously. This would result in clearer images.
2. RSA program

a. An in-house program should be written for distortion correction. At the moment an external, web-based program (located at zunzun.com) is used to fit a polynomial function to the points from the distortion grid and provide the coefficients for that polynomial.

b. An image dewarping function could be incorporated as an alternative to polynomial fitting to provide distortion correction. This would also alleviate the need to rely on an external program.

c. The RSA program should be made more user-friendly for those users who may not be comfortable with MATLAB. The program could be given a graphical user interface and much of the individual steps could be incorporated into a single program from the user's perspective.

d. An automated bead detection scheme (Cho and Johnson, 1998) should be added so that all points do not need to be manually digitized. The implementation of such a scheme is very feasible and likely would not require a large amount of additional coding; however, it would require validation.

e. The use of a solidification procedure should be investigated, similar to the one introduced by Chèze *et al.* (1995) for minimizing the effects of skin motion artefact. This will improve the results of RSA by alleviating the effects of any digitization errors in clinical images.

The establishment of this facility provides a seemingly endless list of possible future work, not the least of which is the innumerable surgical follow-up studies that could be accomplished. In the short term, there are several studies that have begun and will continue following the completion of this body of work.

Examination of the rigid body assumption is the first of these studies. Kinematic measurements are usually based on the assumption that bones are rigid bodies and are therefore non-deformable. A rigid body is "a system of mass-points subject to the constraints that the distances between all pairs of points remain constant throughout the motion" (Selvik, 1989). The advantage to the rigid body assumption is that fewer measurements are required to determine the location and orientation of a bone. This is especially relevant to the scapula since it is so thin and under significant dynamic loading. Thus far, no study has challenged the assumption that bones may be considered as rigid bodies. Due to the complicated osseous structure of the scapula and its many large muscle attachment sites, and compounded by the fact that the exact forces applied by the muscles are unknown, this problem cannot be successfully addressed through computational models.

The quantification of skin motion artefact, specifically in the shoulder, is another area in which this system would be particularly useful. Similar to studies by Stagni *et al.* (2005) and Garling *et al.* (2007) that examined skin motion artefact in the knee, a greater understanding of the errors involved in the use of skin markers will enable the results to be better interpreted.

Perhaps most importantly, this work provides a basis for "markerless" RSA. Increasingly the goal is to obtain accurate kinematics without interference with the subject. "Markerless" RSA decreases the ethical concerns associated with this work, removes the requirement of bead implantation during surgery, and allows the study of "normal" subjects. By matching the projections of 3D computer-aided design (CAD) models to the images captured by the fluoroscopes, the orientation of the object of

interest may be determined in six degrees of freedom (Valstar *et al.*, 2001; Kaptein *et al.*, 2004). This has been done with CAD models of implants in the knee (Banks and Hodge, 1996; Hoff *et al.*, 1998; Dennis *et al.*, 2003; Fantozzi *et al.*, 2003; Yamazaki *et al.*, 2004; Mahfouz *et al.*, 2005) and ankle (Komistek *et al.*, 2000), as well as the native knee joint (Asano *et al.*, 2001; Komistek *et al.*, 2003; Li *et al.*, 2004; Li *et al.*, 2005; Anderst *et al.*, 2009), ankle joint (de Asla *et al.*, 2006), and shoulder (Bey *et al.*, 2008; Nishinaka *et al.*, 2008). The work in this thesis has allowed for the expedited development and validation of a "markerless" RSA system at the WOQIL (Allen, 2009).

8.4 SIGNIFICANCE

In conclusion, this work provides the basis for a plethora of potential clinical studies. The ability to examine subjects while in motion with comparable accuracy to that obtained using conventional RSA techniques should enable substantial improvements to the study of even subtle *in-vivo* kinematics. When joints are in motion, the inertias of body segments come into play, thereby allowing more realistic study of the activities of daily living. In addition, this work has shown that RSA need not be performed with orthogonal imaging devices, allowing greater freedom in positioning the equipment and obtaining more desirable x-ray views. And finally, an alternative scapular coordinate system has been introduced that will benefit subjects in shoulder studies by decreasing the radiation required for the creation of bone-based coordinate systems. It is hoped that the system described herein will enable kinematic variables to be quantified in a way that they have not been before at the WOQIL, leading to an increased understanding of the effects of disease progression, surgical techniques and rehabilitation protocols.

8.5 REFERENCES

Allen, A. (2009) Development and validation of a markerless radiostereometric analysis (RSA) system. MESc Thesis, The University of Western Ontario, London.

Anderst, W., Zauel, R., Bishop, J., Demps, E., and Tashman, S. (2009) Validation of three-dimensional model-based tibio-femoral tracking during running. *Med. Eng. Phys.* 31[1], 10-16.

Asano, T., Akagi, M., Tanaka, K., Tamura, J., and Nakamura, T. (2001) In vivo three-dimensional knee kinematics using a biplanar image-matching technique. *Clin. Orthop. Relat. Res.* [388], 157-166.

Banks, S.A. and Hodge, W.A. (1996) Accurate measurement of three-dimensional knee replacement kinematics using single-plane fluoroscopy. *IEEE Trans. Biomed. Eng.* 43[6], 638-649.

Bey, M.J., Kline, S.K., Zauel, R., Lock, T.R., and Kolowich, P.A. (2008) Measuring dynamic in-vivo glenohumeral joint kinematics: technique and preliminary results. *J. Biomech.* 41[3], 711-714.

Chèze, L., Fregly, B.J., and Dimnet, J. (1995) A solidification procedure to facilitate kinematic analyses based on video system data. *J. Biomech.* 28[7], 879-884.

Cho, P.S. and Johnson, R.H. (1998) Automated detection of BB pixel clusters in digital fluoroscopic images. *Phys. Med. Biol.* 43[9], 2677-2683.

Davies, A.G., Cowen, A.R., Kengyelics, S.M., Moore, J., and Sivananthan, M.U. (2007) Do flat detector cardiac X-ray systems convey advantages over image-intensifier-based systems? Study comparing X-ray dose and image quality. *Eur. Radiol.* 17[7], 1787-1794.

de Asla, R.J., Wan, L., Rubash, H.E., and Li, G. (2006) Six DOF in vivo kinematics of the ankle joint complex: Application of a combined dual-orthogonal fluoroscopic and magnetic resonance imaging technique. *J. Orthop. Res.* 24[5], 1019-1027.

Dennis, D.A., Komistek, R.D., and Mahfouz, M.R. (2003) In vivo fluoroscopic analysis of fixed-bearing total knee replacements. *Clin. Orthop. Relat. Res.* [410], 114-130.

Fantozzi, S., Benedetti, M.G., Leardini, A., Banks, S.A., Cappello, A., Assirelli, D., and Catani, F. (2003) Fluoroscopic and gait analysis of the functional performance in stair ascent of two total knee replacement designs. *Gait Posture* 17[3], 225-234.

Garling, E.H., Kaptein, B.L., Mertens, B., Barendregt, W., Veeger, H.E., Nelissen, R.G., and Valstar, E.R. (2007) Soft-tissue artefact assessment during step-up using fluoroscopy and skin-mounted markers. *J. Biomech.* 40[Suppl 1], S18-S24.

Hoff, W.A., Komistek, R.D., Dennis, D.A., Gabriel, S.M., and Walker, S.A. (1998) Three-dimensional determination of femoral-tibial contact positions under *in vivo* conditions using fluoroscopy. *Clin. Biomech.* 13[7], 455-472.

Kaptein, B.L., Valstar, E.R., Stoel, B.C., Rozing, P.M., and Reiber, J.H. (2004) Evaluation of three pose estimation algorithms for model-based roentgen stereophotogrammetric analysis. *Proc. Inst. Mech. Eng. Part H* 218[4], 231-238.

Komistek, R.D., Stiehl, J.B., Buechel, F.F., Northcut, E.J., and Hajner, M.E. (2000) A determination of ankle kinematics using fluoroscopy. *Foot Ankle Int.* 21[4], 343-350.

Komistek, R.D., Dennis, D.A., and Mahfouz, M. (2003) In vivo fluoroscopic analysis of the normal human knee. *Clin. Orthop. Relat. Res.* [410] 69-81.

Li, G., Wuerz, T.H., and Defrate, L.E. (2004) Feasibility of using orthogonal fluoroscopic images to measure in vivo joint kinematics. *J. Biomech. Eng.* 126[2], 314-318.

Li, G., Defrate, L.E., Rubash, H.E., and Gill, T.J. (2005) In vivo kinematics of the ACL during weight-bearing knee flexion. *J. Orthop. Res.* 23[2], 340-344.

Mahfouz, M.R., Komistek, R.D., Dennis, D.A., and Hoff, W.A. (2004) In vivo assessment of the kinematics in normal and anterior cruciate ligament-deficient knees. *J. Bone Joint Surg. Am.* 86[Suppl 2], 56-61.

Nishinaka, N., Tsutsui, H., Mihara, K., Suzuki, K., Makiuchi, D., Kon, Y., Wright, T.W., Moser, M.W., Gamada, K., Sugimoto, H., and Banks, S.A. (2008) Determination of in vivo glenohumeral translation using fluoroscopy and shape-matching techniques. *J. Shoulder Elbow Surg.* 17[2], 319-322.

Seibert, J.A. (2006) Flat-panel detectors: how much better are they? *Pediatr. Radiol.* 36[Suppl 2], 173-181.

Stagni, R., Fantozzi, S., Cappello, A., and Leardini, A. (2005) Quantification of soft tissue artefact in motion analysis by combining 3D fluoroscopy and stereophotogrammetry: a study on two subjects. *Clin. Biomech.* 20[3], 320-329.

Valstar, E.R., de Jong, F.W., Vrooman, H.A., Rozing, P.M., and Reiber, J.H. (2001) Model-based Roentgen stereophotogrammetry of orthopaedic implants. *J. Biomech.* 34[6], 715-722.

Yamazaki, T., Watanabe, T., Nakajima, Y., Sugamoto, K., Tomita, T., Yoshikawa, H., and Tamura, S. (2004) Improvement of depth position in 2-D/3-D registration of knee implants using single-plane fluoroscopy. *IEEE Trans. Med. Imaging* 23[5], 602-612.

Yaffe, M.J. and Rowlands, J.A. (1997) X-ray detectors for digital radiography. *Phys. Med. Biol.* 42[1], 1-39.

APPENDICES

APPENDIX A – INDEX OF TERMS

This appendix contains definitions for some of the terminology used throughout this thesis and is provided to assist the lay reader (except where noted all definitions are taken from Dorland's Pocket Medical Dictionary, WB Saunders Company, Philadelphia, © 1995).

Aberration: A defect in the image formed by a lens or curved mirror.[6]

Abduct: To draw away from the median plane, specifically, in the plane of the scapula.

Adduct: To draw towards the median plane, specifically, in the plane of the scapula.

Acromion: The lateral extension of the spine of the scapula, forming the highest point of the shoulder.

Acromioclavicular: Pertaining to the acromion and the clavicle.

Anatomical landmark: A point, or effectively small area, reliably identifiable within a biological structure (bone).[7]

Anterior: Situated at or directed toward the front; opposite of posterior.

Anthropometry: The science dealing with the measurement of the size, weight, and proportions of the human body. Anthropometric, adj.

Arthroplasty: Plastic repair of a joint.

Articulation: A joint; the place of union or junction between two or more bones of the skeleton.

Astigmatism: A lens defect in which when rays in one plane are in focus those in another plane are not.[8]

Asymptomatic: Not showing any symptoms of disease, whether disease is present or not.[9]

Axiohumeral: Pertaining to the thoracic cage and the humerus.

Axioscapular: Pertaining to the thoracic cage and the scapula.

Cadaveric: Pertaining to a human body preserved for anatomical study.

Caudal: Pertaining to the inferior end of the body.

---

[6] Daintith, J. (Ed.) (2009) *A Dictionary of Physics*, Oxford University Press, Oxford. *Oxford Reference Online*. Oxford University Press.

[7] Cappozzo, A., Catani, F., Leardini, A., Benedetti, M.G., and Croce, U.D. (1996) Position and orientation in space of bones during movement: experimental artefacts. *Clin. Biomech.* 11[2], 90-100.

[8] Daintith, 2009

[9] Martin, E.A. (Ed.) (2007) *Concise Medical Dictionary*, Oxford University Press, New York. *Oxford Reference Online*. Oxford University Press.

Clavicle: Elongated slender, curved bone (collar bone) lying horizontally at the root of the neck, in upper part of thorax.

Coma: The optical aberration produced when an image received on a screen that is not exactly at right angles to the line of propagation of the incident light.

Computed tomography: An imaging method in which a cross-sectional image of the structures in a body plane is reconstructed by a computer program from the x-ray absorption of beams projected through the body in the image plane.

Connective tissue: The tissue that supports, binds or separates more specialized tissues and organs or functions as a packing tissue of the body.[10]

Control marks: Points on the control plane used for determining the focal point of the x-ray units.[11]

Coracoid process: A beaklike process that curves upwards and forwards from the top of the scapula, over the shoulder joint.[12]

Coronary angiography: An x-ray technique for examination of the coronary arteries, often taken to also include examination of the chambers of the heart.[13]

Deltoid: A thick triangular muscle that covers the shoulder joint.[14]

Diaphysis: The shaft of a long bone, between the expanded articular ends of a long bone.

Digital radiography: A technique in which x-ray absorption is quantified by assignment of a number to the amount of x-rays reaching the detector; the information is manipulated by a computer to produce an optimal image.

Distal: Remote, farther from any point of reference.

Dorsal: Pertaining to the back.

Epicondyle: A projection or boss upon a bone, above its condyle.

Extension: The movement by which the two ends of any jointed part are drawn away from each other.

External rotation: Rotation about the longitudinal axis of the humerus laterally.

Extra-osseous: Situated or occurring outside bone.

Femur: Long bone of the thigh.

Fibula: Long bone on the lateral side of the lower leg.

Fiducial marks: Points on the fiducial plane used for determining the relation between the film and the lab.[15]

---

[10] Martin, 2007

[11] Selvik, G. (1989) Roentgen stereophotogrammetry. A method for the study of the kinematics of the skeletal system. *Acta Orthop. Scand. Suppl.* 232, 1-51.

[12] Martin, 2007

[13] Martin, 2007

[14] Martin, 2007

Flexion: Elevation in the sagittal plane of the body.

Fluoroscope: An instrument for visual observation of the form and motion of the deep structures of the body by means of x-ray shadows projected on a fluorescent screen.

Fluoroscopy: Examination by means of the fluoroscope.

Fossa: In anatomy, a hollow or depressed area. (*pl.* fossae)

Frontal plane: A longitudinal plane that divides the body into front and back sections.

Frozen shoulder: Also referred to as adhesive capsulitis. A clinical condition of limited shoulder movement that appears to result from an inflammatory process, which changes the compliance of the joint capsule connective tissues.[16]

Glenohumeral: Pertaining to the glenoid and humerus.

Glenoid: Resembling a pit or socket.

Goniometer: An instrument for measuring angles.

Humerus: Long bone of upper arm.

Inferior: Situated below, or directed downward; in anatomy, used in reference to the lower surface of a structure, or to the lower of two (or more) similar structures.

Infraspinatus: Muscle situated beneath the spine of the scapula that rotates the arm laterally.

Internal rotation: Rotation about the longitudinal axis of the humerus medially.

***In-vitro*:** In an artificial environment.

***In-vivo*:** Within the living body.

Isometric: Maintaining, or pertaining to, the same measure of length.

Joint capsule: The saclike envelope enclosing the cavity of a synovial joint.

Kinematics: The study of movement, independent of forces that cause that movement.[17]

Kinetics: The study of the forces that cause movement.[18]

Lateral: Denoting a position farther from the median plane or midline of the body or a structure.

Ligament: A band of fibrous tissue connecting bones or cartilages, serving to support and strengthen joints.

---

[15] Selvik, 1989

[16] Porterfield, J.A. and DeRosa, C. (2004) Articulations of the shoulder girdle. In: *Mechanical shoulder disorders*. Saunders, St. Louis, Missouri, pp. 91-128.

[17] Winter, D.A. (2005) Biomechanics as an interdiscipline. In: *Biomechanics and motor control of human movement.* John Wiley & Sons, Hoboken, New Jersey. pp. 1-12.

[18] Winter, 2005

Magnetic resonance imaging: An imaging method in which a three-dimensional image of the structures of a body is reconstructed by a computer program from the micromagnetic properties of the corresponding tissues.

Medial: Situated toward the midline of the body or a structure.

Muscle: An organ which by contraction produces movement of an animal organism.

Nuclear magnetic resonance: The absorption and emission of high-frequency radio waves by the nuclei of certain elements when placed in a strong magnetic field. The strongest signal is obtained from hydrogen atoms, which are abundant in the water and organic molecules in the body. In clinical use for magnetic resonance imaging, the signal is highly dependent on the concentration and mobility of water molecules within each tissue.[19]

Orthopaedics: That branch of surgery dealing with the preservation and restoration of the function of the skeletal system, its articulations, and associated structures.

Palpate: Feel with the hand.

Pathology: The structural and functional manifestations of disease.

Percutaneous: Performed through the skin.

Phantom: A device for simulating the *in-vivo* effect of radiation on tissues.

Photocathode: A cathode that emits electrons when light falls upon it, as a result of the photoelectric effect.[20]

Photogrammetry: The science of measuring in photos.[21]

Posterior: Directed towards, or situated at the back; opposite of anterior.

Process: A prominence or projection, as from a bone.

Proximal: Nearest to the point of reference, as to a centre or median line or to the point of attachment or origin.

Radiography: The making of film records (radiographs) of internal structures of the body by passing x-rays or gamma rays through the body to act on specially sensitized film.

Radio-opaque: Obstructing the passage of radiant energy, such as x-rays, the representative areas appearing light or white on the exposed film.

Radiostereometric Analysis: A technique to obtain accurate three-dimensional measurements from radiographs.[22] Synonyms: radiostereometry, roentgen stereophotogrammetric analysis.

Radiostereometry: See Radiostereometric Analysis.

---

[19] Martin, 2007

[20] Daintith, 2009

[21] Linder, W. (2009) Introduction. In: *Digital Photogrammetry: A Practical Course.* Springer Berlin Heidelberg, Berlin, Heidelberg, pp. 1-17.

[22] Karrholm, J. (1989) Roentgen stereophotogrammetry. Review of orthopedic applications. *Acta Orthop. Scand.* 60[4], 491-503.

Radius: Long bone on the lateral side of the forearm.

Roentgenography: Radiography.

Roentgenstereophotogrammetry: See Radiostereometric Analysis.

Rotator cuff: Group of muscle surrounding the glenohumeral joint, consisting of the supraspinatus, subscapularis, infraspinatus and teres minor muscles.

RSA: See Radiostereometric Analysis.

Sagittal plane: A longitudinal plane that divides the body into left and right segments.

Scapula: Wide, thin, triangular bone (shoulder blade) opposite second to seventh ribs in upper part of back.

Scapulohumeral: Pertaining to the scapula and humerus.

Scapulothoracic: Pertaining to the scapula and thorax.

Spherical aberration: A defect in the image formed by a lens or curved mirror where the rays from the object come to a focus in slightly different positions as a result of the curvature of the lens or mirror.[23]

Sternoclavicular: Pertaining to the sternum and the clavicle.

Sternum: Elongated flat bone, forming anterior wall of chest.

Stereoscope: An instrument for producing the appearance of solidity and relief by combining the images of two similar pictures of an object.

Stochastic process: Any process in which there is a random element.[24]

Subacromial: Below the acromion.

Subcutaneous: Beneath the skin.

Subscapularis: Muscle which rotates the arm medially.

Superior: Situated above, or directed upward.

Supine: Lying with the face upward, or on the dorsal surface.

Supraspinatus: Muscle which abducts the arm.

Synovial joint: An articulation permitting more or less free motion, the union of the bony elements being surrounded by an articular capsule enclosing a cavity lined by synovial membrane.

Technical marker: A marker positioned in a location which has no anatomical relevance.[25]

Tendon: A fibrous cord of connective tissue continuous with the fibres of a muscle and attaching the muscle to bone or cartilage.

---

[23] Daintith, 2009
[24] Daintith, 2009
[25] Cappozzo *et al.*, 1996

Third body wear: Wear of a joint surface by hard particles drawn into the contact area.[26]

Thorax: The chest.

Transverse: Extending from side to side; at right angles to the long axis.

Transverse plane: Horizontal plane passing through the body at right angles to the frontal and sagittal planes, dividing the body into superior and inferior segments.

Tuberosity: An elevation or protuberance.

Ulna: Long bone on the medial side of the forearm.

[26] Walker, P.S. (2005) Biomechanics of total knee replacement designs. In: Mow, V.C. and Huiskes, R. (Eds.), *Basic orthopaedic biomechanics and mechano-biology.* Lippincott Williams & Wilkins, Philadelphia. pp. 657-702.

APPENDIX B – MIMICS DIGITIZATION INFORMATION

This appendix describes how to open the files generated by a CT scan in MIMICS, create models of the bones and digitize the locations of any implanted beads and bony landmarks.

B.1 IMPORTING THE SCAN

1. Open MIMICS. You will need to use the Mimics MedCAD module, so when asked if you want to use it select "Yes".
2. Select File → Import Images... and highlight the drive where the files from the scan are saved (Figure B.1).
3. Select the scan you wish to import and then press "Next >>".
4. You will be asked to "check the studies to convert". Delete the check marks from the studies you do not wish to use. Press "Convert".
5. Once the selected study has converted there will be a green check-mark beside it. Press "Open".
6. The "Change of orientation" window (Figure B.2) will then pop up and you will be asked to specify the orientation of the objects in your scan. The Xs indicate unspecified directions. Any of the directions may be changed, but at the very least the Xs must be changed to the appropriate choice of Anterior, Posterior, Top, Bottom, Left or Right. If you are unsure of the orientation, you can scroll through the images in any of the panes using the scroll wheel on your mouse. The images are slices through orthogonal planes of the objects. The orientation that you choose will depend upon how the objects were aligned within the CT scanner.
7. When you are satisfied with the orientation and all the Xs are gone (Figure B.3) select

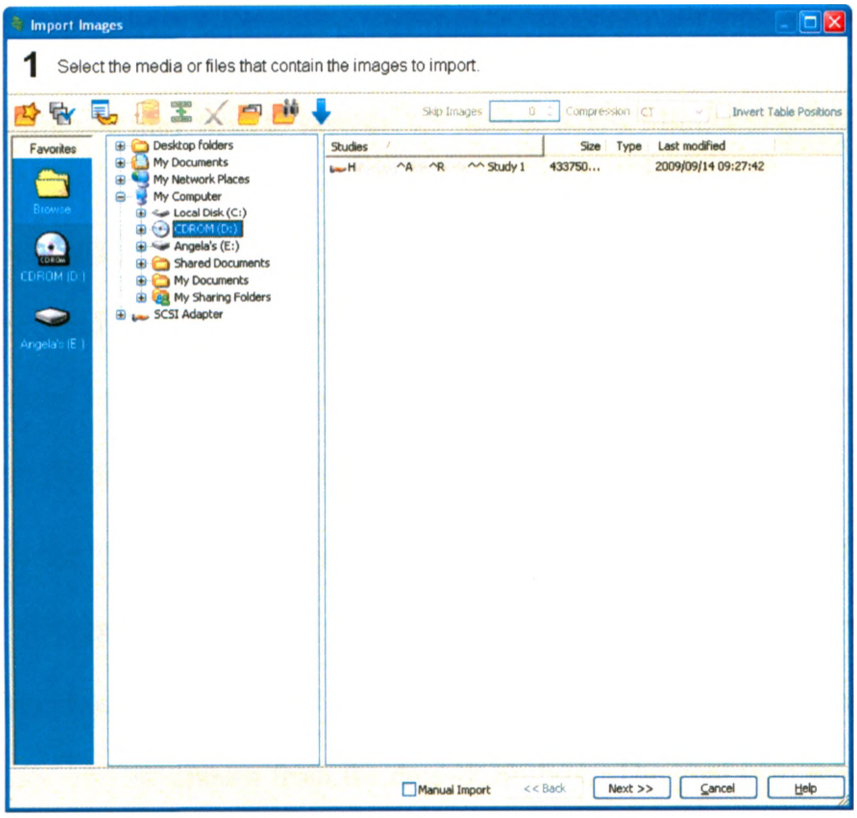

Figure B.1 Import window in MIMCS

Figure B.2 Orientation window in MIMCS

"OK".

8. At this point you may wish to save the CT scan as a new Mimics project file (.mcs).

B.2 Creating Models of the Bones

1. To create solid models of the bones a mask needs to be created of the bony areas. This is done by a process known as thresholding, which separates materials based upon their densities. To create a new mask:
   a. Select the "New" icon from under the Masks tab at the top right of the screen.
   b. The thresholding window (Figure B.4) will pop up. The upper and lower thresholding limits may be altered by moving the sliding bars, and predefined settings may be chosen from the drop-down box. The goal is to select upper and lower limits so that only bone is coloured. Soft tissue and the table below should not be coloured. Some post-thresholding editing may be required. When you are satisfied with your selection, press "Apply". The newly created mask will be shown in colour (Figure B.5).
   c. If the bones are not the only areas that were selected, the mask may be edited using the "Region Growing" or "Multiple Slice Edit" tools. These tools may be found on the toolbar at the top of the screen or in the drop-down menu accessed by the arrow at the bottom of the Masks tab. For example if the original mask looks like the one in Figure B.5 and the region growing tool is used, by clicking on the segments of bone in the top right viewing pane, a second mask, shown in Figure B.6 is created that much more closely matches just the bones.

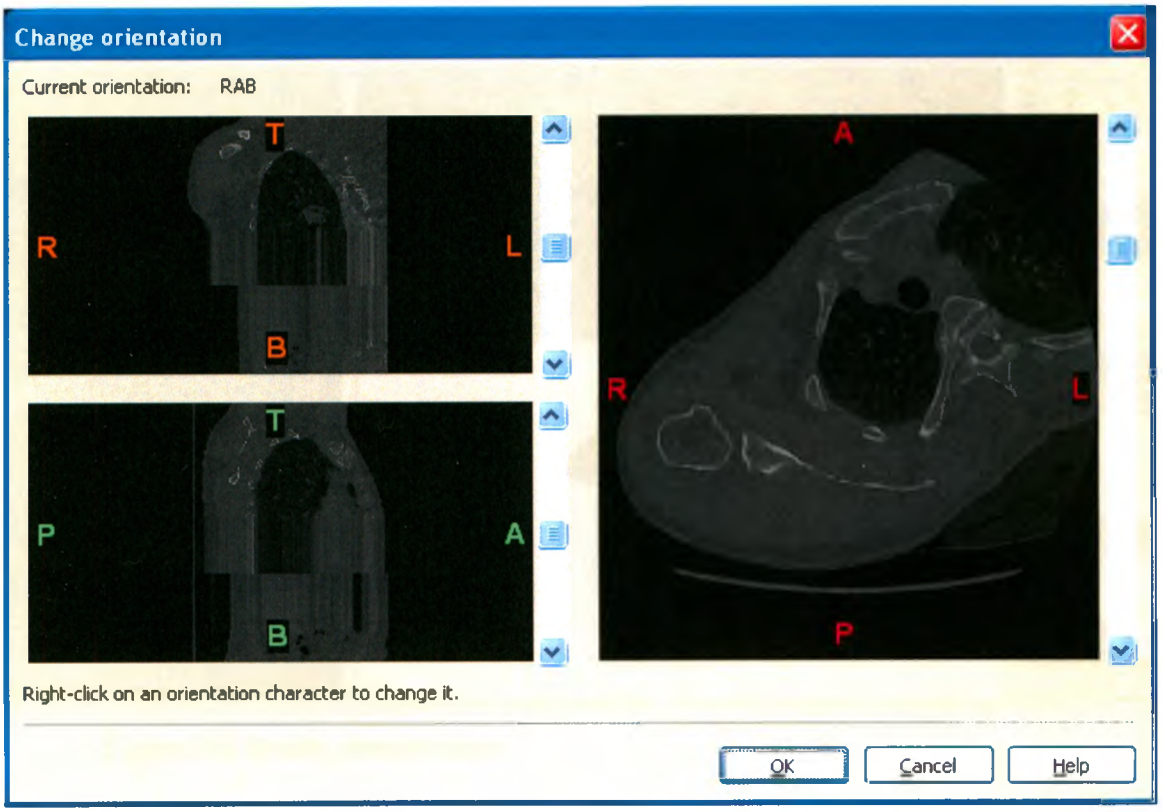

Figure B.3 Orientation complete

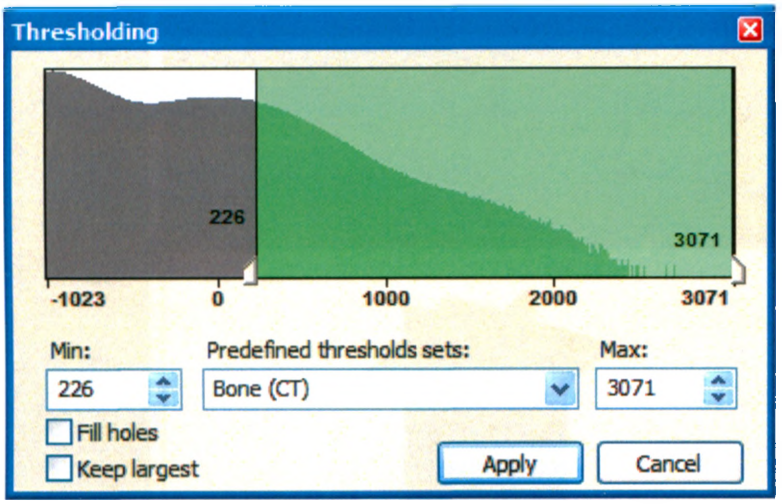

Figure B.4 Thresholding window in MIMICS

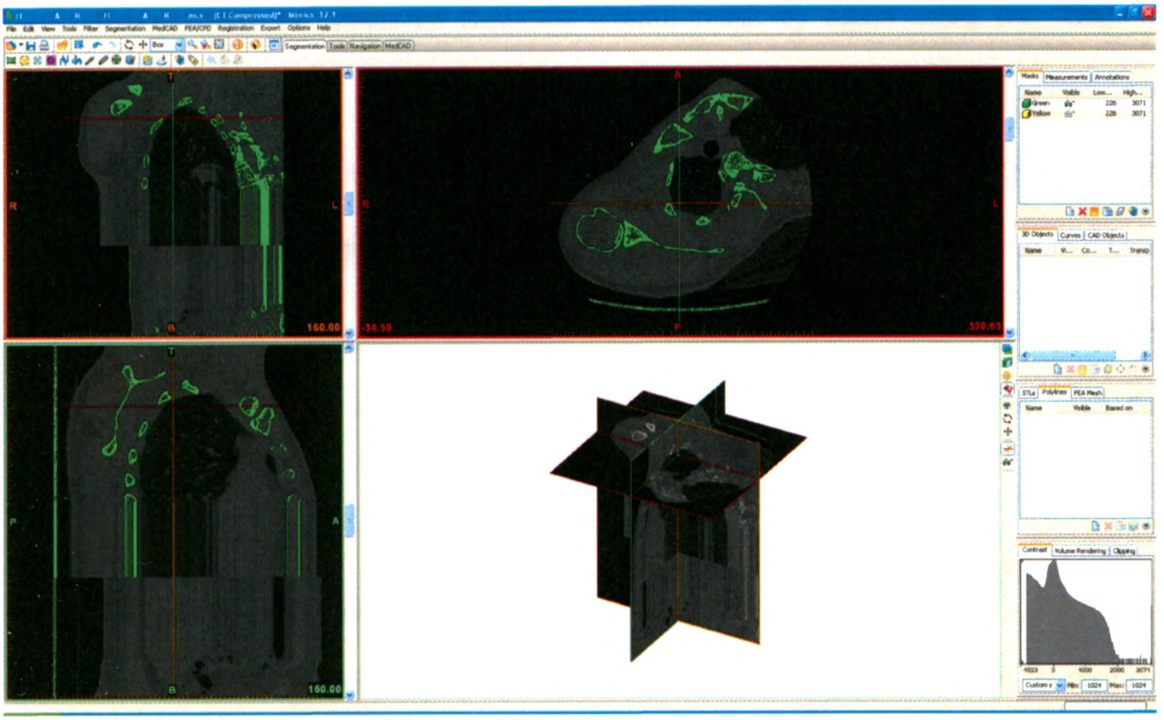

Figure B.5 Newly created mask

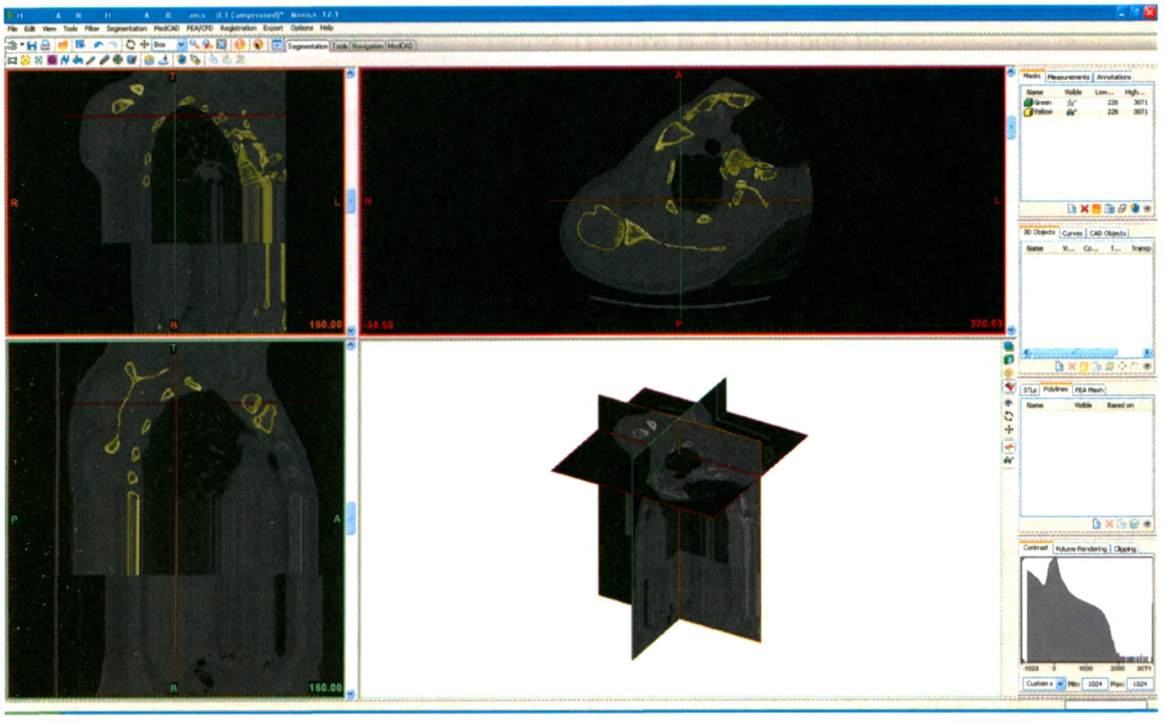

Figure B.6 Mask improved by "Region Growing"

2. Each bone may be separated from the overall mask by again using the "Region Growing" tool.
3. From the masks, 3D models may be created of one or more of the bones using the "Calculate 3D" tool . These will appear in the 3D view (Figure B.7).
4. If the models are very noisy, the masks may be altered further using "Multiple Slice Edit", "Boolean Operations", and "Cavity Fill". The 3D models may then be recreated.

B.3 Locating Beads

1. To determine the locations of any implanted beads a new mask needs to be created using thresholding.
   a. Again, select the "New" icon from under the Masks tab at the top right of the screen and the thresholding window (Figure B.4) will pop up.
   b. Make the minimum and maximum values for thresholding 3071 and press "Apply".
   c. All beads and any hardware (screws, nails, plates, implants) that was implanted during surgery will be selected.
2. The outline of the beads needs to be created. This is done using the "Calculate Polylines" tool .
   a. Pick the mask upon which the polylines should be based and click "OK".
   b. The polylines will appear in the 3D view and in the axial view (Figure B.8).
3. The polylines of each bead much then be separated from the group. This is done using the "Polyline Growing" tool , located under the Polylines tab.

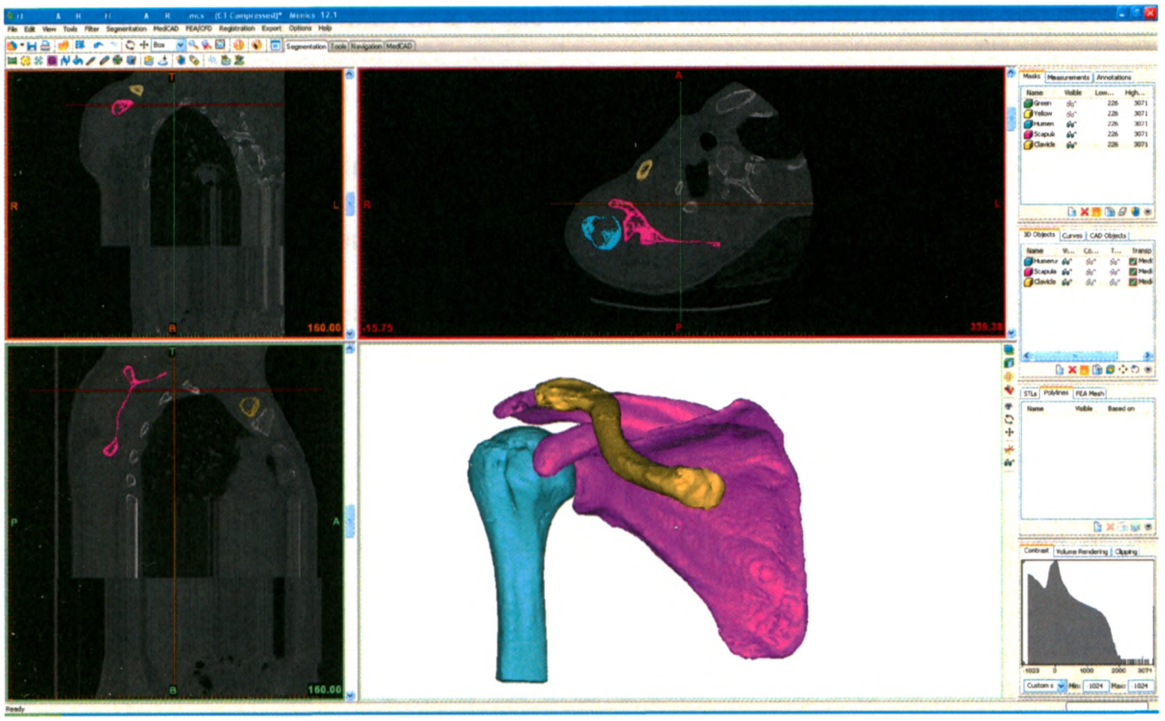

Figure B.7 3D models of the scapula, proximal humerus and clavicle

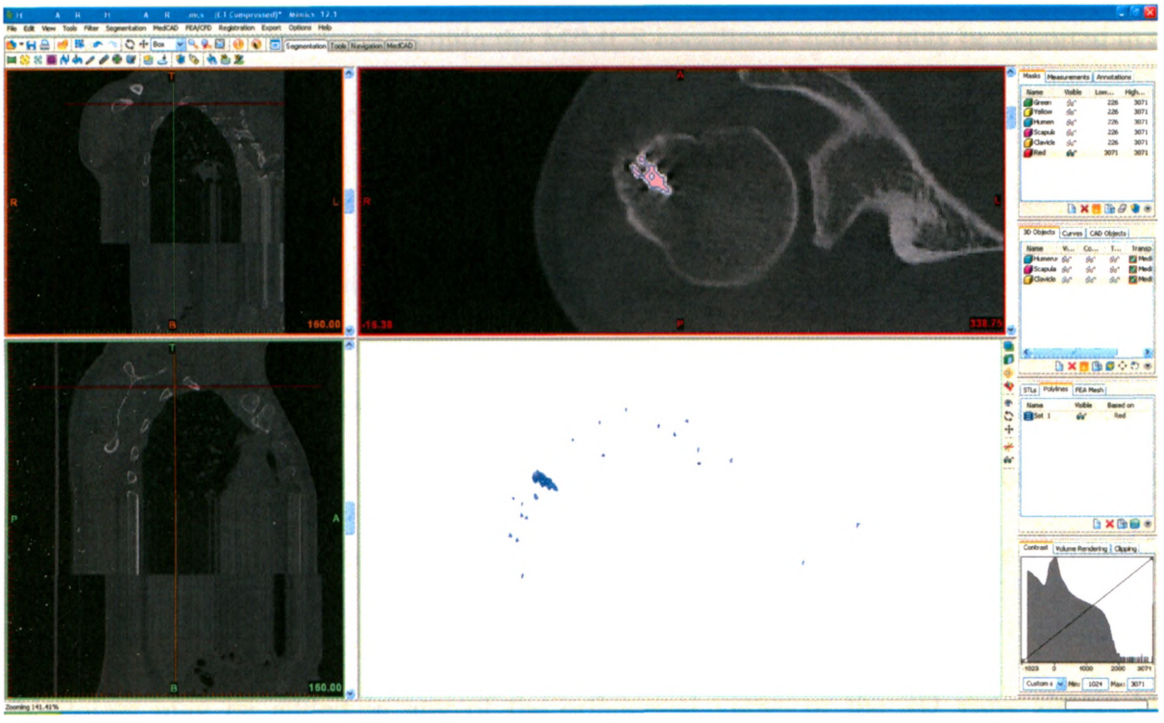

Figure B.8 Polylines of beads and hardware implanted during surgery

a. To select the polylines of a single bead and move them to their own set, click on one of the contours in the axial slices.

b. Continue transferring polylines from "Set 1" to "New Set" until the contours of all the beads are contained in their own sets.

c. Delete the contours of any hardware and any bead that is obviously not anchored in bone.

4. Fit a sphere to the polylines of each bead using the "Fit Sphere" command, which is located in the drop-down menu accessed by the arrow at the bottom of the Polylines tab.

5. The spheres will be listed under the CAD Objects tab and may be re-named there as required. Viewing the models of the bones may help identify where each bead is located (Figure B.9).

6. The locations of the beads within the MIMCS coordinate system may be exported in a single text file using the "Export txt..." command located in the drop-down menu accessed by the arrow at the bottom of the CAD Objects tab. The locations of individual beads may also be viewed using "Properties" button .

B.4 Digitizing Points

1. The locations of bony landmarks or other points of interest are selected using the "Point" command, which may be found in the MedCAD menu. Select Point → Draw.

2. Points may be added in any of the orthogonal views or the 3D view simply by clicking the desired location.

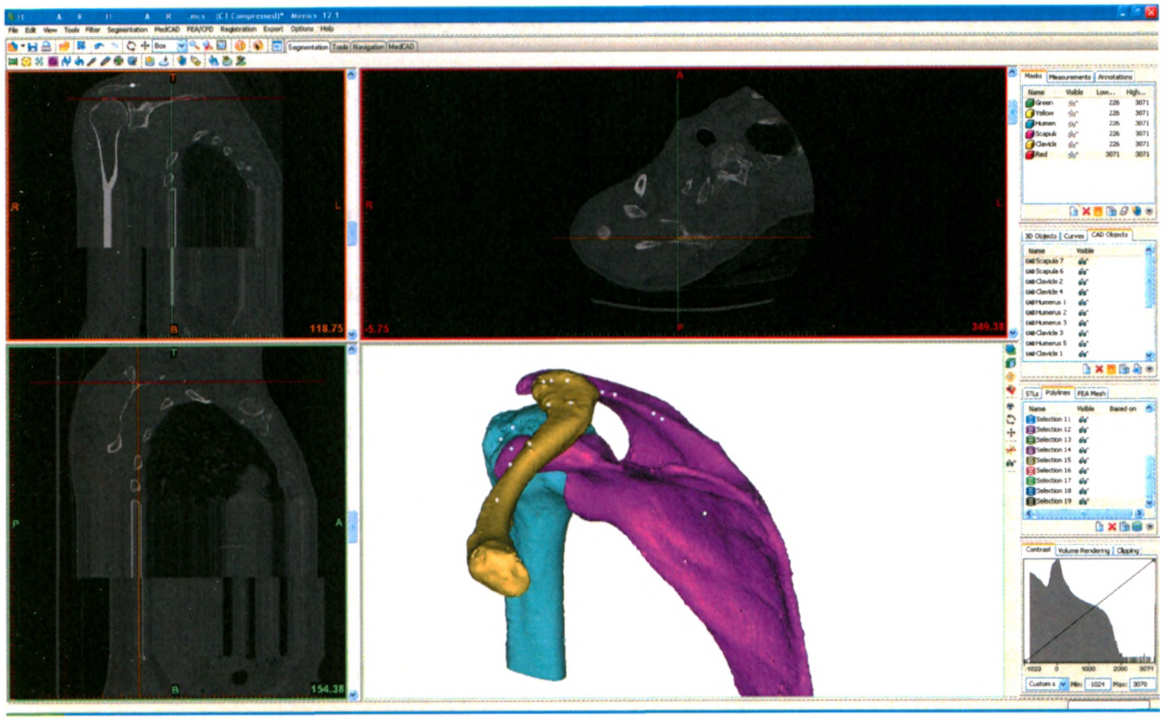

Figure B.9 Beads in the scapula, proximal humerus and clavicle

3. The new point will appear in the CAD Objects tab where it may be renamed as appropriate.
4. The locations of points may be adjusted in the orthogonal views or the 3D view by clicking and dragging to a new location. If the location may be changed within a particular view, a small white circle will appear next to the cursor when it is floated over the point.
5. The coordinates of points may be exported in the same way as the coordinates of the beads (see Section B.3, Step 6).

B.5 Determining the Centre of the Humeral Head

1. To determine the centre of the humeral head a sphere fit of the articular surface is used. To accomplish this, a new mask is again created.
   a. Any minimum and maximum thresholding values may be selected.
   b. The contents of the newly created mask are then erased using the "Clear Mask" tool .
   c. New contents for the mask are manually added using the "Multiple Slice Edit" tool.
   d. Within each slice that contains the articular surface of the humeral head, stamp a circle, using the circle tool from the drop-down box on the left, such that the radius and position of the circle match that of the articular surface (Figure B.10).
2. Create polylines from the mask using the "Calculate Polylines" tool as was described in Section B.3, Step 2.
3. Fit a sphere to the polylines of the humeral head using the "Fit Sphere" command,

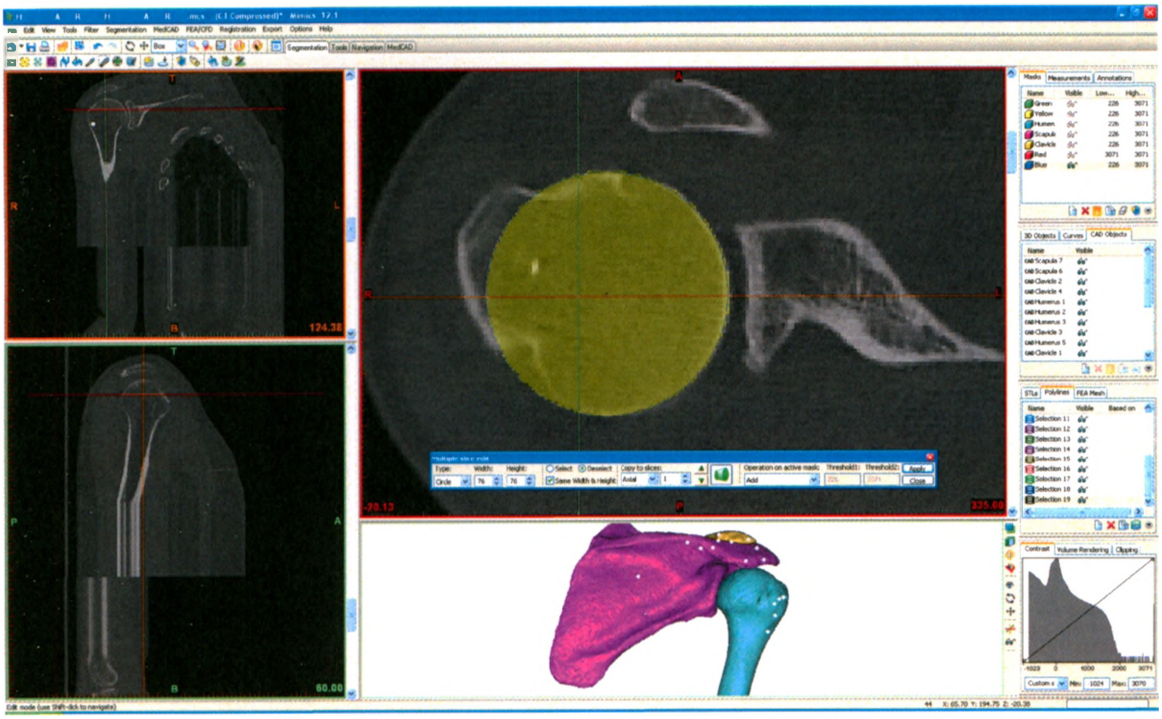

Figure B.10 Creating a custom mask for the humeral head

which is located in the drop-down menu accessed by the arrow at the bottom of the Polylines tab. The sphere will be listed under the CAD Objects tab.

4. If the mask was created carefully a good match between the humeral head articular surface and the sphere should be obtained (Figure B.11).
5. The coordinates of humeral head may be exported in the same way as the coordinates of any beads (see Section B.3, Step 6).

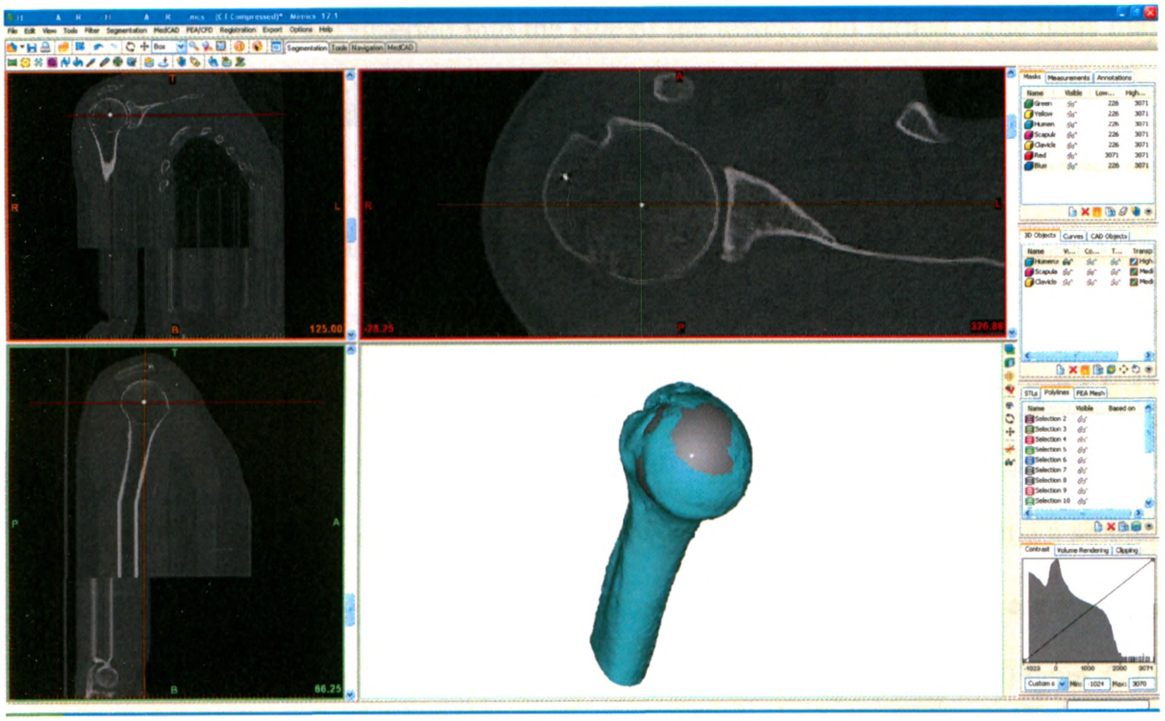

Figure B.11 Sphere fit of the humeral head articular surface.

APPENDIX C – BRIEF USER'S MANUAL FOR THE FLUOROSCOPES

This appendix briefly outlines the components of the fluoroscopy units and summarizes how to operate them at a basic level.

C.1 SWITCHING ON THE FLUOROSCOPES

There are two steps to starting the fluoroscopes. First they must be unlocked using the keys, which are inserted into the side of the towers and turned. The units may be switched on using the  buttons on the control panel of the tower.

C.2 MOVING THE FLUOROSCOPES

The brakes must be released before the fluoroscopes can be moved. To release the brakes, step on the lever above one of the two wheels on either side (Figure C.1). When the levers are horizontal the brakes are off. When the levers are tilted either forward or backward the brakes are on. The fluoroscopes may be moved along a straight line, as dictated by the alignment of the wheels, or pivoted, when the wheels are centrally aligned. The wheels of the fluoroscopes can be turned using the handle (Figure C.1). Pull the handle up to turn the wheels and push it down in the centre position to pivot the fluoroscopes.

The C-arms may be raised and lowered using the arrow keys at either side of the control panel on the fluoroscopy units (Figure C.2). Should the tower not respond to the arrow keys, ensure that the "Stop" button has not been activated. The "Stop" button may be found on front of the base of the unit, at about knee-level. It may be released by turning it, allowing it to pop out. Each C-arm may be further manipulated using three

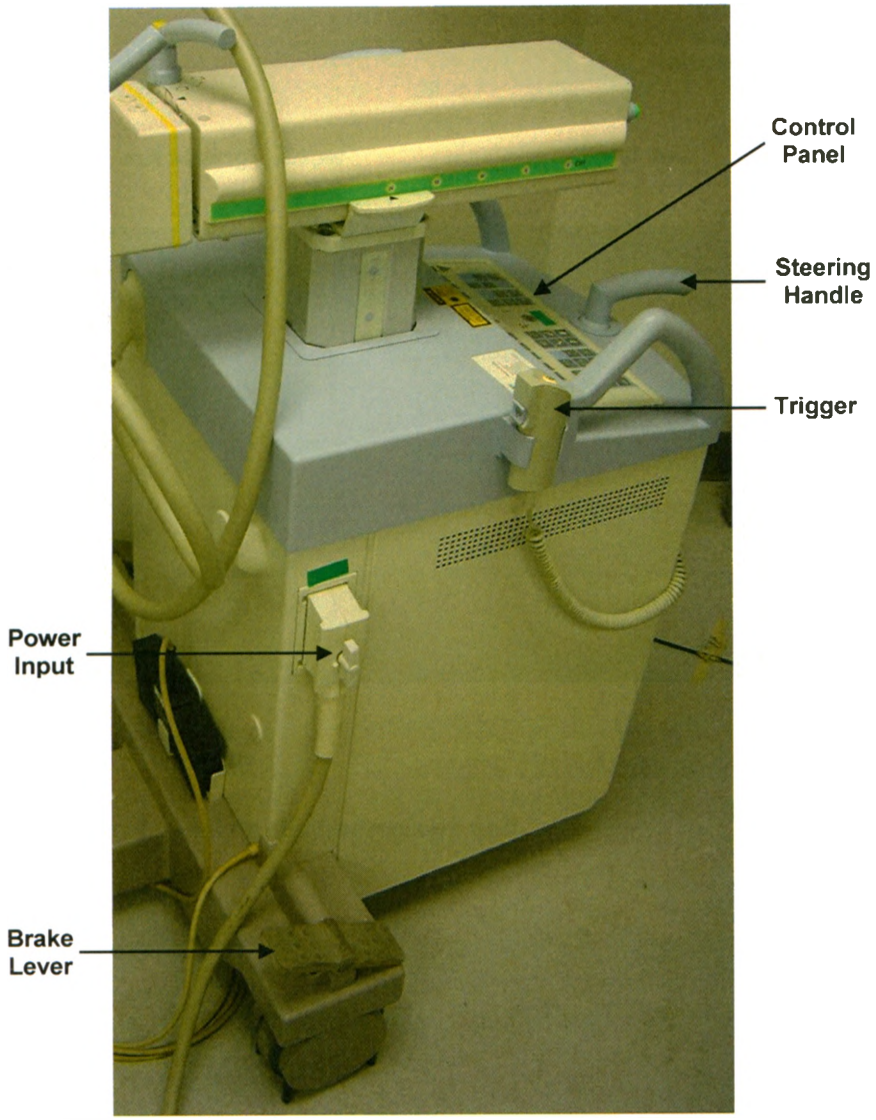

Figure C.1 Base of the fluoroscopy unit

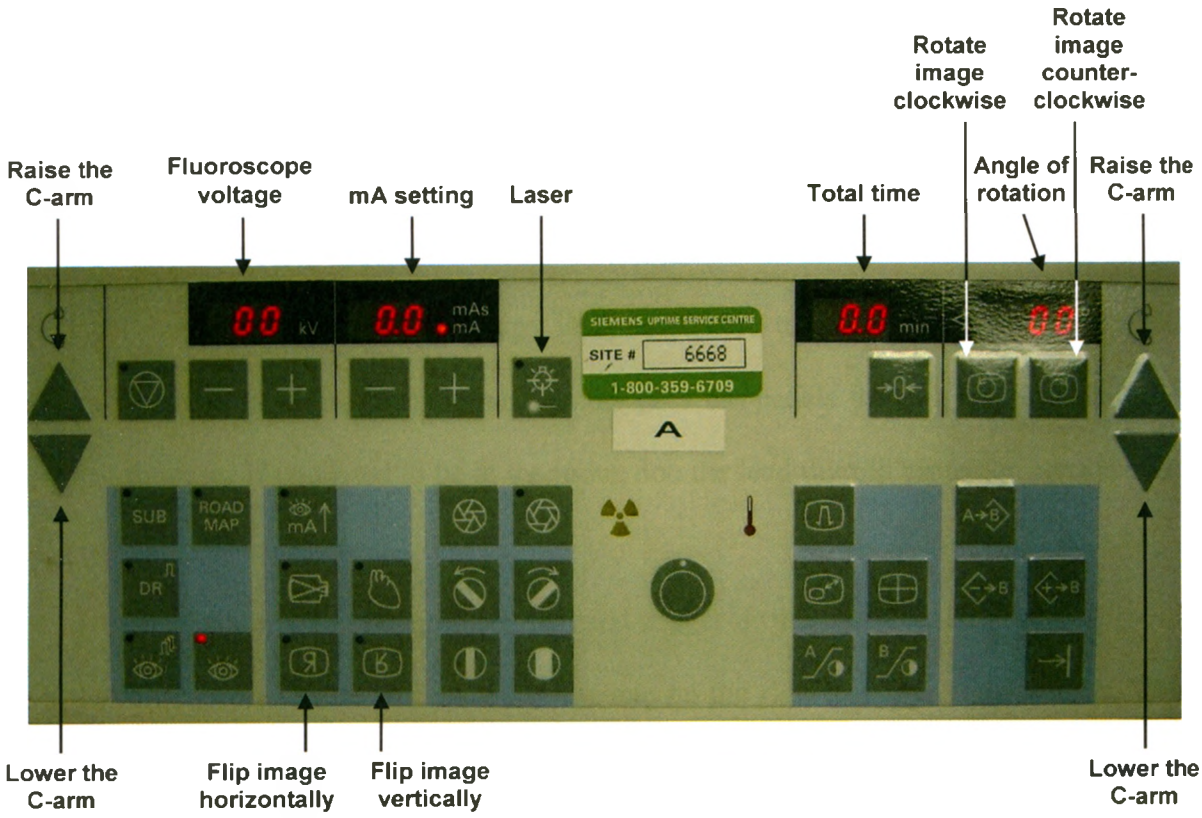

Figure C.2. Control panel on the fluoroscopy unit

rotational axes (colour-coded blue, yellow, and orange) and one translational axis (colour-coded green). To move about or along any axis, turn the colour-coded handle to the unlocked position. Ensure that all axes are locked prior to beginning any data collection.

To aid in positioning the C-arms there is a laser that can be used. It is turned on via the control panel on the fluoroscopy unit (Figure C.2).

C.3 Capturing Images

Prior to taking any fluoroscopy images, be sure to follow the most appropriate action to avoid exposure to radiation. Either pass the pedals through the door into the control room, or if you need to be in the room, don the lead thyroid protector, jersey, skirt and protective eyewear.

Images are taken using either the hand trigger or the foot pedals. The foot pedal on the left captures static images while the one on the right captures fluoroscopy. The three orange lights on the tower (Figure C.3) light up when any of the triggers are pressed. The C-arms are equipped with automatic brightness control to maintain the brightness of the image at a constant level. To accomplish this, the x-ray exposure rate is automatically regulated and the kVp and mA levels are automatically changed. The mA and kVp curves that are followed are shown in the Siemens SIREMOBIL Compact-L mobile C-arms manual. In most cases this will be the appropriate setting to use; however, in some cases in which there are dramatic differences in the contrast of the images it may be more appropriate to turn this off and manually adjust the settings to emphasize the objects of interest. Please see the Siemens SIREMOBIL Compact-L mobile C-arms manual for more detailed instructions if this is the case.

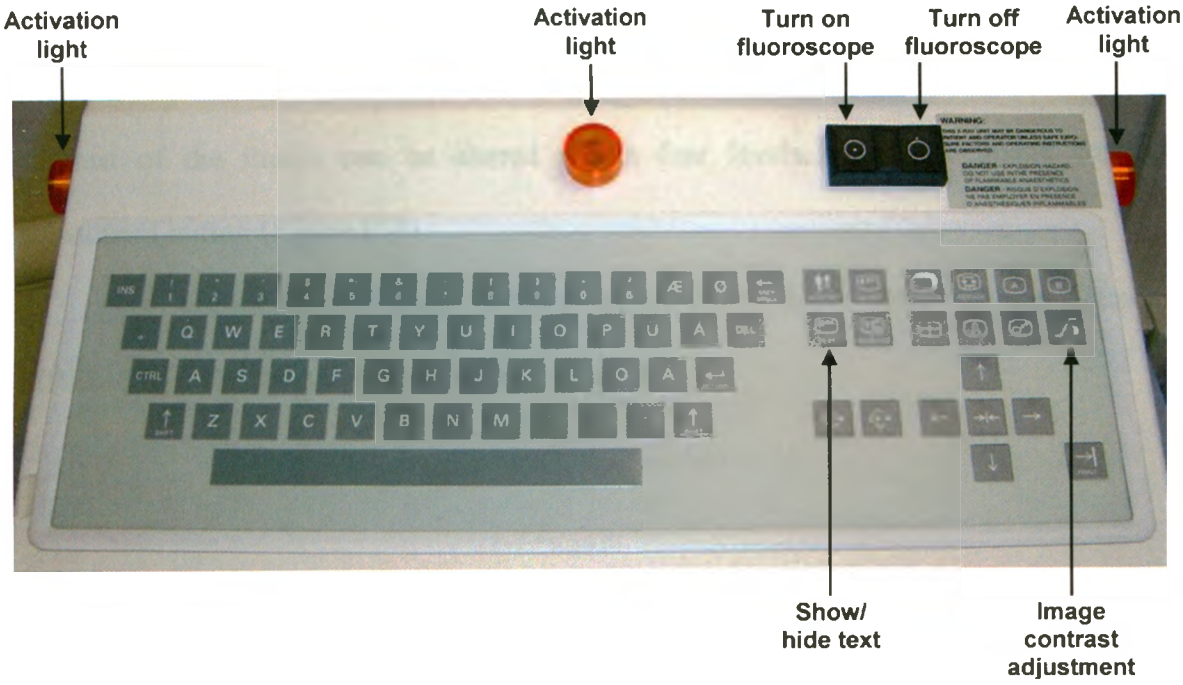

Figure C.3 Control panel on the tower

C.4 MANIPULATING THE IMAGE

There are several lines of text that are always present at the bottom left corner of the image when the fluoroscopes are first turned on. This text will cover part of the image and so it is desirable to turn it off using "show/hide text" button on the control panel on the tower (Figure C.3).

The image orientation may be altered by flipping it either horizontally or vertically using the "flip image horizontally" and "flip image vertically" buttons on the control panel of the fluoroscopy unit. The image can also be rotated (Figure C.2). The contrast of the image can be altered within four levels, using the image contrast adjustment button (Figure C.3).

For additional or more detailed instructions please refer to the Siemens SIREMOBIL Compact-L mobile C-arms manual.

APPENDIX D – CODE

This appendix contains the code, described in Chapters 2 and 6, that was written to select points from the images, correct for image distortion, perform RSA, synchronize the optical motion analysis system data with data from RSA, and calculate the glenohumeral kinematic angles.

D.1 PICK_POINTS.M

```
% Program:       pick_points.m
% Description:   Allows the user to select points from an image of
%                interest.  Returns the coordinates of the centres of
%                the chosen marks as determined by the centre of mass.
% Written by:    Angela Kedgley
% Date written:  May 9, 2007
% Last modified: October 5, 2009
%-------------------------------------------------------------------------

image_type = 'i';
% Obtain the location of the data files from the user
data_folder= input('Enter the name of the folder with the data: ','s');

while ~(strcmp(image_type,'e') || strcmp(image_type,'E'))
   drawnow;
   display('Enter the type of image,');
   image_type = input('Calibration frame (c or C), Distortion Device'…
         '(d or D), EvaRT Synching (s or S), EvaRT Frame (f or F),'…
         'Other (o or O) or Exit (e or E): ', 's');
   if (strcmp(image_type,'e') || strcmp(image_type,'E'))
      break
   else
      image_file = input('Enter the name of the image file: ','s');
      new_file = strcat(image_file, '.tif');
      im = imread(fullfile('drive\directory\folder\', data_folder,…
         new_file));
      im_background = imread(fullfile('drive\directory\folder\',…
         data_folder, new_file));
      im = rgb2gray(im);
      im_background = rgb2gray(im_background);
      im = reflection(im);
      im_background = reflection(im_background);
   end

   % Any object file
   if (strcmp(image_type,'o') || strcmp(image_type,'O'))
      zooming = 'z';
      filter_corners = [0 0 0 0 0];
      colormap(gray(256)); image(im); axis image
```

```
while ~(strcmp(zooming, 'y') || strcmp(zooming, 'n'))
   zooming = input('Do you wish to zoom in? (y/n): ', 's');
      if (strcmp(zooming, 'n'))
         close all;                % Close all figure windows
         im = imcrop(im,[90 15 520 510]);
         im_background = imcrop(im_background,[90 15 520 510]);
         zoom_width = 520;
         zoom_height = 510;
      elseif (strcmp(zooming, 'y'))
         display('Specify the area to be zoomed in on with the…
             cursor by single-clicking the left mouse button.');
         display('Select the top left corner and then the bottom…
             right corner.');
         for z_counter = 1:2
            % Pick the points using ginput
            z_points(z_counter,:) = ginput(1);
            z_points(z_counter,:) = round(z_points(z_counter,:));
         end
         close all;                    % Close all figure windows
         zoom_width = z_points(2,1) - z_points(1,1);
         zoom_height = z_points(2,2) - z_points(1,2);
         im = imcrop(im,[z_points(1,1) z_points(1,2) zoom_width…
            zoom_height]);
         im_background = imcrop(im_background,[z_points(1,1)…
            z_points(1,2) zoom_width zoom_height]);
      else
         display('Please enter one of the available options.')
      end
end

display('Select points on the image with the cursor by…
   single-clicking the left mouse button.');
display('Press the middle mouse button to indicate the last…
   point or to exit.');
colormap(gray(256)); image(im); axis image

% Allow the user to select the points
counter = 1;
while 1
   % User numbers the points while picking them
   names(counter) = counter;
   % Pick the points using ginput
   points(counter,:) = ginput(1);
    % Break out of the loop if middle mouse button is pushed
    if strcmp(get(gcf,'SelectionType'),'extend')
       break
    end
    counter = counter + 1;
end

for n = 1:counter
   % Create subsets of the image surrounding each point
   xmax = round(points(n,1)) + 5;
   xmin = round(points(n,1)) - 5;
   ymax = round(points(n,2)) + 5;
   ymin = round(points(n,2)) - 5;
```

```
    filter_corners(n, :) = [names(n) xmax xmin ymax ymin];
    if ((xmax > zoom_width) || (xmin < 0) || (ymax > zoom_height)…
       || (ymin < 0))
       n
    end
end

for n = 1:counter
    % Find the darkest pixel
    subim = im(filter_corners(n,5): filter_corners(n,4),…
       filter_corners(n,3): filter_corners(n,2), :);
    pix_comp = 300;
    for col = 1:11
       for row = 1:11
          pixRGB = impixel(subim,col,row);
          if pixRGB(1) < pix_comp
             pix_comp = pixRGB(1);
             coords = [col row];
          end
       end
    end
    points(n,:) = [(round(points(n,1)) + coords(1) - 6)…
       (round(points(n,2)) + coords(2) - 6)];
end

for n = 1:counter
    % Create subsets of the image surrounding each new centre
    xmax = points(n,1) + 5;
    xmin = points(n,1) - 5;
    ymax = points(n,2) + 5;
    ymin = points(n,2) - 5;
    filter_corners(n, :) = [names(n) xmax xmin ymax ymin];
    if ((xmax > zoom_width) || (xmin < 0) || (ymax > zoom_height)…
       || (ymin < 0))
       n
    end
end

for n = 1:counter
    columns = [filter_corners(n, 3); filter_corners(n, 3);…
       filter_corners(n, 2); filter_corners(n, 2)];
    rows = [filter_corners(n, 4); filter_corners(n, 5);…
       filter_corners(n, 5); filter_corners(n, 4)];
    im_background = roifill(im_background, columns, rows);
end

% Invert the intensity scales to make white = 0
im = 255 - im;
im_background = 255 - im_background;
im_sub = imsubtract(im, im_background);
colormap(gray(256)); image(im); axis image

% Calculate the location of the centre of each point
for n = 1:counter
    pix_count_sub = 0;      % Count the number of included pixels.
    pix_darkest_sub(n,:) =impixel(im_sub,points(n,1),points(n,2));
```

```
        % Determine the shade of each pixel within each subset
        subim_sub = im_sub(filter_corners(n,5): filter_corners(n,4),…
           filter_corners(n,3): filter_corners(n,2), :);
        for col = 1:11
           for row = 1:11
              pixRGB_sub = impixel(subim_sub,col,row);
              intensity_map_sub(row,col) = pixRGB_sub(1);
           end
        end

        % Find the centre of colour from the weighted pixel shades
        gray_sum_sub = 0;
        x_sum_sub = 0;
        y_sum_sub = 0;

        for col = 1:11
           for row = 1:11
              gray_sum_sub =gray_sum_sub + intensity_map_sub(row,col);
              x_sum_sub = x_sum_sub + intensity_map_sub(row,col)*col;
              y_sum_sub = y_sum_sub + intensity_map_sub(row,col)*row;
              pix_count_sub = pix_count_sub + 1;
           end
        end

        x_bar_sub = x_sum_sub / gray_sum_sub;
        y_bar_sub = y_sum_sub / gray_sum_sub;

        % Calculate the location of the point within the whole image
        global_x_bar_sub = points(n,1) + x_bar_sub - 6;
        global_y_bar_sub = points(n,2) + y_bar_sub - 6;
        if (strcmp(zooming, 'n'))
           centres_sub(n,:) = [names(n) global_x_bar_sub + 89…
              global_y_bar_sub + 14 pix_count_sub];
        elseif (strcmp(zooming, 'y'))
           centres_sub(n,:) = [names(n) global_x_bar_sub +…
           z_points(1,1) global_y_bar_sub+z_points(1,2)…
           pix_count_sub];
        end
     end

  % Calibration frame file
  elseif (strcmp(image_type,'c') || strcmp(image_type,'C'))
     F_filter_corners = [0 0 0 0 0];
     C_filter_corners = [0 0 0 0 0];
     im = imcrop(im, [90 15 520 510]);
     im_background = imcrop(im_background, [90 15 520 510]);

     display('Select points on the image with the cursor by…
        single-clicking the left mouse button.');
     display('If the point is not visible single-click the right…
        mouse button.');
     display('Press the middle mouse button to indicate the last…
        point or to exit.');
     colormap(gray(256)); image(im); axis image

     for F_counter = 1:45
```

```
   display(['Select fiducial point number', num2str(F_counter)]);
   % Pick the points using ginput
   F_points(F_counter,:) = ginput(1
   if strcmp(get(gcf,'SelectionType'),'normal')
      % Create subsets of the image surrounding each point
      xmax = round(F_points(F_counter,1)) + 5;
      xmin = round(F_points(F_counter,1)) - 5;
      ymax = round(F_points(F_counter,2)) + 5;
      ymin = round(F_points(F_counter,2)) - 5;
      F_filter_corners(F_counter, :) = [F_counter xmax xmin ymax…
         ymin];

      if ((xmax>520) || (xmin<0) || (ymax>510) || (ymin<0))
         F_counter
      end
   elseif strcmp(get(gcf,'SelectionType'),'alt')
      F_filter_corners(F_counter, :) = [F_counter 5555 0 0 0];
   % Break out of the loop if the middle mouse button is pushed
   elseif strcmp(get(gcf,'SelectionType'),'extend')
      break
   end
end

for C_counter = 1:45
   display(['Select control point number ', num2str(C_counter)]);
   % Pick the points using ginput
   C_points(C_counter,:) = ginput(1);
   if strcmp(get(gcf,'SelectionType'),'normal')
      % Create subsets of the image surrounding each point
      xmax = round(C_points(C_counter,1)) + 5;
      xmin = round(C_points(C_counter,1)) - 5;
      ymax = round(C_points(C_counter,2)) + 5;
      ymin = round(C_points(C_counter,2)) - 5;
      C_filter_corners(C_counter, :) = [C_counter xmax xmin ymax…
         ymin];
      if ((xmax>520) || (xmin<0) || (ymax>510) || (ymin<0))
         C_counter
      end
   elseif strcmp(get(gcf,'SelectionType'),'alt')
      C_filter_corners(C_counter,:) = [C_counter 5555 0 0 0];
   % Break out of the loop if the middle mouse button is pushed
   elseif strcmp(get(gcf,'SelectionType'),'extend')
      break
   end
end

for F_counter = 1:45
   % Find the darkest pixel
   if F_filter_corners(F_counter, 2) ~= 5555
      subim = im(F_filter_corners(F_counter, 5):…
         F_filter_corners(F_counter, 4), F_filter_corners…
         (F_counter, 3): F_filter_corners(F_counter, 2), :);
      pix_comp = 300;
      for col = 1:11
         for row = 1:11
            pixRGB = impixel(subim,col,row);
```

```
            if pixRGB(1) < pix_comp
               pix_comp = pixRGB(1);
               coords = [col row];
            end
         end
      end
      F_points(F_counter,:) = [(round(F_points(F_counter,1)) +…
         coords(1) - 6) (round(F_points(F_counter,2)) +…
         coords(2) - 6)];
      % Create subsets of the image surrounding each point
      xmax = F_points(F_counter,1) + 7;
      xmin = F_points(F_counter,1) - 7;
      ymax = F_points(F_counter,2) + 7;
      ymin = F_points(F_counter,2) - 7;
      F_filter_corners(F_counter, :) = [F_counter xmax xmin ymax…
         ymin];
      if ((xmax>520) || (xmin<0) || (ymax>510) || (ymin<0))
         F_counter
      end
   end
end

for C_counter = 1:45
   % Find the darkest pixel
   if C_filter_corners(C_counter, 2) ~= 5555
   subim = im(C_filter_corners(C_counter, 5):…
      C_filter_corners(C_counter, 4), C_filter_corners…
      (C_counter, 3): C_filter_corners(C_counter, 2), :);
      pix_comp = 300;
      for col = 1:11
         for row = 1:11
            pixRGB = impixel(subim,col,row);
            if pixRGB(1) < pix_comp
               pix_comp = pixRGB(1);
               coords = [col row];
            end
         end
      end
      C_points(C_counter,:) = [(round(C_points(C_counter,1)) +…
         coords(1) - 6) (round(C_points(C_counter,2)) +…
         coords(2) - 6)];
      % Create subsets of the image surrounding each point
      xmax = C_points(C_counter,1) + 7;
      xmin = C_points(C_counter,1) - 7;
      ymax = C_points(C_counter,2) + 7;
      ymin = C_points(C_counter,2) - 7;
      C_filter_corners(C_counter, :) = [C_counter xmax xmin ymax…
         ymin];
      if ((xmax>520) || (xmin<0) || (ymax>510) || (ymin<0))
         C_counter
      end
   end
end

for F_counter = 1:45
   if F_filter_corners(F_counter, 2) ~= 5555
```

```
        columns = [F_filter_corners(F_counter, 3);…
           F_filter_corners(F_counter, 3); F_filter_corners…
           (F_counter, 2); F_filter_corners(F_counter, 2)];
        rows = [F_filter_corners(F_counter, 4); F_filter_corners…
           (F_counter, 5); F_filter_corners(F_counter, 5);…
            F_filter_corners(F_counter, 4)];
        im_background = roifill(im_background, columns, rows);
    end
end

for C_counter = 1:45
    if C_filter_corners(C_counter, 2) ~= 5555
        columns = [C_filter_corners(C_counter, 3);…
           C_filter_corners(C_counter, 3); C_filter_corners…
           (C_counter, 2); C_filter_corners(C_counter, 2)];
        rows = [C_filter_corners(C_counter, 4);…
           C_filter_corners(C_counter, 5); C_filter_corners…
           (C_counter, 5); C_filter_corners(C_counter, 4)];
        im_background = roifill(im_background, columns, rows);
    end
end

% Invert the intensity scales to make white = 0
im = 255 - im;
im_background = 255 - im_background;
im_sub = imsubtract(im, im_background);
colormap(gray(256)); image(im); axis image

% Calculate the location of the centre of each point
for F_counter = 1:45
    if F_filter_corners(F_counter, 2) == 5555
        F_centres_sub(F_counter,:) = [F_counter 5555 5555 5555];
    else
        pix_count_sub = 0;
        pix_darkest_sub(F_counter,:) = impixel…
           (im_sub,F_points(F_counter,1),F_points(F_counter,2))
        subim_sub = im_sub(F_filter_corners(F_counter, 5):…
           F_filter_corners(F_counter, 4), F_filter_corners…
           (F_counter, 3): F_filter_corners(F_counter, 2), :);
        % Determine the shade of each pixel within each subset
        for col = 1:15;
            for row = 1:15;
                pixRGB_sub = impixel(subim_sub,col,row);
                intensity_map_sub(row,col) = pixRGB_sub(1);
            end
        end
        % Find the centre of colour from the weighted pixel shades
        gray_sum_sub = 0;
        x_sum_sub = 0;
        y_sum_sub = 0;
        for col = 1:15;
            for row = 1:15;
                gray_sum_sub=gray_sum_sub+intensity_map_sub(row,col);
                x_sum_sub = x_sum_sub+intensity_map_sub(row,col)*col;
                y_sum_sub = y_sum_sub+intensity_map_sub(row,col)*row;
                pix_count_sub = pix_count_sub + 1;
```

```
            end
        end
        x_bar_sub = x_sum_sub / gray_sum_sub;
        y_bar_sub = y_sum_sub / gray_sum_sub;
        % Calculate the location of the point within the whole image
        global_x_bar_sub = F_points(F_counter,1) + x_bar_sub + 81;
        global_y_bar_sub = F_points(F_counter,2) + y_bar_sub + 6;
        F_centres_sub(F_counter,:) = [F_counter global_x_bar_sub…
            global_y_bar_sub pix_count_sub];
    end
end

% Calculate the location of the centre of each point
for C_counter = 1:45
    if C_filter_corners(C_counter, 2) == 5555
        C_centres_sub(C_counter,:) = [C_counter 5555 5555 5555];
    else
        pix_count_sub = 0;
        pix_darkest_sub(C_counter,:) = impixel…
            (im_sub,C_points(C_counter,1),C_points(C_counter,2));
        subim_sub= im_sub(C_filter_corners(C_counter, 5):…
            C_filter_corners(C_counter, 4), C_filter_corners…
            (C_counter, 3): C_filter_corners(C_counter, 2), :);
        % Determine the shade of each pixel within each subset
        for col = 1:15;
            for row = 1:15;
                pixRGB_sub = impixel(subim_sub,col,row);
                intensity_map_sub(row,col) = pixRGB_sub(1);
            end
        end
        % Find the centre of colour from the weighted pixel shades
        gray_sum_sub = 0;
        x_sum_sub = 0;
        y_sum_sub = 0;
        for col = 1:15;
            for row = 1:15;
                gray_sum_sub=gray_sum_sub+intensity_map_sub(row,col);
                x_sum_sub = x_sum_sub+intensity_map_sub(row,col)*col;
                y_sum_sub = y_sum_sub+intensity_map_sub(row,col)*row;
                pix_count_sub = pix_count_sub + 1;
            end
        end
        x_bar_sub = x_sum_sub / gray_sum_sub;
        y_bar_sub = y_sum_sub / gray_sum_sub;
        % Calculate the location of the point within the whole image
        global_x_bar_sub = C_points(C_counter,1) + x_bar_sub + 81;
        global_y_bar_sub = C_points(C_counter,2) + y_bar_sub + 6;
        C_centres_sub(C_counter,:) = [C_counter global_x_bar_sub…
            global_y_bar_sub pix_count_sub];
    end
end

% Distortion frame file
elseif (strcmp(image_type,'d') || strcmp(image_type,'D'))
    % ********************************************************
    % The same process as that for the calibration points is   %
    % followed.  The subsets of the image are 11 pixels square %
```

```
    % initially and 15 pixels square for the final location.   %
    % ********************************************************

% Synching with EvaRT coordinate system
elseif (strcmp(image_type,'f') || strcmp(image_type,'F'))
    % ********************************************************
    % The same process as that for the calibration points is   %
    % followed.  The subsets of the image are 39 pixels square %
    % initially and 43 pixels square for the final location.   %
    % ********************************************************

% Synching with EvaRT marker
elseif (strcmp(image_type,'s') || strcmp(image_type,'S'))
    % ********************************************************** %
    % The same process as that for the calibration points is       %
    % followed.  The subsets of the image are 39 pixels square for %
    % the synching marker and 11 pixels square for the other beads %
    % initially and 43 pixels square for the synching markers and  %
    % 11 pixels square for the beads for the final location.       %
    % ********************************************************** %

else
    display('Please enter one of the available options.')
end

if (strcmp(image_type,'c') || strcmp(image_type,'C'))
    % Write the selected points to an Excel spreadsheet
    C_centresfilename_sub = strcat(image_file, 'C_points.xls');
    F_centresfilename_sub = strcat(image_file, 'F_points.xls');
    xlswrite(fullfile('drive\directory\folder\', data_folder,…
        C_centresfilename_sub), C_centres_sub);
    xlswrite(fullfile('drive\directory\folder\', data_folder,…
        F_centresfilename_sub), F_centres_sub);
    close all;                          % Close all figure windows
    clear centresfilename_sub C_centres_sub F_centres_sub new_file…
        im F_counter_sub C_counter_sub F_points C_points;
elseif (strcmp(image_type,'d') || strcmp(image_type,'D'))
    centresfilename_sub = strcat(image_file, '_points.xls');
    xlswrite(fullfile('drive\directory\folder\', data_folder,…
        centresfilename_sub), D_centres_sub);
    close all;
    clear centresfilename_sub D_centres_sub new_file im D_counter…
        D_points;
else
    % Write the selected points to an Excel spreadsheet
    centresfilename_sub = strcat(image_file, '_points.xls');
    xlswrite(fullfile('drive\directory\folder\', data_folder,…
        centresfilename_sub), centres_sub);
    close all;                          % Close all figure windows

    if (strcmp(image_type,'o') || strcmp(image_type,'O'))
        clear centresfilename_sub centres_sub new_file im…
            im_background counter names points new_centres im_sub…
            zooming col columns coords filter_corners global_x_bar_sub…
            global_y_bar_sub gray_sum_sub intensity_map_sub pixRGB…
            pixRGB_sub pix_comp pix_count_sub pix_darkest_sub row;
```

```
      else
         clear centresfilename_sub centres_sub new_file im…
            im_background counter names points new_centres im_sub;
      end
   end
end
clear;
```

D.2 DISTORTION_CORRECTION_POINTS.M

```
% Program:       distortion_correction_points.m
% Description:   Formats the coordinates of points digitized from the
%                distortion grid and their known locations
% Written by:    Angela Kedgley
% Date written:  January 27, 2008
% Last modified: February 5, 2008
%-------------------------------------------------------------------------

% Obtain the location of the file with the points to be corrected for
% distortion from the user
data_folder = input('Enter the name of the folder with the digitized…
      points: ','s');
data_dir = ['drive\directory\folder/' data_folder '\'];
dist_file = input('Enter the name of the file which contains the…
      distortion device points: ','s');
dist_filename = strcat(dist_file, '.xls');

% Two dimensional coordinates of the distortion device points (x,y)
dist_points = xlsread([data_dir,dist_filename],1);
dist_points = dist_points(:,2:3);

% The actual coordinates of the distortion device points
correction_data_dir = ['drive\directory\folder/'];
correction_points_file = 'Distortion correction NEW.xls';
correction_points =
xlsread([correction_data_dir,correction_points_file],1);
correction_points = correction_points(:,6:7);

% Match the collected distortion points to the actual locations
for i = 1:131
    grid_x(i,:) = [dist_points(i,1) dist_points(i,2)…
            correction_points(i,1)];
    grid_y(i,:) = [dist_points(i,1) dist_points(i,2)…
            correction_points(i,2)];
end

% Make points not visible on calibration frame equal zero
total_beads = 131;
for i = 1:131
    if grid_x(i,1) == 5555
        total_beads = total_beads - 1;
    end
end
```

```
for j = 1:2
    for i = 1:total_beads
        if grid_x(i,1) == 5555
            grid_x(i,:) = [];
            grid_y(i,:) = [];
        end
    end
end

grids_filename = strcat(dist_file, '_grid');
xlswrite([data_dir,grids_filename],grid_x,1);
xlswrite([data_dir,grids_filename],grid_y,2);
```

D.3 DISTORTION_CORRECTION.M

```
% Program:        distortion_correction.m
% Description:    Corrects the coordinates of digitized points using a
%                 global polynomial-based approach
% Written by:     Angela Kedgley
% Date written:   January 27, 2008
% Last modified: April 3, 2008
%-------------------------------------------------------------------------

% Obtain the location of the file with the points to be corrected for
% distortion from the user
data_folder = input('Enter the name of the folder with the digitized…
      points: ','s');
data_dir = ['drive\directory\folder/' data_folder '\'];

% Obtain the location of the coefficients from the user
map_file = input('Enter the name of the file which contains the …
      mappings: ','s');
map_filename = strcat(map_file, '.xls');

x_mapping_coefficients = xlsread([data_dir,map_filename],1,'G2:G26');
y_mapping_coefficients = xlsread([data_dir,map_filename],2,'G2:G26');

% Obtain information about a range of files if required
num_files = input('Enter the number of files to be corrected: ');
start_file = input('Enter the value of the first file in the…
      series: ');
data_file1 = input('Enter the start of the name of the file which…
      contains the object data: ','s');

for z = start_file:(start_file + num_files - 1)
    if z < 10
        file_num = int2str(z);
        points_filename = strcat(data_file1, '-000', file_num,…
            '_points.xls');
    elseif (z >= 10 && z < 100)
        file_num = int2str(z);
        points_filename = strcat(data_file1, '-00', file_num,…
            '_points.xls');
```

```
elseif (z >= 100 && z < 1000)
    file_num = int2str(z);
    points_filename = strcat(data_file1, '-0', file_num,…
        '_points.xls');
else
    file_num = int2str(z);
    points_filename = strcat(data_file1, '-', file_num,…
        '_points.xls');
end

output_filename = strrep(points_filename, 'points', 'corrected');
output_write = fullfile(data_dir, output_filename);

% Two dimensional coordinates of the points in the image (x,y)
points2correct = xlsread([data_dir,points_filename],1);
numPoints = size(points2correct,1);
points_corrected = zeros(numPoints,3);
points2correct = points2correct(:,2:3);

% Correct all points with nth order polynomial in x and y
for j = 1:numPoints
    x_in = points2correct(j,1);
    y_in = points2correct(j,2);

    temp_x = 0;
    temp_x = temp_x + x_mapping_coefficients(1);
    temp_x = temp_x + x_mapping_coefficients(2) * y_in;
    temp_x = temp_x + x_mapping_coefficients(3) * (y_in ^ 2.0);
    temp_x = temp_x + x_mapping_coefficients(4) * (y_in ^ 3.0);
    temp_x = temp_x + x_mapping_coefficients(5) * (y_in ^ 4.0);
    temp_x = temp_x + x_mapping_coefficients(6) * x_in;
    temp_x = temp_x + x_mapping_coefficients(7) * x_in * y_in;
    temp_x = temp_x + x_mapping_coefficients(8) * x_in *…
        (y_in ^ 2.0);
    temp_x = temp_x + x_mapping_coefficients(9) * x_in *…
        (y_in ^ 3.0);
    temp_x = temp_x + x_mapping_coefficients(10) * x_in *…
        (y_in ^ 4.0);
    temp_x = temp_x + x_mapping_coefficients(11) * (x_in ^ 2.0);
    temp_x = temp_x + x_mapping_coefficients(12) * (x_in ^ 2.0) *…
        y_in;
    temp_x = temp_x + x_mapping_coefficients(13) * (x_in ^ 2.0) *…
        (y_in ^ 2.0);
    temp_x = temp_x + x_mapping_coefficients(14) * (x_in ^ 2.0) *…
        (y_in ^ 3.0);
    temp_x = temp_x + x_mapping_coefficients(15) * (x_in ^ 2.0) *…
        (y_in ^ 4.0);
    temp_x = temp_x + x_mapping_coefficients(16) * (x_in ^ 3.0);
    temp_x = temp_x + x_mapping_coefficients(17) * (x_in ^ 3.0) *…
        y_in;
    temp_x = temp_x + x_mapping_coefficients(18) * (x_in ^ 3.0) *…
        (y_in ^ 2.0);
    temp_x = temp_x + x_mapping_coefficients(19) * (x_in ^ 3.0) *…
        (y_in ^ 3.0);
    temp_x = temp_x + x_mapping_coefficients(20) * (x_in ^ 3.0) *…
        (y_in ^ 4.0);
```

```
        temp_x = temp_x + x_mapping_coefficients(21) * (x_in ^ 4.0);
        temp_x = temp_x + x_mapping_coefficients(22) * (x_in ^ 4.0) *…
            y_in;
        temp_x = temp_x + x_mapping_coefficients(23) * (x_in ^ 4.0) *…
            (y_in ^ 2.0);
        temp_x = temp_x + x_mapping_coefficients(24) * (x_in ^ 4.0) *…
            (y_in ^ 3.0);
        coordinate_x = temp_x + x_mapping_coefficients(25) *…
            (x_in ^ 4.0) * (y_in ^ 4.0);

        temp_y = 0;
        temp_y = temp_y + y_mapping_coefficients(1);
        temp_y = temp_y + y_mapping_coefficients(2) * y_in;
        temp_y = temp_y + y_mapping_coefficients(3) * (y_in ^ 2.0);
        temp_y = temp_y + y_mapping_coefficients(4) * (y_in ^ 3.0);
        temp_y = temp_y + y_mapping_coefficients(5) * (y_in ^ 4.0);
        temp_y = temp_y + y_mapping_coefficients(6) * x_in;
        temp_y = temp_y + y_mapping_coefficients(7) * x_in * y_in;
        temp_y = temp_y + y_mapping_coefficients(8) * x_in *… (y_in ^
            2.0);
        temp_y = temp_y + y_mapping_coefficients(9) * x_in *… (y_in ^
            3.0);
        temp_y = temp_y + y_mapping_coefficients(10) * x_in *… (y_in ^
            4.0);
        temp_y = temp_y + y_mapping_coefficients(11) * (x_in ^ 2.0);
        temp_y = temp_y + y_mapping_coefficients(12) * (x_in ^ 2.0) *…
            y_in;
        temp_y = temp_y + y_mapping_coefficients(13) * (x_in ^ 2.0) *…
            (y_in ^ 2.0);
        temp_y = temp_y + y_mapping_coefficients(14) * (x_in ^ 2.0) *…
            (y_in ^ 3.0);
        temp_y = temp_y + y_mapping_coefficients(15) * (x_in ^ 2.0) *…
            (y_in ^ 4.0);
        temp_y = temp_y + y_mapping_coefficients(16) * (x_in ^ 3.0);
        temp_y = temp_y + y_mapping_coefficients(17) * (x_in ^ 3.0) *…
            y_in;
        temp_y = temp_y + y_mapping_coefficients(18) * (x_in ^ 3.0) *…
            (y_in ^ 2.0);
        temp_y = temp_y + y_mapping_coefficients(19) * (x_in ^ 3.0) *…
            (y_in ^ 3.0);
        temp_y = temp_y + y_mapping_coefficients(20) * (x_in ^ 3.0) *…
            (y_in ^ 4.0);
        temp_y = temp_y + y_mapping_coefficients(21) * (x_in ^ 4.0);
        temp_y = temp_y + y_mapping_coefficients(22) * (x_in ^ 4.0) *…
            y_in;
        temp_y = temp_y + y_mapping_coefficients(23) * (x_in ^ 4.0) *…
            (y_in ^ 2.0);
        temp_y = temp_y + y_mapping_coefficients(24) * (x_in ^ 4.0) *…
            (y_in ^ 3.0);
        coordinate_y = temp_y + y_mapping_coefficients(25) *…
            (x_in ^ 4.0) * (y_in ^ 4.0);

        points_corrected(j,:) = [j coordinate_x coordinate_y];

    end
```

```
    for i = 1:numPoints
        if points_corrected(i,2) > 1000
            points_corrected(i,2) = 5555;
            points_corrected(i,3) = 5555;
        elseif points_corrected(i,2) < -1000
            points_corrected(i,2) = 5555;
            points_corrected(i,3) = 5555;
        end
    end

    xlswrite(output_write, points_corrected,1);
end
```

D.4 RSA.M

```
% Program:        RSA.m
% Description:    Determines the three dimensional-position of markers
%                 from their two dimensional images
% Written by:     Angela Kedgley
% Date written:   November 17, 2005
% Last modified: April 22, 2009
%-------------------------------------------------------------------------

% Initialize variables
i = 0;
F1_counter = 0;
F2_counter = 0;
F1_invisible = [0];
F2_invisible = [0];
C1_counter = 0;
C2_counter = 0;
C1_invisible = [0];
C2_invisible = [0];

% The location of the file with the three-dimensional positions of the
% points on the calibration frame
Frame_points_dir = ['drive\directory\folder/'];

% The name of the calibration file
Frame_points_file = 'small frame';
Frame_points_filename = strcat(Frame_points_file, '.xls');

% Obtain the location of the data files from the user
data_folder = input('Enter the name of the folder with the data:…
      ','s');
data_dir = ['drive\directory\folder/' data_folder '\'];

F1_file = input('Enter the name of the file which contains the F1/C1…
      calibration image points: ','s');
F1_filename = strcat(F1_file, '.xls');
F2_file = input('Enter the name of the file which contains the F2/C2…
      calibration image points: ','s');
F2_filename = strcat(F2_file, '.xls');
```

```
num_files = input('Enter the number of sets of files to be …
      reconstructed: ');
start_file = input('Enter the value of the first file in the series:…
      ');
data_file1 = input('Enter the start of the name of the file which …
      contains the object data for 1: ','s');
data_file2 = input('Enter the start of the name of the file which …
      contains the object data for 2: ','s');
reconstruction_method = input('Reconstruct with best permutation (p) …
      or …with data "as is" (a): ','s');

F1_counter = 0;
F2_counter = 0;
C1_counter = 0;
C2_counter = 0;
z = 0;

% Three dimensional positions of the points on the calibration frame
% Fiducial points
fiducial_points1 = xlsread([Frame_points_dir,Frame_points_file],1);
fiducial_points2 = xlsread([Frame_points_dir,Frame_points_file],2);
% Control points
control_points1 = xlsread([Frame_points_dir,Frame_points_file],3);
control_points2 = xlsread([Frame_points_dir,Frame_points_file],4);

% Two dimensional coordinates of the fiducial marks in the first
% image (x,y)
F1 = xlsread([data_dir,F1_filename],1);
% Two dimensional coordinates of the fiducial marks in the second
% image (x,y)
F2 = xlsread([data_dir,F2_filename],1);

% Find fiducial markers that are not visible
for i = 1:45;
    if F1(i,2)== 5555
        F1_counter = F1_counter + 1;
        F1_invisible(F1_counter) = i;
    end
    if F2(i,2) == 5555
        F2_counter = F2_counter + 1;
        F2_invisible(F2_counter) = i;
    end
end

F1_invisible = fliplr(F1_invisible);
F2_invisible = fliplr(F2_invisible);

% Filter out fiducial markers that are not visible
for i = 1:F1_counter;
    F1_index = F1_invisible(i);
    F1(F1_index,:) = [];
    fiducial_points1(F1_index,:) = [];
end

for i = 1:F2_counter;
```

```
    F2_index = F2_invisible(i);
    F2(F2_index,:) = [];
    fiducial_points2(F2_index,:) = [];
end

 % Part 1: Projective transformations
% Determine the parameters in the transformation functions by the least
% squares approach
[parameters1] = least_squares(fiducial_points1, F1, 1);
[parameters2] = least_squares(fiducial_points2, F2, 2);

% Part 2: Computation of foci coordinates
% Determine the positions of the foci of the x-ray apparatus
% Section A: Find the projections of the control markers on the
% fiducial planes

% Arrays containing the two dimensional coordinates of the control
% points
% In the first image (x, y, z = z(x,y))
C1 = xlsread([data_dir,F1_filename],2);
% In the second image (x = x(y,z), y, z)
C2 = xlsread([data_dir,F2_filename],2);

% Filter out control points that are not visible
for i = 1:45;
    if C1(i,2)== 5555
        C1_counter = C1_counter + 1;
        C1_invisible(C1_counter) = i;
    end
    if C2(i,2) == 5555
        C2_counter = C2_counter + 1;
        C2_invisible(C2_counter) = i;
    end
end

C1_invisible = fliplr(C1_invisible);
C2_invisible = fliplr(C2_invisible);

for i = 1:C1_counter;
    C1_index = C1_invisible(i);
    C1(C1_index,:) = [];
    control_points1(C1_index,:) = [];
end

for i = 1:C2_counter;
    C2_index = C2_invisible(i);
    C2(C2_index,:) = [];
    control_points2(C2_index,:) = [];
end

% Count how many control points are visible
C_dims1 = size(C1);
C_dims2 = size(C2);

for i = 1:C_dims1(1);
```

```
    % Find x and y coordinates
    [projected_points1(i,:)] = project_v2(C1(i,2:3), parameters1, 1,...
      Frame_points_file);
end

for i = 1:C_dims2(1);
    % Find y and z coordinates
    [projected_points2(i,:)] = project_v2(C2(i,2:3), parameters2, 2,...
      Frame_points_file);
end

% Section B: Calculate the foci
[focus1] = calculate_focus_v2(control_points1, projected_points1, 1);
[focus2] = calculate_focus_v2(control_points2, projected_points2, 2);

% Part 3: Object coordinates
% Determine the coordinates of the markers on the object of interest in
% three-space
all_residuals = 0;
largest_residual = 0;
smallest_residual = 1000;

for z = start_file:(start_file + num_files - 1)
    if z < 10
        file_num = int2str(z);
        data_filename1 = strcat(data_file1, '-000', file_num,...
            '_corrected.xls');
        data_filename2 = strcat(data_file2, '-000', file_num,...
            '_corrected.xls');
    elseif (z >= 10 && z < 100)
        file_num = int2str(z);
        data_filename1 = strcat(data_file1, '-00', file_num,...
            '_corrected.xls');
        data_filename2 = strcat(data_file2, '-00', file_num,...
            '_corrected.xls');
    elseif (z >= 100 && z < 1000)
        file_num = int2str(z);
        data_filename1 = strcat(data_file1, '-0', file_num,...
            '_corrected.xls');
        data_filename2 = strcat(data_file2, '-0', file_num,...
            '_corrected.xls');
    else
        file_num = int2str(z);
        data_filename1 = strcat(data_file1, '-', file_num,...
            '_corrected.xls');
        data_filename2 = strcat(data_file2, '-', file_num,...
            '_corrected.xls');
    end

    marker_array1 = xlsread([data_dir,data_filename1],1);
    marker_array2 = xlsread([data_dir,data_filename2],1);

    marker_array_dims = size(marker_array1);
    markers = marker_array_dims(1);
    marker_coordinates = [0 0 0];
```

```
data_filename = strrep(data_filename1, 'corrected', 'output');
data_write = fullfile(data_dir, data_filename);

if reconstruction_method == 'p'
    % Reconstructs the three dimensional positions of the markers
    % with the permutation of the image two data with the smallest
    % sum of the relative residuals from all the markers
    all_combinations = perms(1:markers);
    permutations = size(all_combinations);
    least_residual = 1000;
    second_least_residual = 1000;
    perm_used = 0;

    for i = 1:permutations(1);
        trial_marker_coordinates = [0 0 0];
        total_residual = 0;
        for j = 1:markers;
            Mi1 = [marker_array1(j,2) marker_array1(j,3)];
            Mi2 = [marker_array2(all_combinations(i,j),2)…
              marker_array2(all_combinations(i,j),3)];
            [marker_projected1] = project_v2(Mi1, parameters1, 1,…
              Frame_points_file);
            [marker_projected2] = project_v2(Mi2, parameters2, 2,…
              Frame_points_file);
            [marker_threeD, residual] = calculate_3D_v2…
              (marker_projected1, marker_projected2, focus1,…
              focus2);
            total_residual = total_residual + abs(residual);
            trial_marker_coordinates(j,:) = marker_threeD;
        end
        if total_residual < least_residual
            second_least_residual = least_residual;
            least_residual = total_residual;
            difference = second_least_residual - least_residual;
            relative_difference = least_residual / difference;
            marker_coordinates = trial_marker_coordinates;
            perm_used = all_combinations(i,:);
        end
    end

    xlswrite(data_write, marker_coordinates, 2);
    xlswrite(data_write, least_residual, 2, 'E1');
    xlswrite(data_write, relative_difference, 2, 'E2');
    perm_used = perm_used';
    perm_used = reshape(perm_used, markers, 1);
    xlswrite(data_write, perm_used, 2, 'F1');
end


if reconstruction_method == 'a'
    % Reconstructs the three dimensional positions of the markers
    % with the data in the order given in the file - investigator
    % must manually match up the markers in images 1 and 2
    total_residual = 0;
    for i = 1:markers;
```

```
            Mi1 = [marker_array1(i,2) marker_array1(i,3)];
            Mi2 = [marker_array2(i,2) marker_array2(i,3)];
            [marker_projected1] = project_v2(Mi1, parameters1, 1,…
                  Frame_points_file);
            [marker_projected2] = project_v2(Mi2, parameters2, 2,…
                  Frame_points_file);
            [marker_threeD, residual] = calculate_3D_v2…
                  (marker_projected1, marker_projected2, focus1,…
                  focus2);
            total_residual = total_residual + abs(residual);
            marker_coordinates(i,:) = marker_threeD;
        end

        xlswrite(data_write, marker_coordinates, 1);
        xlswrite(data_write, total_residual, 1, 'E1');
    end
end
```

D.5 SYNCHING.M

```
% Program:        synching.m
% Description:    Calculates the coordinates of a metal reflective
%                 marker in a coordinate system that is common to both
%                 RSA and EvaRT systems for the purposes of synching the
%                 systems
% Written by:     Angela Kedgley
% Date written:   April 20, 2009
% Last modified: April 24, 2009
%-------------------------------------------------------------------------

endline = [0 0 0 1];

% Obtain information about the data to be analyzed from the user
data_folder = input('Enter the name of the folder with the points from…
      RSA and EvaRT: ','s');
data_dir = ['drive\directory\folder/' data_folder '\'];
RSA_coord_filename = input('Enter the name of the RSA coordinate…
      system file: ','s');
RSA_coord_filename = strcat(RSA_coord_filename, '.xls');
data_file = input('Enter the start of the names of the RSA point…
      files: ','s');
num_files = input('Enter the number of RSA files to be examined: ');
start_file = input('Enter the value of the first RSA file: ');
EvaRT_coord_filename = input('Enter the name of the EvaRT coordinate…
      system file: ','s');
trial_name = input('Enter the name of the EvaRT data file: ', 's');

% Create synching coordinate system for RSA
RSA_coord_points = xlsread([data_dir,RSA_coord_filename],1);
RSA_coord_points = RSA_coord_points(:,1:3);
M1_RSA = RSA_coord_points(1,:);
M2_RSA = RSA_coord_points(2,:);
M3_RSA = RSA_coord_points(3,:);
X_RSA = M3_RSA - M1_RSA;
X_RSA_length = norm(X_RSA);
```

```
X_RSA = X_RSA / X_RSA_length;
M2_M1_RSA = M2_RSA - M1_RSA;
Y_RSA = cross(X_RSA, M2_M1_RSA);
Y_RSA_length = norm(Y_RSA);
Y_RSA = Y_RSA / Y_RSA_length;
Z_RSA = cross(X_RSA, Y_RSA);
Z_RSA_length = norm(Z_RSA);
Z_RSA = Z_RSA / Z_RSA_length;
origin_RSA = M1_RSA;
T_RSA = [X_RSA' Y_RSA' Z_RSA' origin_RSA'];
T_RSA = cat(1, T_RSA, endline);
T_RSA = inv(T_RSA);

% Put RSA points into synching coordinate system
counter = 1;
for z = start_file:(start_file + num_files - 1)
    if z < 10
       file_num = int2str(z);
       data_filename = strcat(data_file, '-000', file_num, '_out.xls');
    elseif (z >= 10 && z < 100)
       file_num = int2str(z);
       data_filename = strcat(data_file, '-00', file_num, '_out.xls');
    elseif (z >= 100 && z < 1000)
       file_num = int2str(z);
       data_filename = strcat(data_file, '-0', file_num, '_out.xls');
    else
       file_num = int2str(z);
       data_filename = strcat(data_file, '-', file_num, '_out.xls');
    end
    bead_array = xlsread([data_dir,data_filename],1);
    bead = ([bead_array(1,1:3) 1])';
    bead_RSA_synching = T_RSA * bead;
    moving_bead_RSA(counter,:) = [z bead_RSA_synching(1:3)'];
    moving_bead_RSA(counter + 1,:) = [z bead_RSA_synching(1:3)'];
    counter = counter + 2;
end

% Create synching coordinate system for MA
MA_coord_points = dlmread([data_dir, EvaRT_coord_filename,…
      '.trc'],'\t',6,0);
M1_MA = [MA_coord_points(:,3) MA_coord_points(:,4)…
      MA_coord_points(:,5)];
M2_MA = [MA_coord_points(:,6) MA_coord_points(:,7)…
      MA_coord_points(:,8)];
M3_MA = [MA_coord_points(:,9) MA_coord_points(:,10)…
      MA_coord_points(:,11)];
M1_MA = mean(M1_MA);
M2_MA = mean(M2_MA);
M3_MA = mean(M3_MA);
X_MA = M3_MA - M1_MA;
X_MA_length = norm(X_MA);
X_MA = X_MA / X_MA_length;
M2_M1_MA = M2_MA - M1_MA;
Y_MA = cross(X_MA, M2_M1_MA);
Y_MA_length = norm(Y_MA);
Y_MA = Y_MA / Y_MA_length;
```

```
Z_MA = cross(X_MA, Y_MA);
Z_MA_length = norm(Z_MA);
Z_MA = Z_MA / Z_MA_length;
origin_MA = M1_MA;
T_MA = [X_MA' Y_MA' Z_MA' origin_MA'];
T_MA = cat(1, T_MA, endline);
T_MA = inv(T_MA);

% Put MA points into synching coordinate system
marker_array = dlmread([data_dir,trial_name,'.trc'],'\t',6,0);
markers = [marker_array(:,1) marker_array(:,12) marker_array(:,13)…
      marker_array(:,14)];
marker_dims = size(markers);
zero_counter = 0;
for z = 1:marker_dims(1)
    if markers(z,2:4) == [0 0 0]
        zero_counter = zero_counter + 1;
        zero_array(zero_counter) = z;
    end
end
if zero_counter ~= 0
    zero_array = fliplr(zero_array);
    for i = 1:zero_counter;
        zero_index = zero_array(i);
        markers(zero_index,:) = [];
    end
end
marker_dims = size(markers);
for z = 1:marker_dims(1)
    marker = ([markers(z, 2:4) 1])';
    marker_synching = T_MA * marker;
    moving_marker_MA(z,:) = [markers(z,1) marker_synching(1:3)'];
end

% Match data from RSA to data from MA
RSA_array_dims = size(moving_bead_RSA);
marker_dims = size(moving_marker_MA);
last_index = marker_dims(1) - RSA_array_dims(1) + 1;
index_min_sum = 0;
min_sum_differences = 5000;
for y = 1:last_index
    sum_differences = 0;
    for x = 1:RSA_array_dims(1)
        difference = abs(moving_bead_RSA(x,2:4)…
            - moving_marker_MA((y+x-1),2:4));
        total_difference = norm(difference);
        sum_differences = sum_differences + total_difference;
    end
    if sum_differences < min_sum_differences
        min_sum_differences = sum_differences;
        index_min_sum = moving_marker_MA(y,1);
    end
end

% Output data to Excel spreadsheet
write_filename = strcat('Synching data_', file_num);
```

```
data_write = fullfile(data_dir, write_filename);
xlswrite(data_write, moving_bead_RSA, 2);
xlswrite(data_write, moving_marker_MA, 3);
xlswrite(data_write, index_min_sum, 1, 'A1');
xlswrite(data_write, min_sum_differences, 1, 'C1');
```

D.6 SCAPULOHUMERAL_KINEMATICS.M

```
% Program:       Scapulohumeral_Kinematics.m
% Description:   Calculates the scapulohumeral kinematics from beaded
%                datapoints in conjuntion with anatomical landmarks
% Written by:    Angela Kedgley
% Date written:  March 26, 2009
% Last modified: May 19, 2009
%-------------------------------------------------------------------------

endline = [0 0 0 1];

% Obtain information about the data to be analyzed from the user
data_folder = input('Enter the name of the points' folder: ','s');
data_dir = ['drive\directory\folder\' data_folder '\'];
arm = input('Is this a right(r) or a left (l) arm? ','s');
num_files = input('Enter the number of files to be analyzed: ');
start_file = input('Enter the value of the first file: ');

% Obtain the CT data from the user
anat_landmarks_dir = 'drive\directory\folder\';
anat_landmarks_file = input('Enter the name of the file with the…
   anatomical landmarks from CT: ','s');
anat_landmarks_filename = strcat(anat_landmarks_file, '.xls');
anat_landmarks=xlsread([anat_landmarks_dir,anat_landmarks_filename],1);
beads_mimics = anat_landmarks(10:23,1:3);
anat_landmarks = anat_landmarks(1:6,1:3);

% Scapular Bead Coordinate System in Mimics
S1m = beads_mimics(10,:);
S3m = beads_mimics(12,:);
S5m = beads_mimics(14,:);
S5S1_m = S5m - S1m;
S3S1_m = S3m - S1m;
Xscap_m = cross(S5S1_m, S3S1_m);
Xscap_m_length = norm(Xscap_m);
Xscap_m = Xscap_m / Xscap_m_length;
Zscap_m = cross(S5S1_m, Xscap_m);
Zscap_m_length = norm(Zscap_m);
Zscap_m = Zscap_m / Zscap_m_length;
Yscap_m = cross(Zscap_m, Xscap_m);
Yscap_m_length = norm(Yscap_m);
Yscap_m = Yscap_m / Yscap_m_length;
origin_scap_m = S1m;
Tbead_scap2mimics = [Xscap_m' Yscap_m' Zscap_m' origin_scap_m'];
Tbead_scap2mimics = cat(1, Tbead_scap2mimics, endline);

% Scapular Anatomical Coordinate System in Mimics
% Landmarks: IA=inferior angle, AA=acromial angle, TS=trigonum spinae
```

```
AA = anat_landmarks(3,:);
TS = anat_landmarks(1,:);
IA = anat_landmarks(2,:);
Zscap = AA - TS;
Zscap_length = norm(Zscap);
Zscap = Zscap / Zscap_length;
AA_IA = IA - AA;
Xscap = cross(AA_IA, -Zscap);
Xscap_length = norm(Xscap);
Xscap = Xscap / Xscap_length;
Yscap = cross(Zscap, Xscap);
Yscap_length = norm(Yscap);
Yscap = Yscap / Yscap_length;
origin_scap = AA;
Tscap2mimics = [Xscap' Yscap' Zscap' origin_scap'];
Tscap2mimics = cat(1, Tscap2mimics, endline);
Tmimics2scap = inv(Tscap2mimics);

% Relation between beads and anatomic landmarks in the scapula
Tbeads2scap = Tmimics2scap * Tbead_scap2mimics;
Tscap2beads = inv(Tbeads2scap);

% Humeral Bead Coordinate System in Mimics
H2m = beads_mimics(6,:);
H3m = beads_mimics(7,:);
H4m = beads_mimics(8,:);
Yhum_m = H2m - H4m;
Yhum_m_length = norm(Yhum_m);
Yhum_m = Yhum_m / Yhum_m_length;
H3H4_m = H3m - H4m;
Xhum_m = cross(H3H4_m, Yhum_m);
Xhum_m_length = norm(Xhum_m);
Xhum_m = Xhum_m / Xhum_m_length;
Zhum_m = cross(Xhum_m, Yhum_m);
Zhum_m_length = norm(Zhum_m);
Zhum_m = Zhum_m / Zhum_m_length;
origin_hum_m = H2m;
Tbead_hum2mimics = [Xhum_m' Yhum_m' Zhum_m' origin_hum_m'];
Tbead_hum2mimics = cat(1, Tbead_hum2mimics, endline);

% Humeral Anatomical Coordinate System in Mimics
% Landmarks: LE = lateral epicondyle, ME = medical epicondyle, HC =
% centre of humeral head
LE = anat_landmarks(5,:);
ME = anat_landmarks(4,:);
HC = anat_landmarks(6,:);
midEpi = (LE + ME)/2;
Yhum = HC - midEpi;
Yhum_length = norm(Yhum);
Yhum = Yhum / Yhum_length;
LE_ME = ME - LE;
Xhum = cross(LE_ME, Yhum);
Xhum_length = norm(Xhum);
Xhum = Xhum / Xhum_length;
Zhum = cross(Xhum, Yhum);
Zhum_length = norm(Zhum);
```

```
Zhum = Zhum / Zhum_length;
origin_hum = HC;
Thum2mimics = [Xhum' Yhum' Zhum' origin_hum'];
Thum2mimics = cat(1, Thum2mimics, endline);
Tmimics2hum = inv(Thum2mimics);

% Relation between beads and anatomic landmarks in the humerus
Tbeads2hum = Tmimics2hum * Tbead_hum2mimics;
Thum2beads = inv(Tbeads2hum);

for z = start_file:(start_file + num_files - 1)
    file_num = int2str(z);
    if z < 10
        data_filename = strcat('Fluoro-000', file_num, '_output.xls');
    elseif (z >= 10 && z < 100)
        data_filename = strcat('Fluoro-00', file_num, '_output.xls');
    elseif (z >= 100 && z < 1000)
        data_filename = strcat('Fluoro-0', file_num, '_output.xls');
    else
        data_filename = strcat('Fluoro-', file_num, '_output.xls');
    end
    bead_array = xlsread([data_dir,data_filename],1);

    % Scapular Bead Coordinate System in Lab
    S1l = bead_array(1,1:3);
    S3l = bead_array(3,1:3);
    S5l = bead_array(5,1:3);
    S5S1_l = S5l - S1l;
    S3S1_l = S3l - S1l;
    Xscap_l = cross(S5S1_l, S3S1_l);
    Xscap_l_length = norm(Xscap_l);
    Xscap_l = Xscap_l / Xscap_l_length;
    Zscap_l = cross(S5S1_l, Xscap_l);
    Zscap_l_length = norm(Zscap_l);
    Zscap_l = Zscap_l / Zscap_l_length;
    Yscap_l = cross(Zscap_l, Xscap_l);
    Yscap_l_length = norm(Yscap_l);
    Yscap_l = Yscap_l / Yscap_l_length;
    origin_scap_l = S1l;
    Tbead_scap2lab = [Xscap_l' Yscap_l' Zscap_l' origin_scap_l'];
    Tbead_scap2lab = cat(1, Tbead_scap2lab, endline);
    Tscap2lab = Tbead_scap2lab * Tscap2beads;
    Tlab2scap = inv(Tscap2lab);

    % Humeral Bead Coordinate System in Lab
    H2l = bead_array(11,1:3);
    H3l = bead_array(12,1:3);
    H4l = bead_array(13,1:3);
    Yhum_l = H2l - H4l;
    Yhum_l_length = norm(Yhum_l);
    Yhum_l = Yhum_l / Yhum_l_length;
    H3H4_l = H3l - H4l;
    Xhum_l = cross(H3H4_l, Yhum_l);
    Xhum_l_length = norm(Xhum_l);
    Xhum_l = Xhum_l / Xhum_l_length;
    Zhum_l = cross(Xhum_l, Yhum_l);
```

```
    Zhum_l_length = norm(Zhum_l);
    Zhum_l = Zhum_l / Zhum_l_length;
    origin_hum_l = H2l;
    Tbead_hum2lab = [Xhum_l' Yhum_l' Zhum_l' origin_hum_l'];
    Tbead_hum2lab = cat(1, Tbead_hum2lab, endline);
    Thum2lab = Tbead_hum2lab * Thum2beads;
    Thum2scap = Tlab2scap * Thum2lab;

    % Euler Angle Analysis
    alpha = atan2(-sqrt(Thum2scap(1,2)^2 + Thum2scap(3,2)^2),...
       Thum2scap(2,2));
    beta = atan2((Thum2scap(1,2)/sin(alpha)),...
       (Thum2scap(3,2)/sin(alpha)));
    gamma = atan2((Thum2scap(2,1)/sin(alpha)),...
       (-Thum2scap(2,3)/sin(alpha)));

    alpha = alpha * 180/pi;
    beta = beta * 180/pi;
    gamma = gamma * 180/pi;

    if arm == 'r'
        alpha = -alpha;
        gamma = -gamma;
    else
        alpha = -alpha;
        beta = -beta;
    end

    names = ['Plane - beta    '; 'Angle - alpha  '; 'I/E Rot - gamma';...
       'T-hum wrt scap '];
    cellnames = cellstr(names);
    data_filename = strrep(data_filename, 'output', 'angles');
    data_write = fullfile(data_dir, data_filename);
    xlswrite(data_write, cellnames);
    xlswrite(data_write, beta, 1, 'B1');
    xlswrite(data_write, alpha, 1, 'B2');
    xlswrite(data_write, gamma, 1, 'B3');
    xlswrite(data_write, Thum2scap, 1, 'B4');
end
```

APPENDIX E – SCHEMATIC DRAWINGS

Drawings of the distortion grid, calibration frame, fluoroscopic synching device, device to synchronize data from the optical motion analysis system and bead inserter were created in SolidWorks (Dassault Systèmes SolidWorks Corporation, Concord, MA, USA). All devices were manufactured by University Machine Services at the University of Western Ontario.

E.1 DISTORTION GRID

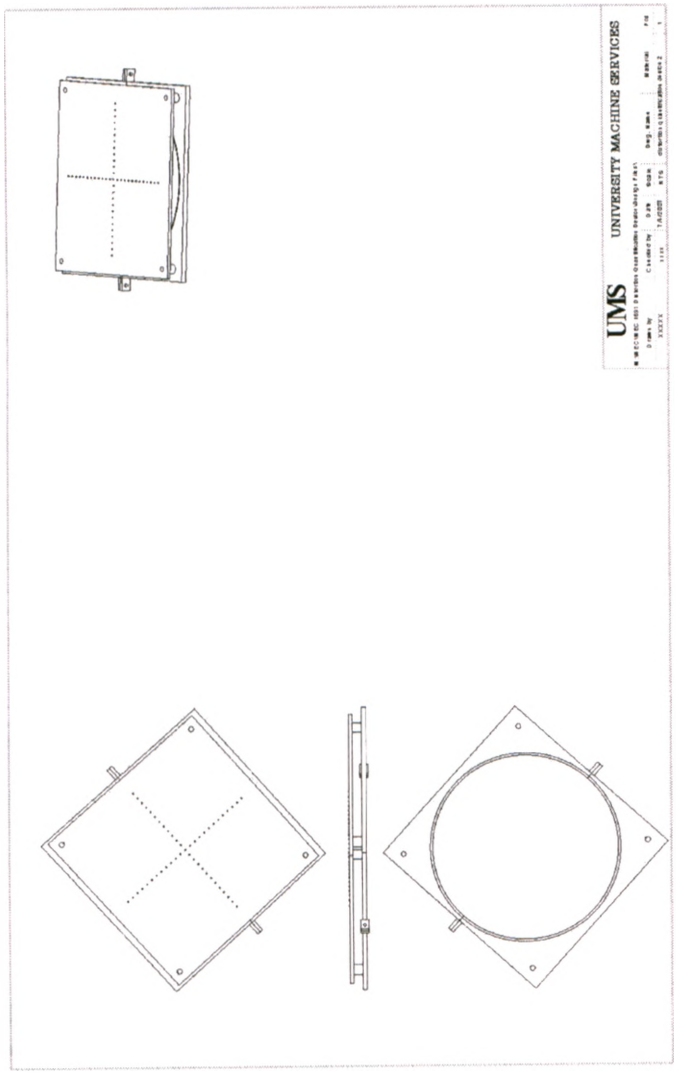

Figure E.1 Schematic drawing of the distortion grid and mounting bracket

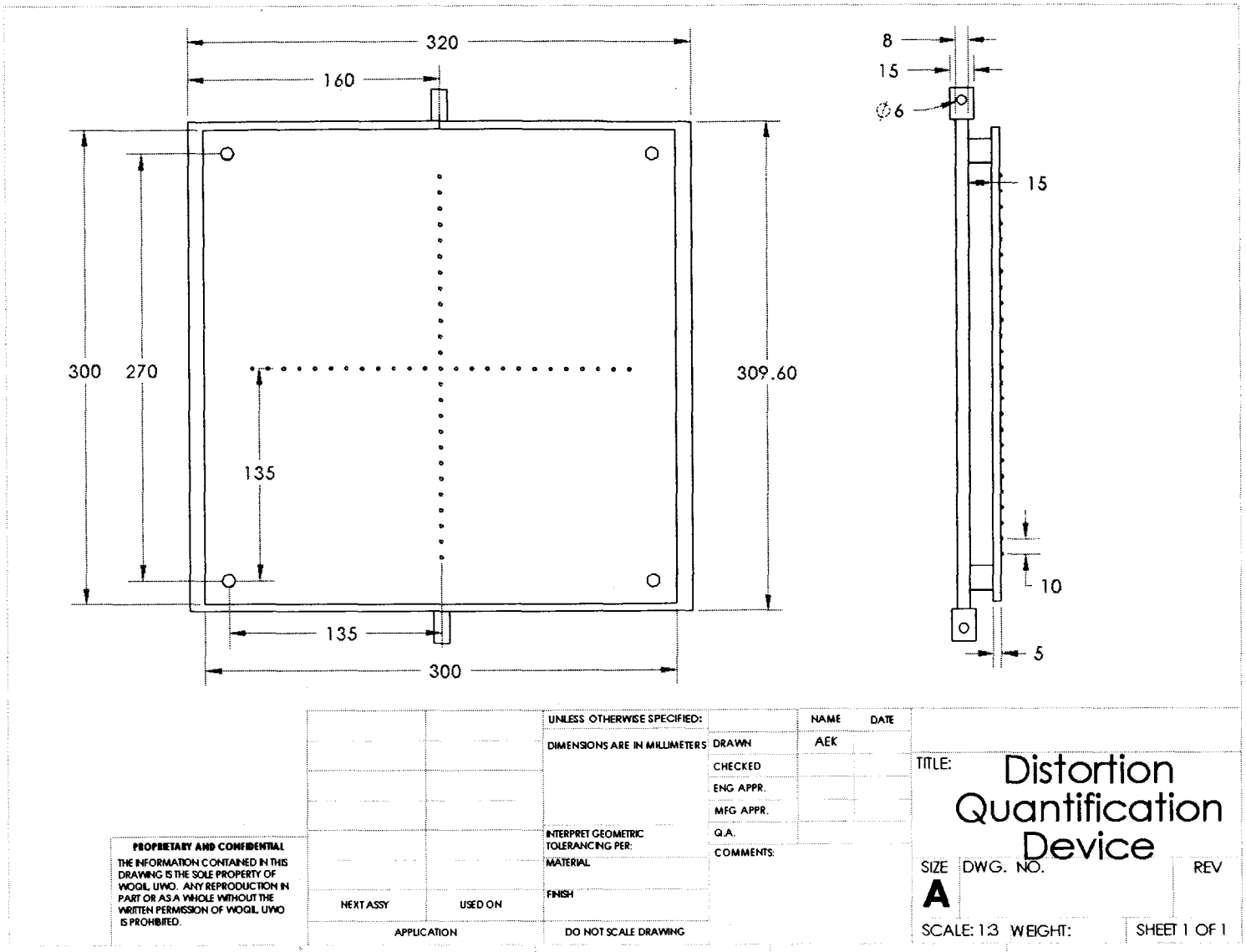

Figure E.2 Schematic drawing of the distortion grid
All dimensions in millimeters.

E.2 CALIBRATION FRAME

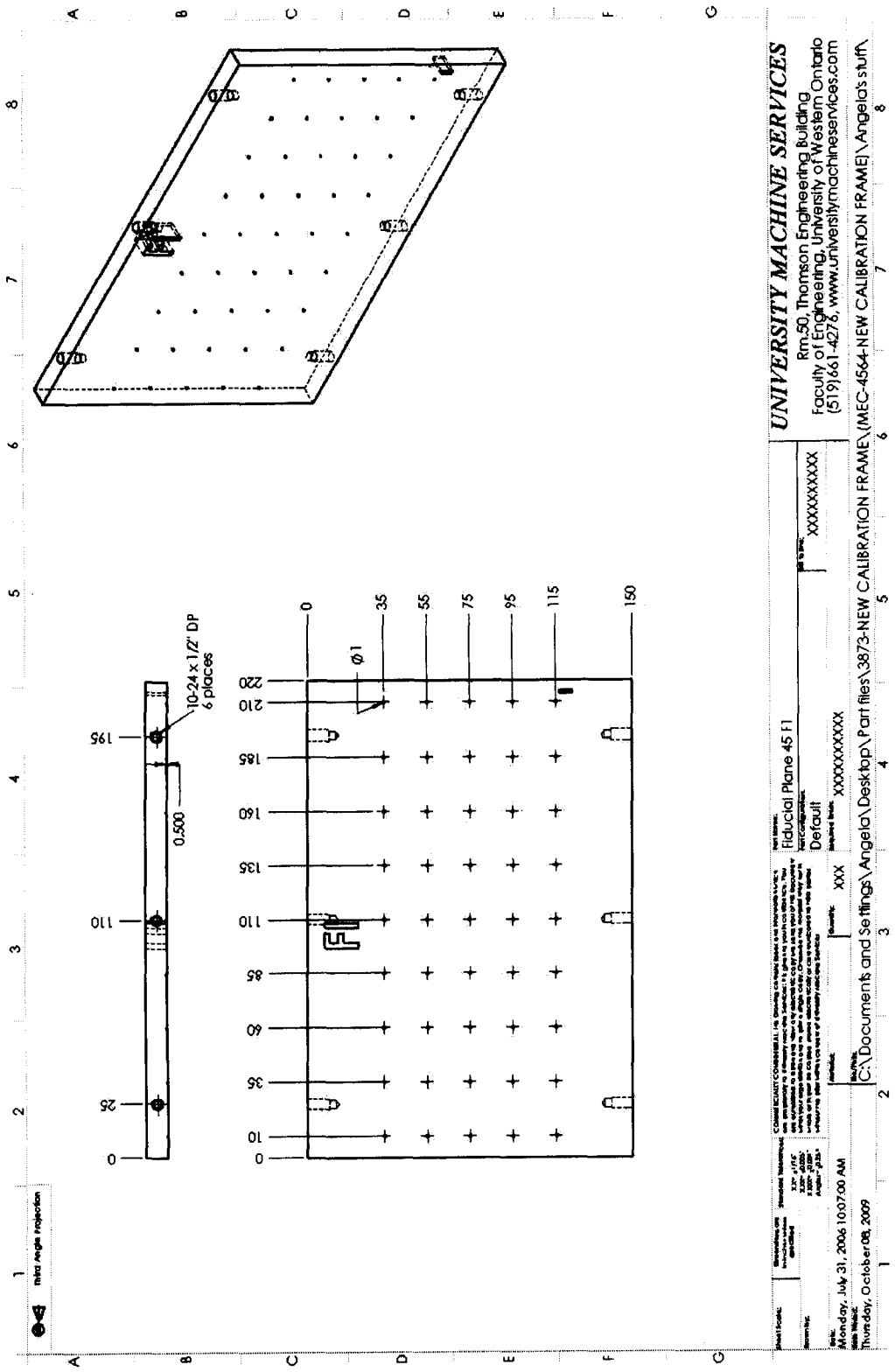

Figure E.3 Schematic drawing of the fiducial plane
All dimensions in millimeters.

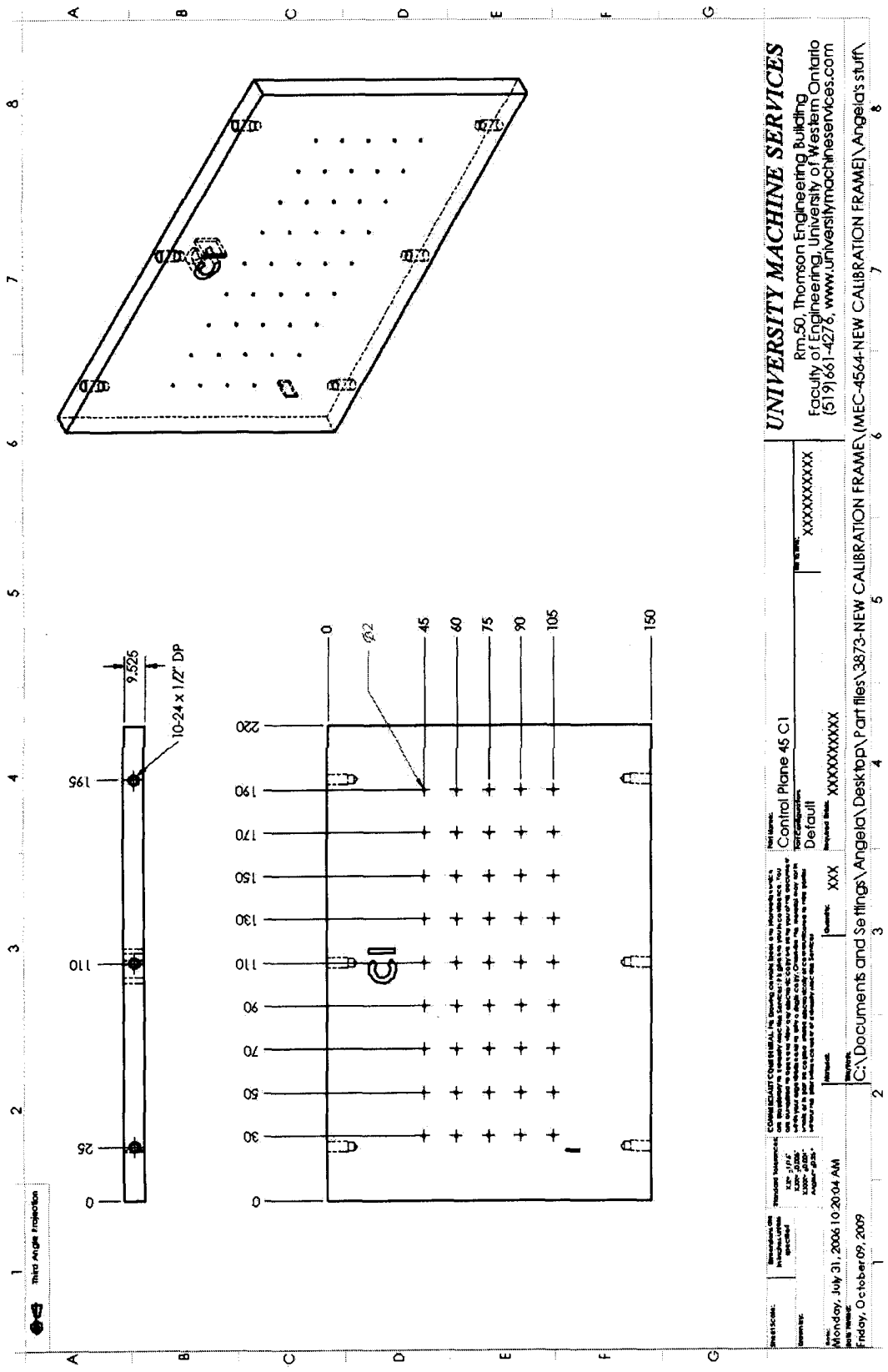

Figure E.4 Schematic drawing of the control plane
All dimensions in millimeters.

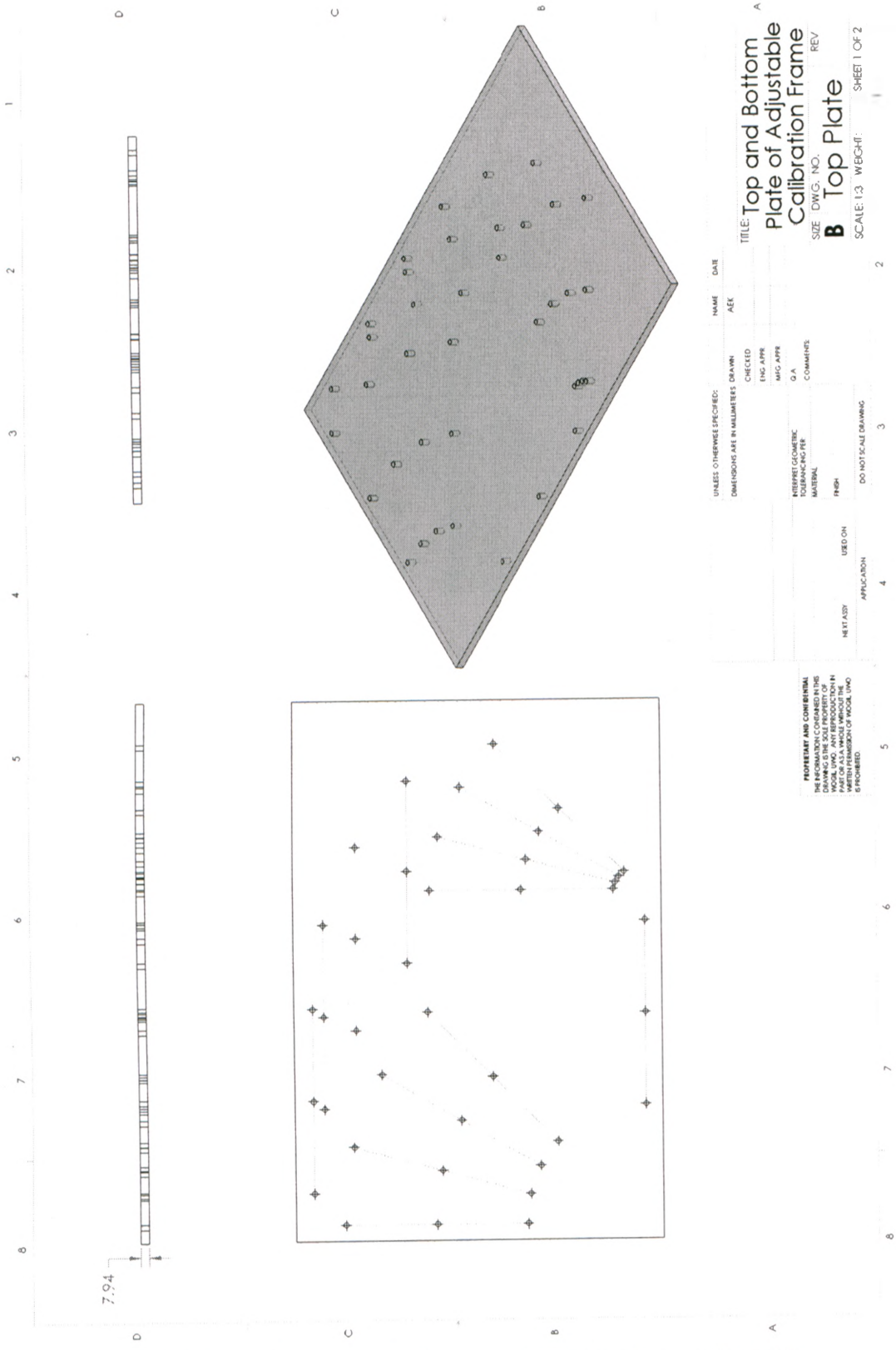

Figure E.5 Schematic drawing of the top and bottom plate – adjustable frame
All dimensions in millimeters.

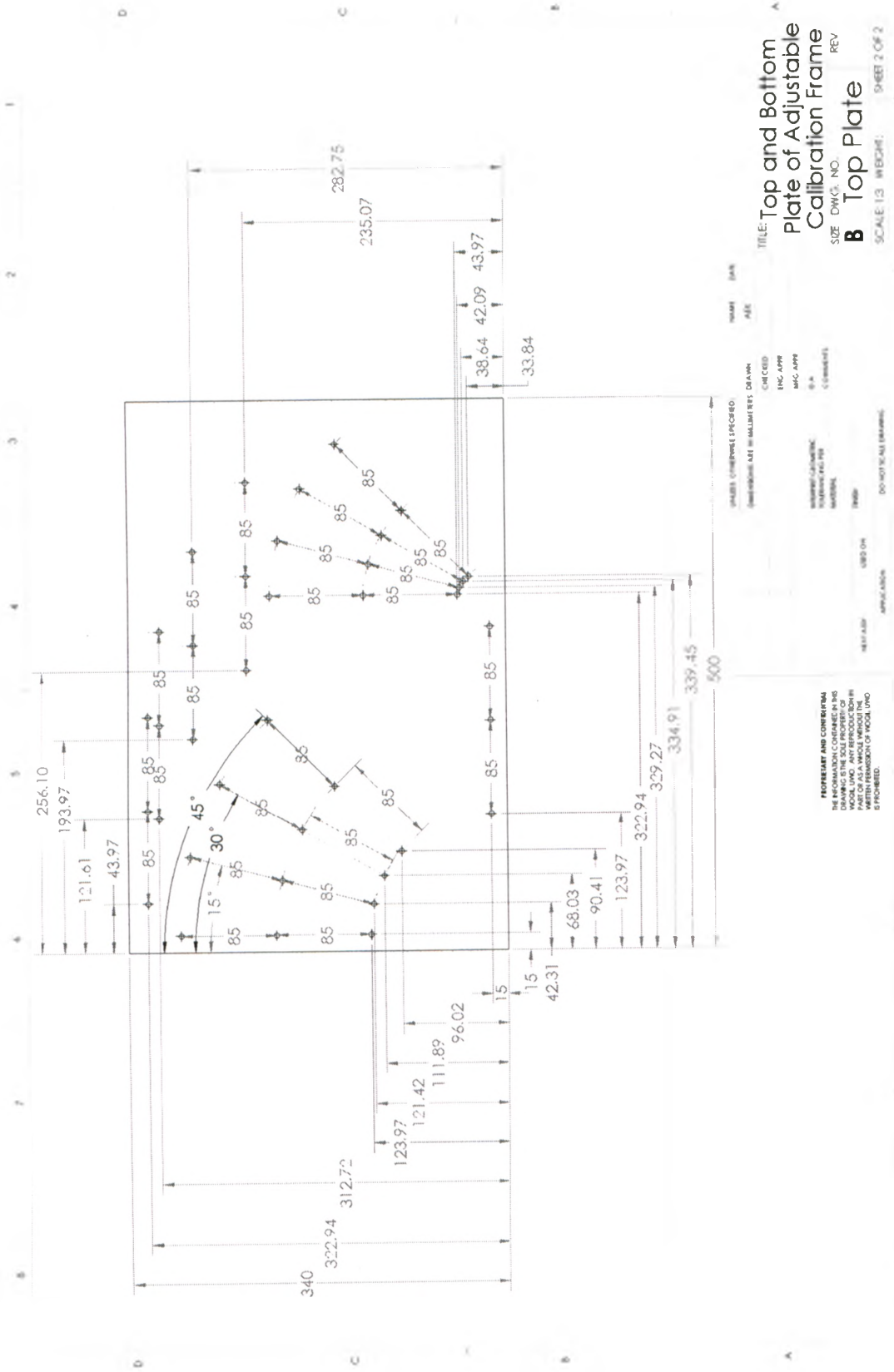

Figure E.6 Dimensions of the top and bottom plate – adjustable frame
All dimensions in millimeters.

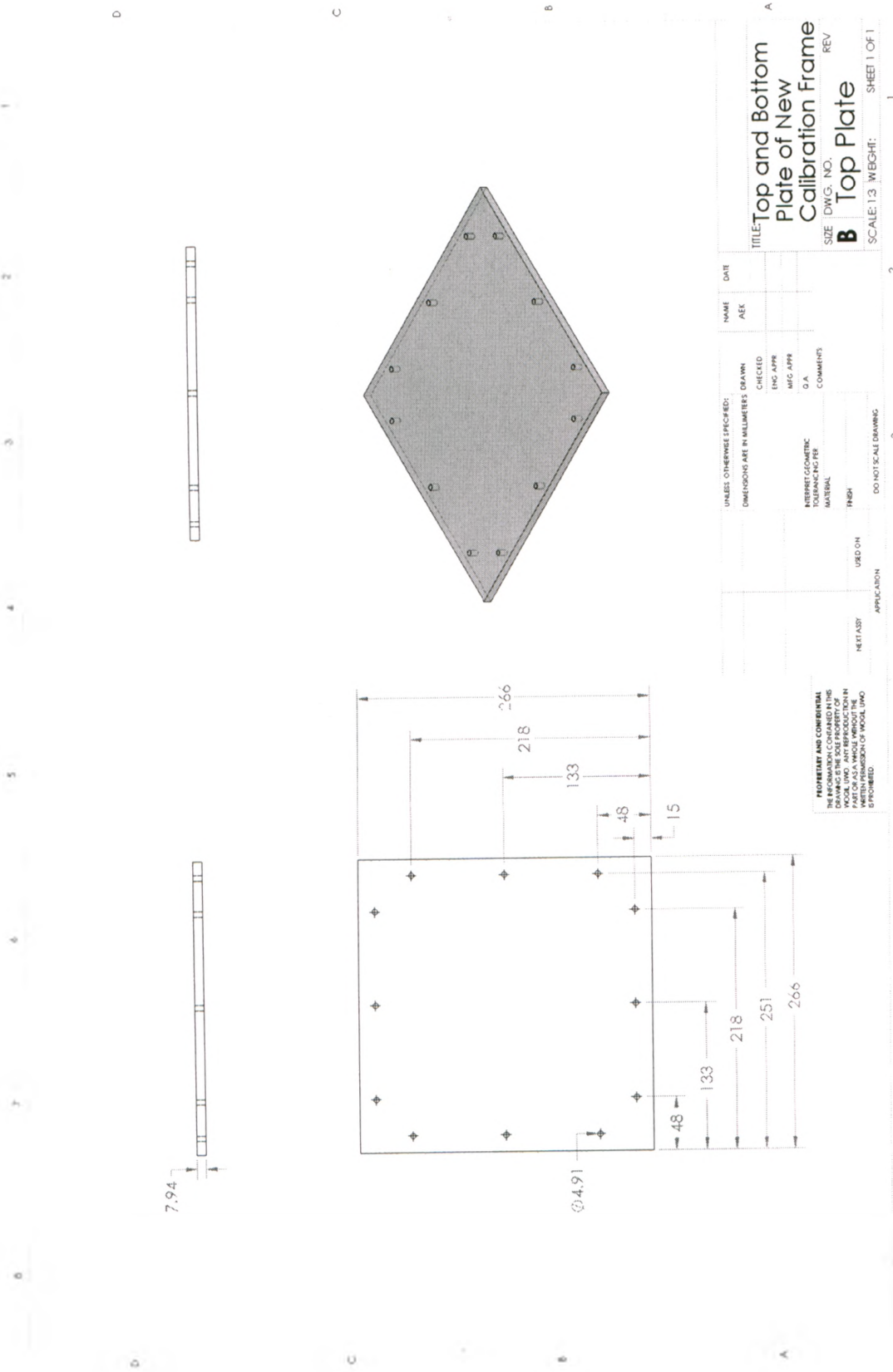

Figure E.7 Schematic drawing of the top and bottom plate – small frame
All dimensions in millimeters.

E.3 FLUOROSCOPIC SYNCHING DEVICE

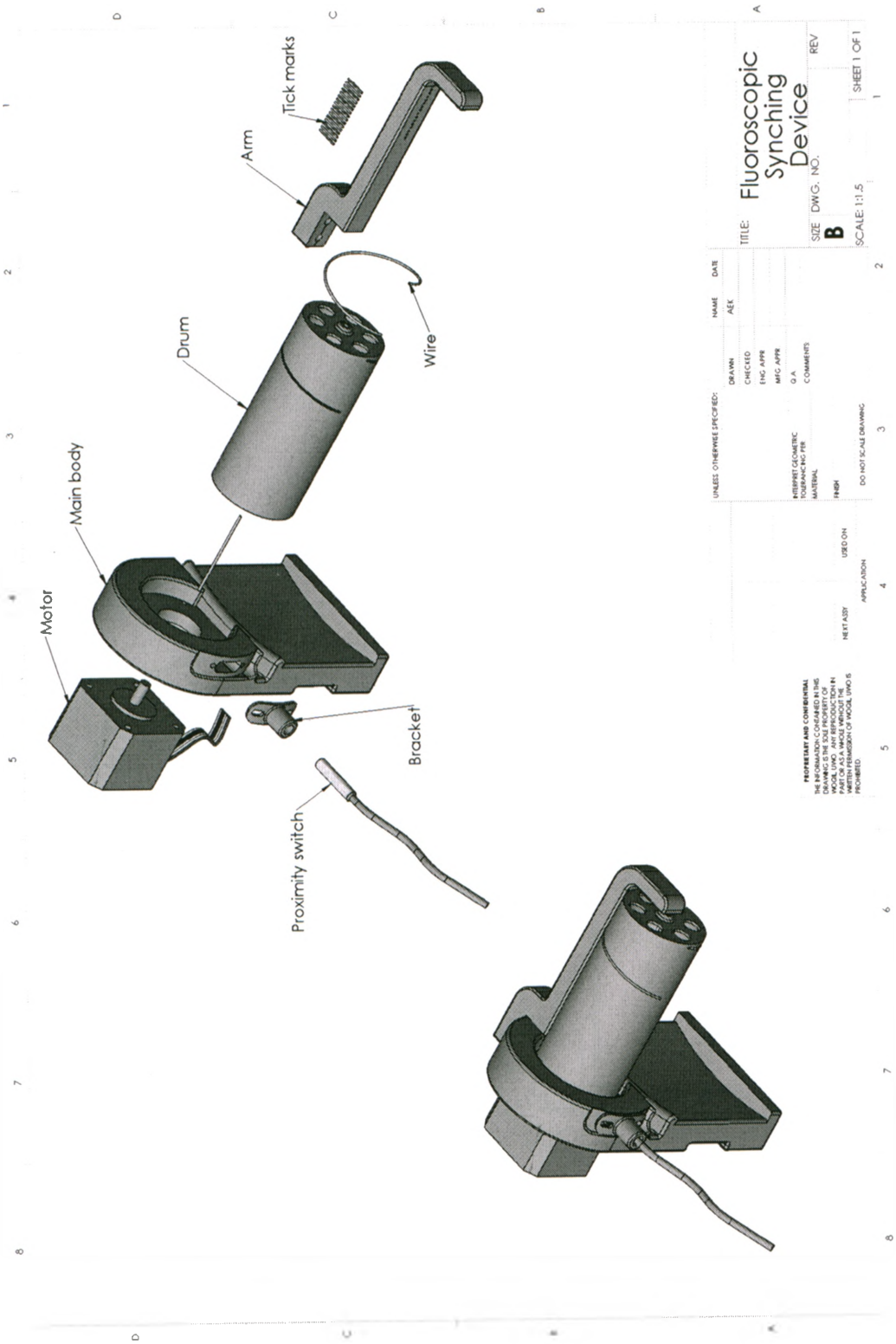

Figure E.8 Assembly and exploded view of the fluoroscopic synching device

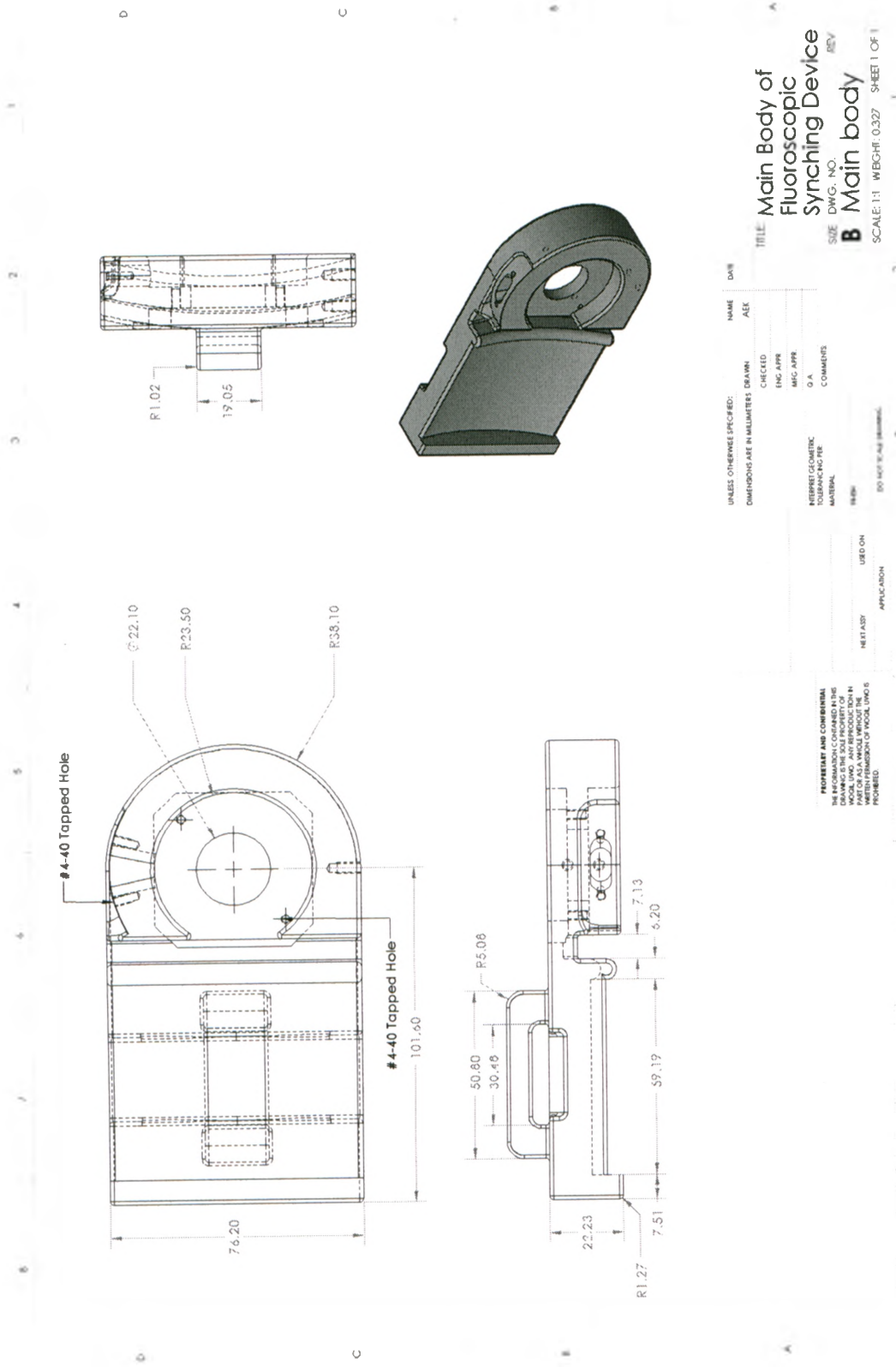

Figure E.9 Schematic drawing of the main body of the fluoroscopic synching device
All dimensions in millimeters.

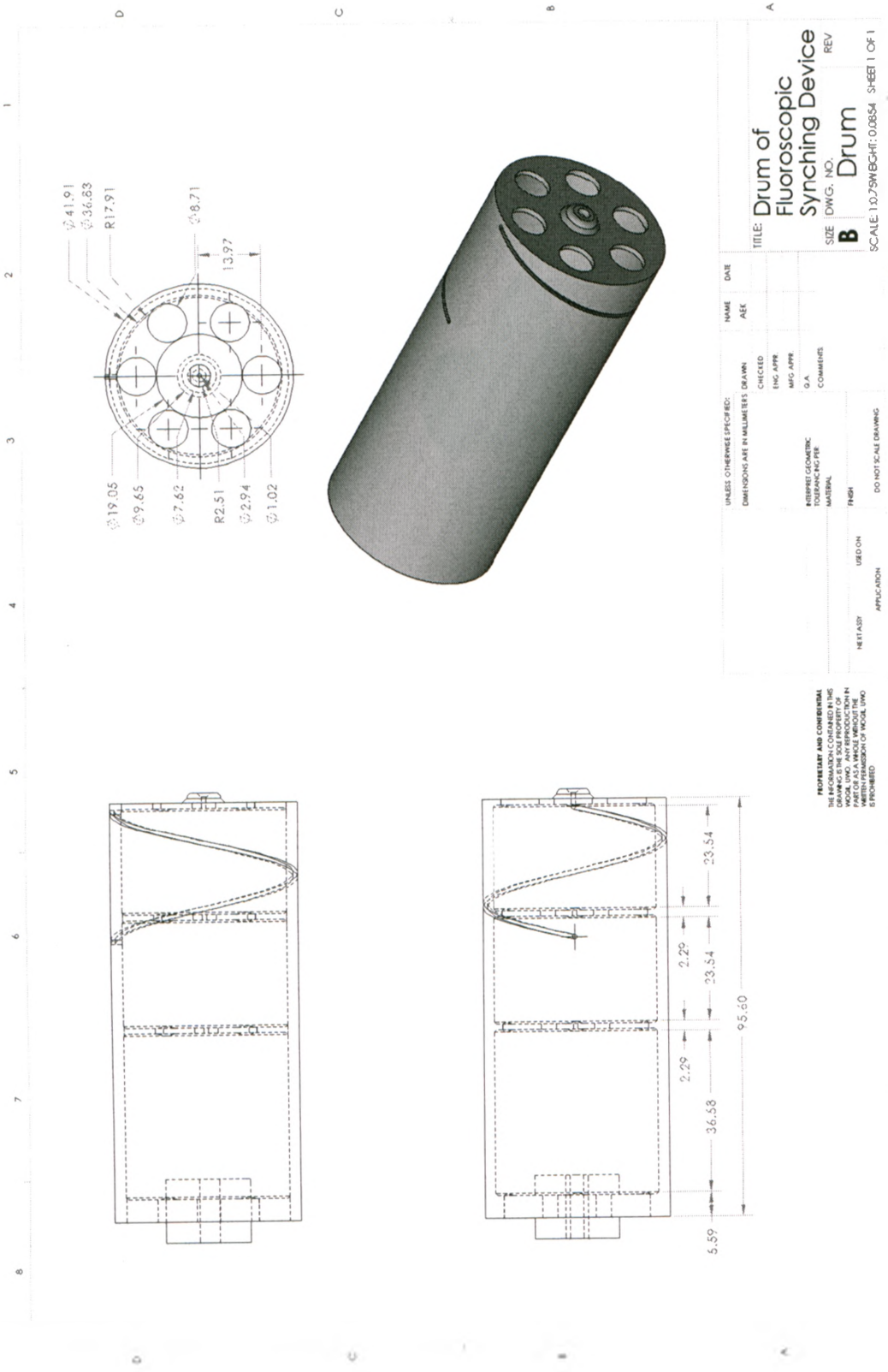

Figure E.10 Schematic drawing of the drum of the fluoroscopic synching device
All dimensions in millimeters.

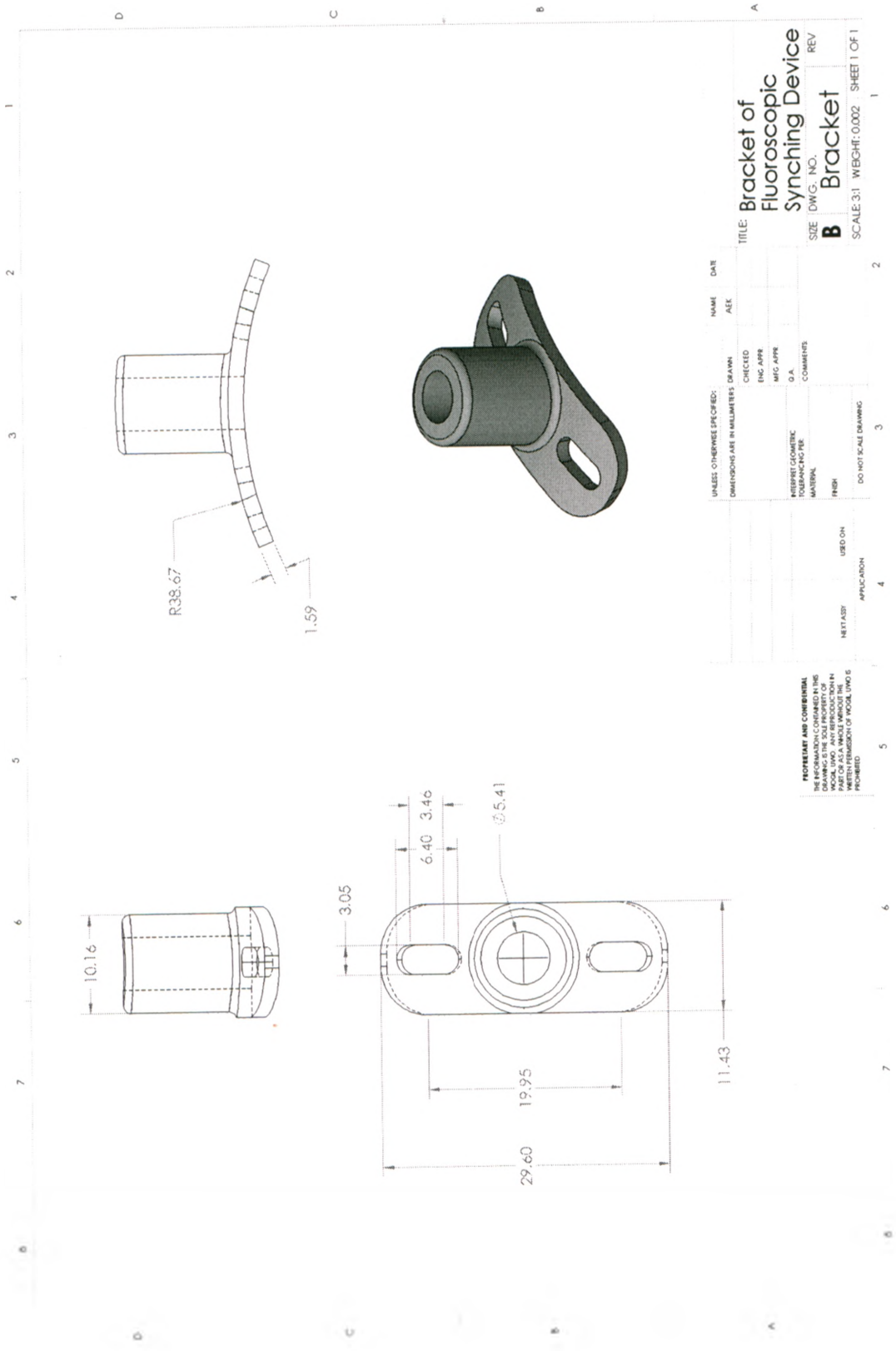

Figure E.11 Schematic drawing of the bracket of the fluoroscopic synching device
All dimensions in millimeters.

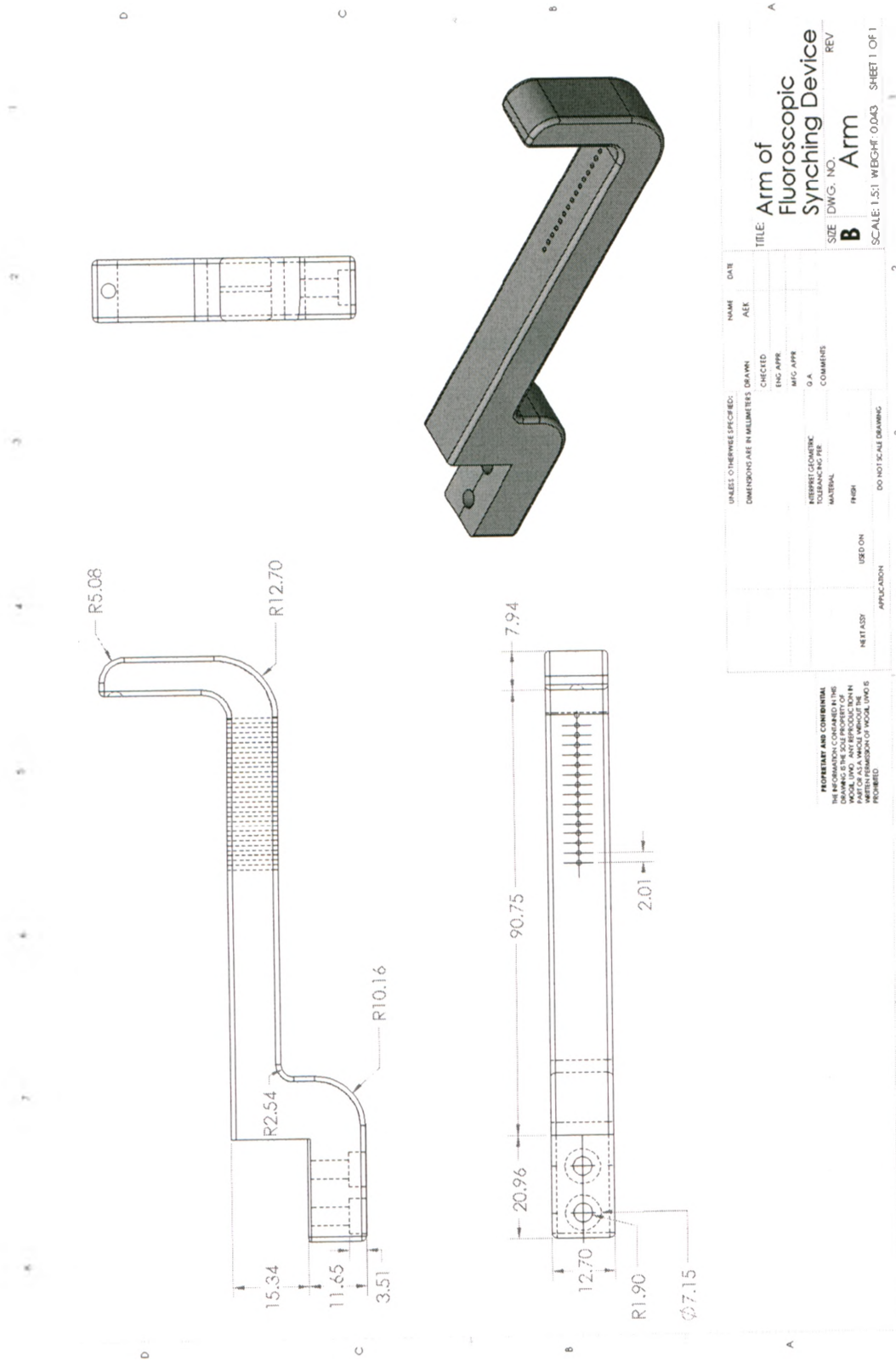

Figure E.12 Schematic drawing of the arm of the fluoroscopic synching device
All dimensions in millimeters.

E.4 Synching Device for the Optical Motion Analysis System

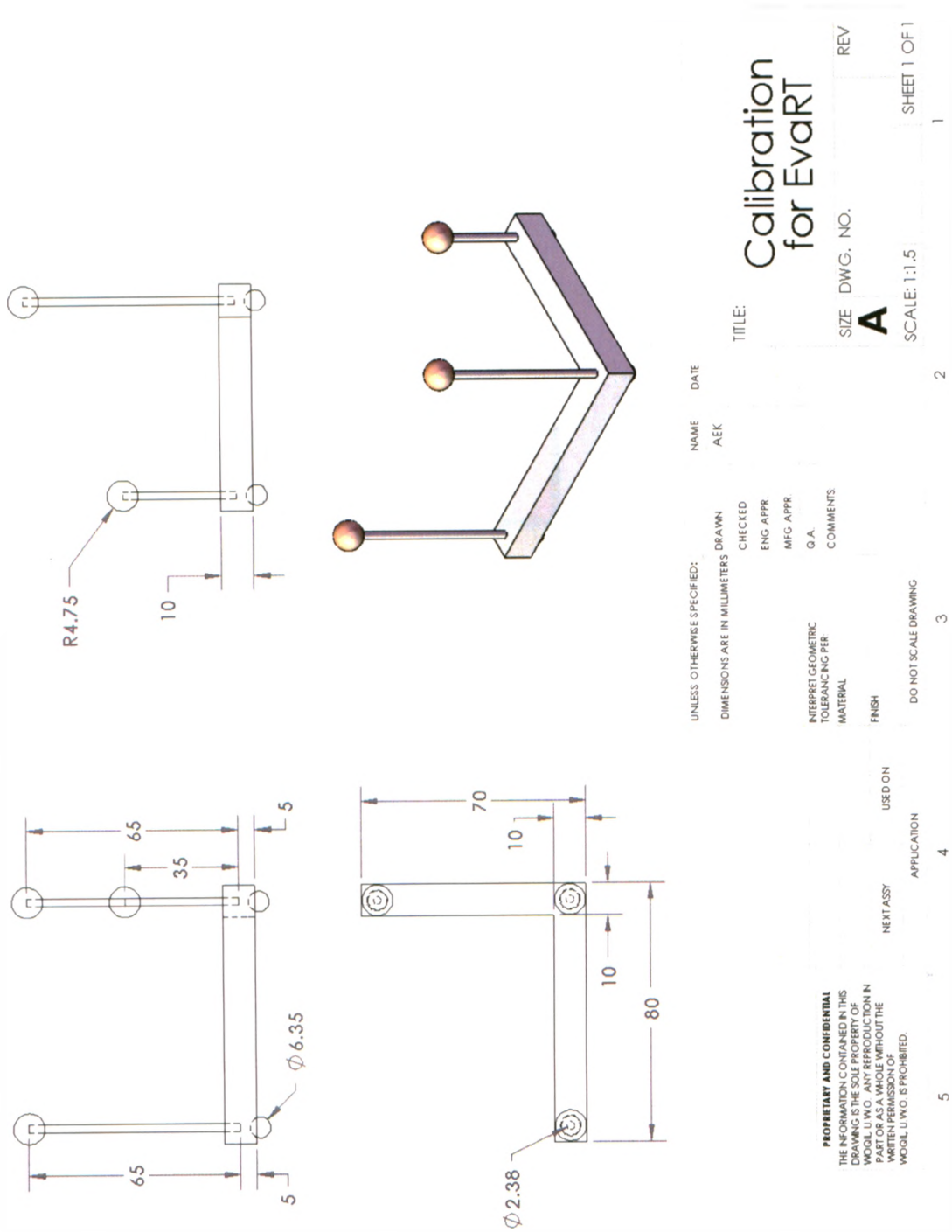

Figure E.13 Schematic drawing of the synching device for the optical motion analysis system
All dimensions in millimeters.

E.5 Simplified Bead Inserter

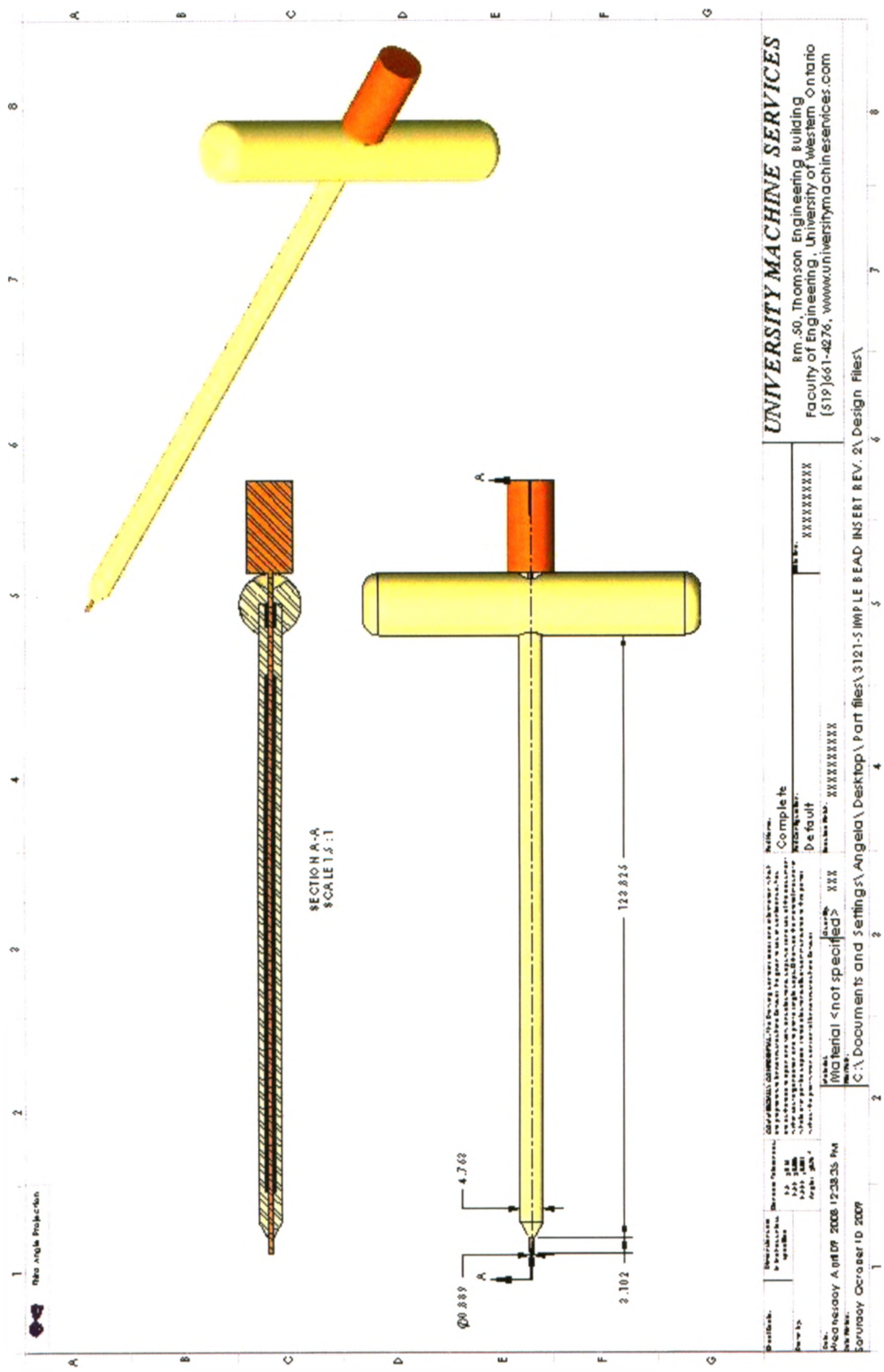

Figure E.14 Schematic drawing of the simplified bead inserter
All dimensions in millimeters.

APPENDIX F – DIGITIZATION OF THE DISTORTION GRID

This appendix describes the process used to precisely locate the positions of the beads on the distortion grid that was described in Chapter 2.

F.1 CMM MACHINE DETAILS

The DEA swift coordinate measuring machine (CMM; Hexagon Metrology Services Ltd.., London, UK; Figure F.1) is a manually operated, vertical bridge-type machine that can make measurements in three axes. The parameters of this machine are listed in Table F.1. The electronic touch probe is mounted from the cross-head and extends in the direction of the Z-axis. It is manually guided by a joystick mechanism.

F.2 DIGITIZATION PROCESS

Inspection of a sphere was specified within the DEA Tutor software package. Each bead was touched 9 times by the digitizing probe in approximately the configuration shown in Figure F.2. The coordinates of the sphere's centre and the diameter of the sphere were calculated and displayed by the Tutor software package. The average diameter of the 221 spheres on the distortion grid was found to be 2.09 mm (± 0.13 mm). The positions of the 121 points that are used in distortion correction, relative to their theoretical locations, can be seen in Figure F.3.

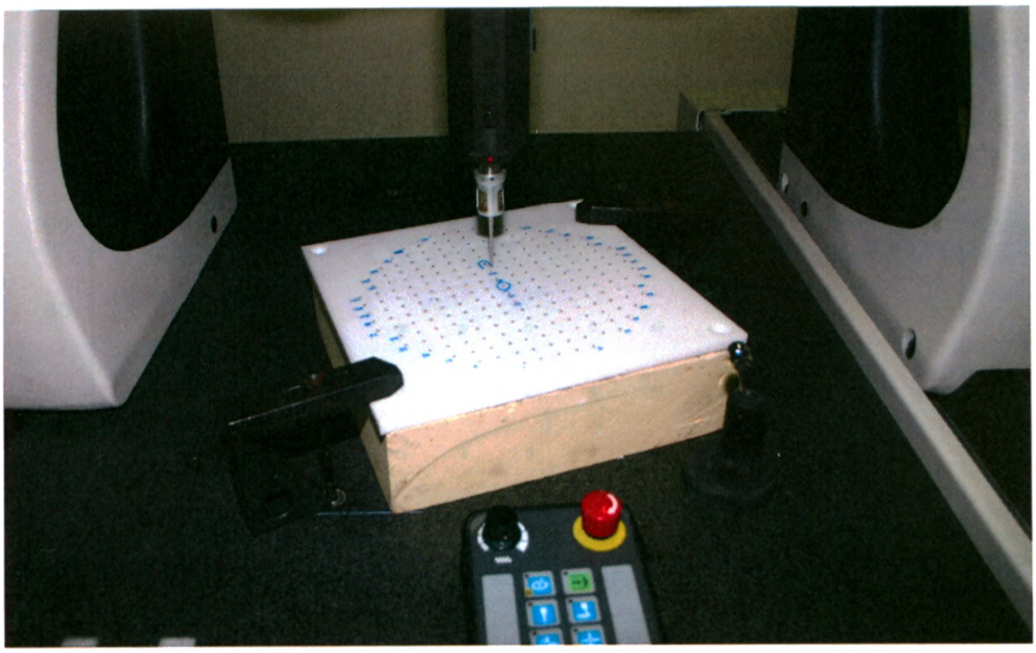

Figure F.1 Digitization of the distortion grid using the CMM
All dimensions in millimeters.

Table F.1 Parameters of the DEA Swift coordinate measuring machine

Work piece capacity	46 cm L x 61 cm W x 38 cm H
Travel capacity	X-axis – 36 cm
	Y-axis – 41 cm
	Z-axis -30 cm
Machine performance	
Linear Accuracy	0.0064 mm
Repeatability	0.0041 mm
Resolution	0.0010 mm

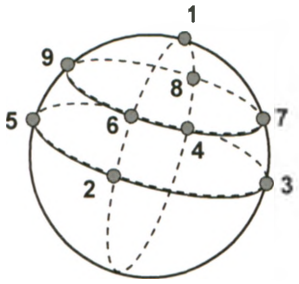

Figure F.2 Configuration of points for digitization of a sphere

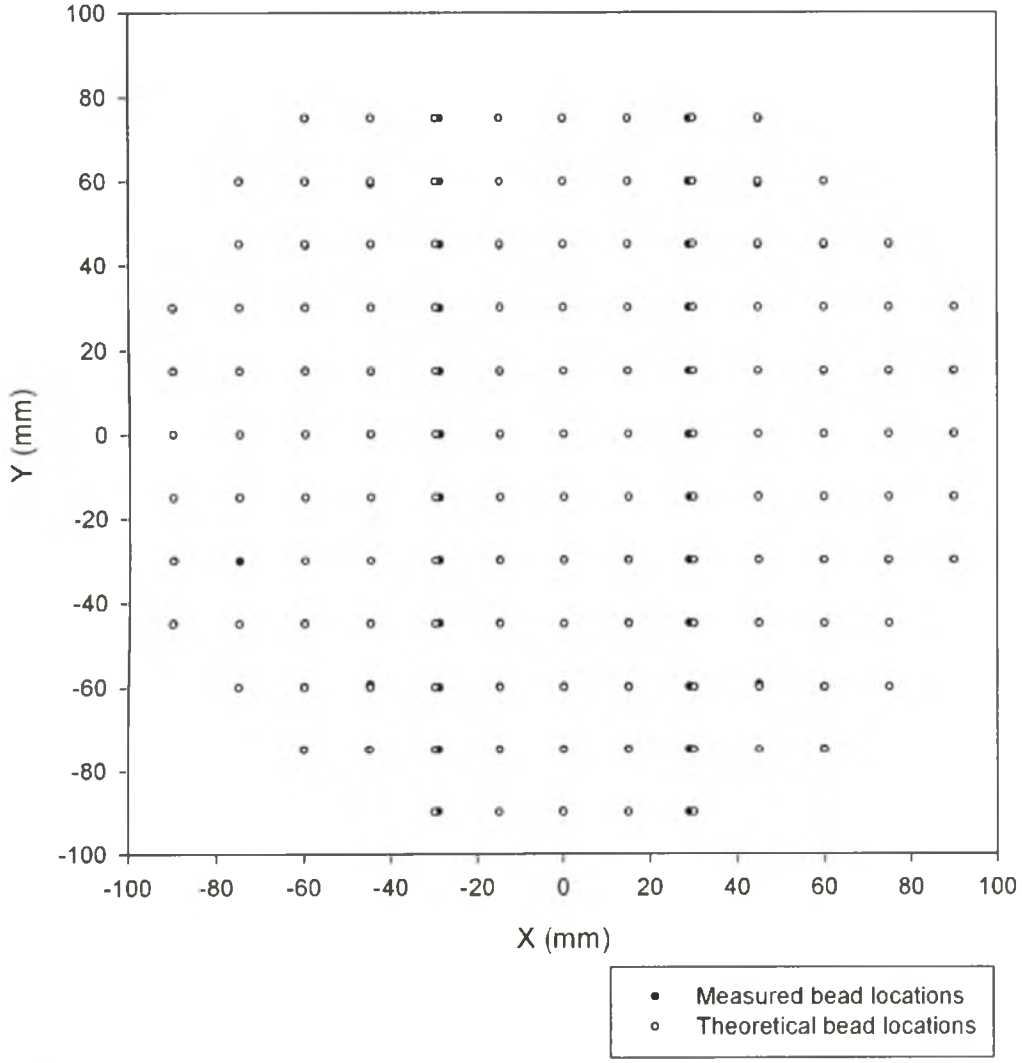

Figure F.3 Measured and theoretical distortion grid beads locations

APPENDIX G – USAGE OF THE DEVICE TO SYNCHRONIZE THE FLUOROSCOPES

This appendix describes how to operate the device for synchronizing the fluoroscopes that was described in Chapter 2.

1. Attach the two drums to the image intensifiers. Be careful not to tighten the straps too much – no load will be applied to the drums so the straps should be just tight enough to stop the drums from slipping. Note that this must be done prior to calibrating the system for RSA, as after calibration images are taken the fluoroscopes cannot be touched.
2. Always ensure that the power button on the control console (Figure G.1) is in the 'off' position before plugging in or unplugging the power cord. This can be tricky as there is no visible sign as to whether the unit is on or off. The power button has less give when in the 'off' position.
3. Once the unit is plugged in, turn the power on by pressing the power button. The green trigger button will begin to flash.
4. Press the green trigger button to begin the timing sequence. If the drums do not begin to rotate within the first five seconds, press the trigger again and switch the rotation speed to be lower. The drums need to be rotating at 2Hz to effectively synchronize the fluoroscopes, but this speed often needs to be attained in stages. Press the trigger again to start the drums. Once the two drums are in time, the green trigger button stops flashing and stays on continuously.
5. If the drums are not rotating at 2Hz, stop them with the trigger and increase the speed

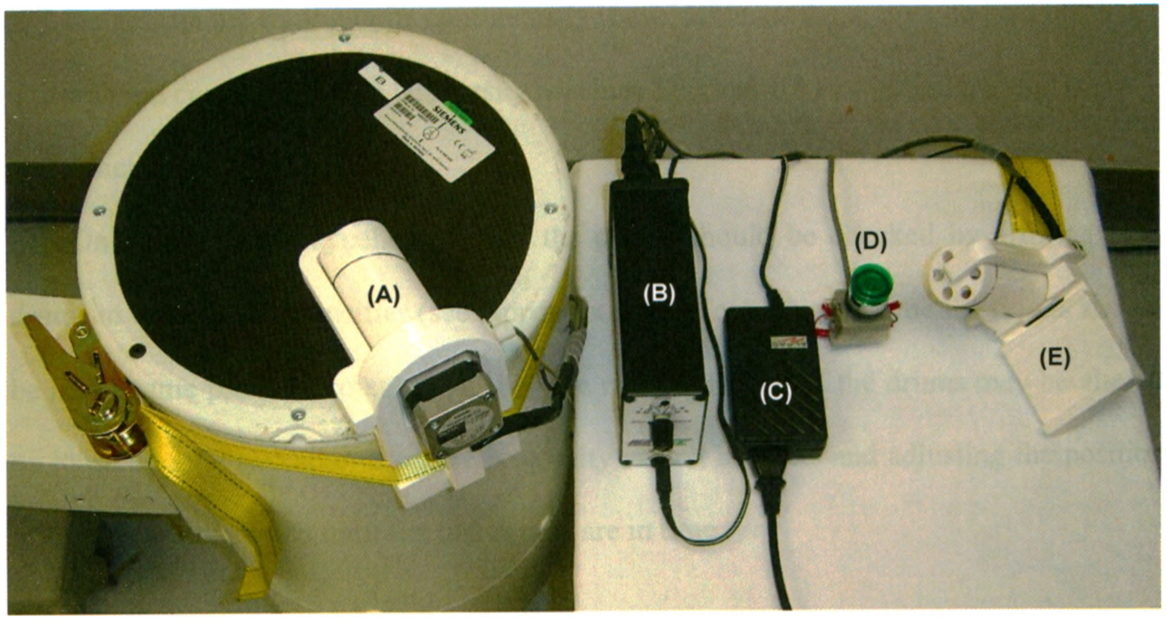

Figure G.1 The device to synchronize the fluoroscopes
(A) Drum 1 mounted to one of the image intensifiers, (B) the control console, (C) the power supply, (D) the trigger, (E) drum 2.

to 2Hz. The drums should be able to achieve 2Hz once they have been started at a lower speed.

6. If for any reason the drums lose synchronicity, the timing sequence will begin again and the trigger will begin flashing again. It will stop once synchronicity is again achieved.

Notes:

*** Do not run the timing units continuously if avoidable, as the motors do heat up. The unit was run continuously by University Machine Services for two hours, but this is not recommended.

*** On occasion, the synchronicity of the drums should be checked by affixing both drums to one image intensifier (see Appendix H). At any point in time the drums should be at the same phase of rotation. If they are not, the timing of the drums may be altered by loosening the two screws on the proximity switch brackets and adjusting the position of the proximity switch until the two drums are in time.

APPENDIX H – VALIDATION OF THE DEVICE TO SYNCHRONIZE THE FLUOROSCOPES

This appendix describes how the device for synchronizing the fluoroscopes was validated and includes details regarding verifying the synchronicity of the drums.

H.1 ENSURING SYNCHRONICITY OF THE DRUMS

The first step in the validation of the fluoroscopic synching device was to ensure that the two drums were rotating synchronously. To do this, both drums were mounted to one of the image intensifiers. Videos were captured of the units moving together (Figure H.1). One drum was slightly ahead of the other so the drums were stopped and the two screws on the proximity switch brackets (Figure H.2) were loosened to alter the switches' positions. The drums were then restarted and synchronicity was again checked. The proximity switches were adjusted until the two drums were in time.

H.2 METHOD OF VALIDATION

The two fluoroscopes were aligned such that the image intensifiers were at 90° to one another and at approximately equal vertical height (Figure H.3). The drums of the fluoroscopic synching device were attached to each image intensifier. A sloping tube was positioned such that it was approximately equidistant to the centre of each fluoroscopy unit and passed through the middle of each field of view. It was secured in this location. Three operators (one very experienced, one experienced, and one novice) were asked to begin imaging with both fluoroscopy units by depressing both foot pedals at the same time. They were then asked to place a 5/16" diameter brass ball into the tube

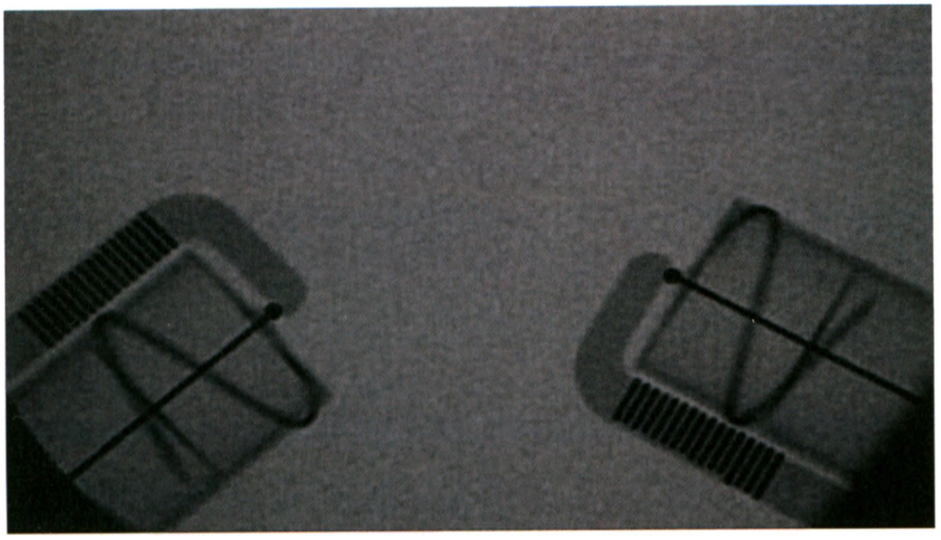

Figure H.1 Image of the two drums mounted on one image intensifier

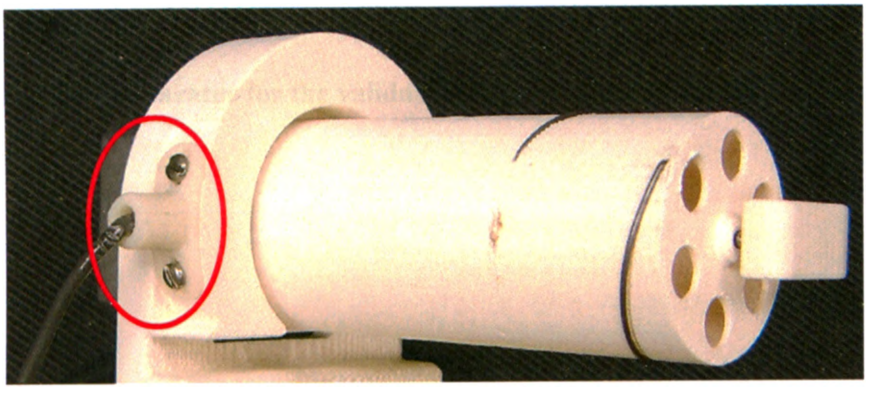

Figure H.2 The proximity switch bracket
Indicated by the oval.

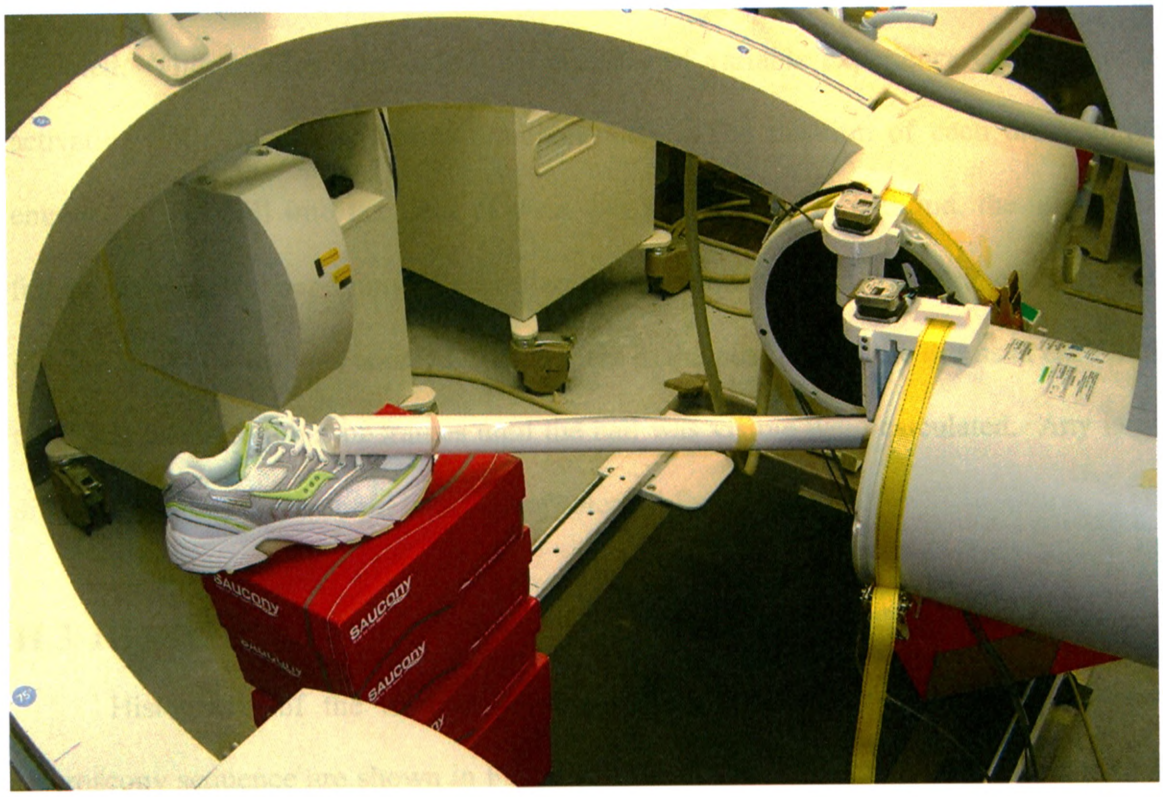

Figure H.3 Apparatus for the validation of the fluoroscopic synching device

and record its passage past the image intensifiers. The passage of the ball tested the potential for any aliasing that could occur due to the cyclic nature of the synching device. As the drums rotate at 2Hz, half a second can elapse before aliasing occurs. Each operator repeated this process 20 times.

The position of each drum at the beginning of each fluoroscopic sequence was recorded. This defined how closely an operator of variable experience could come to activating both fluoroscopy units simultaneously. The position of each drum at the entrance of the ball into the field of view was also noted. In addition, the number of frames between the beginning of each fluoroscopy sequence and the entrance of the ball into the field of view was counted. Differences in the positions of the drums at each time point and in the number of frames until the ball was visible were calculated. Any large differences in the latter could indicate the potential for aliasing.

H.3 Results

Histograms of the relative positions of the drums at the beginning of each fluoroscopy sequence are shown in Figure H.4 for the three operators over 20 trials each and in Figure H.5 for all operators over 60 trials. Given that each "tick" on the scale corresponds to one frame, the experienced operator triggered the fluoroscopes with an absolute difference of 1.15 ± 1.20 frames. The moderately experienced operator and the inexperienced operator triggered the fluoroscopes with an absolute difference of 0.70 ± 0.44 frames and 1.23 ± 1.07 frames respectively.

The passage of the brass ball past the image intensifiers could be clearly seen in the frame-by-frame analysis of the videos (Figure H.6). As the image intensifiers were located at approximately the same vertical position, the ball entered both fields of view at

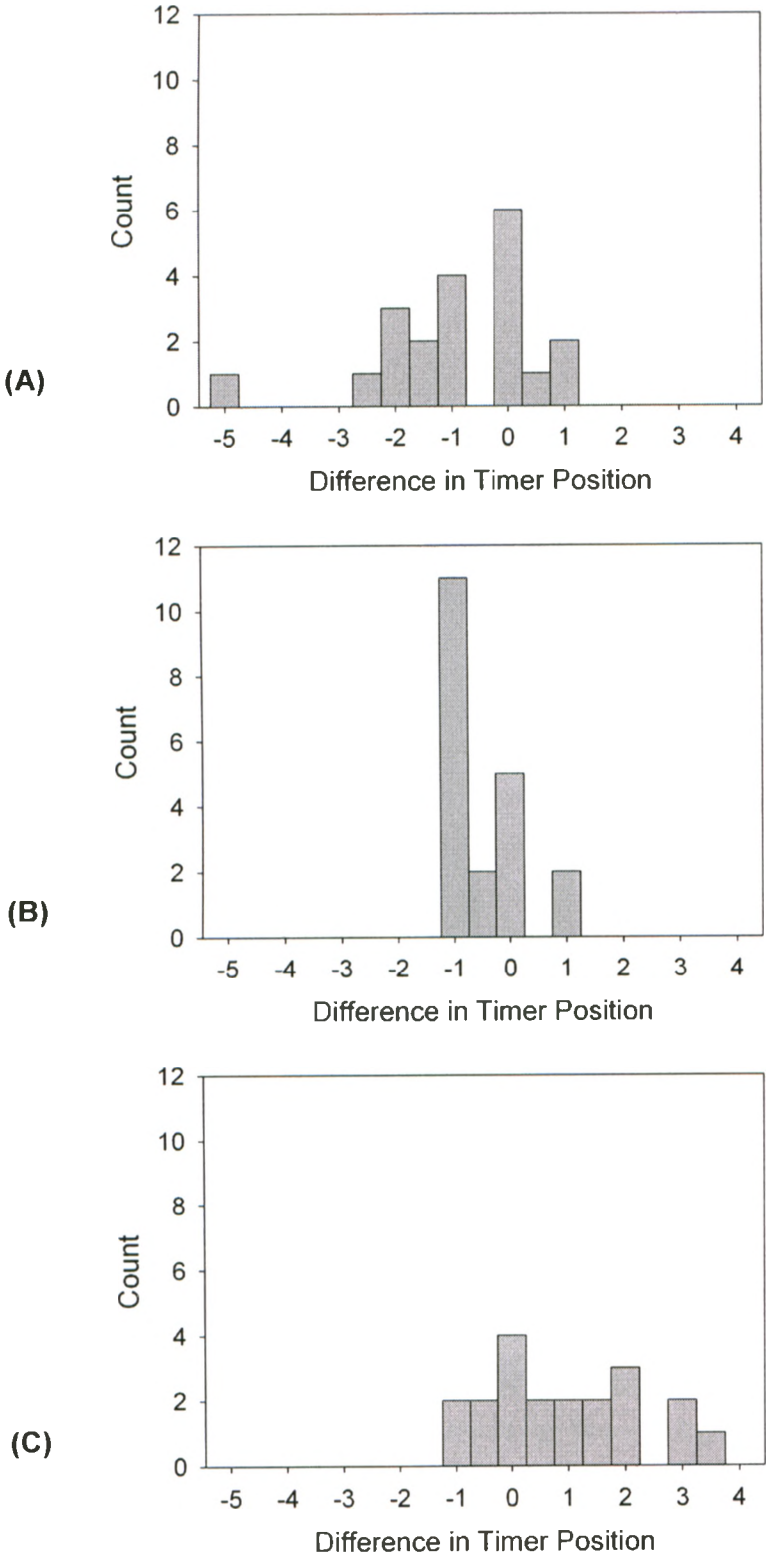

Figure H.4 Histograms of the difference in timer position between the two fluoroscopes at the time the two fluoroscopes are triggered
20 trials each for **(A)** an experienced operator, **(B)** a moderately experienced operator, and **(C)** an inexperienced operator.

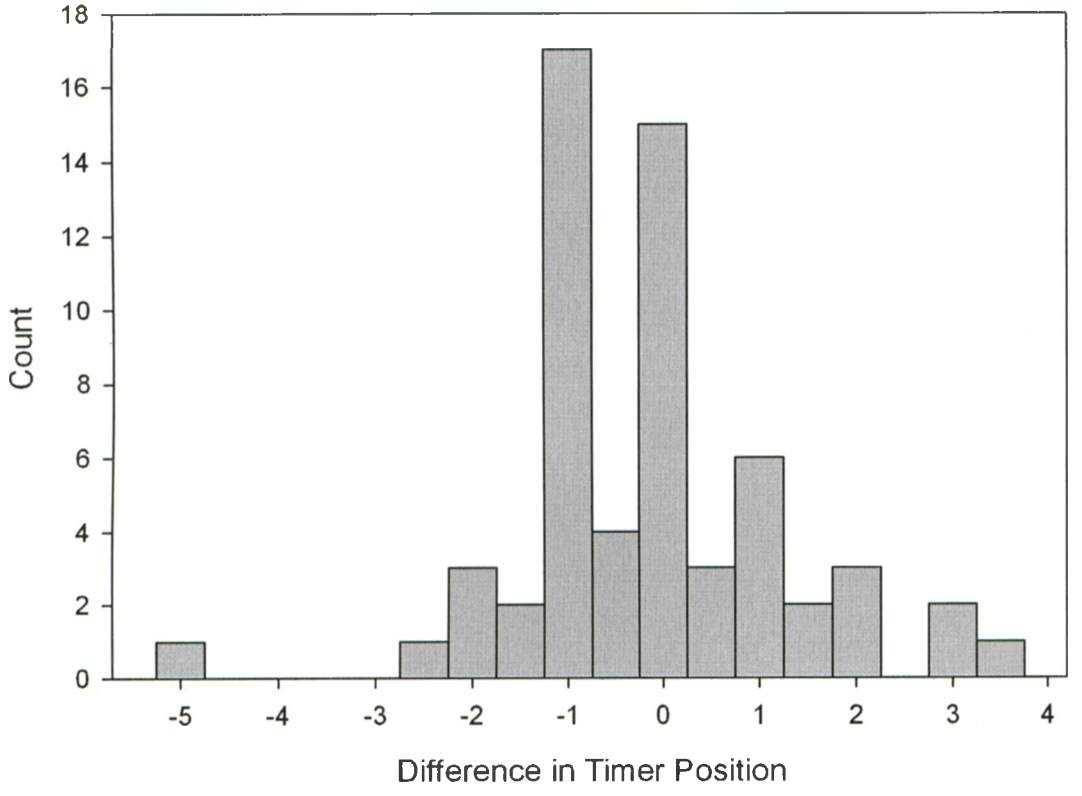

Figure H.5 Difference in timer position for all operators
Total of 60 trials.

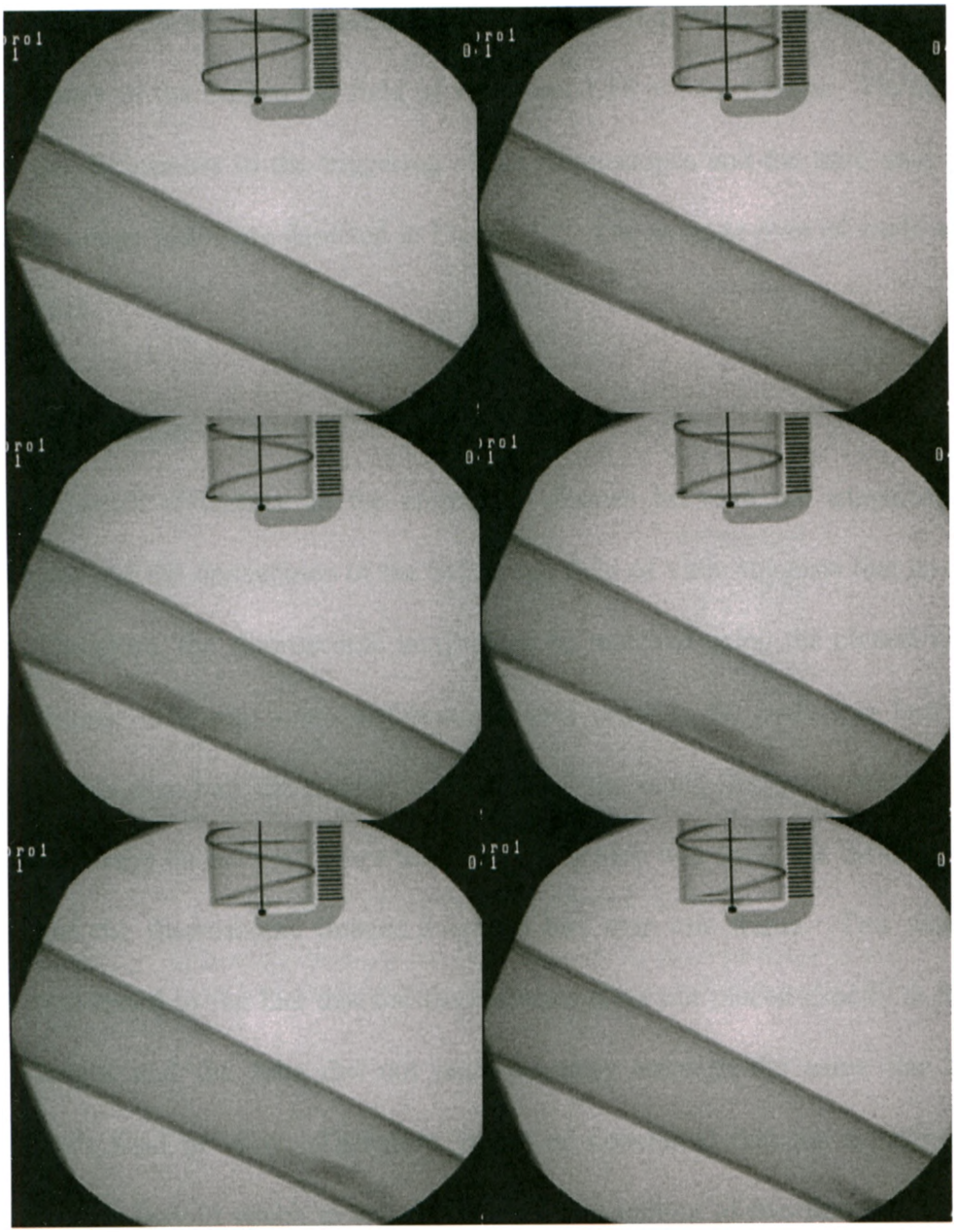

Figure H.6 Frames showing the passage of the brass ball past one of the fluoroscopes

approximately the same time. Over all 60 trials the difference in the positions of the drums at the time the ball entered the field of view was 0.22 ± 0.56 "ticks". The difference in the number of frames between the triggering of the fluoroscopy units and the appearance of the ball in the field of view was 1.18 ± 1.02 frames. The difference between the differences in the triggering of the fluoroscopes and the time until the ball entered the image frame are depicted in Figure H.7. The average over 60 trials was 0.53 ± 0.65 frames.

H.4 DISCUSSION

The small difference in the number of frames between the triggering of the fluoroscopes and the appearance of the ball in the field of view suggests that no aliasing occurs. Therefore, the fluoroscopic images can be matched using the closest matching drum positions. The maximum difference in start times in 60 trials was four frames, which was less than half the number of "ticks" on the scale, indicating that the closest match will always be correct. Once the synching device was used, the difference in the matching of the fluoroscopic images averaged less than one frame. This small error could be attributed to the fact that the fluoroscopes were not placed exactly at the same vertical height and the tube did not pass precisely through the same line in each fluoroscope's field of view. Therefore, it can be concluded that the synching device offers a reliable way in which to visually verify the matching of two fluoroscopy images in time for the purposes of RSA.

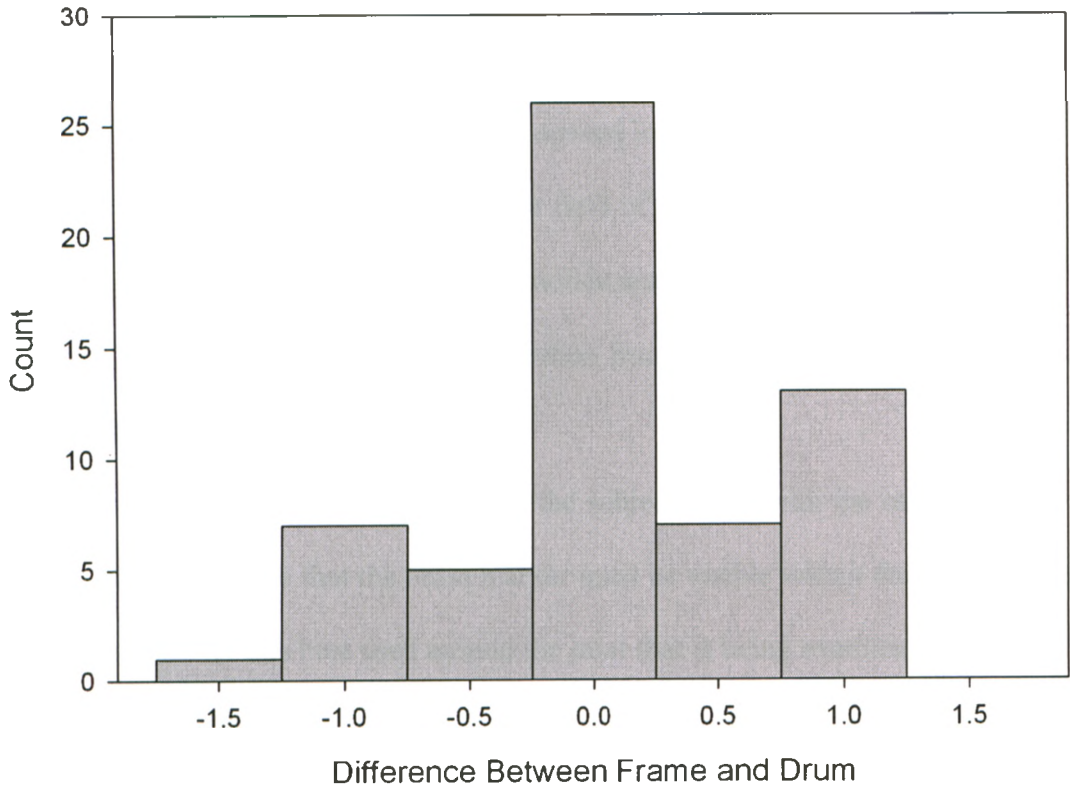

Figure H.7 Difference between the difference in the start position of the fluoroscopy units and the number of frames until the ball appeared in the field of view

APPENDIX I – USAGE OF THE DEVICE TO MATCH DATA FROM THE OPTICAL MOTION ANALYSIS SYSTEM

This appendix contains instructions for synchronizing data obtained from the RSA and optical motion analysis systems.

1. Warm up and calibrate the optical motion analysis system.
2. Position the fluoroscopes in their desired locations.
3. Place the calibration frame in the field of view of both fluoroscopes, ensuring it can also be 'seen' by the optical motion analysis system.
4. Capture the position of the calibration frame using both the fluoroscopes and the optical system.
5. Affix the brass optical marker to the subject along with the other required optical markers. Note that the brass marker must be visible within the fluoroscopes' field of view so it is best used around the joint that is being examined.
6. Collect both fluoroscopic and optical motion analysis data of the motions of interest.
7. Digitize the positions of the calibration frame markers and the brass optical marker in the fluoroscopic images and correct these for distortion. Determine the positions of these markers in the fluoroscopic laboratory coordinate system.
8. Track the motion analysis data of all markers.
9. Run the comparison program (synching.m).
    a. This creates a coordinate system using the calibration frame markers in both the fluoroscopic and optical laboratory coordinate systems.

b. It then transforms the position of the brass optical marker in the two laboratory coordinate systems into the respective frames.

10. The frames at which the position of the marker is the most similar will be outputted into the Excel file.

APPENDIX J – VALIDATION OF DEVICE TO MATCH DATA FROM THE OPTICAL MOTION ANALYSIS SYSTEM

The tertiary coordinate system for synchronizing data obtained from the RSA and optical motion analysis systems was validated as described in this appendix.

J.1 METHOD OF VALIDATION

The optical motion analysis system was calibrated. The fluoroscopes were positioned such that the image intensifiers were approximately orthogonal. The small calibration frame was used to define the RSA laboratory coordinate system. A reflective marker made of brass was mounted to the moveable tabletop of a precision cross-slide table (Model VCT514, Sowa Tool and Machine Co. Ltd., Kitchener, Ontario, Canada), which was placed such that it was angled at approximately 45° with respect to both fluoroscopes (Figure J.1). The location of the reflective marker was tracked in three-dimensional space using a four-camera real-time optical motion analysis system (Hawk cameras, EvaRT system, Motion Analysis Corp., Santa Rosa, California, USA) and also by the fluoroscopic RSA system. The position of the cross-slide table was altered in increments of approximately 4 mm along a total length of approximately 80 mm. The brass reflective marker was then placed on the end of a carbon fibre rod and moved through the RSA capture volume.

The synching device for the optical motion analysis system was used to create a tertiary coordinate system in both the optical and RSA coordinate systems, creating a common reference frame for both. The position of the brass reflective marker was determined in the common reference frame and the best match between the optical and

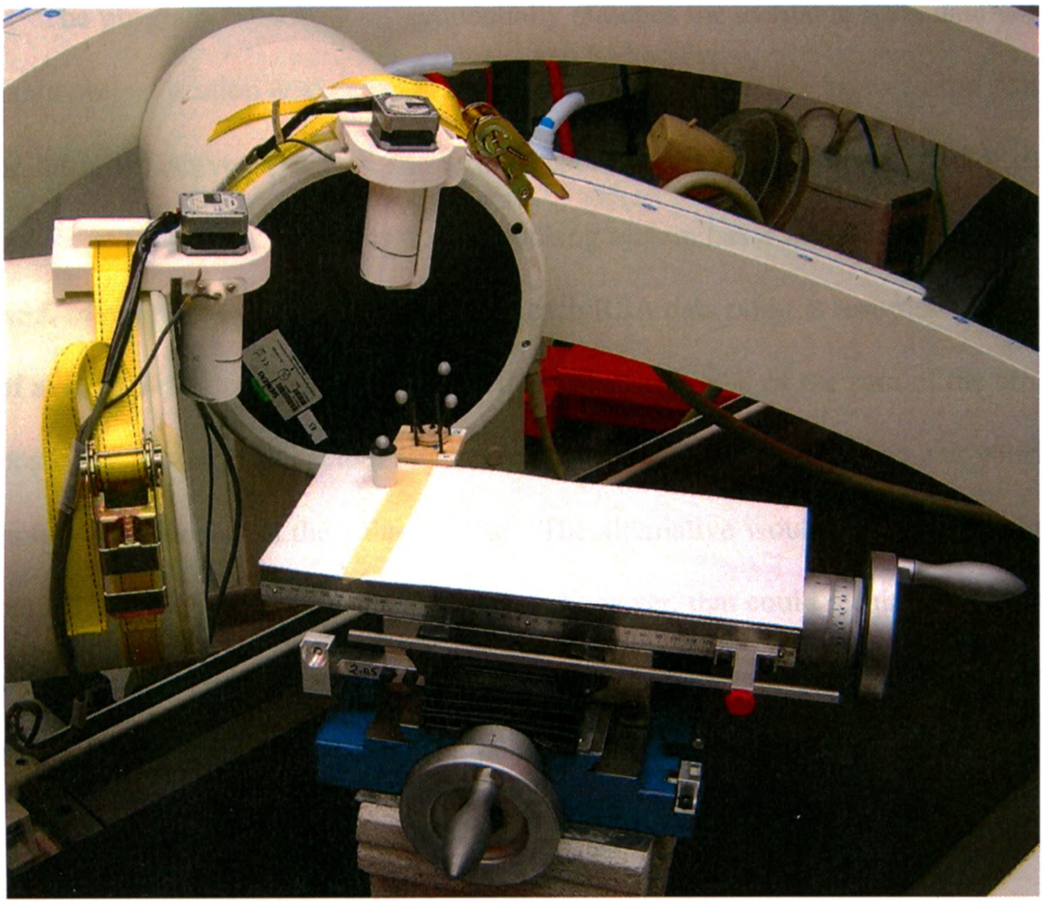

Figure J.1 Apparatus for the validation of the method to match data from the optical motion analysis system with that obtained using RSA

RSA data was found using the program "synching.m" (see Appendix D) for both step-wise and continuous test conditions. In the case of the step-wise displacements a correct match of the frames could be evaluated numerically. In the case of the continuous motion a graphical evaluation was conducted with the complete data set obtained from the optical tracking system and four small sections of data from the RSA system.

The program "synching.m" sequentially matches the available RSA data with the available optical motion analysis data and calculates the difference between the positions of the brass reflective marker in the tertiary coordinate system as a result of RSA and optical motion tracking. Since the optical tracking system has a sample rate of 60 Hz and the RSA system has a sample rate of 30 Hz, each RSA data point is recorded twice in the list of available data points. This inflates the numerical value of the sum of the errors in the positions; however the actual number is not of importance. The frame at which the minimum value occurs is the value to note. The alternative would be to remove half of the optical motion analysis system data points; however, that could result in a suboptimal match between the two systems. The optical motion analysis frame with which the first RSA data point should be matched is outputted by the program.

J.2 RESULTS

The absolute position of the reflective brass marker within the frame of the optical synching device was not the same when calculated by RSA and optical motion analysis. It was consistently different by approximately 2 mm.

The program "synching.m" correctly matched the frames of the step-wise displacements. The program "synching.m" also correctly matched the frames of the continuous tests, as may be seen in Figure J.2 and Table J.1 for one sample of 11 RSA

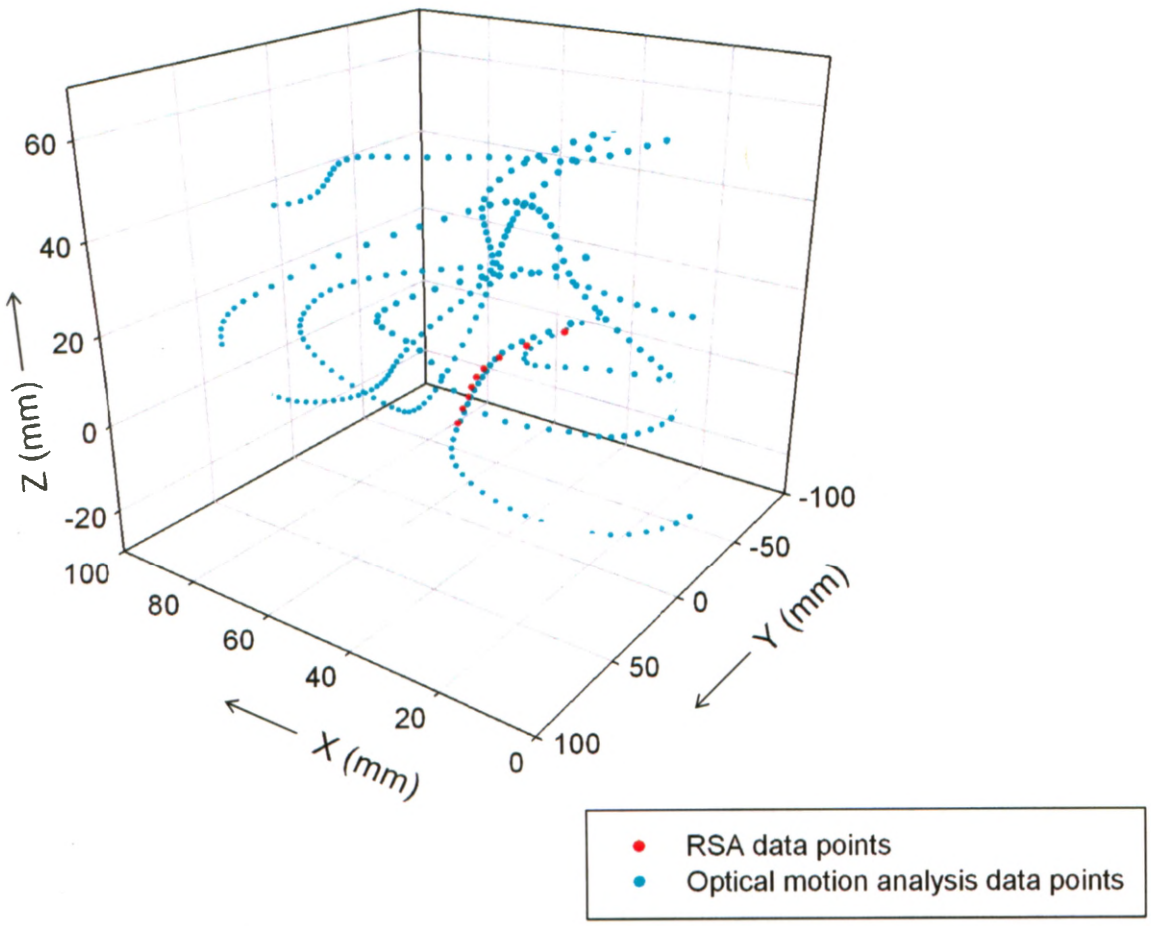

Figure J.2 Visually verifying the method to match data from the optical motion analysis system with that obtained using RSA

Table J.1 Sum of the errors in matching the data from the optical motion analysis system with that obtained using RSA

Sum for 11 data points obtained using RSA. Matched to correct location in 1112 data points obtained using the optical motion analysis system. The first point in the RSA data should be aligned with the 558th frame in the optical motion analysis data.

Optical Motion Analysis Frame Number	Sum of Errors (mm)
549	880.2
550	791.6
551	703.1
552	614.4
553	525.2
554	435.5
555	346.6
556	261.9
557	189.8
558	148.0
559	160.0
560	222.0
561	307.1
562	402.2
563	505.5
564	616.9
565	728.7
566	835.4
567	935.7

data points compared with the data obtained in 18.5 s with the optical motion analysis system.

J.3 Discussion

While the position of the brass marker was not the same in RSA and optical motion analysis systems, it was consistently offset, allowing the program to correctly match the data points taken with each system. Both step-wise and continuous trials were matched correctly.

The most difficult part about using this system of synchronization is maintaining visibility of the synchronizing marker in both optical motion analysis and RSA systems. It does not need to be simultaneously visible at all times, just enough to allow matching to take place, which as shown in the example, may be done reliably with only eleven frames.

APPENDIX K – STEPS TO FOLLOW FOR USE OF THE WOQIL LABORATORY

This appendix outlines the steps that should be followed to obtain data from the RSA system in the WOQIL laboratory.

1. Calibrate the optical tracking system while the fluoroscopes are to the side, if it is to be used – this allows for the best calibration possible.
2. Place the fluoroscopes in their desired locations.
3. If the optical tracking system is to be used, ensure that it can still "see" the desired capture volume.
4. Affix the synching devices for the fluoroscopes to the image intensifiers.
5. Calibrate the positions of the fluoroscopes either before or after the data is collected, but to be safest calibrate before so that there is the option of re-calibrating if the fluoroscopes get bumped.
   a. Be sure to place the calibration frame such that the two fiducial planes are adjacent to the two IIs.
   b. Ensure that the fiducial and control points can be identified in the images by using the markers. Record the locations of the markers in each image.
   c. Note the orientation of the calibration frame. Record which fluoroscope 'sees' F/C1 and F/C2.
6. Collect optical and fluoroscopic data being sure to turn on the synching devices prior to recording any dynamic trials.

7. Following the collection of data, place the small calibration frame for synching the data from RSA and the optical motion tracking system such that it can be located by both systems. Capture its position.
8. Image the distortion grid on each of the fluoroscopes in turn.
9. Run "pickpoints.m". (Remember to move the mouse between clicking for points that are not visible.)
    a. Digitize the calibration frame images.
    b. Digitize the distortion grid images.
    c. Digitize the images of the device for synching the optical motion analysis system.
    d. Digitize the images of any objects to be located with RSA.
10. Run "distortion_correction_points.m" for the file containing the coordinates of the points on the distortion grid.
11. Obtain the coefficients of the polynomials for distortion correction from the website www.zunzun.com.
12. Put the coefficients into the files that contain the coordinates of the points on the distortion grid.
13. Run "distortion_corection.m" for the files containing the fiducial, control, optical motion analysis synching device, and object points.
14. Run "RSA.m" for the optical motion analysis synching device and all other objects to be located.
15. Run "synching.m" to match the data from RSA and the optical motion tracking system.

16. Perform any kinematic analysis required using the three-dimensional positions of the points obtained using RSA.

Volume number	42
Issue number	9
Pages	5
Type of Use	Thesis / Dissertation
Portion	Full article
Format	Print
You are an author of the Elsevier article	Yes
Are you translating?	No
Order Reference Number	
Expected publication date	Dec 2009
Elsevier VAT number	GB 494 6272 12
Permissions price	0.00 USD
Value added tax 0.0%	0.00 USD
Total	0.00 USD

Terms and Conditions

INTRODUCTION

1. The publisher for this copyrighted material is Elsevier. By clicking "accept" in connection with completing this licensing transaction, you agree that the following terms and conditions apply to this transaction (along with the Billing and Payment terms and conditions established by Copyright Clearance Center, Inc. ("CCC"), at the time that you opened your Rightslink account and that are available at any time at http://myaccount.copyright.com).

GENERAL TERMS

2. Elsevier hereby grants you permission to reproduce the aforementioned material subject to the terms and conditions indicated.

3. Acknowledgement: If any part of the material to be used (for example, figures) has appeared in our publication with credit or acknowledgement to another source, permission must also be sought from that source. If such permission is not obtained then that material may not be included in your publication/copies. Suitable acknowledgement to the source must be made, either as a footnote or in a reference list at the end of your publication, as follows:

"Reprinted from Publication title, Vol /edition number, Author(s), Title of article / title of chapter, Pages No., Copyright (Year), with permission from Elsevier [OR APPLICABLE SOCIETY COPYRIGHT OWNER]." Also Lancet special credit - "Reprinted from The Lancet, Vol. number, Author(s), Title of article, Pages No., Copyright (Year), with permission from Elsevier."

4. Reproduction of this material is confined to the purpose and/or media for which permission is hereby given.

5. Altering/Modifying Material: Not Permitted. However figures and illustrations may be altered/adapted minimally to serve your work. Any other abbreviations, additions, deletions and/or any other alterations shall be made only with prior written authorization of Elsevier Ltd. (Please contact Elsevier at permissions@elsevier.com)

6. If the permission fee for the requested use of our material is waived in this instance, please be advised that your future requests for Elsevier materials may attract a fee.

7. Reservation of Rights: Publisher reserves all rights not specifically granted in the combination of (i) the license details provided by you and accepted in the course of this licensing transaction, (ii) these terms and conditions and (iii) CCC's Billing and Payment terms and conditions.

8. License Contingent Upon Payment: While you may exercise the rights licensed immediately upon issuance of the license at the end of the licensing process for the transaction, provided that you have disclosed complete and accurate details of your proposed use, no license is finally effective unless and until full payment is received from you (either by publisher or by CCC) as provided in CCC's Billing and Payment terms and conditions. If full payment is not received on a timely basis, then any license preliminarily granted shall be deemed automatically revoked and shall be void as if never granted. Further, in the event that you breach any of these terms and conditions or any of CCC's Billing and Payment terms and conditions, the license is automatically revoked and shall be void as if never granted. Use of materials as described in a revoked license, as well as any use of the materials beyond the scope of an unrevoked license, may constitute copyright infringement and publisher reserves the right to take any and all action to protect its copyright in the materials.

9. Warranties: Publisher makes no representations or warranties with respect to the licensed material.

10. Indemnity: You hereby indemnify and agree to hold harmless publisher and CCC, and their respective officers, directors, employees and agents, from and against any and all claims arising out of your use of the licensed material other than as specifically authorized pursuant to this license.

11. No Transfer of License: This license is personal to you and may not be sublicensed, assigned, or transferred by you to any other person without publisher's written permission.

12. No Amendment Except in Writing: This license may not be amended except in a writing signed by both parties (or, in the case of publisher, by CCC on publisher's behalf).

13. Objection to Contrary Terms: Publisher hereby objects to any terms contained in any purchase order, acknowledgment, check endorsement or other writing prepared by you, which terms are inconsistent with these terms and conditions or CCC's Billing and Payment terms and conditions. These terms and conditions, together with CCC's Billing and Payment terms and conditions (which are incorporated herein), comprise the entire agreement between you and publisher (and CCC) concerning this licensing transaction. In the event of any conflict between your obligations established by these terms and conditions and those established by CCC's Billing and Payment terms and conditions, these terms and conditions shall control.

14. Revocation: Elsevier or Copyright Clearance Center may deny the permissions described in this License at their sole discretion, for any reason or no reason, with a full refund payable to you. Notice of such denial will be made using the contact information provided by you. Failure to receive such notice will not alter or invalidate the denial. In no event will Elsevier or Copyright Clearance Center be responsible or liable for any costs, expenses or damage incurred by you as a result of a denial of your permission request, other than a refund of the amount(s) paid by you to Elsevier and/or Copyright Clearance Center for denied permissions.

LIMITED LICENSE

The following terms and conditions apply to specific license types:

15. **Translation**: This permission is granted for non-exclusive world **English** rights only unless your license was granted for translation rights. If you licensed translation rights you may only translate this content into the languages you requested. A professional translator must perform all translations and reproduce the content word for word preserving the integrity of the article. If this license is to re-use 1 or 2 figures then permission is granted for non-exclusive world rights in all languages.

16. **Website**: The following terms and conditions apply to electronic reserve and author websites:
Electronic reserve: If licensed material is to be posted to website, the web site is to be password-protected and made available only to bona fide students registered on a relevant course if:
This license was made in connection with a course,
This permission is granted for 1 year only. You may obtain a license for future website posting,
All content posted to the web site must maintain the copyright information line on the bottom of each image,
A hyper-text must be included to the Homepage of the journal from which you are licensing at http://www.sciencedirect.com/science/journal/xxxxx or, for books, to the Elsevier homepage at http://www.elsevier.com,
Central Storage: This license does not include permission for a scanned version of the material to be stored in a central repository such as that provided by Heron/XanEdu.

17. **Author website** for journals with the following additional clauses:

All content posted to the web site must maintain the copyright information line on the bottom of each image, and
The permission granted is limited to the personal version of your paper. You are not allowed to download and post the published electronic version of your article (whether PDF or HTML, proof or final version), nor may you scan the printed edition to create an electronic version,
A hyper-text must be included to the Homepage of the journal from which you are licensing at http://www.sciencedirect.com/science/journal/xxxxx,
Central Storage: This license does not include permission for a scanned version of the material to be stored in a central repository such as that provided by Heron/XanEdu.

18. **Author website** for books with the following additional clauses:
Authors are permitted to place a brief summary of their work online only.
A hyper-text must be included to the Elsevier homepage at http://www.elsevier.com.
All content posted to the web site must maintain the copyright information line on the bottom of each image
You are not allowed to download and post the published electronic version of your chapter, nor may you scan the printed edition to create an electronic version.
Central Storage: This license does not include permission for a scanned version of the material to be stored in a central repository such as that provided by Heron/XanEdu.

19. **Website** (regular and for author): A hyper-text must be included to the Homepage of the journal from which you are licensing at http://www.sciencedirect.com/science/journal/xxxxx or, for books, to the Elsevier homepage at http://www.elsevier.com.

20. **Thesis/Dissertation**: If your license is for use in a thesis/dissertation your thesis may be submitted to your institution in either print or electronic form. Should your thesis be published commercially, please reapply for permission. These requirements include permission for the Library and Archives of Canada to supply single copies, on demand, of the complete thesis and include permission for UMI to supply single copies, on demand, of the complete thesis. Should your thesis be published commercially, please reapply for permission.

21. **Other conditions:** None

v1.5

Gratis licenses (referencing $0 in the Total field) are free. Please retain this printable license for your reference. No payment is required.

If you would like to pay for this license now, please remit this license along with your payment made payable to "COPYRIGHT CLEARANCE CENTER" otherwise you will be invoiced within 30 days of the license date. Payment should be in the form of a check or money order referencing your account number and this license number 2214831483752.
If you would prefer to pay for this license by credit card, please go to http://www.copyright.com/creditcard to download our credit card payment authorization form.

Make Payment To:
Copyright Clearance Center
Dept 001
P.O. Box 843006
Boston, MA 02284-3006

If you find copyrighted material related to this license will not be used and wish to cancel, please contact us referencing this license number 2214831483752 and noting the reason for cancellation.

Questions? customercare@copyright.com or +1-877-622-5543 (toll free in the US) or +1-978-646-2777.

L.2 For Material Contained in Chapter 4

Subject	**Re: Request for Permission to Reproduce An Article**
From	JOURNAL <journal@aapm.org>
Date	Tuesday, June 23, 2009 12:53 pm
To	Angela Elizabeth Kedgley

Hi Angela,

Yes, you may have permission to reproduce the article. Thanks for checking.

Penny

----- Original Message -----
From: Angela Elizabeth Kedgley
Date: Tuesday, June 23, 2009 11:50 am

Subject: Request for Permission to Reproduce An Article
To: journal@aapm.org

Journal Manager, Medical Physics Journal
Ms Penny Slattery
AAPM
One Physics Ellipse
College Park, MD 20740-3846

Dear Ms Slattery,

I would like to request permission to reproduce the article entitled, "RSA Calibration Accuracy of a Fluoroscopy-Based System Using Non-Orthogonal Images for Measuring Functional Kinematics" by Angela Kedgley and Thomas Jenkyn which was recently published in Medical Physics (July 2009, 36[7], 3176-3180). The purpose of the reproduction is my doctoral thesis which is to be published by the University of Western Ontario. The anticipated publicated date is December 2009. Full acknowledgement of the material will be included.

Thank you very much,

Sincerely,

Angela Kedgley

APPENDIX M – ADDITIONAL COORDINATE SYSTEM DATA FROM CHAPTER 6

A second coordinate system was considered as an alternative to that recommended by the ISB. The results of its definition as well as the proposed alternative definition are compared through the kinematic angles that were presented in summary form in Chapter 6.

A graphical representation of the axes of the three scapular coordinate systems is shown in Figure M.1. The results of the kinematic analysis of the fifteen different relative orientations of the scapula and humerus models are provided in Tables M.1 through M.17. From these data it was concluded that the second alternative coordinate system was not a viable option to replace the ISB standard.

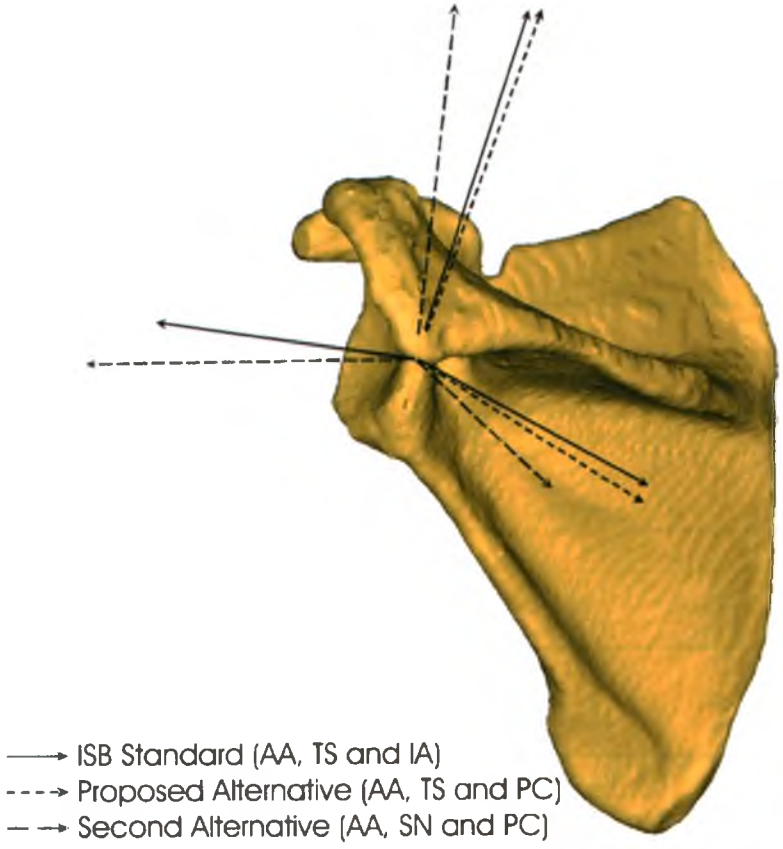

Figure M.1 Comparison of the ISB recommended axes and two alternative axes

ISB axes are based on AA, TS and IA, proposed alternative axes are based on AA, TS and PC, and second alternative axes are based on AA, SN and PC. The z-axis of the proposed alternative axes is the same as the z-axis of the ISB axes. (Image of a model created from a clinical CT scan.)

Table M.1 Coordinate system comparison – position 1

Kinematic Angle (°)	Coordinate System		
	ISB Standard	Proposed Alternative	Second Alternative
Plane of Elevation – β	31.61	20.38	1.09
Angle of Elevation – α	14.33	12.99	27.64
Internal/External Rotation - γ	23.54	11.99	10.76

Table M.2 Coordinate system comparison – position 2

Kinematic Angle (°)	Coordinate System		
	ISB Standard	Proposed Alternative	Second Alternative
Plane of Elevation – β	21.58	14.96	-2.03
Angle of Elevation – α	24.01	23.05	37.69
Internal/External Rotation - γ	15.08	7.86	9.17

Table M.3 Coordinate system comparison – position 3

Kinematic Angle (°)	Coordinate System		
	ISB Standard	Proposed Alternative	Second Alternative
Plane of Elevation – β	15.80	11.34	-5.01
Angle of Elevation – α	33.88	33.17	47.75
Internal/External Rotation - γ	11.07	5.73	8.04

Table M.4 Coordinate system comparison – position 4

Kinematic Angle (°)	Coordinate System		
	ISB Standard	Proposed Alternative	Second Alternative
Plane of Elevation – β	11.80	8.48	-7.71
Angle of Elevation – α	42.27	41.74	56.23
Internal/External Rotation - γ	8.66	4.19	7.11

Table M.5 Coordinate system comparison – position 5

Kinematic Angle (°)	Coordinate System		
	ISB Standard	Proposed Alternative	Second Alternative
Plane of Elevation – β	6.19	3.81	-12.26
Angle of Elevation – α	51.98	51.71	65.98
Internal/External Rotation - γ	2.60	-1.25	2.68

Table M.1 Coordinate system comparison – position 1

Kinematic Angle (°)	Coordinate System		
	ISB Standard	Proposed Alternative	Second Alternative
Plane of Elevation – β	31.61	20.38	1.09
Angle of Elevation – α	14.33	12.99	27.64
Internal/External Rotation - γ	23.54	11.99	10.76

Table M.2 Coordinate system comparison – position 2

Kinematic Angle (°)	Coordinate System		
	ISB Standard	Proposed Alternative	Second Alternative
Plane of Elevation – β	21.58	14.96	-2.03
Angle of Elevation – α	24.01	23.05	37.69
Internal/External Rotation - γ	15.08	7.86	9.17

Table M.3 Coordinate system comparison – position 3

Kinematic Angle (°)	Coordinate System		
	ISB Standard	Proposed Alternative	Second Alternative
Plane of Elevation – β	15.80	11.34	-5.01
Angle of Elevation – α	33.88	33.17	47.75
Internal/External Rotation - γ	11.07	5.73	8.04

Table M.4 Coordinate system comparison – position 4

Kinematic Angle (°)	Coordinate System		
	ISB Standard	Proposed Alternative	Second Alternative
Plane of Elevation – β	11.80	8.48	-7.71
Angle of Elevation – α	42.27	41.74	56.23
Internal/External Rotation - γ	8.66	4.19	7.11

Table M.5 Coordinate system comparison – position 5

Kinematic Angle (°)	Coordinate System		
	ISB Standard	Proposed Alternative	Second Alternative
Plane of Elevation – β	6.19	3.81	-12.26
Angle of Elevation – α	51.98	51.71	65.98
Internal/External Rotation - γ	2.60	-1.25	2.68

Table M.6 Coordinate system comparison – position 6

Kinematic Angle (°)	Coordinate System		
	ISB Standard	Proposed Alternative	Second Alternative
Plane of Elevation – β	6.71	5.16	-11.80
Angle of Elevation – α	62.90	62.58	76.90
Internal/External Rotation - γ	6.71	3.31	6.66

Table M.7 Coordinate system comparison – position 7

Kinematic Angle (°)	Coordinate System		
	ISB Standard	Proposed Alternative	Second Alternative
Plane of Elevation – β	4.89	3.87	-13.53
Angle of Elevation – α	71.40	71.17	85.40
Internal/External Rotation - γ	7.52	4.32	7.91

Table M.8 Coordinate system comparison – position 8

Kinematic Angle (°)	Coordinate System		
	ISB Standard	Proposed Alternative	Second Alternative
Plane of Elevation – β	3.21	2.68	-15.25
Angle of Elevation – α	80.18	80.02	94.16
Internal/External Rotation - γ	6.95	3.87	7.74

Table M.9 Coordinate system comparison – position 9

Kinematic Angle (°)	Coordinate System		
	ISB Standard	Proposed Alternative	Second Alternative
Plane of Elevation – β	0.88	0.84	-17.76
Angle of Elevation – α	89.18	89.14	103.12
Internal/External Rotation - γ	8.56	5.52	9.95

Table M.10 Coordinate system comparison – position 10

Kinematic Angle (°)	Coordinate System		
	ISB Standard	Proposed Alternative	Second Alternative
Plane of Elevation – β	9.23	7.05	-9.06
Angle of Elevation – α	54.24	53.81	68.23
Internal/External Rotation - γ	39.28	35.57	38.56

Table M.11 Coordinate system comparison – position 11

Kinematic Angle (°)	Coordinate System		
	ISB Standard	Proposed Alternative	Second Alternative
Plane of Elevation – β	9.45	7.20	-9.43
Angle of Elevation – α	53.39	52.95	67.38
Internal/External Rotation - γ	-27.16	-30.92	-27.94

Table M.12 Coordinate system comparison – position 12

Kinematic Angle (°)	Coordinate System		
	ISB Standard	Proposed Alternative	Second Alternative
Plane of Elevation – β	24.11	18.11	-0.01
Angle of Elevation – α	25.83	24.73	39.38
Internal/External Rotation - γ	-6.99	-13.62	-13.61

Table M.13 Coordinate system comparison – position 13

Kinematic Angle (°)	Coordinate System		
	ISB Standard	Proposed Alternative	Second Alternative
Plane of Elevation – β	23.81	18.34	0.14
Angle of Elevation – α	27.92	26.83	41.49
Internal/External Rotation - γ	60.28	54.12	54.04

Table M.14 Coordinate system comparison – position 14

Kinematic Angle (°)	Coordinate System		
	ISB Standard	Proposed Alternative	Second Alternative
Plane of Elevation – β	74.53	72.28	32.53
Angle of Elevation – α	22.69	19.78	30.65
Internal/External Rotation - γ	93.47	91.06	67.33

Table M.15 Coordinate system comparison – position 15

Kinematic Angle (°)	Coordinate System		
	ISB Standard	Proposed Alternative	Second Alternative
Plane of Elevation – β	89.03	88.94	51.54
Angle of Elevation – α	33.39	30.35	37.54
Internal/External Rotation - γ	114.83	114.72	91.63

Table M.16 Coordinate system comparison – average difference between the ISB and alternative coordinate systems
Over all 15 positions.

	Coordinate System	
Kinematic Angle (°)	**Proposed Alternative**	**Second Alternative**
Plane of Elevation – β	-3.29	-23.46
Angle of Elevation – α	-0.90	12.80
Internal/External Rotation - γ	-4.53	-5.62

Table M.17 Coordinate system comparison – standard deviation in the difference between the ISB and alternative coordinate systems
Over all 15 positions.

	Coordinate System	
Kinematic Angle (°)	**Proposed Alternative**	**Second Alternative**
Plane of Elevation – β	3.03	7.46
Angle of Elevation – α	0.92	2.84
Internal/External Rotation - γ	2.64	8.63

APPENDIX N – ETHICS PERMISSIONS

The following are the ethics approvals that were obtained in order to conduct the clinical study described in Chapter 7.

Office of Research Ethics
The University of Western Ontario
Room 4180 Support Services Building, London, ON, Canada N6A 5C1
Telephone: (519) 661-3036 Fax: (519) 850-2466 Email: ethics@uwo.ca
Website: www.uwo.ca/research/ethics

Use of Human Subjects - Ethics Approval Notice

Principal Investigator: Dr. T.R. Jenkyn
Review Number: 15278 **Revision Number:** 1
Review Date: April 30, 2009 **Review Level:** Expedited
Protocol Title: *Determination of normal and pathological glenohumeral joint motion using bi-planar x-ray fluoroscopy*
Department and Institution: Mechanical & Materials Engineering, University of Western Ontario
Sponsor:
Ethics Approval Date: June 9, 2009 **Expiry Date:** June 30, 2009
Documents Reviewed and Approved: Revised co-investigators, revised study methodology, revised risks, and revised Letter of Information and Consent Form dated May 22, 2009.
Documents Received for Information:

This is to notify you that The University of Western Ontario Research Ethics Board for Health Sciences Research Involving Human Subjects (HSREB) which is organized and operates according to the *Tri-Council Policy Statement: Ethical Conduct of Research Involving Humans* and the Health Canada/ICH Good Clinical Practice Practices: Consolidated Guidelines; and the applicable laws and regulations of Ontario has reviewed and granted approval to the above referenced revision(s) or amendment(s) on the approval date noted above. The membership of this REB also complies with the membership requirements for REB's as defined in Division 5 of the Food and Drug Regulations.

The ethics approval for this study shall remain valid until the expiry date noted above assuming timely and acceptable responses to the HSREB's periodic requests for surveillance and monitoring information. If you require an updated approval notice prior to that time you must request it using the UWO Updated Approval Request Form.

During the course of the research, no deviations from, or changes to, the protocol or consent form may be initiated without prior written approval from the HSREB except when necessary to eliminate immediate hazards to the subject or when the change(s) involve only logistical or administrative aspects of the study (e.g. change of monitor, telephone number). Expedited review of minor change(s) in ongoing studies will be considered. Subjects must receive a copy of the signed information/consent documentation.

Investigators must promptly also report to the HSREB:

a) changes increasing the risk to the participant(s) and/or affecting significantly the conduct of the study;
b) all adverse and unexpected experiences or events that are both serious and unexpected;
c) new information that may adversely affect the safety of the subjects or the conduct of the study.

If these changes/adverse events require a change to the information/consent documentation, and/or recruitment advertisement, the newly revised information/consent documentation, and/or advertisement, must be submitted to this office for approval.

Members of the HSREB who are named as investigators in research studies, or declare a conflict of interest, do not participate in discussion related to, nor vote on, such studies when they are presented to the HSREB.

Chair of HSREB: Dr. Joseph Gilbert

Ethics Officer to Contact for Further Information			
☐ Janice Sutherland	☒ Elizabeth Wambolt	☐ Grace Kelly	☐ Denise Grafton

This is an official document. Please retain the original in your files.

cc: ORE File
LHRI

LAWSON HEALTH RESEARCH INSTITUTE

CLINICAL RESEARCH IMPACT COMMITTEE

RESEARCH OFFICE REVIEW NO.: R-08-490

PROJECT TITLE: Determination of normal and pathological glenohumeral joint motion using bi-planar x-ray fluoroscopy

PRINCIPAL INVESTIGATOR: Dr. T Jenkyn

DATE OF REVIEW BY CRIC: February 12, 2009

Health Sciences REB#: 15278

Please be advised that the above project was reviewed by the Clinical Research Impact Committee and the project:

Was Approved

PLEASE INFORM THE APPROPRIATE NURSING UNITS, LABORATORIES, ETC. BEFORE STARTING THIS PROTOCOL. THE RESEARCH OFFICE NUMBER MUST BE USED WHEN COMMUNICATING WITH THESE AREAS.

Dr. David Hill
V.P. Research
Lawson Health Research Institute

All future correspondence concerning this study should include the Research Office Review Number and should be directed to Sherry Paiva, CRIC Liaison, LHSC, Rm. C210, Nurses Residence, South Street Hospital.

cc: Administration